FZD-501

ANNUAL REPORT 2007

INSTITUTE OF SAFETY RESEARCH

Forschungszentrum
Dresden Rossendorf

Annual Report 2007

Institute of Safety Research

Editors:
Prof. Dr. Frank-Peter Weiss
Prof. Dr. Udo Rindelhardt

Forschungszentrum
Dresden Rossendorf

Cover Picture: Swirling flow in an electrochemical cell.
The flow is driven by electromagnetic forces due to a horizontal magnetic field and the current density distribution between the electrodes (vertical red lines). Streamlines in the volume and velocity contours in a cross section are shown.

CONTENTS

Preface

Selected reports

Preface

The Institute of Safety Research (ISR) is one of the six Research Institutes of Forschungszentrum Dresden-Rossendorf e.V. (FZD e.V.), which is a member institution of the Wissenschaftsgemeinschaft Gottfried Wilhelm Leibniz (Leibniz Association).

Together with the Institute of Radiochemistry, ISR implements the research programme „Safety and Environment", which is one of the three scientific programmes of FZD. In the framework of this research programme, the institute is responsible for the programme areas "Plant and Reactor Safety" and "Thermal Fluid Dynamics", respectively (see Table 1). By participating in the development and operation of a pulsed photo-neutron source at the radiation source ELBE (**E**lectron **l**inear accelerator for **b**eams of high brilliance and low **e**mittance), we also contribute to the project "Neutron Induced Processes", which is part of the FZD programme dedicated to the structure of matter.

The research of ISR aims at assessing and enhancing the safety of industrial plants and at improving the environmental sustainability of the processes involved. The applications are mainly related to nuclear power plants of present and future designs.

To achieve the goals that were previously mentioned, the institute performs research in nuclear reactor physics, thermal fluid dynamics including magneto-hydrodynamics (MHD), and in materials sciences.

The activities in materials are related to the irradiation induced ageing of nuclear reactor components. The thermal fluid dynamics research work is essentially based on the experiments performed at the **T**ransient Tw**o**-**P**hase **Flow** Test Facility, TOPFLOW. TOPFLOW is one of the large research and user facilities of FZD and represents the reference thermal hydraulic experiment of the so-called "German CFD (Computational Fluid Dynamics) Initiative" in nuclear reactor safety research. The development and validation of our reactor dynamics code DYN3D coupled to thermal hydraulic computation models for the safety analyses of current and future nuclear reactors is a further asset of ISRs portfolio. DYN3D became an integral part of the European software platform NURESIM for the numerical simulation of nuclear reactors. There are about 12 organisations using DYN3D in seven European countries and Russia.

Programme / Programme area	Project / User facility
Safety and environment / Plant and reactor safety	Accident analysis of nuclear reactors
	Safety of materials and components
	Particle and radiation transport
Safety and environment / Thermal fluid dynamics	Magneto-Hydrodynamics
	Thermal fluid dynamics of multi-phase flows
Safety and environment / User facility TOPFLOW	Transient two-phase flow test facility
Structure of matter / Sub-atomic physics	Neutron induced processes

Table 1. Research projects and user facility of the Institute of Safety Research, 2007

Our work is financed through the basic funding of FZD, as well as by external funds from public research grants and from contracts with the industry. In 2007, 43 % (3.173 k€) of our total expenditure were covered by such external funds with 13 % from research grants of the Federal Government, 15 % originated from Deutsche Forschungsgemeinschaft, 6 % from the EU, and 9 % from research contracts mainly with the industry (see Fig.1). The deployment of the total budget on the different projects and the user facility TOPFLOW (see Table 1) is illustrated in Fig. 2.

Together with the Dresden Technical University and with the Zittau University of Applied Sciences, the ISR represents the East German Centre of Competence in Nuclear Technology (Kompetenzzentrum Ost für Kerntechnik) which in turn is a member of the German Alliance for Competence in Nuclear Technology (Kompetenzverbund Kerntechnik). As such, the ISR also takes care to keep and promote the expertise in nuclear engineering. For that end, a strategic partnership was established between Kompetenzzentrum Ost and Vattenfall Europe Nuclear Energy (VENE).

Beyond this, ISR in general cares for the next generation of young scientists by supervising PhD, Master, and Diploma students for example. The quality of the education at ISR is underlined by the prizes awarded to our PhD students. Hans-Georg Willschütz was awarded the Karl-Wirtz-Preis 2007 of the German Nuclear Society for his theses on the thermo-mechanical analysis and simulation of a reactor pressure vessel during the late phase of a core melt accident. André Bieberle became award winner of the ICONE-15 (15th International Conference on Nuclear Engineering) Students Competition in Nagoya/Japan for his presentation on the measurement of the void distribution in BWR fuel elements by gamma ray tomography which was performed in close collaboration with AREVA.

Amongst the many excellent results obtained in 2007, two deserve particular reference.

Nuclear reactor pressure vessels (RPV) are subject to ageing due to fast neutron irradiation during operation. This effect is of growing importance in the context of the utilities efforts for lifetime extension of their reactors up to 60 years. The assessment of the margins to brittle fracture relies on the irradiation of so-called surveillance specimens which are exposed to higher fast neutron flux than the RPV. The influence of the neutron flux on the materials damaging at equal fluence has been insufficiently studied. To cope with this problem, additional safety factors are often applied when transferring the fracture mechanical properties obtained for the surveillance specimens to the RPV. Therefore, a typical weld material was exposed to the same fluence at neutron fluxes which differed by a factor of 34. Small angle neutron scattering analyses revealed that the sizes of the irradiation induced defects containing vacancies and foreign atoms (e.g. Cu) differ by factor 2 whilst the integral defect contents of the material is almost identical. Applying a rate theoretical model to the growth kinetics of the defects, it became clear that the growth rate is almost flux independent at low flux φ while it goes with $1/\sqrt{\varphi}$ at higher fluxes (Bergner, F., et al., Flux dependence of cluster formation in neutron irradiated weld material, J. of Physics: Condensed Matter 20 (2008) 104262). The theory also provided the transitional flux φ_t separating those two typical ranges. The comparison with that value showed that for the given irradiation conditions the lower flux was less than φ_t and the higher one being far above that value. Nevertheless, the different defect sizes had no significant influence on the mechanical properties of the weld material. This fact substantiates the hypothesis that the mechanical properties are mainly determined by the integral volume content of the defects, whereas the defect sizes seem to be of minor influence. However, this hypothesis has to be underpinned by further studies.

In the field of thermal hydraulics, the Rossendorf wire mesh sensors have been the standard technology for the tomography of two-phase flows at high volumetric void contents. The disadvantage of this technology is that it is intrusive and therefore leads to slight disturbances of the flow. This disadvantage can now be overcome by our ultra fast electron beam X-ray computed tomography. The innovative technology is based on a deflected electron beam scanning a circular tungsten target which surrounds the pipe flow. The resulting scanned X-ray spot radiates through the flow covering an angle range of almost 360°, as the spot travels

across the target. The detectors are also azimuthally arranged around the flow with a slight axial displacement from the tungsten target. This arrangement allows image rates of up to 7 kHz with a spatial resolution in the millimetre range (Bieberle, M., et al., Ultra fast limited-angle type X-ray tomography, Appl. Phys. Lett. 91, 123516, 2007). The new technology provides unique insights into the dynamic structure of two-phase flows. The patented technique (Hampel, U. et al., Anordnung zur Röntgen-Computertomographie mit abgelenktem Elektronenstrahl, Patent DE 102007040778.7-54) represents the world record in flow tomography.

During the reporting period, the ISR organised important meetings and workshops with international participation, such as the international workshop on "Multi-Phase Flow: Simulation, Experiment and Application", which was jointly hosted by ISR and ANSYS/CFX®, and which continues the series of meetings on that topic in Dresden-Rossendorf. Moreover, we organised and hosted the "2nd International Workshop on Measuring Techniques for Liquid Metal Flows", which was supported by Deutsche Forschungsgemeinschaft in the framework of the Collaborative Research Centre SFB 609 "Electromagnetic flow control in metallurgy, crystal growth, and electro-chemistry". Finally, it is worth mentioning the "International Conference on Multi-Phase Flow" (ICMF) that took place in Leipzig in July 2007. The ISR supported this conference as member of the Local Organising Committee.

Meetings such as these underline the national and international scientific reputation of the Institute of Safety Research.

In November 2007, the scientific quality of FZD was evaluated by the "Deutscher Wissenschaftsrat". The result of this evaluation will also constitute the base for the decision about the future assignment of FZD to one of the German Science Associations. The staff members of the ISR excellently presented their results and prospective research programmes to the evaluation committee, which was impressed by the quality of the work performed at FZD. The first response of the committee members gives rise to hope for a very positive result of the evaluation.

I would like to thank all staff members of the institute for their high quality work and for making the year 2007 another successful one for ISR.

F.-P. Weiß   Rossendorf, 7 April 2008

Fig. 1: Funding sources 2007

basic budget
57%

research orders
(industry, public orders)
9%

research grants from EU
6%

research grants
from DFG
15%

public research grants
from BMBF, BMWi, DAAD, ...
13%
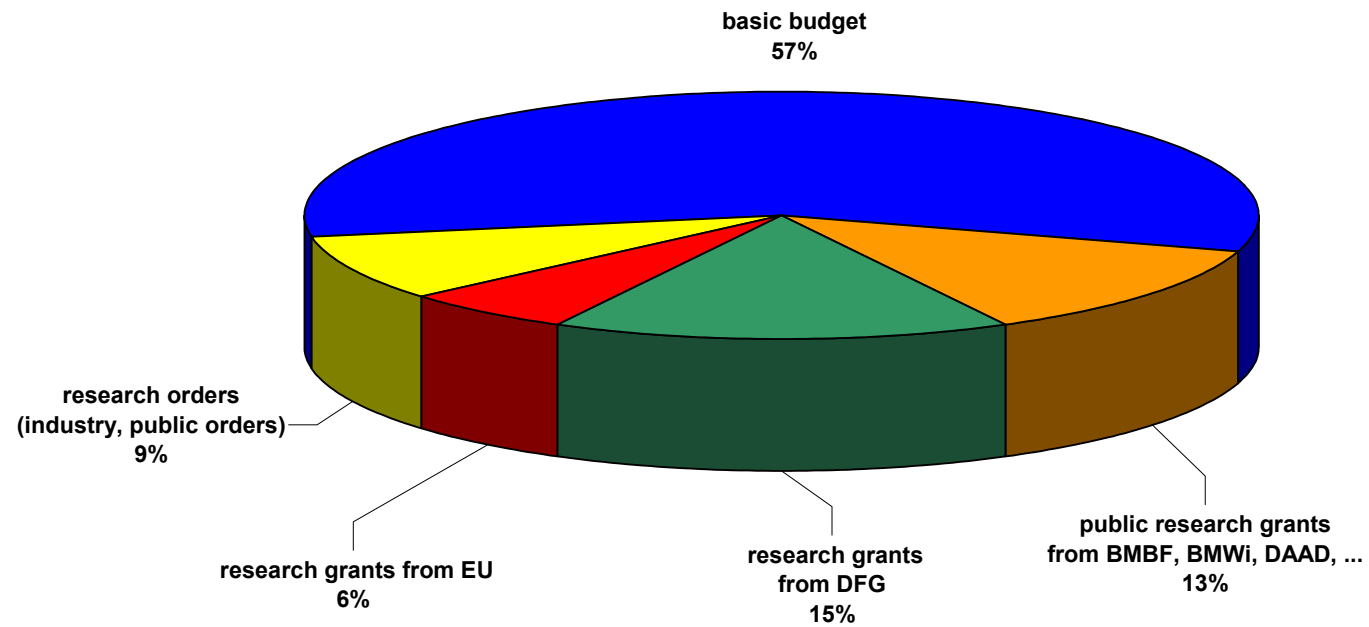
Fig. 2: Deployment of funding on the projects and user facilities 2007

TOPFLOW
13%

Thermal fluid dynamics of
multi-phase flows
18%

Accident analysis of
nuclear reactor
17%

Safety of material and
components
20%

Magneto-hydrodynamics
28%

Neutron induced
processes
1%

Particle and radiation
transport
3%
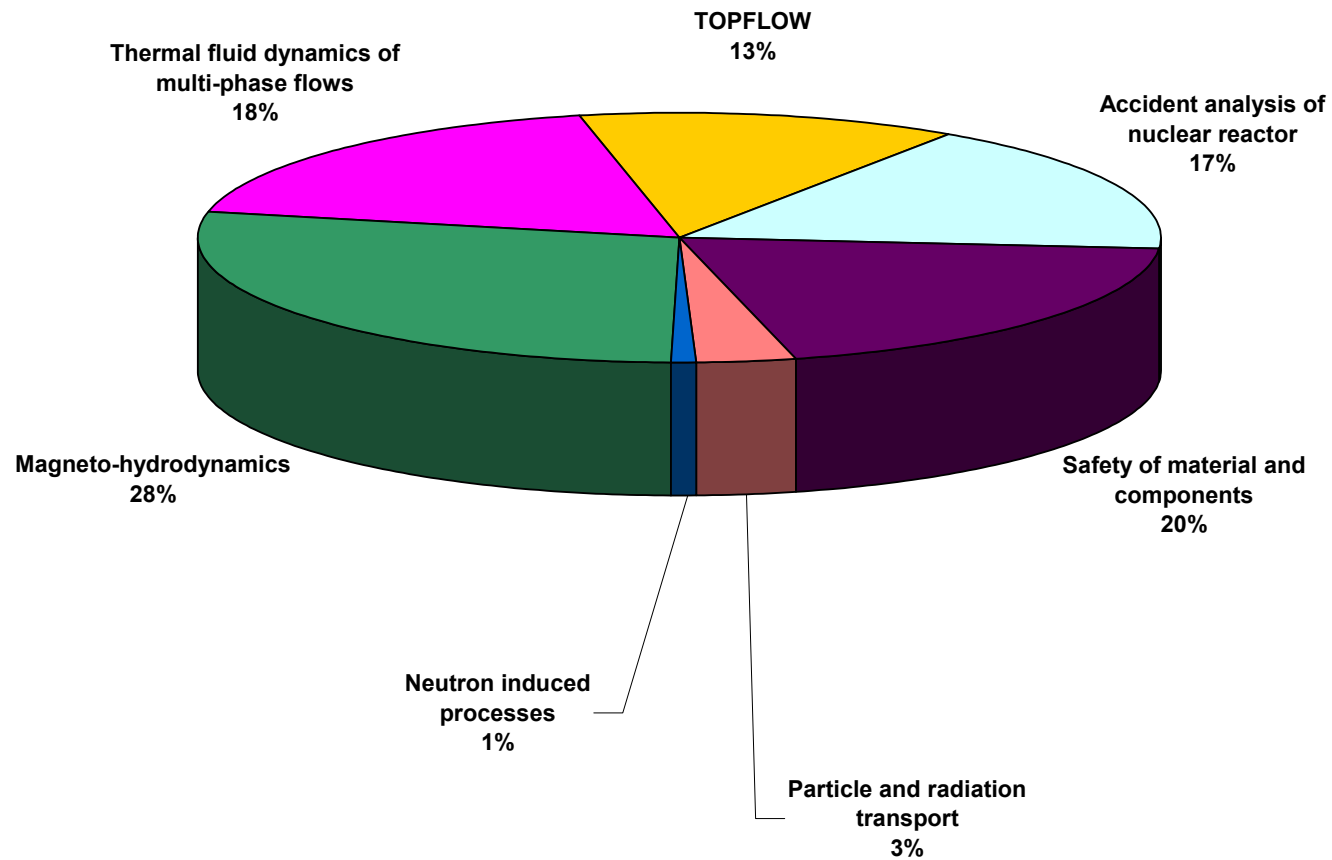
Selected reports

EXPERIMENTS AND CFD-MODELLING OF INSULATION DEBRIS TRANSPORT PHENOMENA IN WATER FLOW—DEVELOPMENT AND VALIDATION OF A CFD-STRAINER MODEL

Alexander Grahn, Gregory Cartland-Glover, Eckhard Krepper, Sören Alt[1], Wolfgang Kästner[1], and André Seeliger[1]

1.   Introduction

The investigation of insulation debris generation, transport and sedimentation becomes important with regard to nuclear reactor safety, when considering the long-term behaviour of emergency core cooling systems during all types of loss of coolant accidents (LOCA). The insulation debris released near the break during a LOCA incident can be transported into the containment sump and obstruct the suction strainer plates of the emergency core cooling system (Fig. 1).
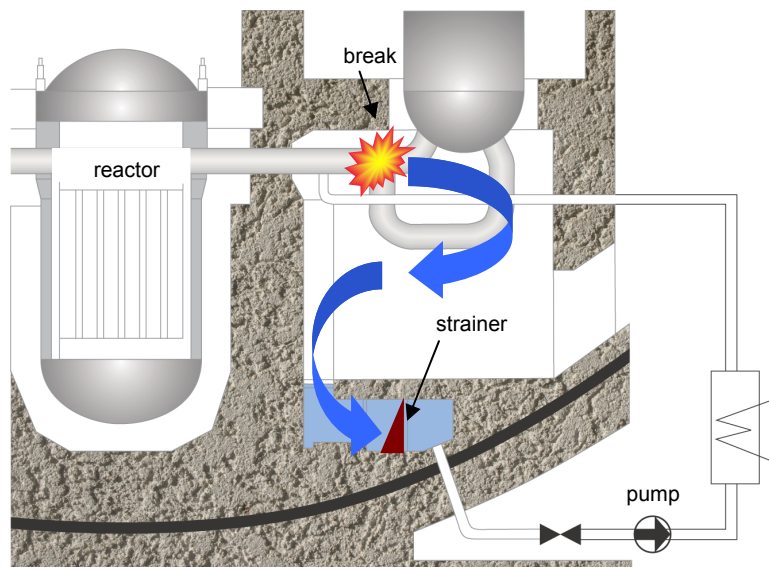
Fig. 1: Loss of coolant accident

A joint research project performed in cooperation between the University of Applied Science Zittau/Görlitz and Forschungszentrum Dresden-Rossendorf deals with the experimental investigation of particle transport phenomena in coolant flow and the development of CFD models for its simulation [1]. The present paper reports on efforts in modelling the pressure drop buildup at strainers obstructed by fibrous materials and the implementation of the strainer model into the commercial, general-purpose CFD code ANSYS-CFX.

2.   Theoretical strainer model

Filter cakes composed of fibrous materials have two particular features: (1) They are of very high porosity, and (2), due to the deformability of the fibers, such cakes can be easily compressed under the action of fluid drag forces or an external compacting pressure. A semi-empirical model has been developed for calculating the pressure drop across beds of this class of materials as a function of superficial velocity and material properties [2].

---

[1] University of Applied Sciences Zittau/Görlitz

The general relationship between superficial velocity U of the continuous phase and the pressure drop Δp over a layer of porous material of thickness L in streamwise direction reads

$$\frac{\Delta p}{L} = -\left(a\mu U + b\rho U^2\right)$$ (1)

where μ and ρ are dynamic viscosity and density of the continuous phase. Hence, the flow resistance of a porous layer is made up of two parts. The first one, which results from viscous forces, depends linearly on velocity, while the second one, resulting from inertial effects, is proportional to the square of velocity. The relative importance of both parts is weighted by empirical coefficients a and b. Even at Reynolds numbers less than 1, based on the pore diameter, inertial effects become significant.

For flow through beds of fibrous material with constant porosity Davies [3] suggested

$$\frac{\Delta p}{L} = -\left\{a\left(A_S\rho_S\right)^2\left(1-\varepsilon\right)^{1.5}\left[1+a_0\left(1-\varepsilon\right)^3\right]\mu U + b\frac{A_S\rho_S\left(1-\varepsilon\right)}{\varepsilon^3}\rho U^2\right\}$$ (2)

where A_S is the mass specific surface of the fibers, ρ_S their material density and ε the bed porosity (index "s" denotes "solid"). Based on a large amount of experimental data, Ingmanson et al. [4] found universal values of 3.5 and 57 for coefficients a and a_0, while b takes a value of 0.66.

A simple force balance shows that the compacting pressure resulting from fluid drag increases in streamwise direction along the fiber bed. As fiber beds are compressible, this leads to a porosity distribution with a maximum at the upstream and a minimum at the downstream end, Fig. 2. Therefore, Eq. (2) can only be used to calculate the differential pressure drop $d(\Delta p)/dx$ from local porosity values $\varepsilon(x)$. Hence, integration of Eq. (2) in streamwise direction is required to obtain the total pressure drop Δp over the fiber bed length L.
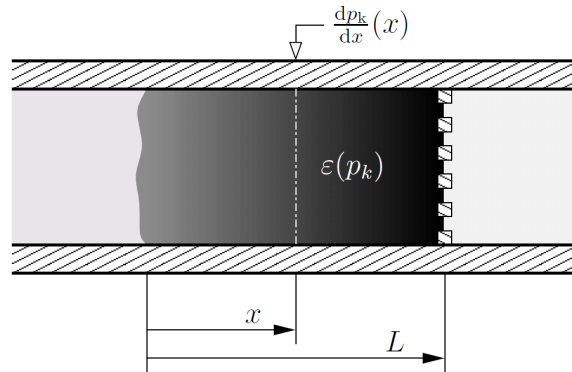
Fig. 2: Fiber bed at a strainer

The local change in compacting pressure dp_k/dx and the pressure drop $d(\Delta p)/dx$ of the flow have the same absolute value but are opposite in sign. For dp_k/dx it follows from eq. (2)

$$\frac{dp_k}{dx} = -\frac{d(\Delta p)}{dx} = a\left(A_s\rho_s\right)^2\left(1-\varepsilon\right)^{1.5}\left[1+a_0\left(1-\varepsilon\right)^3\right]\mu U + b\frac{A_s\rho_s\left(1-\varepsilon\right)}{\varepsilon^3}\rho U^2$$ (3)

As stated above, porosity itself is a function of the compacting pressure. For a given insulation material this relationship must be determined experimentally. The measurement principle is depicted in Fig. 3.
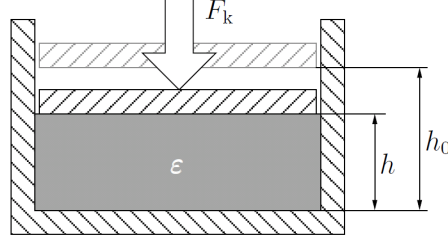
Fig. 3: Compacting measurement principle

A known quantity m_S of insulation material, placed into a vertical cylinder with cross sectional area A, is subject to a uniform compacting pressure p_k, resulting from an externally applied force F_k.

The porosity ε is calculated from height h as

$$\varepsilon = 1 - \frac{m_\mathrm{s}}{\rho_\mathrm{s} A h} \tag{4}$$

The four parameter empirical equation

$$\varepsilon(p) = \varepsilon_\infty + (\varepsilon_0 - \varepsilon_\infty) e^{-Cp^D} \tag{5}$$

has proved to reproduce measured profiles $\varepsilon(p_\mathrm{k})$ especially well. Fig. 4 illustrates the expected profile as well as two of the parameters, the porosities and at zero and infinite compacting pressures.
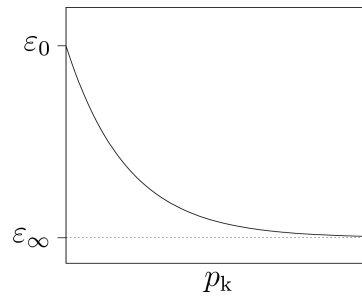
Fig. 4: Typical compaction curve $\varepsilon(p_k)$

Differential equation (3), material equation (5) and a differential equation for the local mass load change

$$\frac{dN_\mathrm{s}}{dx} = \rho_\mathrm{s}(1 - \varepsilon) \tag{6}$$

constitute an initial value problem with initial conditions $p_k = 0$, $\varepsilon = \varepsilon_0$ and $N_S = 0$ at the upstream end of the fiber bed. The initial value problem has been solved by numerical

integration with respect to x. Integration stops as soon as the prescribed fiber mass load N_S of the strainer has been reached, yielding the total length (streamwise thickness) L of the compressed fiber bed. The pressure difference over the entire fiber bed follows directly from the compacting pressure at the strainer position as

$$\Delta p = -p_k(L). \tag{7}$$

3. Validation of the strainer model

The system of equations (3), (5) and (6) was implemented and solved numerically by means of GNU Octave [5]. Compaction properties of the mineral wool material MD2-1999 were experimentally determined using the technique described above and values of $\varepsilon_0 = 0.9833$, $\varepsilon_\infty = 0.9147$, $C = 0.00712467$ Pa$^{-0.5197}$ and $D = 0.5197$ of the parameters in Eq. (5) were found. The mass specific surface A_S of the fibrous material was estimated to be 160 m^2/kg and water at room temperature was assumed as liquid phase. The total pressure drop Δp was determined, both numerically and experimentally, as a function of the superficial velocity. The curves shown in Fig. 5 represent different experimental conditions, i. e. strainer mass loads and fluid properties, which are summarized in Table 1. Although pressure drops tend to be underestimated for lower and overestimated for higher strainer mass loads, the non-linear relationship between pressure drop and superficial velocity could be qualitatively reproduced. The result may be improved by replacing empirical parameters a, a_0 and b in Eq. (3) by more appropriate values found in experiments.
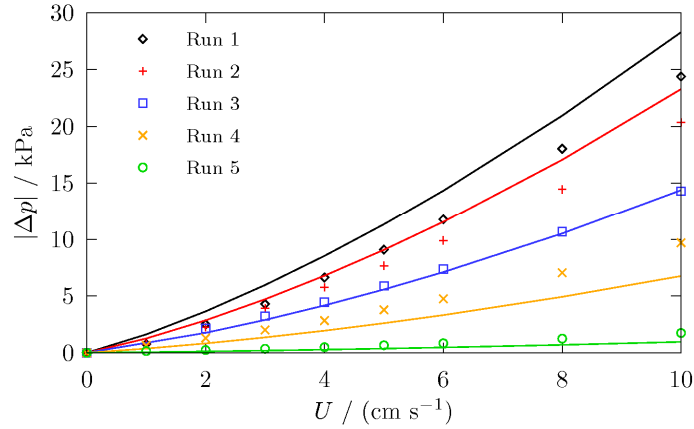
Fig. 5: Pressure drop vs. superficial velocity at different experimental conditions, experiments (points), computed profiles (lines)

Tab. 1: Experimental conditions

Run	N_s / kg m^{-2}	T / °C	ρ / kg m^{-3}	μ / mPa s
1	6.01	44.6	990.4	0.601
2	6.01	59.0	983.7	0.474
3	3.87	58.9	983.8	0.475
4	1.96	59.7	983.4	0.469
5	0.32	59.7	983.3	0.469

4. Implementation into ANSYS-CFX

The implementation of the model into a general purpose code such as ANSYS-CFX requires the transition from a point-like to a two-dimensional representation of the strainer plate. Moreover, the model should be applicable to the simulation of transient flows. The former task is addressed by placing a subdomain of fixed thickness d into the flow geometry. It represents the filter cake and the strainer plate and separates the upstream from the downstream region, as illustrated in Fig. 6. The cross-stream distribution of the strainer resistance is made up by a parallel connection of multiple resistances, the magnitude of each depending on the local particle mass load and superficial velocity values.
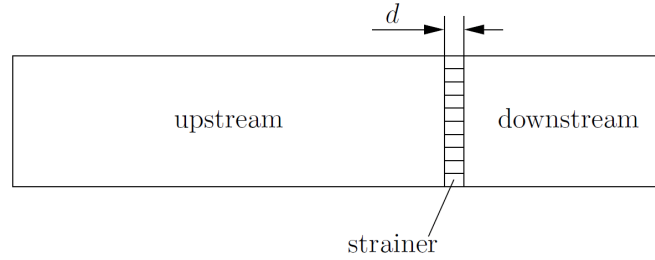
Fig. 6: Strainer represented as CFX subdomain

In order to make allowance for transient flows, the strainer mass load distribution N_s at time t has to be calculated by integrating the particle phase mass flow passing through the strainer subdomain with respect to time. Based on N_s distributions the pressure drop Δp across the fibre bed is computed from the local superficial velocity by solving Eqs. (3), (5) and (6). The flow resistance the liquid phase experiences within the strainer subdomain is modelled as source S_m in the momentum transport equation using the 'Linear Directional Loss Model' of CFX:

$$S_m = -C\mu u_\perp , \qquad (8)$$

where $u_\perp$ denotes the strainer normal velocity. The coefficient C is obtained from the previously determined pressure drop Δp as

$$C = \left| \frac{\Delta p}{\mu u_\perp d} \right| . \qquad (9)$$

5. 3D simulation with ANSYS-CFX

A step-like flow geometry, Fig. 7, was constructed that allows for three dimensional flow fields and a non-uniformly distributed particle phase leading to partially or at least unevenly loaded strainers. The channel segments are discretized by cubic elements of 1 cm edge length, whereas the strainer is discretized into three layers of elements of size $1 \times 1 \times 1/3$ cm^3.
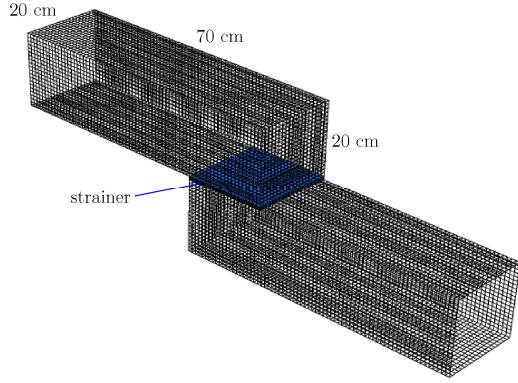
Fig. 7: Flow geometry
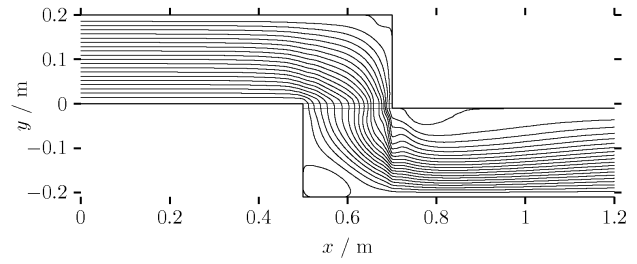
Fig. 8: Flow field (streamlines) in the channel mid plane after 40 s of simulation time

The flow field in the channel mid-plane, visualized by streamlines, is shown in Fig. 8. In this particular run, a linear volume fraction profile of the particle phase with zero volume fraction at the top and a value of 0.015 at the bottom of the channel inlet was maintained in order to achieve a non-uniform impingement onto the strainer. The inlet water velocity was set to 4 cm/s. The particle laden strainer acts like a rectifier which forces the flow into the vertical direction while smoothing out velocity differences. This becomes clearer in Fig. 9 which plots flow velocity profiles along the strainer for different simulation times. The velocity maximum at the right end of the strainer decreases during the simulation. This rectifying effect is caused by the high pressure drop across the clogged strainer, Fig. 10, leading to a pressure gradient whose maximum is in the strainer normal direction.
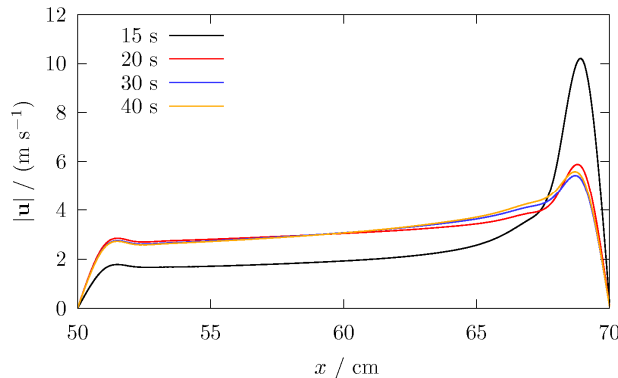
Fig. 9: Flow velocity distribution along the strainer at the channel mid plane
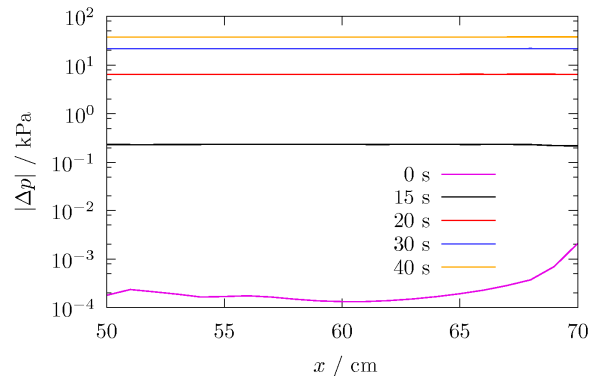
Fig. 10: Pressure drop distribution along the strainer at the channel mid plane

6. Summary

A method was developed that allows to calculate the pressure drop in compressible beds of mineral fibrous materials. The system of model equations constitutes an initial value problem which is solved numerically for given strainer mass load, flow velocity and static compaction properties of the fibre material. The model is well suited for implementation into system codes for nuclear reactor and containment simulation.

The model has been successfully implemented as an extension to the general-purpose CFD code ANSYS-CFX. Its capability to simulate the transient pressure drop build-up at non-uniformly loaded strainers in arbitrary three-dimensional geometries has been demonstrated using a step-like flow geometry with a horizontally embedded strainer plate.

8

References

[1]   Krepper, E.; Cartland-Glover, G.; Grahn, A.; Weiss, F.-P.; Alt, S.; Hampel, R.; Kästner, W.; Seeliger, A., 2007. CFD-modelling of insulation debris transport phenomena in water flow, The 12th International Topical Meeting on Nuclear Reactor Thermal Hydraulics (NURETH-12), 30.09.-04.10.2007, Pittsburgh, USA

[2]   Grahn, A.; Krepper, E.; Alt, S.; Kästner, W., 2006. Modelling of differential pressure buildup during flow through beds of fibrous materials, Chemical Engineering and Technology 29, 997 – 1000

[3]   Davies, C. N, 1952. The separation of airborne dust and particles. Proc. Inst. Mech. Engrs. 1B (1952), 185–198

[4]   Ingmanson, W. L. et al., 1959. Internal pressure distributions in compressible mats under fluid stress. TAPPI Journal, 42, 840–849

[5]   Eaton, J. W. et al. GNU Octave. URL http://www.octave.org

Acknowledgement

ANALYSIS OF ANTICIPATED TRANSIENTS WITHOUT SCRAM AT PWR USING THE COUPLED CODE SYSTEM DYN3D/ATHLET

Sören Kliem, Siegfried Mittag, and Ulrich Rohde

1. Introduction

The complete failure of the reactor scram system upon request during an operational transient is called anticipated transient without scram (ATWS). This mechanical failure of control-rod insertion is very unlikely and does not belong to the design basis accidents. The long-term subcriticality of the reactor during such transients is ensured by the injection of highly borated water from an auxiliary system actuated by a signal introduced specifically for ATWS purposes. According to the guidelines of the German Reactor Safety Commission (RSK), postulated ATWS events have to be analyzed with regard to their consequences on the safety of the nuclear power plants [1]. Such analyses are carried out in order to show that the mechanical integrity of the primary circuit and the coolability of the reactor core are ensured, at any time.

Since the course of ATWS transients is determined by a strong interaction of the neutron kinetics with the thermal hydraulics of the system, coupled 3D neutron kinetic/thermal hydraulic code systems are adequate tools for the analysis of such transients. In the following, the coupled code system DYN3D/ATHLET is applied to the analysis of an ATWS transient. It is the objective of the present work to quantify differences in the course and the results of transients, which arise from the variation of neutron-physical conditions.

The presented calculations are methodical studies - not licensing calculations.

2. Scenario and neutronic conditions of the analysis

Typically, the complete failure of the main feed water supply is assumed to be the bounding ATWS event with regard to the maximum primary coolant pressure, which can be reached during the transient. The situation is aggravated if the main coolant pumps remain in operation. For this particular transient, the influence of different neutron-physical conditions, i.e. core loadings, was analyzed.

An input data set for a generic four-loop PWR at the nominal power of 3750 MW was created. All four loops with their primary and secondary sides were modeled separately.

Table 1: Core loading patterns for the analyses

Legend	193 UO$_2$/0 MOX FA	129 UO$_2$/64 MOX FA	0 UO$_2$/193 MOX FA

Three different core loading patterns were generated for the analyses by varying the number of MOX (mixed oxide) fuel assemblies (FA) in the core [2]. In standard FA, ^{235}U is the fissile material, whereas ^{239}Pu is used in MOX fuel. This plutonium either comes from dismantled nuclear weapons or is produced by reprocessing spent fuel. In both types of FA, the fissile material is embedded into a matrix of ^{238}U, which is not the subject to fission in the reactor type under consideration. Usually, the share of fissile material is not higher than 5 %.

The first core configuration studied does not contain any MOX elements; the second one has 64 MOX FA and the third configuration is a full MOX loading. Table 1 shows the three core loadings.

In the calculations, all 193 FA were modeled in neutron kinetics as well as in thermal hydraulics [3].

3.   Analysis of the core loading patterns

In a first step, the reactivity effects of the three core loading patterns were examined. All corresponding stationary calculations have been carried out for the beginning of cycle (BOC), at full power, i.e. for the initial state of the transient. Assuming the same nodal burnup distribution in all three cases, the three core loadings would have different values of critical boron concentration at BOC. To be able to compare the results, it was decided to use the same boron concentration of 1000 ppm in all calculations. For this reason, the three curves in Figs. 1 and 2, which show the reactivity response of the three cores under investigation, do not start from the same initial value. The range of the coolant density and the fuel temperature shown in these figures corresponds to the range reached by these parameters during the transient.

Different core loadings cause differences in the reactivity dependence on moderator density, as seen in Fig. 1. With increasing density, the reactivity growth is the smallest in case of the core without MOX. Thus, a reactivity reduction due to moderator expansion or voiding is stronger in the case of MOX. This behavior can be explained by the fact that MOX fuel provides a harder neutron spectrum, which means that, for the given configuration, MOX is deeper under-moderated than UO_2 fuel. Stronger under-moderation results in stronger dependence of reactivity on the density of moderating nuclei (see also Tab. 2). Both Fig. 2 and Tab. 2 depict a stronger negative fuel temperature coefficient for MOX. The physical reason is found in the fact, that Pu-239 and Pu-240 own strong absorption resonances at 0.3 eV and 1 eV, respectively, increasing the Doppler feedback in comparison to U-235.
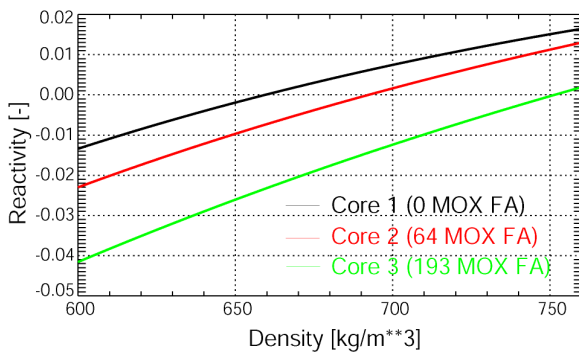

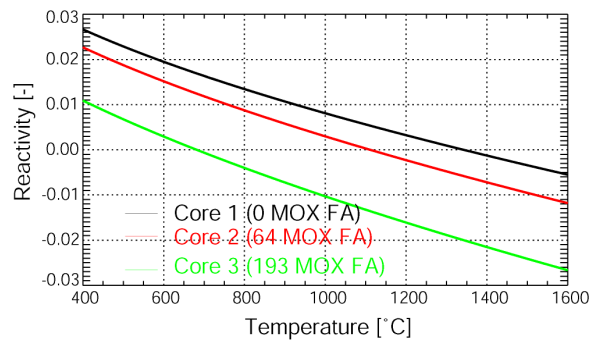Fig. 1: Dependence of the reactivity on the moderator density

Fig. 2: Dependence of the reactivity on the fuel temperature

11

The last column in Tab. 2 gives the boron efficiency. The harder spectrum of MOX fuel is the reason that boron-10, being a strong absorber for thermal neutrons, contributes less to the total neutron absorption in MOX than it does in UO_2. Thus, the boron efficiency decreases with increasing MOX share in the core.

Tab. 2 (third column) also shows the weak influence of the pure moderator temperature on reactivity, not including the moderator density effect given in the second column. This moderator-temperature reactivity coefficient, which is also called "spectral" moderator coefficient, may be estimated not very accurately by a two-group diffusion code like DYN3D. However, at a boron concentration of 1000 ppm, typical for BOC, it is always clearly positive, without remarkable dependence on the MOX content of the core. As the average energy of thermalized neutrons increases with moderator temperature, boron-10 and hydrogen-1 absorption rates will decrease, due to the 1/v dependence of the respective cross sections, which leads to a reactivity growth.

Table 2: Global reactivity coefficients for the core loadings in the initial state of the transient (beginning of cycle, full power, boron concentration: 1000 ppm)

Loading (Number of MOX FA)	Reactivity coefficient			
	Moderator density [pcm/kg/m^3]	Moderator temperature [pcm/K]	Fuel temperature [pcm/K]	Boron concentration [pcm/ppm]
1 (0)	15.09	3.267	-2.441	-7.051
2 (64)	18.94	3.186	-2.632	-5.479
3 (193)	23.64	3.043	-2.882	-3.810

4. Results of the ATWS calculations

Transient calculations for the loss-of-feed-water accident were carried out, using the three core loading patterns described above. All thermal hydraulic conditions as well as the modeling and settings of all systems are identical in the calculations.

At t = 0 s, the main feed water supply fails. This loss of feed water causes a trip of the turbine and a steam release through the bypass station. As a consequence, the core produces more heat than can be removed by the steam generators. The coolant pressure and primary-circuit steam-generator-outlet temperature begin to rise. The pressure growth takes effect immediately in the whole primary circuit, while the coolant temperature in the core rises with a delay of several seconds. The higher pressure compresses the coolant/moderator to a higher density. Thus, due to the moderator-density reactivity coefficient (Tab. 2), reactor power goes up during the first seven seconds. The increase of about 45 MW is nearly identical in all three calculations (Fig. 3).

The described processes can be explained by the time course of the single reactivity contributions, shown in Fig. 4. Starting from the stable initial state the total reactivity increases slightly, due to the moderator density effect. The reactivity change caused by the growth of power and, therefore, fuel temperature, is negative, which attenuates the increase of total reactivity. About five seconds after the transient started, hotter coolant, coming from the steam-generator, reaches the reactor core. On the one hand, this temperature rise is accompanied by an additional (small) positive reactivity insertion, because the "spectral" reactivity coefficient of the moderator temperature is positive for all three loadings (see

Tab. 2). On the other hand, the moderator density decrease, connected with the temperature growth, becomes the dominating effect, and the reactivity contribution from the moderator density starts to decrease. Some nine seconds after the transient was initiated, the total reactivity reaches the zero line, and power drops below its initial value.
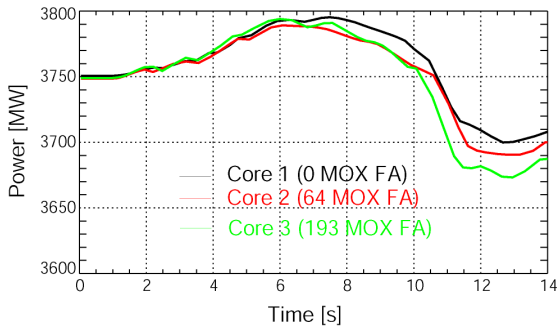
Fig. 3: Core power (first part of the transient)
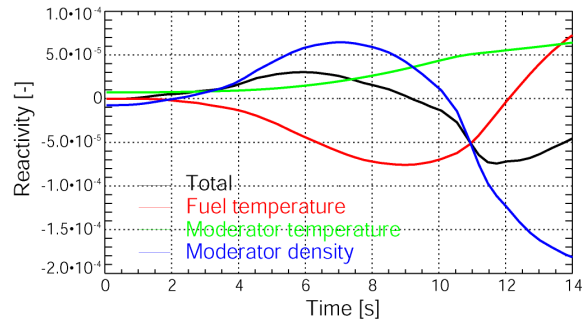
Fig. 4: Reactivity contributions (core loading with 64 MOX FA)

First remarkable differences between the three calculations begin to develop at about t = 18 s. From this time on, differences in the moderator-density influence on reactivity are seen (Fig. 5). As expected from the steady-state reactivity curves, the MOX-free calculation provides a smaller reactivity drop for the same density change. For this reason, the power does not decrease that strong; and in the following, the density goes further down than in a core with MOX (Fig. 6).
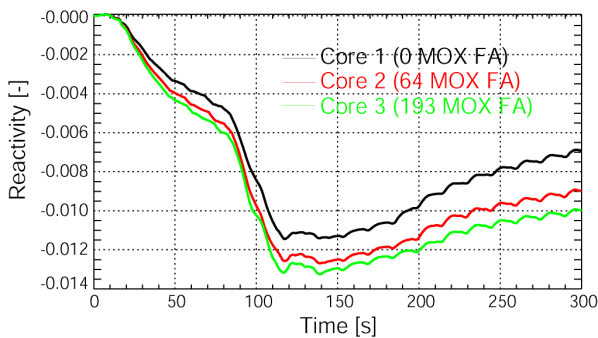
Fig. 5: Moderator density reactivity effect
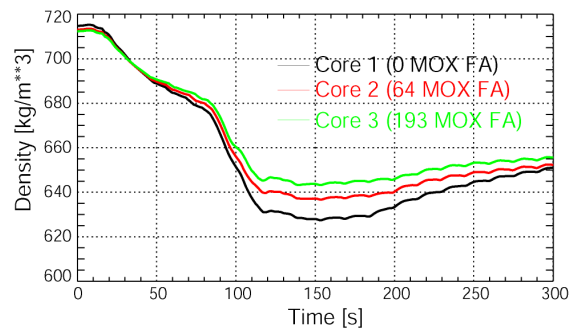
Fig. 6: Core average moderator density

Decreasing power in all calculations leads to dropping average fuel temperature. The differences in the Doppler coefficient counteract the differences in the moderator density coefficient, thus reducing the deviations in power.

The lowest moderator density, observed in the calculation for the MOX-free core, is the result of the highest moderator temperature (at roughly the same pressure). As the moderator-temperature ("spectral") reactivity effect is also nearly identical in the three cases (Tab. 2), the largest temperature increase leads to the biggest positive moderator spectral effect in the MOX-free core.

The sum of the three reactivity effects leads to the power behavior shown in Fig. 7, left part, where the full-MOX-core power decreases to the lowest level. This lowest power level in the full-MOX case would have persisted until the end of the transient, if the boron concentration in the reactor core would not change. However, a small amount of highly borated water is slowly injected through the auxiliary borating system, the boron concentration increasing from the initial value of 1000 ppm to 1063 ppm within 300 s. This injection is identical in all

three calculations. The increase in the average boron concentration results in the biggest power-reducing effect in the MOX-free core, due to the remarkably higher boron efficiency there (Tab. 2). Thus, after about t = 150 s, the full-MOX calculation provides the highest power and the MOX-free core shows the lowest one (Fig. 7).
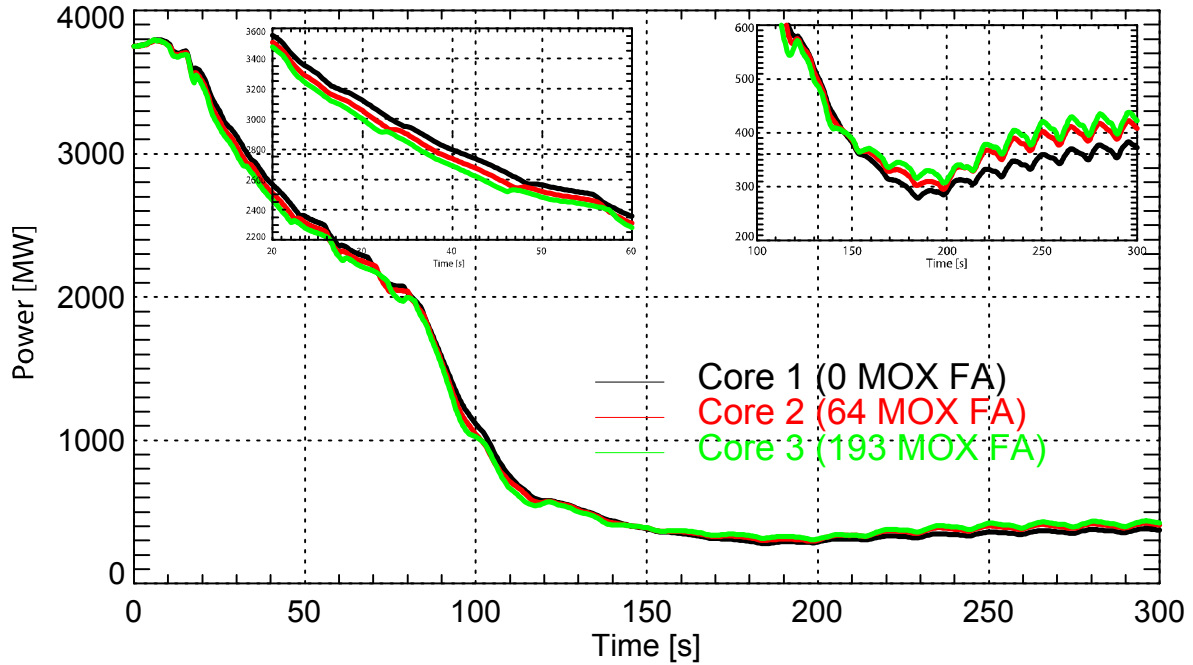
Fig. 7: Reactor power

One of the most relevant safety parameters in ATWS is the coolant pressure in the primary circuit. It is clear that a too high pressure has a direct influence on the mechanical integrity of the primary circuit, which must not be affected as mentioned above.

The transient history of the pressure is shown in Figs. 8 and 9. The pressure increases immediately after the start of the transient was discussed above. During the next tens of seconds the pressure behavior is controlled by the opening and closing of the pressurizer relief and safety valves. The emergency feed water injected into the steam generators is not able to prevent the full evaporation of the steam generator inventory, which takes place some 90 s after the start of the transient. The heat removal by the steam generators descents further and a second pressure peak occurs in the primary circuit.
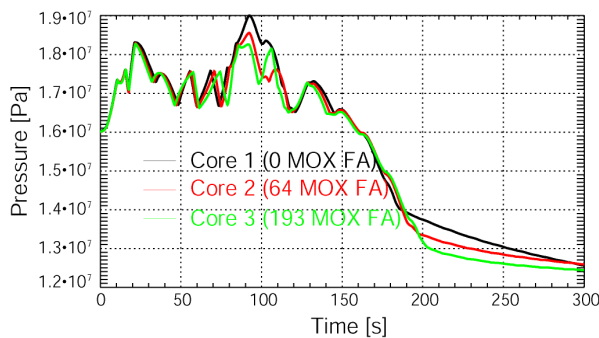
Fig. 8: Primary pressure
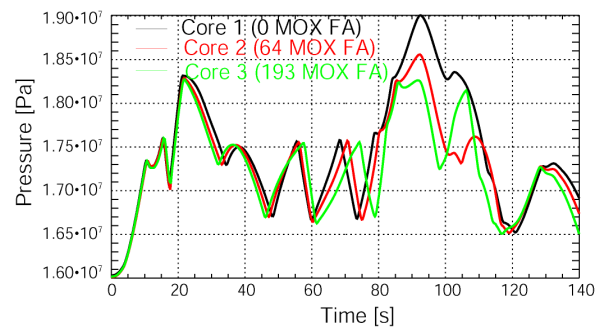
Fig. 9: Primary pressure (zoom)

The first pressure peak shortly after the start of the transient is nearly identical in all calculations, differences resulting from the different core loadings are not observed. But the second pressure peak shows remarkable influences of the core design. The MOX–free calculation gives the highest pressure peak (19.0 MPa). The height of this peak decreases with increasing number of MOX FA. In the calculation for the full MOX core, the second pressure peak is even slightly lower than the first one. The differences in the pressure peak are related to the different core powers. As discussed above, during the respective time of the second pressure peak, the power level will be the higher, the smaller the MOX portion in the core is. Although the differences in the power are relatively small (at t = 92 s the three values differ by 80 MW only) they cause the corresponding differences in the pressure peak.

5.   Conclusion

The ATWS transient "Loss of main feed water supply" was analyzed using the coupled code system DYN3D/ATHLET. It was shown that the variation of the number of MOX FA in the core has a remarkable influence on the reactivity coefficients of the fuel temperature and the moderator density. These two parameters mainly influence the behavior of the coolant pressure in the first part of the transient. It has been demonstrated that the pressure maximum decreases with increasing number of MOX FA in the core.

The second safety goal mentioned above, the coolability of the reactor core, is not affected during the analyzed transient. The mass flow rate through the reactor core is so high during the whole time span, that the coolant does not boil and a heat transfer crisis cannot occur.

References

[1]   Reaktor-Sicherheitskommission (1996), RSK-Leitlinien für Druckwasserreaktoren, 34 S.
[2]   S. Mittag, U. Grundmann, R. Koch, J. Semmrich (2002), Erzeugung und Nutzung von Bibliotheken von Zwei-Gruppen-Diffusionsparametern zur Berechnung eines KWU-KONVOI-Reaktors mit dem Reaktordynamikprogramm DYN3D, Rossendorf, Report FZR-346, ISSN 1437-322X.
[3]   S. Kliem (2007), Realistische Simulation von Reaktivitätsstörfällen mit gekoppelten neutronenkinetisch-thermohydraulischen Systemcodes – Abschlussbericht zum VGB-Projekt: SA „AT" 51/04, Dresden, FZD\FWS\2007\11, 113 S.

FRACTURE MECHANICAL ANALYSIS OF A VVER-440 PTS SCENARIO

Martin Abendroth and Eberhard Altstadt

1.   Introduction

The paper describes the modelling and evaluation of a pressurized thermal shock (PTS) scenario in a VVER-440 reactor pressure vessel due to a safety injection. An axially oriented semi-elliptical crack is assumed to be located in the core welding seam. Two versions of fracture mechanical evaluation are performed: the analysis of a sub-cladding crack and of a surface crack. Three-dimensional finite element (FE) models are used to compute the global transient temperature and stress-strain fields. By using a three-dimensional submodel, which includes the crack, the local crack stress-strain field is obtained. Within the subsequent postprocessing using the J-integral technique the stress intensity factors K_I along the crack front are obtained. The FE results are compared to analytical calculations proposed in the VERLIFE code. The stress intensity factors are compared to the fracture toughness curve of the weld material.

2.   Description of the scenario

The PTS scenario caused by a LOCA is characterised by a sudden cool down of the inner surface of RPV wall due to cold water injection while the system pressure is still at a high level. Such a situation can occur through various event sequences. The scenario, which is discussed here, starts with a stuck open pressurizer relief valve. The pressure drop leads to the initiation of the emergency core cooling system i.e. to a cold water injection through two the main coolant pipes. After one hour, the relief valve is closed inadvertently, which leads to a quick re-increase of the primary pressure (see Fig. 1).

The quenched region includes the core welding seam, which is supposed to be one of the most embrittled regions of the RPV due to neutron irradiation. Additionally, weld lines are also likely locations for cracks or flaws. Therefore,
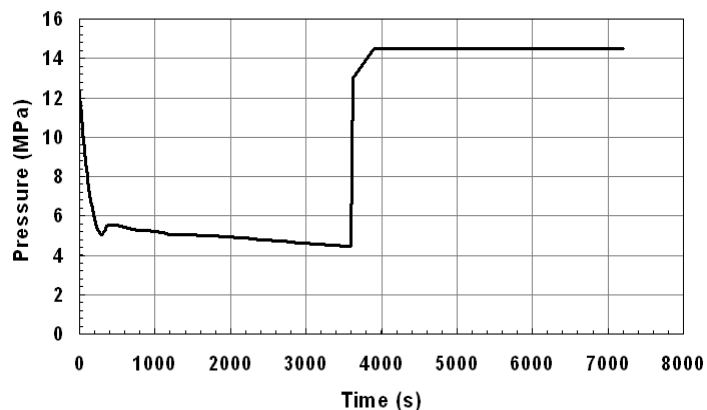
Fig. 1: Primary pressure vs. time

the scenario postulates an axially oriented semi-elliptical underclad crack. The axial orientation is chosen because the maximum principal stress in a pressurized cylindrical vessel is acting in circumferential direction and so perpendicular to the faces of the postulated crack. The cooled inner surface of the RPV including the crack are exposed to tensile stress. The re-pressurization of the RPV after 3600 seconds will suddenly increase the tensile stress and is assumed to be the crucial phase of the scenario. The scenario is specified in [3].

The main questions of the investigation are: i) what is the loading of the crack region (stress intensity factor K_I) during the scenario and ii) what is the maximum allowable temperature of

brittleness of the material at which the RPV would just not fail by brittle fracture? Or the other way round: What is the allowable stress intensity factor at a given state of the material's embrittlement (ductile to brittle transition temperature)?

The component of interest is a VVER-440/V-213 RPV, which has an inner radius of 1771 mm. The inner surface has an austenitic cladding with a thickness of 9 mm. The thickness of the base material in the cylindrical part of the vessel is 140 mm. The geometry of the two opposite cold plumes (see Fig. 2) were obtained by a thermal hydraulic simulation, which was performed with RELAP5 in [1].

3. Modelling

We developed a three-dimensional finite element (FE) model of one quarter of the RPV using the code ANSYS®. Since the region of interest (core weld 5/6) is far away from the in- and outlets, these nozzles have been neglected in the model. This global model does not contain any crack so far. It is used to compute the transient thermal field and the stress and strain field. The subsequent fracture mechanical analysis is done with a submodel which contains the detailed crack geometry. The boundary conditions for the submodel are obtained from the solutions of the global model.

The thermal calculation is based on the fluid temperatures and the heat transfer coefficients. Due to the thermal isolation of the RPV it can be assumed that the outer surface is adiabatic. The stress free temperature of the clad vessel is 267°C. Figure 2 shows the computed thermal field at the time t = 1000 s. On the right part of the figure the cold plume is clearly to be seen. The injected cold water leads to a general cool down of the inner surface of the RPV, but especially in the cold plum region the temperatures are up to 50 K lower than in the ambient region. This leads to elevated tensile stresses in circumferential and vertical direction in the cold plum region of the inner surface of the RPV.

Fig. 2: Temperature field at t = 1000 s

The subsequent mechanical solution is obtained by using the thermal field as a body load and by applying the time dependent internal pressure, the gravity, and the initial residual stresses in the welds. The weld material has the same thermal-physical and tensile properties as the base material but is supposed to have residual stresses both in axial and circumferential orientation. These residual stresses result from the welding process. The postulated semi-elliptical underclad crack is located at the core weld 5/6 at a level of 3.485 m below the inlet nozzle. The supposed axially oriented crack is 15 mm deep (1/10 of the wall thickness) and the aspect ratio is 0.3. Figure 3 shows the computed hoop stress at t = 1000 s. It can be seen that in general the highest hoop stresses are located in the cladding which is directly in contact with the coolant. In the upper part, where the vessel wall thickness is greater than in the lower part, in general we obtain higher hoop stress values than in the lower part. Moreover, the cold plum region in the lower part is also a region with elevated hoop stress.

To perform the fracture mechanical analysis we use a sub-modelling technique. Two different cracks are assumed, an underclad crack as defined in [3] and a surface crack (see Fig. 4). Only the crack and a reasonable large surrounding is modelled. At the cut boundaries of the submodel the interpolated degree of freedom results (displacements) of the global (coarse) model are applied. The thermal field and the gravity loads are used as body loads, the pressure (see Fig. 1) is applied at the inner surface.

In case of the underclad crack there is a principal problem, since the cladding itself contains no crack and has common nodes with the base material, the crack mouth is virtually clamped close, which results in a second straight and sharp crack front at the interface between cladding and base material.
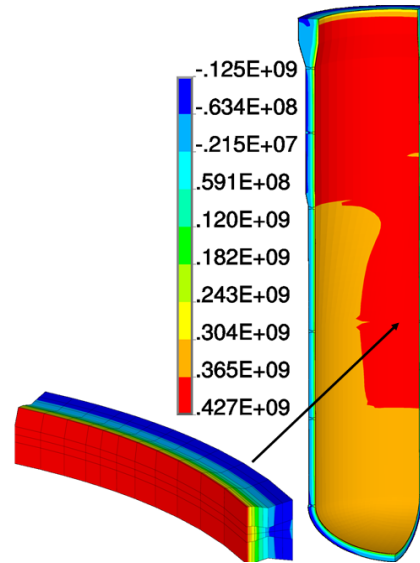
Fig. 3: Hoop stress [Pa] at t = 1000 s
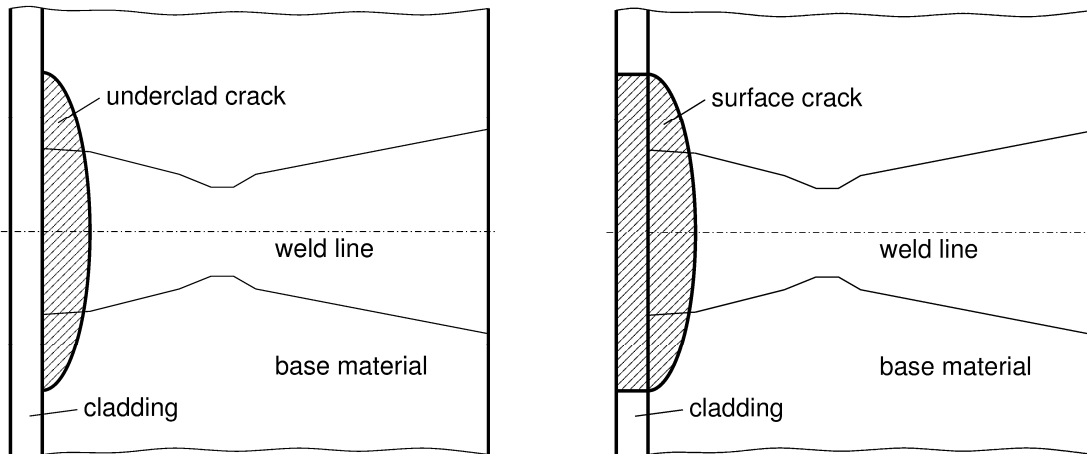
Fig. 4: Two types of crack in the core weld seam: underclad crack (left) and surface crack (right)

To evaluate the consequences resulting from a non-intact cladding (as assumed in [2]) a second submodel is used, which includes a surface crack which goes through the cladding. Fig. 5 shows the hoop stress at t = 1000 s. Here, the crack face (dark blue) is clearly distinguishable from the rest of the model and we note the high (red) stresses at the crack tip.

4.   Stress intensity factors and critical temperatures of brittleness

The computation of the stress intensity factors (SIF) is done in the postprocessing. The procedure is based on the J-integral concept:

$$K_I = \sqrt{\frac{E \cdot J_1}{1 - \nu^2}}$$
(1)

The details of the calculation of J_1 are described in [4] and [5]. Fig. 6 shows the variation of the stress intensity factor K_I computed for the deepest point of the underclad crack (a = 15 mm) and a point (a = 2 mm) below the cladding-base material interface. The point at a = 2 mm is already located outside of the weld, since the length of the crack front is larger

than the height of the weld seam. Therefore it was assumed, that in this location there are no residual stresses.
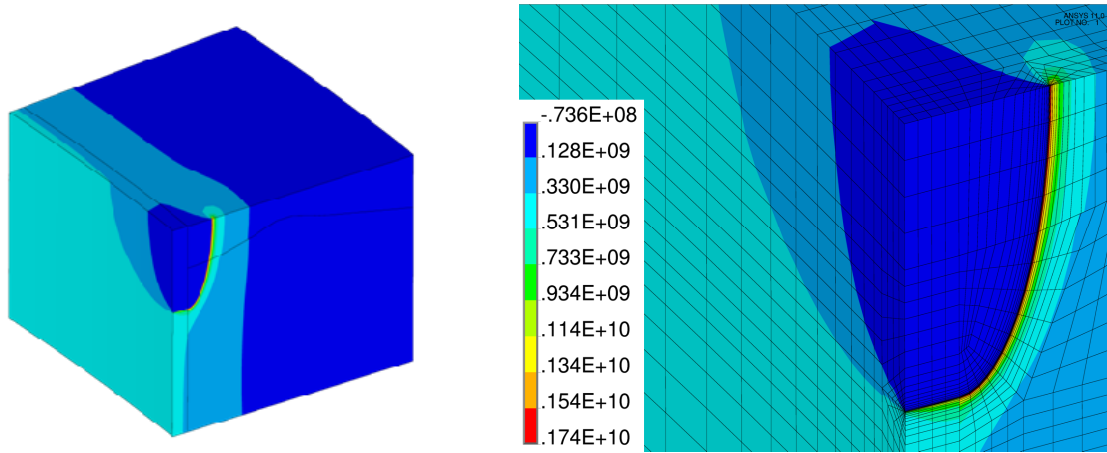
Fig. 5: Hoop stress [Pa] in the crack region calculated with the submodel (surface crack)

There is a slight decrease of K_I at the beginning due to the pressure reduction, then an increase up to the maximum at 1000 seconds due to the thermal shock effects. It follows a decrease again, as the temperature gradient through the vessel wall decreases. The re-pressurization is the critical phase for this scenario, a sudden increase of K_I can be noted. To judge these results, K_I has to be compared to the fracture toughness of the material, which is described by the following equation [2]:

$$[K_{IC}]_3(T) = \min\left\{26 + 36 \cdot \exp[0.02 \cdot (T - T_K)]; 200\right\} \quad \text{MPa}\sqrt{m} \tag{2}$$

where T_K is the critical temperature of brittleness (ductile to brittle transition temperature). T_K has to be determined experimentally for given material, e.g. via the master curve concept. Equation 2 corresponds to a fracture probability of 1%. In Fig. 7, K_I is plotted as a function of the crack tip temperature for all computed pairs of K_I and T together with the critical $[K_{Ic}]_3$-curve. It is obvious that the re-pressurization causes the critical $K_I = 40.2$ MPa$\sqrt{m}$ at a crack tip temperature of $T = 68.9°C$. The maximum value of $K_I = 43$ MPa$\sqrt{m}$ occurs at $t = 1000$ s where the crack tip temperature is $T = 170 °C$, which is an uncritical state. The allowable critical temperature is obtained from:

$$T_K^a = \min\left[T - 50 \cdot \ln\left(\frac{K_I - 26\text{MPa}\sqrt{m}}{36\text{MPa}\sqrt{m}}\right)\right] \geq T_K \tag{3}$$

The results for the surface crack are shown in Fig. 8. As expected we obtain higher values for the stress intensity factors. Here also the re-pressurization of the RPV causes the critical value of $K_I = 67$ MPa$\sqrt{m}$ at a crack tip temperature of $T = 68.9 °C$.

Table 1 summarizes the main results, as there are the maximum $K_I(T)$ and T_K^a values for the underclad and the surface crack located in the most embrittled weld line of a WWER-440 RPV during a thermal shock scenario. For comparison additional values are given, which are obtained using a simplified analytical approach given in the VERLIFE code [2], which however does not take into account the existence of the cladding. The VERLIFE simplified engineering approach uses the stress components normal to the crack face for K_I computation. These stresses were taken from the calculation with the global FE model.
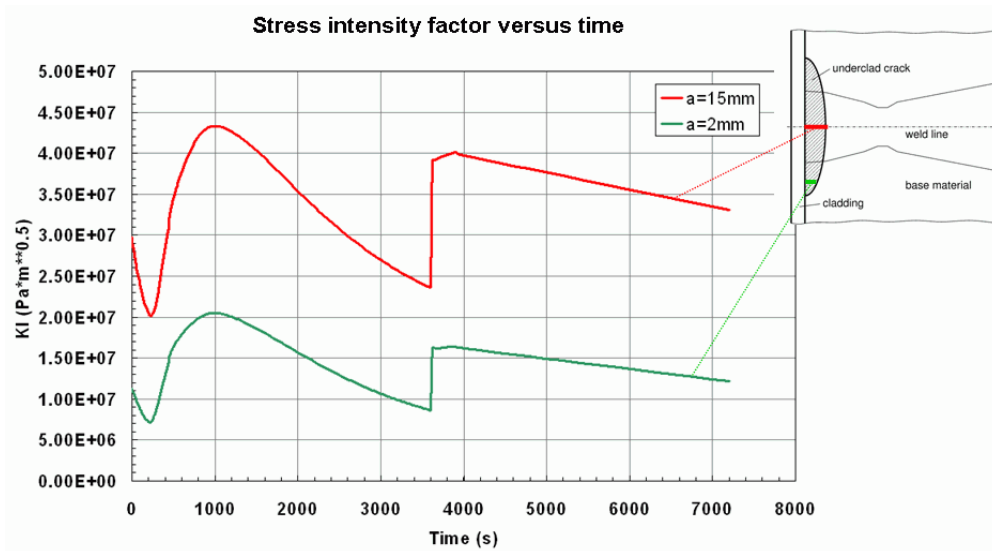
Fig. 6: K_I vs. time fort two positions at the crack front, underclad crack
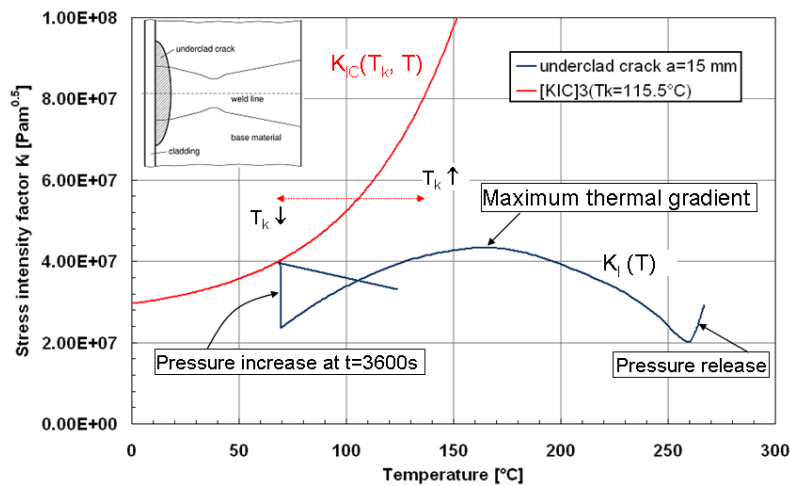
Fig. 7: SIF vs. temperature and fracture toughness curve for T_K=115.5 °C, underclad crack
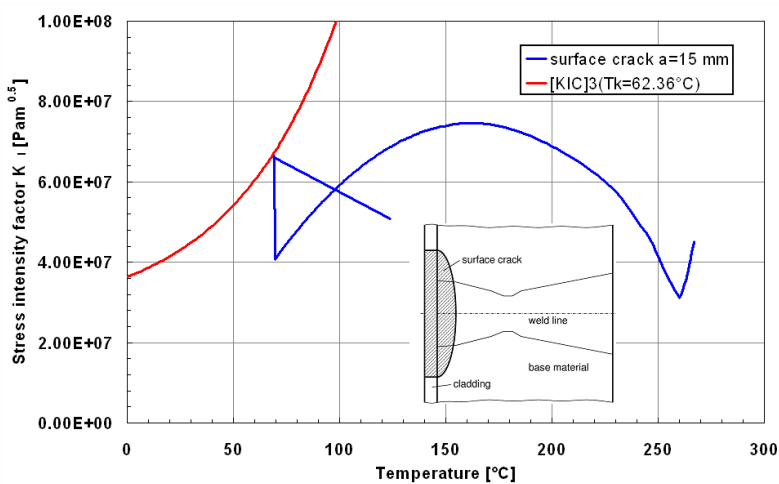
Fig. 8: SIF vs. temperature and fracture toughness curve for T_K=62.4 °C, surface crack

20

Table 1: Maximum stress intensity factors and allowable critical temperatures for the underclad crack and the surface crack.

	Underclad crack		Surface crack	
	ANSYS	Analytical [2]	ANSYS	Analytical [2]
K_I [MPa$\sqrt{m}$]	40.2	51.8	67.0	67.6
T_K [°C]	115.5	85.0	62.4	61.7

5.   Conclusions

A PTS scenario for a VVER-440/213 RPV was investigated. Based on the stress calculations with a global FE model the SIFs were evaluated with two methods: a fracture mechanical analysis by a FE submodel and by using an engineering approach. Two limiting assumptions concerning the crack were investigated: underclad and surface crack. The results show that the engineering approach provides a strongly conservative value for the underclad crack. For the surface crack the K_I value is only slightly conservative, compared to the one obtained with the j-integral method.

The finite element crack modelling for the underclad crack is a crucial point. The VERLIFE code allows to assume a completely intact cladding, if the cladding integrity is assured by non destructive testing. As mentioned in the sections above the common nodes of the cladding and the base material cause an artificial crack mouth clamping, which results in an underestimation of K_I for an underclad crack. A better approach might be to define a crack, which affects both cladding and base material (Fig. 9). The postulation of a surface crack leads to more conservative results.
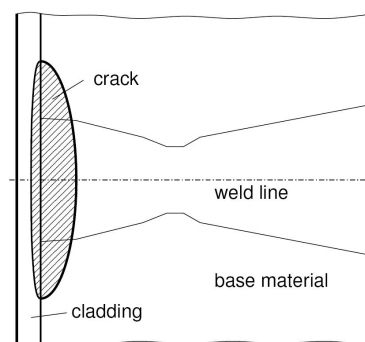
Fig. 9: Crack with partially affected cladding

A critical T_K of about 60 °C is not unusual for VVER-440 reactors. Therefore, the integrity in a PTS scenario might be only be ensured, if the cladding is proved to be intact, or if the RPV is regularly annealed to guarantee a low transition temperature.

References

[1]   Pistora, V., Kral, P.: Evaluation of pressurised thermal shocks for VVER440/213 reactor pressure vessel in NPP Dukovany. Trans.17th Int. Conf. on Struct. Mech. Reactor Technology (SMIRT-17), 2003 Paper G01-3.

[2]   Brumovsky, M.: Unified Procedure for Lifetime Evaluation of Components and Piping in WWER NPPs – VERLIFE, September, 2003, Final Report of EU project FIKS-CT-2001-20198.

[3]   Pistora, V., Brumovsky, M.: COVERS-WP4-Benchmark No. 1, Report of EU project COVERS (12727 - FI60), March 2006

[4]   Abendroth, M., Willschütz, H.-G., Altstadt, E.: Fracture mechanical evaluation of an in-vessel melt retention scenario, Annals of Nuclear Energy (2007), 10.1016/j.anucene.2007.08.007

[5]   Abendroth, M.; Altstadt, E.: COVERS WP4 Benchmark 1 – Fracture mechanical analysis of a thermal shock scenario for a VVER-440 RPV. Wissenschaftlich-Technische Berichte Forschungszentrum Dresden-Rossendorf; FZD-474, 2007, ISSN 1437-322X

ULTRA FAST SCANNED ELECTRON BEAM X-RAY CT FOR TWO-PHASE FLOW MEASUREMENT

Uwe Hampel, Frank Fischer, Eckhard Schleicher, and Dietrich Hoppe

1. Introduction

Multiphase flows occur in many industrial areas, such as light water nuclear reactors, chemical reactors, hydrodynamic machines, mineral oil exploration, biochemical processing and water resource management. A key issue to improve our knowledge of multiphase flow physics is the availability of an adequate measurement technology. Though there are many physical parameters which may be of interest in multiphase flow, e. g. phase holdup, interfacial area density, species concentration, temperature, velocity and pressure fields, there are some common features which are to be attributed to an ideal measurement technique. First of all, these are high spatial and temporal resolution, secondly non-intrusiveness. In the past, different measurement techniques have been proposed for multiphase flow measurement but not all of them account for high spatial and temporal resolution. Most commonly applied today is high speed optical video imaging using advanced CMOS camera technology. Such devices enable flow imaging at frame rates of more than 100,000 Hz. They are, however, restricted to optically transparent media, require optical access to the flow and fail to provide quantitative data at presence of multiple phases. Tomographic techniques which have been proposed by some groups are electrical tomography, magnetic resonance imaging, gamma and X-ray tomography and radioactive particle tracking.

Electrical tomography, either based on resistance, capacitance or impedance measurement, has long been considered as the most potential candidate since it can be made very fast (1 kHz frame rate or higher) and is comparatively inexpensive [1, 2]. Spatial resolution, however, is a major limitation. MRI has first been investigated and used by Gladden et al. [3]. It can achieve frame rates of up to 50 Hz and spatial resolution below 1 mm. Moreover, it can discriminate chemical species and is capable of measuring local flow velocity. It cannot be used with magnetic materials and is therefore hardly applicable to pressurized vessels. Fast tomographic techniques based on isotopic or X-ray sources have also been introduced in the past. Thus, Johansen et al. built an isotopic scanner with 5 stationary Am-241 sources which achieves a frame rate up to 100 Hz [4]. Misawa [5] and Hori [6] introduced pulsed multi-source X-ray scanners which run at frame rates of up to 2 kHz. Particle tracking techniques have been developed both for single photon emitters [7] and positron emitters [8]. Especially the latter, called positron emission particle tracking (PEPT) is suited to track the motion of single particles in opaque flow with millisecond time resolution.

In the medical field the fastest tomographic hard field modality today is electron beam CT [9] which is widely used in cardiac diagnostics, e. g. detect non-invasively coronary artery calcifications or to measure ventricular volume. Though in medicine frame rates do not exceed 30 Hz this technology presents by far the greatest versatility to be used in fast multiphase flow measurement. Besides fast 2D imaging it offers capabilities for phase velocity measurement, fast volume imaging as well as high energy X-ray CT.

In 2007 developers at Institute of Safety Research accomplished the implementation of a fast scanned electron beam X-ray CT scanner with primary application in two-phase flow measurement. The scanner is operated at an electron energy of up to 150 keV and electron beam

power up to 10 kW. It reaches a spatial resolution of about 1 mm and frame rates up to 7 kHz. First tests of the scanner have been performed on a simple vertical column operated in two-phase flow mode.

2. Design of the fast electron beam CT scanner

The working principle of the fast scanned electron beam X-ray CT is illustrated in Fig. 1 along with a scheme of its major components in Fig. 2. The electron gun produces an electron beam by electrostatic acceleration of electrons emitted from a heated tungsten cathode. The electron beam passes an electromagnetic lens system for beam focusing and centering. Further down the beam path an electromagnetic deflection unit consisting of quadrupole coils provides two-dimensional beam deflection capability. The electron beam is steered onto a semicircular metal target placed about 1 m away from the gun. On the target the electrons are stopped producing X-rays. Via the electromagnetic beam deflection the focal spot can be swept rapidly along the target on a circular path. A fast X-ray detector consisting of multiple zinc-cadmium-telluride detector crystals which is enclosed by the target measures the intensity of X-rays passing through the object inside this arrangement. In this way radiographic projection data is generated which is eventually processed to cross-sectional slice images by tomographic image reconstruction software. As a matter of course, all components required to form and guide the electron beam are inside a vacuum enclosure, which is not shown in Fig. 1. Also not shown are further assisting components and circuits such as vacuum pump, target cooling and beam monitoring equipment. The electron gun and the high voltage generator enable to continuously generate electron beams of maxi-

Fig.1: Principle of fast scanned electron beam X-ray CT

mum 150 kV tube voltage, 65 mA beam current and thus about 10 kW beam power. The target has an optimized design to dissipate the 10 kW heating power transferred by the electron beam. The beam deflection system can be operated up to 15 kHz, however, the required elliptical deflection pattern has a limiting frequency of 7 kHz, which is the maximum frame rate achievable with the current device.

The detector comprises 240 elements with an active area of 1.5 x 1.5 mm² for each pixel. The detector elements are coupled to fast amplifier and digitizer circuits and a special design digital data acquisition hardware that enables to read out the detector at 1 MHz fully synchronously. With 1 MHz detector sampling we acquire 142 projections per full focal spot revolu-

tion at 7 kHz and 1000 projections at 1 kHz scan rate. The focal spot on the target is about 1 mm in diameter. One particular problem associated with the target-detector arrangement is the axial offset between the focal spot plane and the detector plane. This problem is also known from medical electron beam X-ray CT and produces small artifacts especially for small objects such as bubbles or particles. However, to some degree this problem can be tackled by suitable image processing algorithms.
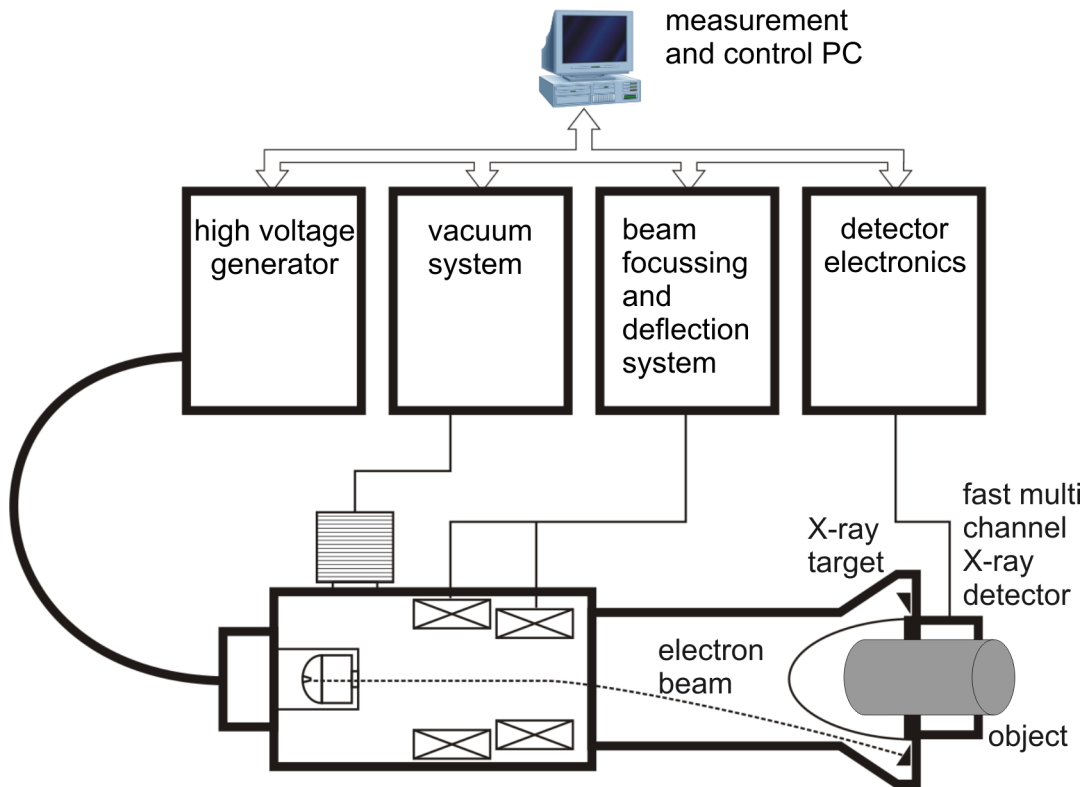
Fig. 2: Components of the fast scanned electron beam X-ray CT scanner

For measurement along larger vertical pipes a special gantry has been built which allows continuous vertical positioning of the scanner (Fig. 3). Beside the scanner, which includes electron beam generator, vacuum system, target, and detector, the CT system further comprises a separate high-voltage generator and a rack with all control electronics, such as vacuum controller, coil current amplifiers, detector electronics and control PC (Fig. 4).

Image reconstruction is performed offline on a separate PC. After appropriate calibration and conversion steps for the raw data we use the filtered backprojection technique for image reconstructions. A sequence of 1000 images takes about 3 minutes to download from the detector hardware to the PC and then about two minutes to perform full reconstruction. The software also includes algorithms for data binarization and extraction of parameters, such as bubble size and integral phase holdup.

3. Application

Among other objects we tested the new scanner on a bubble column of 60 mm inner diameter and 500 mm height made of Perspex. Gas was injected at different flow rates from the bottom by a single injector needle. Measurement was taken 150 mm above bottom. Fig. 4 shows reconstructed cross-sectional images along with synthesized central axial cut images at three

different flow rates scanned at 1000 frames per second for 0.5 s scan duration. As it can be seen the gas accumulates in the centre and for high gas rates plug flow is not yet developed at this measurement position. The example serves as a test case for the scanner. Bubbles are well resolved and even the thin liquid film between the single bubbles can be recognized. The noise figure in the images has been estimated to be about 3% in standard deviation from the mean foreground and background pixels values, which permits reliable bubble detection and discrimination for further processing.
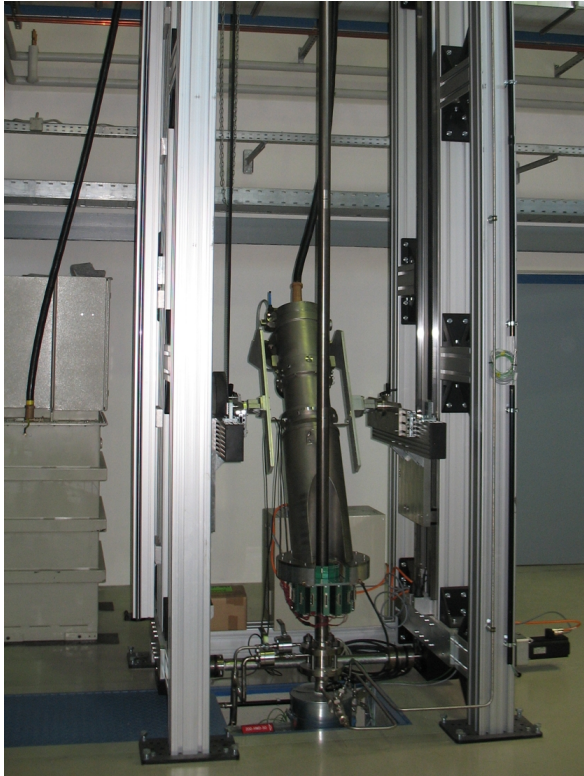
Fig. 3: Scanner mounted at a vertical test section at FZD's TOPFLOW facility
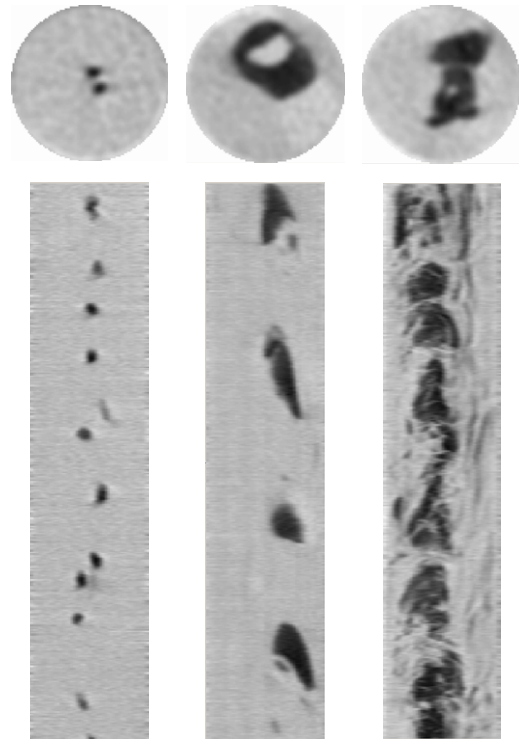
Fig. 4: Cross-sectional images (top) and central axial section images (bottom) of two-phase flow in a bubble column (the vertical axis has the dimension of time)

4. Conclusions

We reported on the development, implementation, and test of a new fast scanned electron beam X-ray CT scanner for two-phase flow measurement. The scanner achieves frame rates of up to 7 kHz and 1 mm spatial resolution. As a first test case two-phase flow in a bubble column could be visualized. One upcoming application for this new device will be two-phase flow measurement in vertical pipes.

References

[1]   R. A. Williams and M. S. Beck (1995), Process Tomography: Principles, Techniques and Applications, Oxford, UK: Butterworth-Heinemann.
[2]   T. York (2001), Status of electrical tomography in industrial applications, J. Electron. Imaging 10, 608-19.
[3]   L. F. Gladden, M. H. M. Lim, M. D. Mantle, A. J. Sederman and E. H. Stitt (2003), MRI visualisation of two-phase flow in structured supports and trickle-bed reactors, Catal. Today 79-80, 203-210.

[4]   G. A. Johansen, T. Frøystein, B. T. Hjertaker and Ø. Olsen (1996), A dual sensor flow imaging tomographic system, Meas. Sci. Technol. 7, 297-307.

[5]   M. Misawa, I. Tiseanu, H.-M. Prasser, N. Ichikawa and M. Akai (2003), Ultra-fast x-ray tomography for multi-phase flow interface dynamic studies, Kerntechnik 68, 85-90.

[6]   K. Hori, T. Fujimoto, K. Kawanishi and H. Nishikawa (2000), Development of an ultrafast X-ray computed tomography scanner system: Application for measurement of instantaneous void distribution of gas-liquid two-phase flow, Heat. Trans. Asian Res. 29, 155-65.

[7]   M. P. Dudukovic (2002), Opaque multiphase flows: experiments and modeling, Exp. Therm. Fluid. Sci. 26, 747-761.

[8]   D. J. Parker, R. N. Forster, P. Fowles and P. S. Takhar (2002), Positron emission particle tracking using the new Birmingham positron camera, Nucl. Instrument. Meth. A 477, 540-545.

[9]   D. P. Boyd and M. J. Lipton (1983), Cardiac computed tomography, Proc. IEEE 71, 298-307.

A NEW CAPACITANCE WIRE-MESH SENSOR FOR TWO-PHASE FLOW MEASUREMENT

Marco Jose Da Silva, Eckhard Schleicher, and Uwe Hampel

## 1.	Introduction

The experimental investigation of multiphase flows plays an important role in many research and industrial applications. Some examples of that are found in the safety assessment of nuclear reactors, device optimization in the chemical industry or in decision making for control strategies of industrial plants.

Wire-mesh sensors allow the study of flows with high spatial and temporal resolution. This type of sensor was introduced about ten years ago [1] and since then it has been employed to investigate a number of two-phase flow phenomena. Two sets of wires are crosswise spanned in a pipe forming an angle of 90° and having a small separation between them. An associated electronics measures the local conductivity through the gaps at all crossing points. This technique allows void fraction and bubble size measurements with temporal resolution of up to 10,000 frames per second (fps) and spatial resolution of up to 2 mm [2].

Since the measuring principle of a conductivity wire-mesh sensor requires at least one continuous conductive phase, wire-mesh sensors have almost exclusively been used for the investigation of air-water or steam-water systems. Nevertheless, non-conducting fluids such as oil or organic liquids often occur in industrial applications, for instance, in chemical and petrochemical industry. The experimental investigation of multiphase flows involving non-conducting fluids is therefore of large interest. For this reason we developed a novel wire-mesh sensor based on the measurements of the electrical permittivity (capacitance) which is suitable for the investigation of non-conducting fluids.

## 2.	System description

For verification of the capacitance measurement technique we have used a laboratory wire-mesh sensor with rectangular section (50 mm x 50 mm), which has previous been employed for conductivity measurements. The sensor is made of two layers with 16 stainless steel wires (diameter 0.12 mm) having 1.5 mm axial plane distance. The distance between the wires in one layer is 3.12 mm. The wires are mounted in a rectangular acrylic frame that itself is part of a rectangular flow channel.

The time-multiplexed excitation scheme used in previous conductivity wire-mesh systems [1] has been maintained, i.e. the transmitter electrodes are activated consecutively, while the receiver electrodes are measured in parallel. However, while the conductivity wire-mesh sensor is excited by bipolar voltage pulses and currents are measured with a dc measuring scheme, for the capacitance wire-mesh sensor an appropriate ac excitation and measuring scheme was employed. That is, we now apply a sinusoidally alternating voltage for excitation. Figure 1 depicts the block diagram of the novel electronics design.

The excitation voltage is generated by means of a direct digital synthesizer (DDS) circuit with selectable frequency in the range of 0.1 to 10 MHz. This signal is then time-multiplexed to each of the excitation electrodes by means of an analog multiplexer (MAX396). In order to create a low impedance path, the outputs of the switches are buffered by operational

amplifiers (opamp). Furthermore, when the multiplexer output is not activated, i.e. it is in a high impedance state, a resistor (470 Ω) grounds the opamp input, thus grounding the corresponding electrode wire. The currents flowing from transmitter to receiver electrodes are converted to voltages by means of transimpedance amplifiers (OPA656 based). These sine wave voltages are demodulated using logarithmic detectors (AD8307), i.e. converting them into dc proportional voltages. In addition the dc voltages carrying the information about the permittivity are digitized by the USB data acquisition card (Measuring Computing Inc., USB1616FS, 16 bit resolution, max. 10 kHz sampling rate per channel by simultaneous sampling of the 16 channels). A PIC microcontroller operates the multiplexer, programs the DDS and controls the analog-to-digital conversion (ADC) timing. The USB data acquisition card is connected to a computer, where the measured data are processed and visualized. The maximum frame rate which can currently be achieved is 625 fps. It is determined by the maximum sampling rate per channel of the data acquisition card divided by the total number of receiver wires, i.e. 10,000/16. Thus, the actual frame rate is still low due to the comparatively slow data acquisition card, but it will be increased to above 10,000 fps in the future by integration of a faster ADC and digital processing electronics.
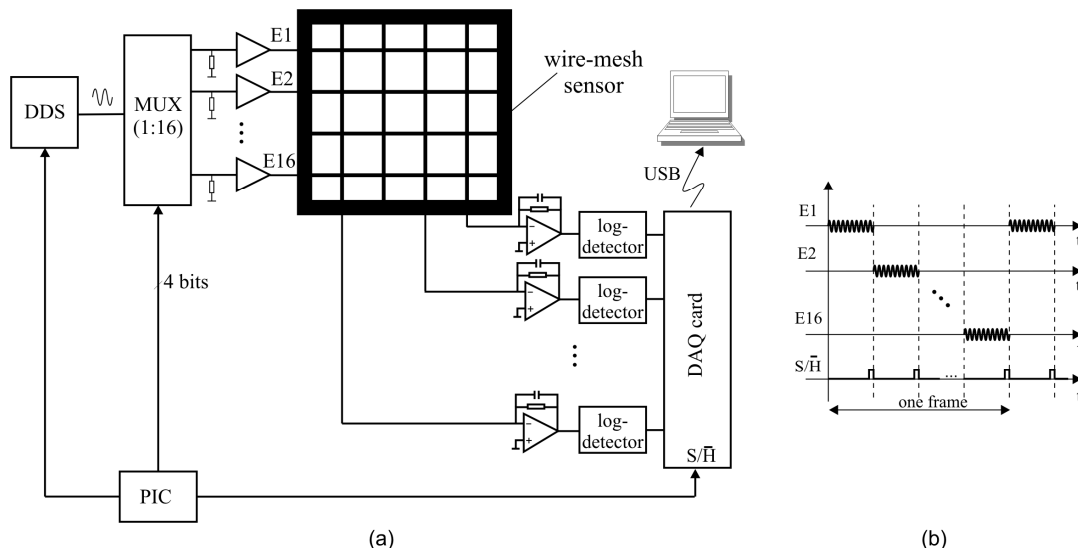
Fig.1: (a) Block diagram of the wire-mesh sensor electronics. (b) Excitation scheme of the wire-mesh sensor electronics.

To achieve an independent local phase fraction measurement in each crossing point, i.e. to suppress the crosstalk between the individual sub-regions, the following excitation scheme is employed, as exemplified in figure 1b. The transmitter electrodes are activated consecutively, while keeping all other transmitter electrodes at ground potential. All currents flowing from transmitter to receiver electrodes at the other wire plane are measured in parallel as described above. Since the receiver electrodes are also at ground potential by the opamp's virtual ground, the electrical field is concentrated along the active transmitter wire and the current measured at one receiver wire is only proportional to the capacitance (permittivity) of the surrounding flow phase at the crossing point.

3. Permittivity measurement

For the permittivity measurement of the crossing points we have employed an ac-based capacitance measuring method. This method has been successfully employed in electrical capacitance tomographs [3]. It gives a high signal-to-noise ratio and stray capacitance immunity. Figure 2 shows an equivalent circuit for one crossing point, where V_i is the input

voltage, C_x represents the crossing point capacitance, C_{s1} and C_{s2} represent the stray capacitances to ground generated for instance by the cables or the other grounded electrodes, and C_f and R_f represent the feedback network.
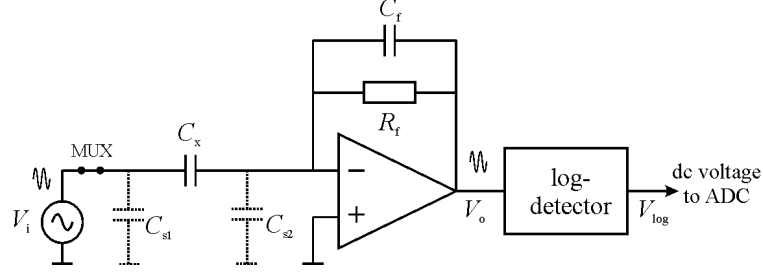
Fig. 2: Equivalent capacitance measuring circuit for one crossing point.

Assuming that the opamp is ideal and that the internal resistance of the analog multiplexer is zero, the output voltage V_o is determined by [3]

$$V_o = -V_i \cdot \frac{C_x}{C_f}. \tag{1}$$

In principle, the stray capacitances have no influence in the circuit, since C_{s1} is directly driven by the source voltage and C_{s2} is virtually grounded by the opamp. The ac output voltage V_o is thus directly proportional to the unknown capacitance of the crossing point. Furthermore, the capacitance of a crossing point is proportional to the relative permittivity ε_r of the phase between the transmitter and receiver wires and can be calculated by

$$C_x = \varepsilon_r \cdot \varepsilon_0 k_g. \tag{2}$$

where ε_0 is the permittivity of vacuum (8.85 pF/m) and k_g is a geometry factor, which depends on the geometry of the problem. Hence, from (1) and (2), it can be stated that V_o is proportional to the relative permittivity of the phase at the crossing point. We expect a high signal dynamics in the voltage V_o by measurements on different substances, therefore a logarithmic detector scheme was employed in the system for the demodulation of this ac signal. Even very small changes in the capacitance or permittivity (and consequently in V_o) can be measured by maintaining a fast response time. The log-detector output is in the form

$$V_{\log} = V_a \cdot \ln\left(\frac{V_o}{V_b}\right) \tag{3}$$

where V_a and V_b are constants of the integrated circuit. Rearranging (1)-(3) it is possible to demonstrate that

$$V_{\log} = a \cdot \ln\left(\varepsilon_r\right) + b \tag{4}$$

where a and b are constants that encompass the geometry factor k_g, feedback components, the log-detector constants, the measuring frequency f and the input voltage V_i. It is obvious that some of these parameters are not necessarily the same for each crossing point or transmitter and receiver circuits due to, for instance, the small differences in the geometry factor or the tolerance of electronic components. In order to compensate this variance, application of a calibration routine is required, which is described as follows.

The measured voltages $V_{\log}$ of all crossing points for each frame are saved in a $16 \times 16 \times N_t$ data matrix, where N_t is the number of acquired time steps. In the calibration routine, first the cross section is filled up with a substance with low permittivity ε_r^L and for this situation a data matrix $V^L(i,j)$ is acquired. Normally average values over a certain time are used to reduce statistical signal fluctuations. In a second situation, the entire cross section is covered with another substance having a higher permittivity ε_r^H and the same procedure is repeated, getting the data matrix $V^H(i,j)$. In this fashion, applying equation (4) for both calibration data matrixes is possible to calculate the constants of (4) as

$$a(i,j) = \frac{V^H(i,j) - V^L(i,j)}{\ln(\varepsilon_r^H) - \ln(\varepsilon_r^L)},$$

(5)

$$b(i,j) = \frac{V^L(i,j)\ln(\varepsilon_r^H) - V^H(i,j)\ln(\varepsilon_r^L)}{\ln(\varepsilon_r^H) - \ln(\varepsilon_r^L)}.$$

(6)

Finally, we can calculate the relative permittivity distribution over the sensor cross section by inverting (4) and applying it for every crossing point, thus

$$\varepsilon_r(i,j) = \exp\left(\frac{V_{\log} - b(i,j)}{a(i,j)}\right)$$

(7)

For the calculation of the local phase fraction distribution $\alpha(i,j)$, a linear relationship between the measured permittivity and the phase fraction is assumed

$$\alpha(i,j) = \frac{\varepsilon_r^H - \varepsilon_r(i,j)}{\varepsilon_r^H - \varepsilon_r^L}.$$

(8)

4.   Results

4.1.   System accuracy and noise

The newly developed wire-mesh sensor was initially investigated regarding its accuracy and ability of distinguishing different substances. For this purpose the wire-mesh sensor was entirely covered by some selected substances and 10 frames at the maximum sampling frequency of 625 fps were recorded and averaged in order to suppress random noise. The excitation frequency was set to 5 MHz and the input voltage amplitude to 3 V_{pp}. Since we have five substances and not two as described in section 3, the calibration routine was slightly modified. Instead of using a two point calibration we perform a linear least-square regression of (4) for each crossing point. That means (5) and (6) were replaced for their least-squares versions. Table 1 shows the selected substances and their reference relative permittivity (taken from [4]), as well as the measured mean value of all crossing points $\bar{\varepsilon}_r$. A good agreement is found in the permittivity measurements with deviations below 10%.

In order to investigate the individual crossing points, the measured voltage for all crossing points $V_{\log}$ in dependence of the relative permittivity for the measured substances was plotted (figure 4). From that, the linear dependence of $V_{\log}$ over the logarithm of ε_r becomes evident, as anticipated by (4). The individual lines obtained represent different linear and angular coefficients, i.e. parameters a and b in (4), thus indicating the need of a calibration routine.

There is a group of lines which are dislocated from the most of the other lines. These outliers all come from the same receiver channels and may be attributed to a larger component tolerance deviation. Even so, after calibration, these lines produced permittivity values under the 10% tolerance.

Table 1: Results for the measurement with different substances.

Substance	reference ε_r^{ref} (-)	measured $\bar{\varepsilon}_r$ (-)	deviation (%) $\frac{\bar{\varepsilon}_r - \varepsilon_r^{ref}}{\varepsilon_r^{ref}}$
Air	1.0	1.02	1.68
Silicone Oil	2.0	1.92	-3.91
2-propanol	20.1	20.27	0.85
Glycol	41.1	45.18	9.92
Deionized water	80.1	73.98	-7.64
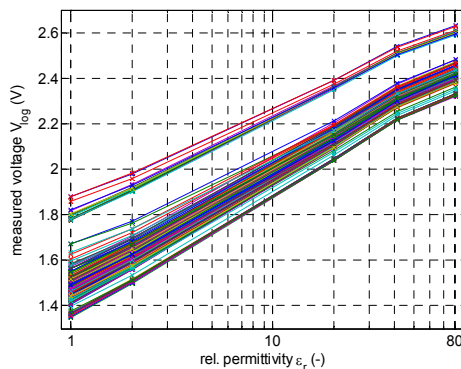
Fig. 4: Measured logarithmic voltage V_{log} in dependence of the relative permittivity ε_r.

The system was then investigated regarding instrumental noise. The wire-mesh sensor was covered with silicone oil and 1000 frames were recorded at 625 fps. Again, voltage amplitude of 3 V_{pp} and excitation frequency of 5 MHz were used. The standard deviation of the measured relative permittivity over the 1000 frames was used to estimate the instrumental noise. A maximum value of the standard deviation over all 256 crossing points of 0.27% was obtained. This noise level is much smaller than the maximum deviation as shown in table 1 and can therefore be neglected.

4.2.   Bubbly flow measurement

The capacitance wire-mesh sensor has been employed to measure a silicone oil/air stagnant two-phase flow. The vertical flow channel with the integrated wire-mesh sensor was filled with silicone oil ($\varepsilon_r = 2.8$) and air was injected at the bottom of the column through a set of holes located in the bottom of the channel. The wire-mesh sensor was set up to acquire data at the maximum frame rate possible of 625 fps. Two reference images for the calibration routine with 100% gas and 100% liquid were acquired at the beginning of the experiments. Figure 5 shows images of the void fraction distribution obtained after calibration. The four cross-section images show details of one single bubble for selected time frames. The image on the left is an axial slice image taken from electrode number 8, i.e. along a central chord of the channel showing two larger bubbles. Note that the vertical axis has the dimension of time and not space. For known gas velocities the time coordinate may however be transformed into an spatial coordinate.
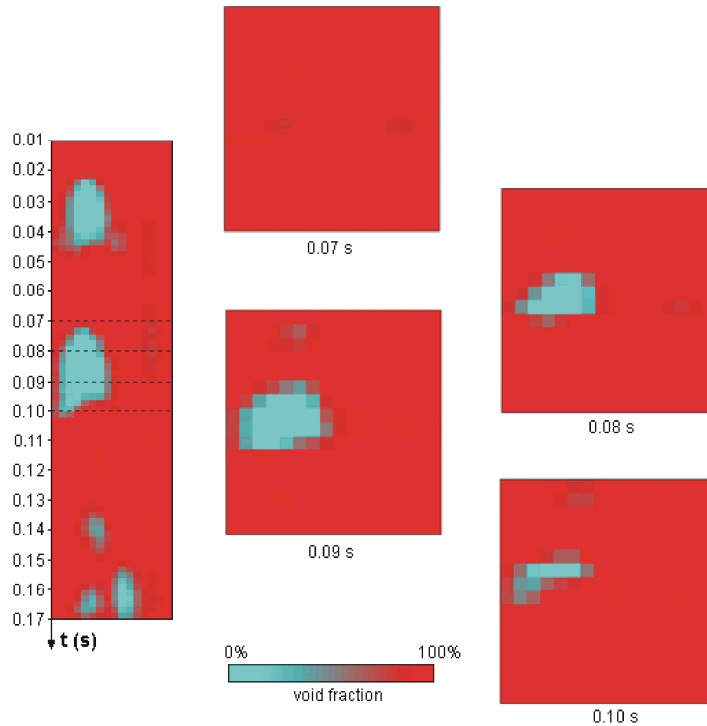
Fig. 5: Axial (left) and cross-sectional (right) slice images of an oil/air bubbly two-phase flow acquired with the capacitance wire-mesh sensor.

5.   Conclusions

We developed and tested a novel wire-mesh sensor based on capacitance (permittivity) measurements. The sensor can measure the phase fraction distribution in a flow cross-section with high spatial and temporal resolution. Further, this new sensor is capable of measuring in non-conducting and slightly conducting fluids. Beside the improved range of measurable substances another special advantage of the capacitance wire-mesh sensor is the possibility to use electrically isolated wires, which enables to operate a sensor with protective wire coatings, for instance in aggressive media. The evaluation of the prototype wire-mesh sensor system has shown good reproducibility and accuracy in permittivity measurements even at a rather fast response time, thus allowing the system to be employed in the investigation of a wide range of substances even with close relative permittivity values, such as for air and oil. The actual maximal frame rate of 625 fps can be easily increased by using an improved digital signal processing electronics. Frame frequencies above 10,000 fps are expected to be reached in the future.

References

[1]   H.-M. Prasser, A. Böttger and J. Zschau (1998), A New Electrode-Mesh Tomograph for Gas-Liquid Flows. Flow Measurement and Instrumentation Vol. 9, 111-119.
[2]   H.-M. Prasser , J. Zschau, D. Peters, G. Pietzsch, W. Taubert, and M. Trepte (2002), Fast wire-mesh sensors for gas–liquid flows visualization with up to 10 000 frames per second. In: Proc. Int. Congr. on Advanced Nuclear Power Plants, Hollywood, USA. Paper #1055.
[3]   W.Q. Yang and T.A. York (1999), New AC-based capacitance tomography system. IEE P-Sci Meas Tech Vol. 146, 47-53
[4]   D.R. Lide (2005), CRC Handbook of Chemistry and Physics 85th ed. (pp. 6-155 - 6-177), Boca Raton, FL: CRC Press.

ANALYSIS OF SAFETY VALVE CHARACTERISTICS USING MEASUREMENTS AND CFD SIMULATIONS

Thomas Höhne, Davide Moncalvo[1], and Lutz Friedel[2]

1. Introduction

The main purpose of the safety valve (Fig. 1) in nuclear plants is to protect the primary loop of a pressurized water reactor against over-pressure: at a given set pressure the valve opens and releases the medium (steam, water) from the reactor into the flash tank. Additional valves are installed in the primary loop to relieve pressure at a level below the set pressure of the safety valve to release steam to the flash tank. Valves are also mounted in the main steam system to protect the steam generator from over-pressure.

The basic elements of the design (Fig. 1) consist of a mutually perpendicular valve body with the valve inlet or nozzle, mounted on the pressure-containing system. The outlet connection may be attached to a piping discharge system. However, in some applications, such as compressed air systems, the safety valve may not have an outlet discharge line and the fluid may in those cases be directly vented into the atmosphere.

The disc is held against the nozzle seat (under normal operating conditions) by the spring, which is housed in an open or closed arrangement (or bonnet) mounted on top of the body. The discs used in the rapid opening (pop type) safety valves are surrounded by a shroud, disc holder or huddling chamber which helps to produce the rapid opening sequence.

Fig. 1 Safety valve. Courtesy of Leser GmbH

A nuclear power plant has several safety valves. Failure of a valve can cause inability of a train to operate as designed. If the safety system has redundancy, then such a train failure reduces (or eliminates) the inherent redundancy. Safety valves might also fail due to a common-cause failure. Therefore, continuous improvements are needed through tests and surveillance [1]. For that reason the OECD-CSNI GAMA Report of WG3 "Extension of CFD to Two-Phase Flow Safety Problems" contains the flow in safety valves as a nuclear reactor safety issue [2].

[1] LESER GmbH & Co. KG, Technisches Büro
[2] TU Hamburg-Harburg, Institut für Strömungsmechanik

Computational fluid dynamics (CFD) codes can help to improve the design and sizing of safety valves. In order to validate the ANSYS CFX code measurements were conducted at the Institut für Strömungsmechanik of the TU Hamburg-Haburg (TUHH). Due to the continuous improvement of the physical models and numerics of the CFD codes it is now possible to simulate the very complex flow in safety valves. This is a combination of complex phenomena like jets, stream separation, dead zones and also supercritical flows. The test rig at the Institut für Strömungsmechanik at the TUHH can be operated in single as well as in two-phase flow regimes. The gaseous phase is dried ambient air, while the liquid component ranges from tap water to aqueous solutions of glycerin, glucose and polyvinylpyrrolidone K90 at several viscosity levels. Measurements are recorded only when the facility operates steadily to allow a repeatable assessment of safety valve flow capacity.

2.   CFD Simulation

ANSYS CFX [3] was used for simulating the flow in a safety valve. ANSYS CFX is an element-based finite-volume method with second-order discretisation schemes in space and time. It uses a coupled algebraic multigrid algorithm to solve the linear systems arising from discretisation. The discretisation schemes and the multigrid solver are scalably parallelized. ANSYS CFX works with unstructured hybrid grids consisting of tetrahedral, hexahedral, prism and pyramid elements. In the calculations shown below, the High-Resolution (HR) discretisation scheme of ANSYS CFX was used to discretise the convective terms in the model equations. The non isotropic Reynolds stress model (RSM) proposed by Launder et al. [4], which is based on the Reynolds Averaged Navier-Stokes Equations (RANS), was applied in combination with an ω-based length scale equation (BSL model) to model the effects of turbulence on the mean flow. Steady state calculations were performed using different pressure conditions at the inlet and outlet. The calculations were performed on the FZD LINUX cluster and they took 2 weeks to complete. Four processors

Fig. 2: Grid model Leser 441 safety valve

were used for the above mentioned simulations in a parallel mode with the partitioning algorithm pvm (parallel virtual machine). The geometric details of the safety valve internals have a strong influence on the flow field. Therefore, an exact representation of the inlet region, the seat and disc region and the shape of the valve body were necessary (Fig. 2). In the current study, these geometric details were modeled using the ANSYS CFX Meshbuild software. Different mesh densities were studied according to the Best Practice Guidelines [5]. Finally, the production mesh contained one million hexahedral elements (Fig. 2). Hexahedral elements were selected instead of tetrahedral elements to reduce the numerical diffusion and to minimize the numerical effort. To have the same grid density as the final production mesh approximately five to seven times more tetrahedral elements would be necessary. The mesh was refined at the regions of possible high velocity gradients. According to the experiments, four different types of fluid composition were used with a constant disc hub of 5.5 mm:

- Water at a stagnant pressure range from 2.07 bar to 6.98 bar (temperature: 17°C)
- Air at a stagnant pressure range from 1.34 bar to 3.06 bar (temperature range: from 15.86°C to 18°C)
- Aqueous glucose at a stagnant pressure range from 2.57 bar to 9.74 bar (temperature range: from 17°C to 18.76°C)
- Air/Water two phase mixture at a stagnant pressure range from 5.52 bar to 8.55 bar (temperature range: from 18.96°C to 19.57°C)

In addition two different disc hub positions for water flow were compared 5.4 mm (2.07 bar to 7.3 bar) and 5.9 mm (2.35 bar to 6.35 bar). The following initial and boundary conditions were applied:

- pressure at the inlet and at the subdomain (inlet part volume until the disc) taken from experiments
- pressure at outlet of flow domain taken from experiments
- measured temperature in the whole domain
- in addition for the two phase flow calculations the volume fraction of the mixture of air and water at the inlet was taken from the experiments
- density and viscosity according to experimental values for calculations with aqueous glucose

For comparison two numerical grids were generated with different disc hub positions. The CFD calculations were performed in accordance with the experiments as steady state calculations; transient processes, like the opening or closing of the valve, were not part of this investigation.

3. Results
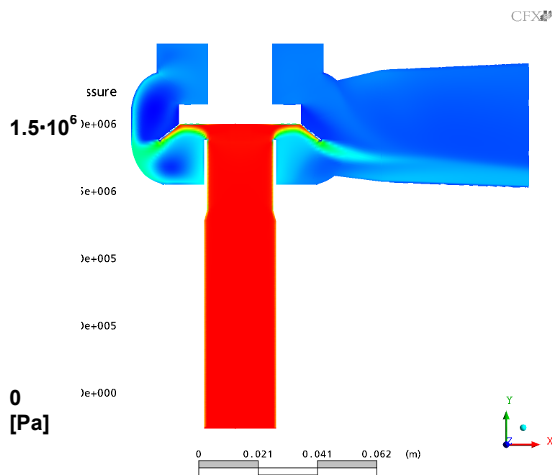
Fig. 3: Pressure distribution at 14 bar over-pressure
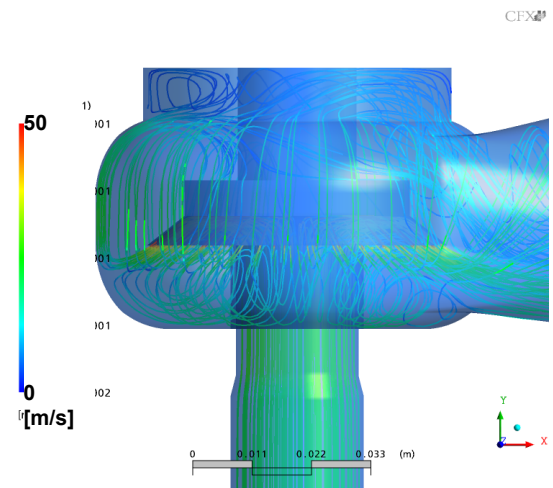
Fig. 4: Velocity distribution at 14 bar over-pressure (3D view with streamlines)

A reference calculation with the fluid water was performed at 14 bar over-pressure. The pressure contours at the center plane of the valve are shown in Fig. 3, while Fig. 4 represents the 3D velocity distributions using streamlines. Jets, flow separation, dead water and recirculation regions and highly dissipative zones with larger decelerations and depressurizations are present. From the observation of the streamlines it can be discerned that the flow presents two main recirculation areas, one above and the other below the disc. A third smaller one is also found in the upper most part of the valve. The disc lift influences the velocity and pressure gradients.

Fig. 5 shows the quantitative comparison of characteristics for different fluids and valve lifts used in the experiments and calculated using CFD methods. In most of the diagrams the stagnation pressure is used. The stagnation (total) pressure is the pressure at a stagnation point in a fluid flow, where the kinetic energy is converted into pressure energy; it is the sum of the dynamic pressure and static pressure. The quantitative validation of the CFD calculations against experiments in the case of water flows with 5.5 mm lift is shown in Fig.5a for five cases. For all of them the agreement between experimental and numerical results is very good with deviations between 0.02% and 4%. Fig. 5b represents the validation of the numerical calculations in case of air at the same lift. The calculations show good agreement with the measured mass capacities at lower stagnation pressures with a deviation of around 0.9% but it also shows bigger discrepancies at higher pressure levels with a maximum of 27%.
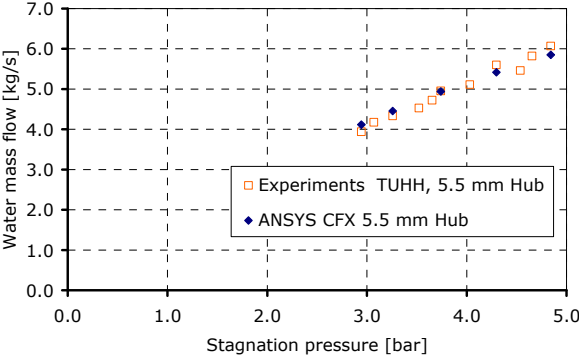
a) Mass flow rate [kg/s] vs. stagnation pressure [bar] for water
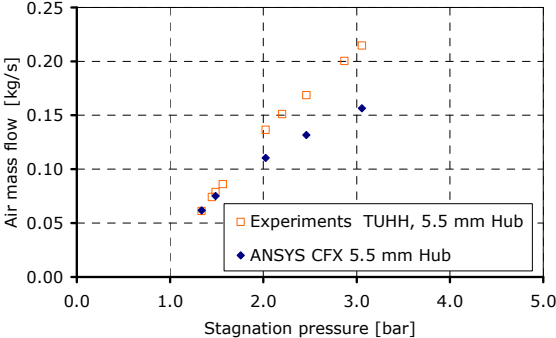
b) Mass flow rate [kg/s] vs. stagnation pressure [bar] for air
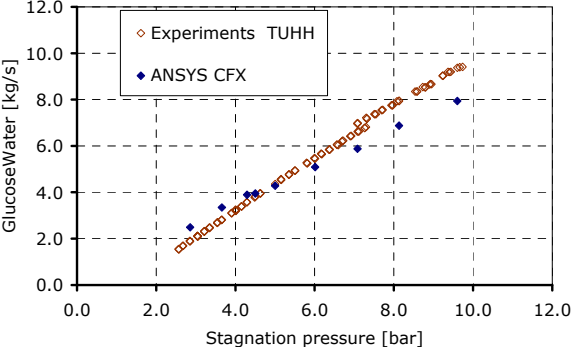
c) Mass flow rate [kg/s] vs. stagnation pressure [bar] for aqueous glucose
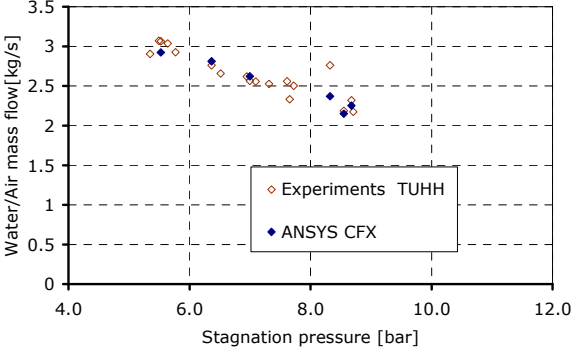
d) Mass flow rate [kg/s] vs. stagnation pressure [bar] for two-phase air/water
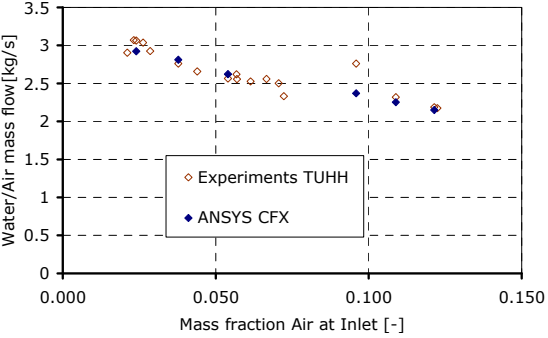
e) Mass flow rate [kg/s] vs. mass fraction air at the inlet [-] for two-phase air/water
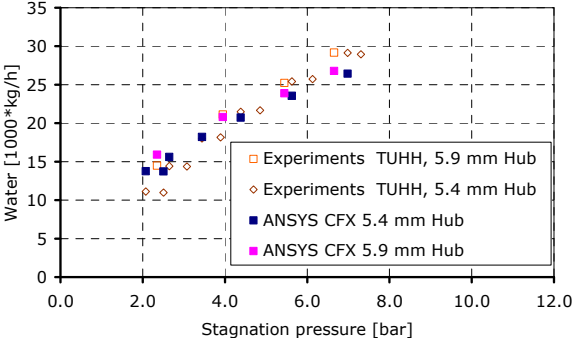
f) Mass flow rate [kg/s] vs. stagnation pressure [bar] for water, 5.4 mm hub vs. 5.9 mm hub

Fig. 5: Comparison of experiments vs. CFD calculations

36

Fig. 5c displays the validation of the CFD calculation in case of aqueous glucose: the numerical results approach the measurements but at a closer detail the CFD code underestimates the effective rate of mass flow increment with the stagnation pressure. At lower pressures the mass flow rate is over predicted with a modest deviation of 3.2% and underestimated at higher pressures with a deviation of 15%. In Figures 5d and 5e the calculated and measured total mass flow capacities are compared for the two phase flow of air and water at different stagnant pressures and inlet air mass fractions for six steady-state cases. The maximum deviation reaches 4.6%. Finally, in Fig. 5f the quality of the grid adaptation of the CFD code on the exactness of results is validated for five water flows at the disc lifts of 5.4 and 5.9 mm. The overall agreement between experimental and numerical results is acceptable with a maximum deviation of 9% for the 5.9 mm lift and 24% for the 5.4 mm. Measurements and calculations agree that with a wider lift of 5.9 mm larger mass flow rates are obtained when the same stagnation conditions are imposed.

4.   Summary

Thanks to the constant improvement of the physical models and numerics of the CFD codes it is now possible to simulate very complex situations, particularly flows in control and safety valves. In order to validate the CFD-code ANSYS CFX, measurements were performed with the fluids air, water, aqueous glucose and the two-phase mixture air/water at the Institut für Strömungsmechanik at the Technical University Hamburg-Haburg (TUHH). Since, the geometric details of the safety valve have a strong influence on the dissipations and the velocity distribution, an exact representation of the inlet region, the seat and disc zones and the shape of the valve body cavity were necessary. The computational grid for the whole geometry contained around one million nodes. For code validation purposes the influence of the different disc lifts was studied as well. In all tested cases a good agreement between measurements and numerical results could be achieved with existing models within the CFD code. Bigger discrepancies using the fluid air were found at higher pressure levels. As a result the CFX input deck can be used at lower pressure levels for further optimization and safety studies of safety valves.

References

[1]   Nuclear Power Plant Operating Experiences from the IAEA / NEA Incident Reporting System, OECD NEA OECD Publications, 2, rue André-Pascal, 75775 Paris Cedex 16, France, 2000, www-ns.iaea.org/downloads/ni/irs/npp-op-ex-96-99.pdf
[2]   OECD-CSNI GAMA Report of WG3 « Extension of CFD to Two-Phase Flow Safety Problems » 2005 NEA/SEN/SIN/AMA(2006)2
[3]   ANSYS CFX-11 User Manual 2007, *ANSYS-CFX*.
[4]   Launder, B.E., Reece, G.J., Rodi, W. Progress in the development of a Reynolds-stress turbulence closure. J. Fluid Mech. 68 (3), 537–566, 1975.
[5]   F. Menter 2002. CFD Best Practice Guidelines for CFD Code Validation for Reactor Safety Applications. *ECORA FIKS-CT-2001-00154*.

COUNTER-CURRENT FLOW LIMITATION EXPERIMENTS IN A MODEL OF THE HOT LEG OF A PRESSURISED WATER REACTOR

Christophe Vallée, Deendarlianto, Dirk Lucas, Matthias Beyer,
Heiko Pietruske, and Helmar Carl

1.   Introduction

In pressurised water reactors (PWR), different scenarios of small break Loss of Coolant Accident (LOCA) lead to the reflux-condenser mode in which steam enters the hot leg from the reactor pressure vessel (RPV) and condenses in the steam generator. A part of the condensate flows back towards the RPV in counter current to the steam. During the reflux-condenser mode, a counter-current flow limitation (CCFL, also referred to as flooding) could occur, compromising the core cooling. The simulation of CCFL conditions, which is dominated by 3D effects, requires the use of a computational fluid dynamics (CFD) approach. These methods are not yet mature and have to be validated against sound experiments before they can be applied to nuclear reactor safety analyses. Therefore, dedicated experimental data is needed with high resolution in space and time.

In order to investigate the two-phase flow behaviour in a complex reactor-typical geometry and to supply suitable data for CFD code validation, a model of the hot leg of a pressurised water reactor (PWR) was built at *Forschungszentrum Dresden-Rossendorf* (FZD). Experiments were performed during air/water counter-current flow before and around the onset of flooding. The measured global parameters like water levels and pressure drop will be analysed in order to characterise the flow. Furthermore, the comparison with detailed visual observations will be used to explain this behaviour. Finally, the onset of flooding as revealed by the data will be discussed in comparison to proposals of other investigators.

2.   The hot leg model

The hot leg model (Figs. 1 and 2) shall allow the application of optical measurement techniques, therefore, a flat test-section design was chosen with a width of 50 mm. The test-section represents the hot leg of the German *Konvoi* PWR at a scale of 1:3, which corresponds to a channel height of 250 mm in the straight part of the hot leg. The test-section is mounted
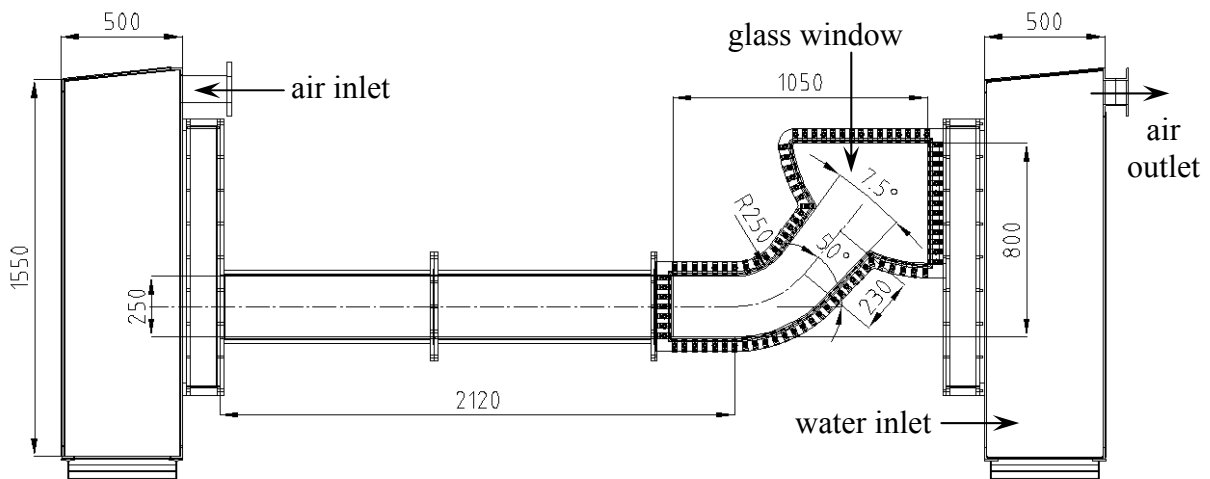
Fig. 1: Schematic view of the hot leg model test section (dimension in mm)

between two separators, one simulates the reactor pressure vessel and the other is connected to the steam generator inlet chamber. This allows to perform co-current as well as counter-current flow experiments. Moreover, the hot leg model is built in in the pressure chamber of the TOPFLOW facility of FZD (Fig. 2), which is used to perform high-pressure experiments under pressure equilibrium between the test-section inside and the chamber atmosphere. Therefore, the test section can be designed with thin materials and equipped with big size windows like in the hot leg model. The presented air/water experiments focus on the flow structure observed in the region of the riser and of the steam generator inlet chamber during counter-current flow at room temperature and pressures up to 3 bars.
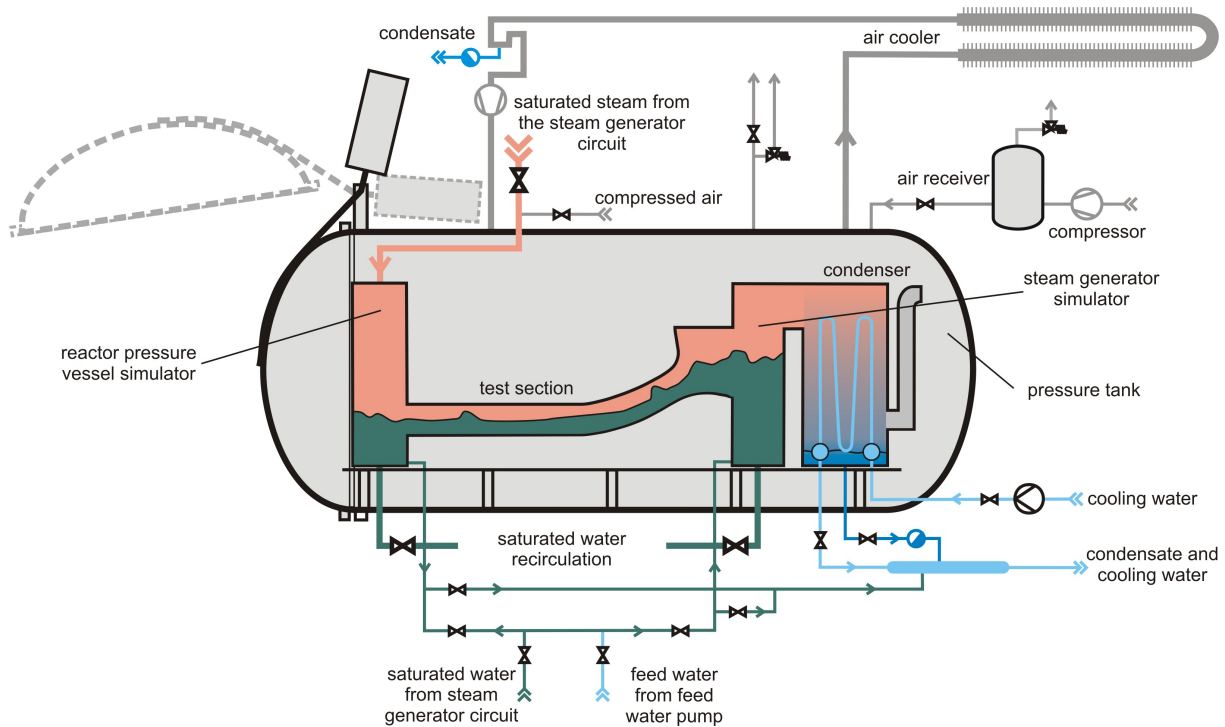
Fig. 2: Schematic view of the experimental setup

3. Experiments and results

During the experiments, a constant water flow rate was injected into the SG separator, while the air flow rate injected into the RPV simulator was stepwise increased to reach the flooding conditions. The measurement of global parameters (e.g. flow rates, water levels, pressures) was complemented by video observations for local information on the flow structure. As an example, one of the experiments is chosen to explain the methodology used to analyse the measured data. This run was performed at the following boundary conditions: a system pressure of 1.58 bar, a water flow rate of 0.59 kg/s at a temperature of 21.0°C and an air temperature of 18.5°C.

3.1. Characterisation of the counter-current flow limitation from global parameters

The measured global parameters include the injected flow rates of air and water, the system pressure, the water levels inside both separators and the pressure drop over the test-section, which were acquired at 1 Hz. The analysis of the evolution of the global parameters over time (Fig. 3) allows to characterise the flow behaviour. Especially the water levels measured in the separators and the pressure difference between them give indication of the flow regime. Furthermore, the increase of the water level in the RPV simulator allows to determine the water flow rate streaming through the test-section, which quantifies the intensity of the CCFL.
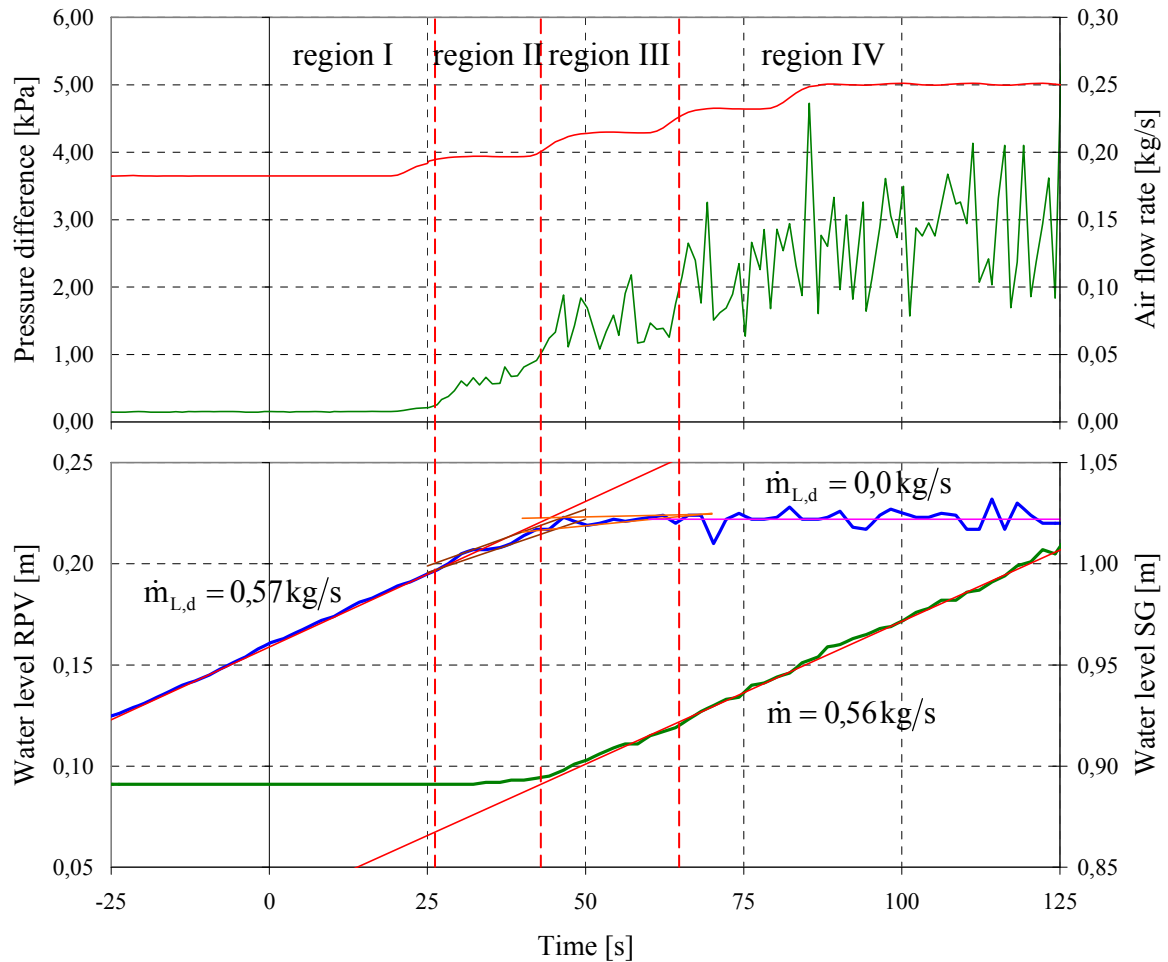
Fig. 3: Variation of the air mass flow rate (top diagram, red curve), of the pressure drop over the test-section (top diagram, green curve), of the water level in the RPV simulator (bottom diagram, blue curve) and in the SG separator (bottom diagram, green curve)

In the diagrams shown in Fig. 3, linear interpolations and envelope lines were added. Based on the trend indicated by these lines, the experiment was divided into 4 regions:

I. At an air flow rate of 0.182 kg/s (for t < 27 s), the water level in the SG separator is constant and the slope of the water level increase in the RPV simulator corresponds to a water flow rate of 0.57 kg/s, which is very close to the mass flow rate injected in the SG separator. This indicates a stable counter-current flow, confirmed by the constant and very low pressure drop over the test-section (0.15 kPa).

II. After the first increase of the air flow rate to 0.197 kg/s (27 < t < 43 s), the pressure drop over the test-section increases to about 0.6 kPa and the slope of the water level in the RPV decreases indicating a reduction of the water flow rate through the test-section. At this stage, the counter-current flow limitation starts.

III. For 43 < t < 65 s, the air flow rate is increased to 0.214 kg/s. This provokes a significant water level increase in the SG separator, showing the effect of the CCFL at the other end of the test-section. As a consequence, the water level increase in the RPV simulator is slowing down. Furthermore, the pressure difference between the separators becomes unstable and fluctuates between 1 and 2 kPa.

IV. With a further increase of the air flow rate to 0.232 kg/s (for t > 65 s), the averaged water level in the RPV simulator keeps constant and the zero penetration point is reached. The pressure drop over the test-section is strongly fluctuating between 1.5 and 4.7 kPa. The last increase of the air flow rate to 0.250 kg/s has almost no influence on the flow behaviour.

40

3.2. High-speed video observations

The two-phase flow in the region of the riser and of the steam generator inlet chamber was captured at a frame rate of 100 Hz with a high-speed video camera. The camera was synchronised with the data acquisition system and was recording in the time from 0 to 110 s (time reference of Fig. 3). Pictures were selected to show the typical flow behaviour in each region defined in the previous section (Fig. 4). The pictures show the evolution of the distribution of the stratified interface and of the two-phase mixture (droplet and bubbles) in each region of the experiment:

I. Stable counter-current flow: a thin supercritical water layer (i.e. $Fr > 1$) flows down the riser to the RPV simulator. Just small waves are observed, which do not affect the flow.

II. Start of the counter-current flow limitation: water accumulates in the horizontal part of the channel due to a flow reversal at the interface. The high air velocity generates waves at the water surface with spume at the crest. A hydraulic jump appears at the transition between the down flowing water from the SG separator and the accumulated water.

III. Counter-current flow limitation: the first slugs blocking an important part of the cross-section are observed, which explains the high pressure fluctuations mentioned in the previous section. The slugs collapse in the riser but droplets detach at the slug front, transporting water to the SG inlet chamber. At the junction between horizontal channel and riser, a recirculation zone emerges: the water flowing down the riser from the SG inlet chamber is deflected by the slugs arriving from the other direction.

IV. Zero penetration: the interface has a pronounced 3-dimensional shape and the flow shows highly mixed two-phase zones. Big slugs are observed which flow up the riser and shift water into the SG separator.

(I) t = 10.00 s

(II) t = 34.60 s

(III) t = 55.00 s

(IV) t = 76.00 s
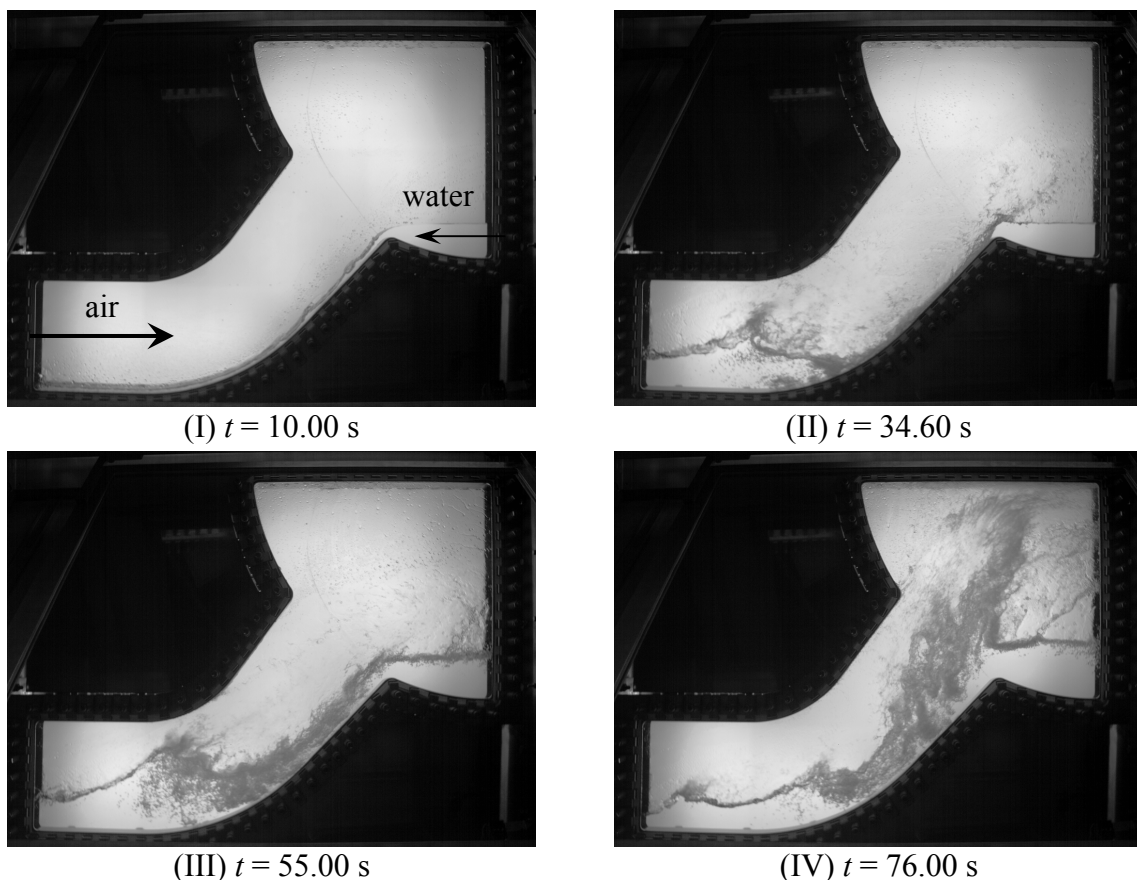
Fig. 4: Flow behaviour during air/water counter-current flow at $\dot{m}_L$ *= 0.59 kg/s and* p = *1.58 bar*

3.3. Comparisons of the present CCFL data with previous work

The plot of the air flow rate versus the water flow rate to the RPV simulator for each region of the experiment leads to the flooding graph. The data obtained in this way was compared with different empirical correlations (Fig. 5) for hot leg typical geometries (i.e. a horizontal conduit connected to a riser) available in the literature: Richter et al. [1], Ardron & Banerjee [2], Ohnuki et al. [3], Lopez-De-Bertodano [4], Kang & No [5], Kim & No [6] and Navarro [7]. Since all the mentioned correlations are for circular pipes, the Wallis parameter J^* was used for the comparison with the present data. For the phase i, this non-dimensional parameter is defined as follows:

$$J_i^* = j_i \cdot \sqrt{\frac{\rho_i}{g \cdot D \cdot (\rho_L - \rho_G)}} \qquad (i = L, G) \tag{1}$$

with j the superficial velocity, g the acceleration of gravity, D the pipe diameter and ρ the fluid density. The subscripts L and G stand for the liquid and gaseous phase respectively.

In order to calculate the Wallis parameter for a horizontal channel with rectangular cross-section, the length term D is substituted by the duct height H. This was done by Hihara et al. [8], who examined the slugging of counter-current gas/liquid in a horizontal rectangular channel. Furthermore, this way is supported by Zapke & Kröger [9], who investigated counter-current flows in rectangular ducts. From experiments in channels with different rectangular cross-sections, they concluded that the flooding gas velocity depends only on the height of the channel and not on its width.
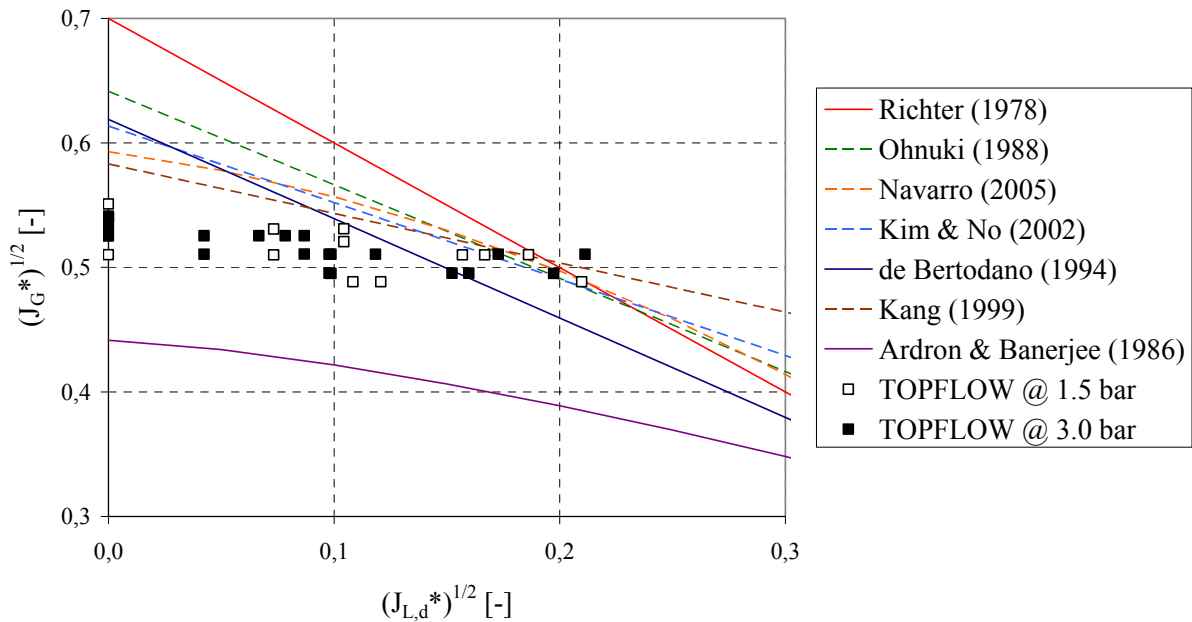
Fig. 5: Comparison of the present data with different CCFL correlations obtained for hot leg typical geometries

As shown in Fig. 5, the present data come closer together with the correlations reported by Ohnuki et al., Lopez-De-Bertodano, Kang & No, and Kim & No, especially at higher liquid discharge flow rates. The trend indicated by the experimental points is similar to those found by previous investigators, but the slope is lower. Therefore, the zero liquid penetration was obtained at lower values of the gaseous Wallis parameter. One main difference could explain this deviation: all the flooding correlations found in the literature are based on pipe experiments, whereas the hot leg model has a rectangular cross-section. Therefore, the deviation revealed in Fig. 5 is probably caused by these geometrical differences.

4. Summary and conclusions

The counter-current flow limitation was investigated experimentally in a flat model of the hot leg of a pressurised water reactor. Counter-current flow limitation, or the onset of flooding, was found by analysing the water levels measured in the separators. A confrontation with the high-speed observation images indicates that the initiation of flooding coincides with the reversal of the flow in the horizontal part of the hot leg due to high air velocities. Furthermore, the CCFL data was compared with empirical correlations for hot leg typical geometries available in the literature. This comparison shows that the Wallis-parameter can be applied to rectangular cross-sections by using the channel height as typical length, instead of the diameter. The obtained flooding curve is similar to those reported by other investigators, but its slope and the gaseous Wallis parameter for zero penetration are lower. This can be attributed to the rectangular cross-section of the hot leg model.

Nevertheless, this analysis of the data shows that it is suitable for CFD code validation. Image processing methods will be applied in order to extract local quantitative information from the high-speed camera images. This will be used for comparison with CFD simulations. Furthermore, similar experiments are planned with steam and water at saturation in order to investigate the phenomenon at reactor typical boundary conditions.

References

[1]   Richter, H. J., Wallis, G. B., Carter, K. H., Murphy, S. L. (1978). Deentrainment and Counter-current Air-Water Flow in a Model PWR Hot Leg. NRC-0193-9.
[2]   Ardron, K. H., Banerjee, S. (1986). Flooding in an elbow between a vertical and a horizontal or near-horizontal pipe. Part II: theory. International Journal of Multiphase Flow 12, 543-558.
[3]   Ohnuki, A., Adachi, H., Murao, Y. (1988). Scale effects on countercurrent gas-liquid flow in a horizontal tube connected to an inclined riser. Nuclear Engineering Design 107, 283-294.
[4]   Lopez-De-Bertodano, M. (1994). Counter-current gas-liquid flow in a pressurized water reactor hot leg. Nuclear Science and Engineering 117, 126-133.
[5]   Kang, S. K., No, H. C. (1999). Air-water counter-current flow limitation in a horizontal pipe connected to an inclined riser. Journal of Korean Nuclear Society 31, 548-560.
[6]   Kim, H. Y., No, H. C. (2002). Assessment of RELAP5/MOD3.2.2γ against flooding database in horizontal-to-inclined pipes. Annals of Nuclear Energy 29, 835-850.
[7]   Navarro, M. A. (2005). Study of countercurrent flow limitation in a horizontal pipe connected to an inclined one. Nuclear Engineering and Design 235, 1139-1148.
[8]   Hihara, E., Soejima, H., Saito, T. (1985). Slugging of countercurrent gas-liquid flow in a horizontal channel, Nippon Kikai Gakkai Ronbunshu (B) 51, 394-397 (Japanese).
[9]   Zapke, A., Kröger, D. G. (2000). Countercurrent gas-liquid flow in inclined and vertical ducts-I: Flow patterns, pressure drop characteristics and flooding. International Journal of Multiphase Flow 26, 1439-1455.

Acknowledgements

A NEW DATABASE ON TWO-PHASE FLOWS IN A VERTICAL PIPE

Johannes Kussin, Matthias Beyer, and Dirk Lucas

1.   Introduction

A new high quality database suitable for CFD-code development and validation for two-phase flows, especially regarding models for bubble coalescence and break-up, was generated. It presents the evolution of air/water flow in a vertical pipe with a nominal diameter of 200 mm. Based on experiences of preceding experimental series [1,2] special attention was paid to the consistency of the data regarding the evolution of the flow.

In the experiments with variable gas injection, the measurement plane is always at the upper tube end while the gas is injected through orifices in the tube wall at different distances to this measurement plane (see Fig. 1). For the preceding experimental series the pressure was almost constant at the measurement plane. This causes different pressures at the individual positions of the gas injection due to the pressure drop along the test section height. At a relatively small void fraction (gas fraction) the effect of the increase in bubble size, which is caused by the decrease of pressure with increasing test section height, can have a larger influence on the bubble size distribution than coalescence and fragmentation effects. Therefore, in the new series the pressure was kept constant at the respective gas injection (p = 0.25 MPa (abs.)). The measurement data represent the development of the flow along the pipe, as it would be observed during an injection at a constant height position with an associated shift of the measurement plane. Moreover, contrary to the past measurements, the temperature was constant at all measurements (T = 30 °C +/- 1 K). This is important because the coalescence rate and break-up frequency sensitively depend on the temperature dependent surface tension. In addition, the number of the measured combinations of air and water volume flows was increased in comparison to former measurements.

The plausibility of the data was examined with the help of the continuous development of time averaged radial void profiles and the bubble size distribution with increasing relative height scale L/D. Moreover, the gas volume flow rates derived from the measured data were compared with injected gas flow rates. This allows to perform an overall error evaluation.

2.   Experiments

To analyse the development of the flow, especially bubble size distributions and gas fraction profiles, a particular design of the vertical test section DN200 with an inner diameter of 195.3 mm was chosen. It is the so-called variable gas injection at the thermal-fluid dynamic test facility TOPFLOW, which has been built and installed in a previous project [1,3]. Fig. 1 shows the construction of the variable gas injection with six injection modules distributed logarithmically over the total height. The distance between the modules and the sensor varies from 0.2 m to 7.8 m. Gas is injected through orifices in the pipe wall. Injection chambers with two different diameters of the orifices (1 and 4 mm) are available to vary the initial bubble size distribution. The injection through wall offers the advantage that the two-phase flow is almost not influenced by the injection devices within the tube at other height positions.

For the experiments, a new low temperature wire-mesh sensor with two measuring planes was used. Each plane is composed of 64 x 64 wires. It consists of two printed circuit boards (material thickness: 2.5 mm). Both of them are equipped with pre-stressed wire electrodes being soldered at a 90° angle to each other on the upper and lower surface. The wires have a lateral distance of 3 mm. In order to make the mechanical sealing of the sensor possible, the wire electrodes with a diameter of 0.125 mm were mounted in approx. 0.3 mm deeply in-milled slots on the printed circuit board. As a result of this construction form, the distance between the two grid levels is approximately 2 mm. Data were obtained with a measuring frequency of 2500 frames/s over a total measurement time of 10 s. References [4,5] give further information on the construction of wire-mesh sensors.

The experiments were done for 48 combinations of superficial air and water velocities varying from 0.04 m/s to 1.6 m/s for the liquid and between 0.0025 m/s to 3.2 m/s for the air. The combinations can be grouped into four test series, with the superficial velocities of the liquid J_L or gas phase J_G remaining constant in two test series each (0.405 m/s and 1.017 m/s for J_L and 0.0096 m/s and 0.219 m/s for J_G). This selection has the advantage that the flow phenomena dependents only on one of these parameters. So the effect of this parameter on the phase transport can be separated. Data were obtained for 12 different values of L/D in case of the 1 mm orifices and for 6 different L/D in case of the 4 mm orifices.

3.   Results

3.1.   Experimental data

From the 3-dimensional matrix of instantaneous void fraction values quantitative data suitable for CFD code development and validation were obtained by time averaging. Most important data are radial gas

Fig. 1: Vertical test section of the TOPFLOW facility with variable gas injection system (DN 200)

volume fraction profiles, radial profiles of the gas velocity, bubble size distributions and radial volume fraction profiles decomposed according to the bubble size. In Fig. 2 examples of such results are given. Fig. 2a) shows the evolution of the radial gas fraction profile along the test section height. While a wall maximum of the gas fraction can be identified close to the gas injection, for this special case, a core maximum of the gas fraction is formed with increasing distance due to the action of lateral bubble forces. The radial profile of the gas velocity presented in Fig. 2b) has a maximum at the wall close to the injection, caused by the acceleration of the liquid by the injected bubbles. As the bubbles distribute of the pipe cross section with increasing L/D the maximum gas velocity is found in the pipe centre. The bubble size distribution is broad near the gas injection and develops into a mono-modal narrow distribu-

tion (Fig. 2c). All data show a high consistency regarding the evolution with increasing L/D, but also regarding the trends due to variations of the superficial velocity. This makes the data suitable for the development and validation of closure models, e.g. for bubble coalescence and breakup.
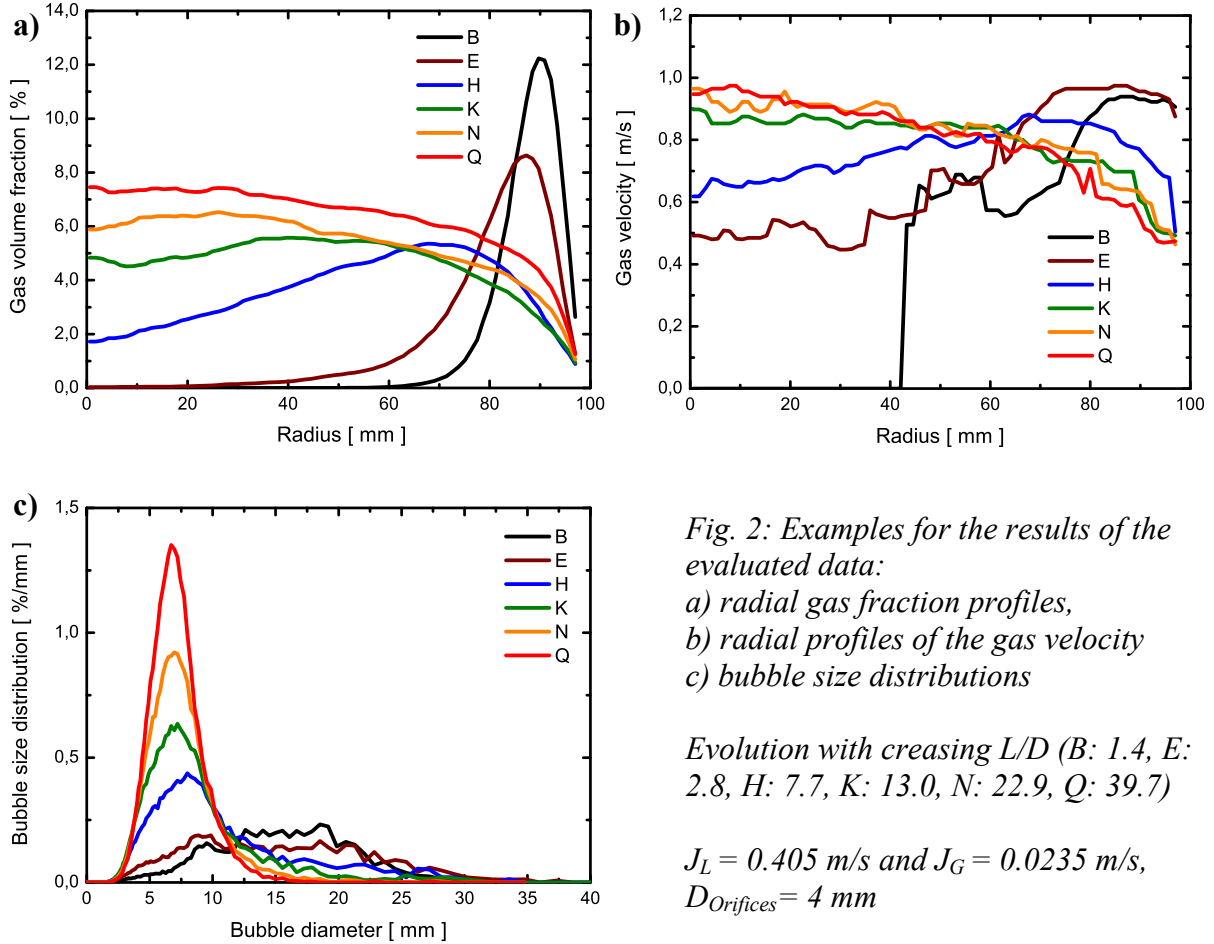
Fig. 2: Examples for the results of the evaluated data:
a) radial gas fraction profiles,
b) radial profiles of the gas velocity
c) bubble size distributions

Evolution with creasing L/D (B: 1.4, E: 2.8, H: 7.7, K: 13.0, N: 22.9, Q: 39.7)

J_L = 0.405 m/s and J_G = 0.0235 m/s, $D_{Orifices}$= 4 mm

3.2. Accuracy check based on superficial gas velocities

For the global error assessment, the value $J_{G,in}$ calculated from the measured void fraction $\varepsilon(r)$ and the velocity of the gas phase $u_G(r)$ is compared with the set value of the injected gas flow rate J_G. The superficial gas velocity $J_{G,S}$ at the sensor position integrated over the cross-section can be calculated from:

$$J_{G,S} = \frac{\dot{V}_G}{A} = \frac{2}{R^2}\int_0^R u_G(r)\cdot\varepsilon(r)\cdot r\cdot dr = <\varepsilon\cdot U_G> \tag{1}$$

where R is the pipe radius, A the cross-sectional area and $\dot{V}_G$ the gas volume flow rate. The superficial gas velocity at the injection is obtained by the Boyle-Mariotte`s law:

$$J_{G,in} = J_{G,S}\cdot\frac{p_{Sensor}}{p_{in}} \tag{2}$$

with the pressure at the wire-mesh sensor p_{Sensor} and the pressure at the gas injection p_{in}. Fig. 3 shows the comparison for the test series I at the maximum relative test section height.

In the logarithmic representation, a good agreement between the set value and the superficial gas velocity becomes visible. Only in the range of the smallest superficial velocities $J_G < 0.2$ m/s, the measured values overestimate the set values. Based on the superficial gas velocities, the accuracy check can be performed in a wide range of 0.0025 m/s $\leq J_G \leq 3.2$ m/s.
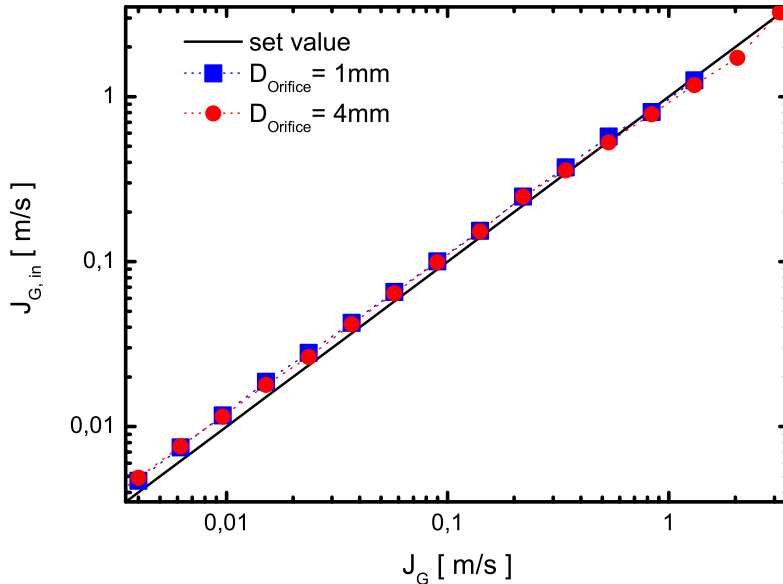
Fig. 3: Comparison of the calculated superficial gas velocity $J_{G,in}$ with the set value J_G at maximum L/D for the test series I ($J_L = 1.017$ m/s) with different injection diameter $D_{Orifice} = 1$ and 4 mm

3.3. Drift velocity and integral void fraction

For the further evaluation of the plausibility of the measured values, theoretically expected void were calculated using drift velocity correlations available in the literature, and compared to measured values. Starting from the definition of the drift velocity:

$$U_D = U_G - J = J_G / \varepsilon - (J_G + J_L) \tag{3}$$

with the total superficial velocities J ($= J_G + J_L$), the void fraction reads:

$$\varepsilon = \frac{J_G}{J_G + J_L + U_D} \tag{4}$$

To check the plausibility of this data, two different assumptions about the drift velocity were introduced:

- a constant value of $U_D = 0.235$ m/s that applies to single bubbles with an equivalent diameter of approx. 6.5 mm, in spite the characteristic size range of the bubbles is approx. between 4 mm to 10 mm (calculation A)
- a "weighted" value, which considers both the measured radial gas fraction profiles and the bubble size distributions (calculation B).

These two gas fraction curves are presented together with the measured curves in dependence on the distance between gas injection and the measuring plane (Fig. 4) for $J_L = 1.017$ m/s and two different superficial gas velocities. The dependence of the gas fraction on L/D is, on the one hand, due to the pressure change, and, on the other hand, due to a change of the drift ve-

locity. Calculation A with the fixed drift velocity assumption considers only the first effect. Accordingly the gas fraction increases about linearly along the tube height. For large L/D the slope of the curve corresponds to that of the experimental values, but there are significant deviations within the range of small L/D, which are caused by injection effects. For small and medium gas fractions (i.e. measurement points with small superficial gas velocity and large superficial liquid velocity), the gas fraction decreases with increasing L/D until approx. L/D = 7 and rises about linearly with further increase of L/D (Fig. 4a). The behavior of the gas fraction at small L/D results from the wall injection of the bubbles. At small gas fraction, the profile of the liquid velocity is only little affected, i.e. within the near wall region the liquid velocity is clearly smaller than in the centre. Therefore, assuming that the relative velocity depends only on the bubble size, the cross-section averaged drift velocity is also smaller compared to equally distributed bubbles or a flow with a core peak of the gas volume fraction. The smaller drift velocity causes higher gas fraction values close to the injection, which afterwards drops with increasing L/D and rises linearly due to the decreasing pressure.

In contrast to that, at large gas fractions (i.e. measurement points with large superficial gas velocities and small superficial liquid velocities), there is a substantial influence of the injected gas upon the profile of the liquid velocities. The liquid near to the wall is accelerated causing also higher gas velocities (compare Fig. 2b) and a more effective transport of the gas. Consequently the cross-section averaged drift velocity is larger near to the injection and the gas fraction is smaller (see Fig. 4b).
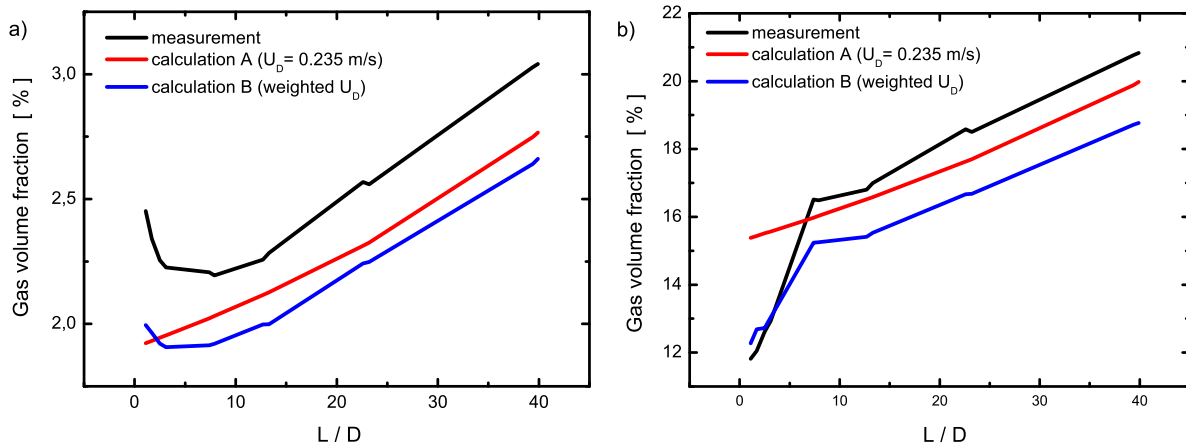
Fig. 4: Development of the measured and calculated gas volume fractions with increasing L/D. 1mm injection, $J_L = 1.017$ m/s, a) $J_G = 0.023$ m/s, b) $J_G = 0.219$ m/s

4.   Summary

The results of the latest test series in the vertical pipe DN200 are characterized by high quality and consistency. The results can be used for the validation of CFD models for two-phase flows and especially for models on bubble coalescence and break-up. Shortcomings of previous measuring series could be overcome by operating the test section at constant inlet temperature of water and setting the pressure to a constant value at the position of the respectively activated injection chamber. Resulting from the high number of measurement points, as well as from the change of the combinations of superficial air and water velocities, various characteristical flow patterns were adjusted. Detailed plausibility checks and error assessments of the measured data were done. The results essentially show a good quality of the measurement

methods and establish the basis for extensive analyses of the obtained data. A detailed measurement report discusses all details of the facility, instrumentation, calibration, data evaluation, results, error assessment and conclusions [6].

References

[1]   H.–M. Prasser, M. Beyer, H. Carl, A. Manera, H. Pietruske, P. Schütz (2007), Experiments on upwards gas/liquid flow in vertical pipes, FZD-Bericht, Nr: 482

[2]   H.-M. Prasser, (2007b). Evolution of interfacial area concentration in a vertical air-water flow measured by wire-mesh sensors. Nuclear Engineering and Design 237 1608-1617.

[3]   H.-M. Prasser, M. Beyer, H. Carl, A. Manera, H. Pietruske, P.Schütz and F.-P- Weiß (2006). The multipurpose thermalhydraulic test facility TOPFLOW: an overview on experimental capabilities, instrumentation and results. Kerntechnik 71

[4]   H. Pietruske, H.-M. Prasser (2007), Wire-mesh sensors for high-resolving two-phase flow studies at high pressures and temperatures. Flow measurement and instrumentation 18-2 (2007)

[5]   H.-M. Prasser, D. Scholz, C. Zippe (2001). Bubble size measurement using wire-mesh sensors. Flow Measurement and Instrumentation, Vol. 12, 2001, S. 299-312.

[6]   M. Beyer, D. Lucas, J. Kussin, P. Schütz (2008). Air-water experiments in a vertical DN200-pipe. FZD-report.

INVESTIGATION OF HYDRODYNAMICS IN ELECTROLYTIC CELLS

Markus Schubert, Holger Kryk, Günther Hessel, and Vinod V. Kumar

1.   Introduction

The continuous progress of electrochemical engineering involves studying and designing more and more efficient electrochemical reactors. In electrolytic capillary gap cells with anode and cathode compartment separated by a membrane, it is necessary to obtain high mass transfer rates of the relevant species through the membrane and thus high conversion of these compounds. Therefore, it is evident to operate at such hydrodynamic conditions which lead to optimized residence time distribution (RTD) inside the cell. The key factor for reliable designing of an optimally operating electrolytic cell is the velocity distribution and the backmixing, which affect the area-specific electricity yield and the overall performance of the electrolytic cell. In addition, the structures of membrane stabilizing spacers, of the electrodes, and of the liquid distributors clearly affect the flow structure in the compartments.

It was the main objective of a previous project to develop reliable measuring technique for the study of the effects of spacer grid and pressure drop between the compartments on the RTD in electrolytic cells. RTD analyses for the overall cell as well as at selected individual regions were conducted using different cell configurations. The characterization of the overall mixing behavior was based on the axial dispersion coefficient and the mean velocity. The measurements provided the base for optimization of the flow structures that diverge from the expected symmetric flows. The aim of the research was to get a better understanding regarding the RTD behavior and to draw conclusions on the cell behavior.

Contrary to classical conductometric measurement methods which cannot by applied in electrochemical systems, this work dealt with the investigation of the liquid RTD using laser induced fluorescence (LIF) visualization which is an alternative and reasonable technology [1].

2.   Experimental setup and measurement procedure

2.1.   Electrolytic cell configuration

The electrolytic cell (see Fig. 1) used for the RTD measurements consisted of an anode compartment and a cathode compartment. Both volumes were separated by an anion-exchange membrane with an area of 0.11 m^2. The anode was a plane metal grid while the cathode was segmented into stainless steal plates each of 0.02 m^2 arranged one upon the other with a gap of 0.01 m between the plates to ensure observability of the fluorescent light. The cathode segments were embedded in an acrylic glass frame which contains the cathode volume as well. A plastic grid (4 cells per square centimeter; total grid thickness of 1 mm) between the cathode segments and the membrane can serve as spacer to avoid direct contact that would compromise the membrane performance. The whole electrolytic active cell length was 1.11 m. The spotlighted cathode compartment had a width of 0.105 m and a depth of 4 mm. The inlet distributor of the cathode volume consisted of 7 equispaced holes.
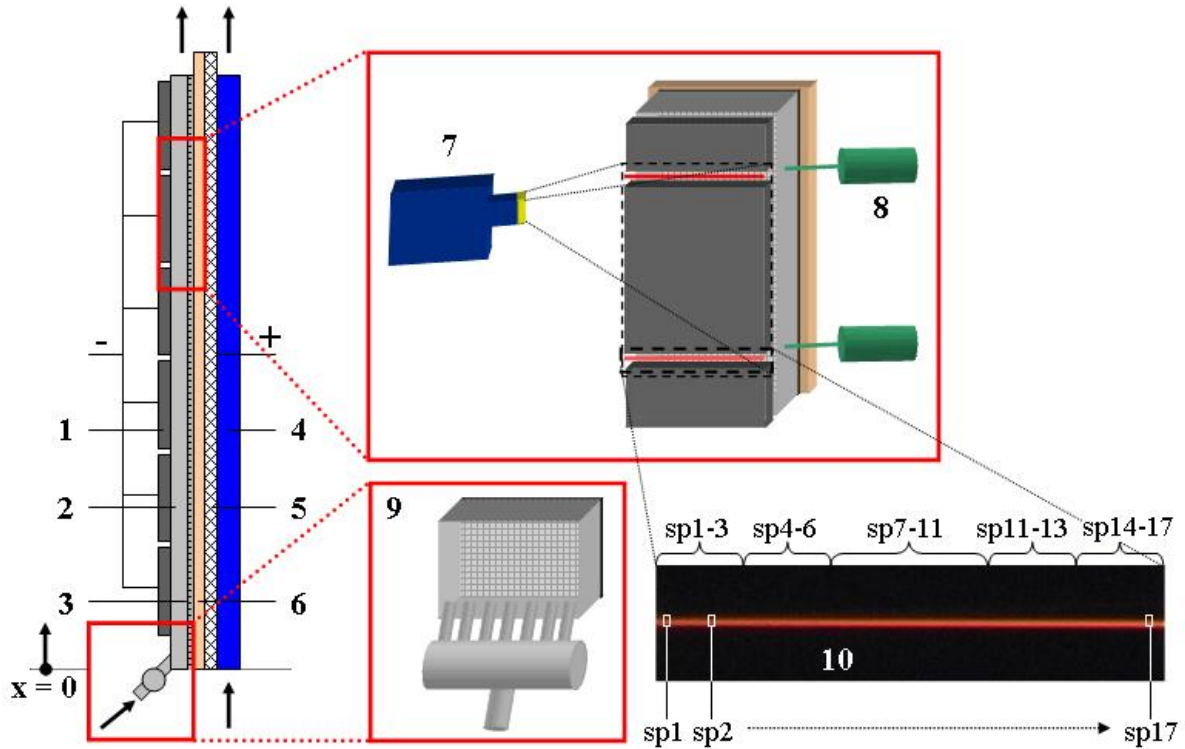
Fig. 1: Experimental setup and measurement principle (1 – segmented cathode, 2 – cathode compartment, 3 – spacer grid, 4 – anode compartment, 5 – anode, 6 – membrane, 7– CCD camera, 8 – laser, 9 – inlet distributor, 10 – laser beam)

2.2.   LIF setup and detection principle

The principle of the LIF is the measurement of the fluorescence intensity of a dye tracer excited by a laser beam. The measurement system employed in this study consisted of a laser system (laser modules GLM-5 by Roithner Lasertechnik, 532 nm, 5...10 mW) and a digital imaging system (Panasonic NV-GS400). The lasers were horizontally justified and arranged at different heights to expose the respective volume laterally by the laser beam (as shown in Fig. 1). The temporal laser induced fluorescence intensity was recorded frontally as a sequence of red-green-blue color signal (RGB) pictures.

Sulforhodamine B (SRB) was used as the chemical fluorescent dye, which fluoresces when induced by a green laser beam. SRB is a suitable dye as it is photo-stable, pH-stable and the sorptivity of SRB on the membrane material is low. Signal separation is easily possible due to the emission maximum at a wave length of 583 nm that differs from excitation wave length. To enhance the signal isolation, a long-pass filter (type 550FH90-50 by L.O.T.-Oriel, cut wavelength 550 nm) was mounted in front of the camera lens so that only fluorescence emissions were recorded.

Preliminary experiments using different SRB concentrations and aperture values were carried out in a cell with dimensions comparable to the electrolytic cell to determine the range of linear response between the fluorescence intensity and SRB concentration which is a requirement for the application of LIF. The fluorescent dye concentration was adjusted to approximately $6.7 \cdot 10^{-10}$ mol_{SRB}/mol_{water}.

2.3. Measurement procedure and data analysis

The RTD measurements using laser-induced fluorescence were performed at different heights downstream from the bottom entrance into the cathode volume. The effect of the liquid flow rate was investigated in the range from 60 to 90 $l \cdot h^{-1}$. For each flow rate, laser-induced fluorescence reference images were recorded for the cell perfused by the water and by the concentrated tracer solution, respectively. The images for the pure liquid represent the noise background I_B. The tracer solution image gives the reference intensity I_{REF} for the red light. Square wave tracer solution pulses of 10 sec were introduced. RGB pictures of the tracer response were recorded with a frame rate of 25 fps and analyzed using an in-house software package in order to get the exact position of the beams and the red light intensity $I(t)$. The response curves were read out an average response considering sections of the fluorescent beam (see sp1…17 in Fig. 1). As a two-point measurement method was implemented, the response curves $E(t)$ were calculated by Equation (1) at each height level.

$$E(t) = \frac{I(t) - I_B}{I_{REF} - I_B} \tag{1}$$

The tracer response functions $E(t)$ were analyzed by curve fitting in the time domain. The axial dispersion model (ADM) was used to obtain mean residence time (mean liquid velocity) and axial dispersion coefficients. The governing differential equation for the tracer in the cell that has an advective transport and dispersion in flow direction x is given in Equation (2).

$$\frac{\partial E}{\partial t} = D_{ax} \frac{\partial^2 E}{\partial x^2} - u \frac{\partial E}{\partial x} \tag{2}$$

D_{ax} is the axial dispersion coefficient and u the liquid velocity. The closed-closed boundary conditions were chosen (Danckwerts boundary conditions) [2]. The calculation of D_{ax} based on the least squares minimization method was done by in MatLab7.

3. Results and discussion

3.1. Typical residence time distributions

An example of the measured normalized response curves at different heights of the cathode compartment without spacer grid at a flow rate of 70 $l \cdot h^{-1}$ is shown in Fig. 2. Simulated and measured response functions match quite well for the onset part and for the amplitude, which makes the dispersion model applicable to the characterization of the liquid flow in the electrolytic cell. Small deviations are found only for the decay with a longer tail of the response curve (see Fig. 2a).

Furthermore, Fig. 2 shows the comparison between the measured response functions and the residence-time-corrected inlet pulses representing ideal plug flow behavior for each height level (a – d).
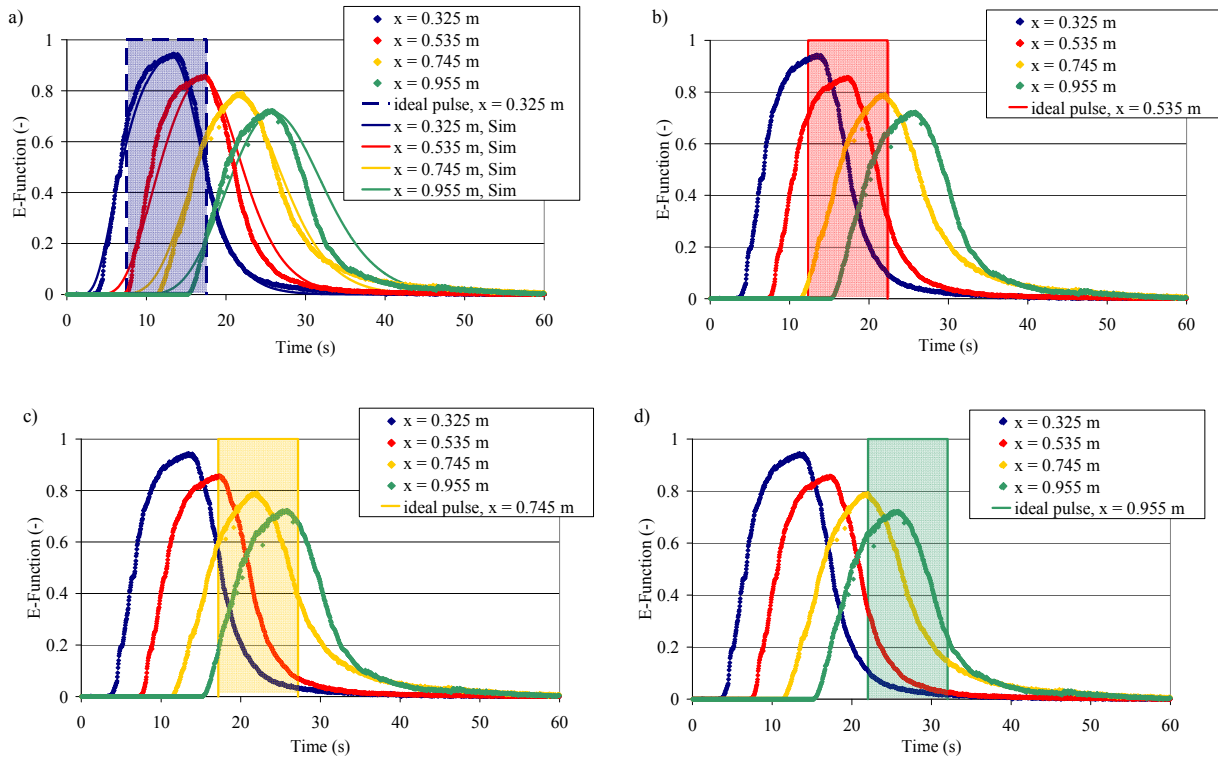
Fig. 2: Response functions of the tracer injection compared to the plug flow behavior (without grid, 70 l·h⁻¹)

3.2. Effect of liquid velocity and spacer grid

Estimated cross-section-averaged RTD curves were analyzed and axial dispersion coefficients plotted as a function of the experimental determined liquid mean velocity (Fig. 3a).
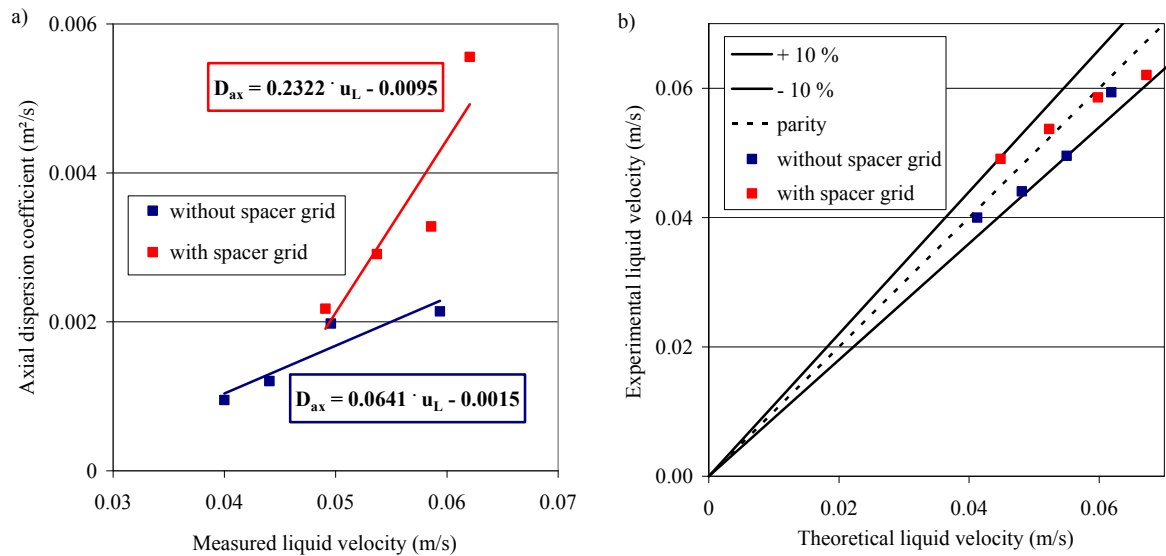
Fig. 3: (a) axial dispersion coefficient and liquid mean velocity based on ADM, (b) parity plot

A linear correlation between axial dispersion coefficients and liquid mean velocity is assumed in the range investigated. Higher dispersion was measured using a spacer grid, indicating small stagnant liquid ratio and dead zones.

53

Based on the mass balance, measured liquid mean velocities cannot go below the theoretical liquid velocities assuming plug flow since the minimal velocity is determined by the geometry of the cathode compartment. Thus, the parity plot (Fig. 3b) shows a maximum deviation of 10 %. The slightly reduced cross section due to the spacer grid was considered.

3.3. Spatial analysis, velocity profiles

Even though global analysis (cross-section-averaged RTD curves) provided good results, visually observed temporal development of the fluorescent beam led to the conclusion that a spatial analysis could provide additional information. Therefore, response functions from individual zones of the horizontal beam were calculated at 17 equidistantly located positions beginning close to the walls (see sp1 to sp 17 in Fig. 1). The red value is averaged over an area of 3 pixels width and 10 pixels height. All 17 spatial distributed response functions are illustrated exemplarily in Fig. 4 for the cathode compartment without spacer grid measured at a liquid flow rate of 70 l·h^{-1} at a height of 0.745 m. To get a general idea about the spatial distributions, three arrays (see Fig. 1) are defined which are drawn with the same colour.
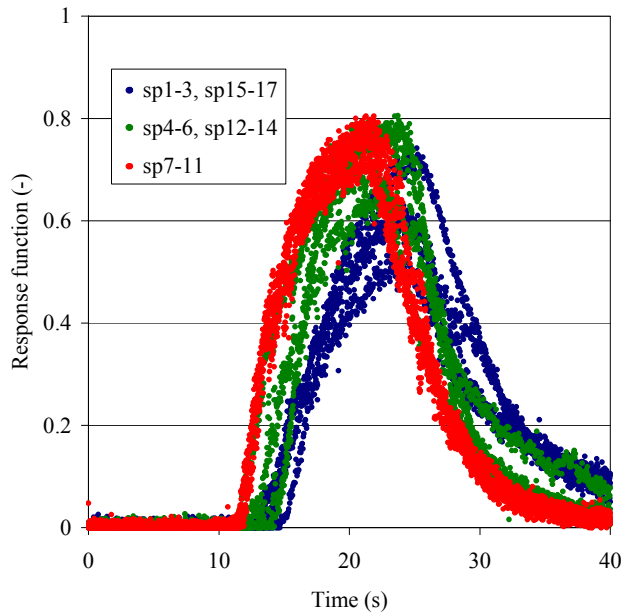
Fig. 4: Horizontally distributed response function at 70 l·h^{-1} without spacer grid

The response functions of the central array (tagged with red symbol) start at first, followed by the middle arrays (tagged with green symbols). The response functions of the outer arrays (tagged with blue symbols) appear with a delay of up to 5 seconds, indicating a lower flow rate in wall region. Additionally, the amplitude is clearly lower compared to the central part.
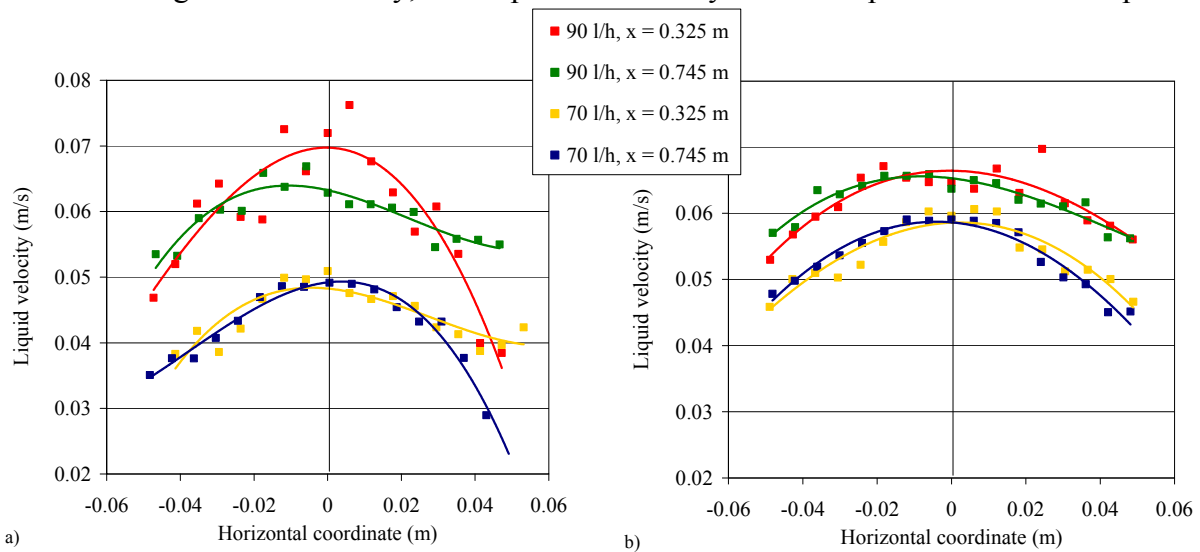
Fig. 5: Liquid velocity profile at 70 l·h^{-1}, (a) without spacer grid, (b) with spacer grid

For the spatial distributed response functions, liquid velocity (see Fig. 5) was calculated using the dispersion model. Velocity profiles obtained without spacer grid indicate clear asymmetric behaviour. Application of the spacer damps the profile. The velocity profile changes only slightly over the height of the cell.

3.4. Effect of the membrane positioning

In contrast to the fixed cathode volume in the single compartment measurements, the membrane installation resulted in flexible volumes of both compartments due to pressure forced membrane positioning. Fig. 6 shows the effect of the membrane position on the RTD in the cathode compartment at a differential pressure of 100 mbar ($p_{cathode}$>p_{anode}).
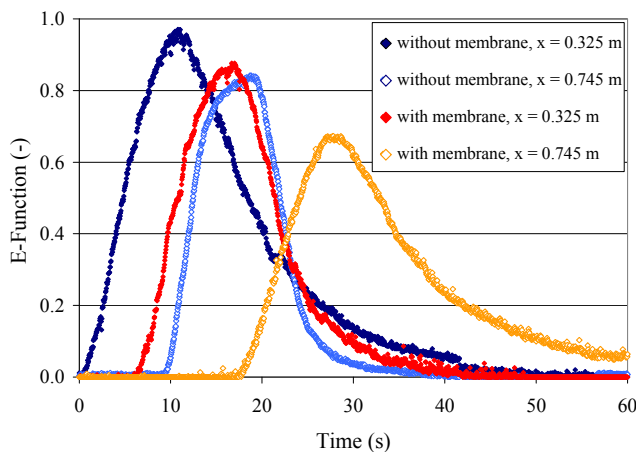
Fig. 6: Effect of membrane on the tracer response functions (without grid, 90 l·h⁻¹)

The tracer response onset starts clearly later indicating a higher cathode volume and convex bent membrane. The determined axial dispersion coefficients do not follow the linear equations shown in Fig. 3a.

4. Conclusions

The study mainly concerned the hydrodynamic investigation of the liquid flow in an electrolytic capillary gap cell. Tracer response functions were measured using a new laser induced fluorescence method and analysed using the axial dispersion model.

The dispersion behaviour was correlated with a linear function based on the liquid mean velocity. A spacer grid clearly enhances the dispersion. However, application of the spacer grid damps the velocity profile and prevents strong profile changes.

For the design of cells with membrane a stable membrane positioning should be realized to avoid non-reproducible hydrodynamic effects due to a moving membrane.

References

[1] C.F. von Carmer (2000), LDA-LIF System zur Untersuchung großräumiger kohärenter Strukturen in flacher turbulenter Strömung, in A. Delgado et al. (Eds.): Lasermethoden in der Strömungsmesstechnik, 8. GALA-Fachtagung, Shaker Verlag, Aachen

[2] P.V. Danckwerts (1953), Continuous flow systems. Distribution of residence times, Chem. Eng. Sci. 2, 1-13.

LORENTZ FORCE DRIVEN FLOWS IN ELECTROCHEMICAL SYSTEMS

Tom Weier, Christian Cierpka, Gerd Mutschke, and Gunter Gerbeth

1. Introduction

Research on magnetic field effects in electrochemical systems has a relatively long history. Bucherer [1] gives an overview of the early attempts. About 40 years ago renewed interest in this area arose, namely with the work of Gak [2] and Fahidy and colleagues [3]. The state of the art has been reviewed from time to time [4-7].

While the influence of magnetic fields on material properties and electrode kinetics is discussed controversially, an influence of the magnetic field on mass transport is widely accepted and commonly referred to as "MHD effect". In this context MHD is an abbreviation for magnetohydrodynamics.

For a binary system with excess of supporting electrolyte, mass transport is described by the convection-diffusion equation [8]

$$\frac{\partial c_i}{\partial t} + (\mathbf{u} \cdot \nabla)c_i = D_i \nabla^2 c_i \tag{1}$$

That is, the distribution of the concentration c_i of the electroactive component i depends on its diffusion coefficient D_i and on the velocity field $\mathbf{u}$. The momentum balance given by the Navier-Stokes equation for incompressible flow

$$\frac{\partial \mathbf{u}}{\partial t} + (\mathbf{u} \cdot \nabla)\mathbf{u} = -\frac{1}{\rho}\nabla p + \nu \nabla^2 \mathbf{u} + \frac{\Delta\rho}{\rho}\mathbf{g} + \frac{1}{\rho}\mathbf{F}_L \tag{2}$$

contains body force terms for buoyancy $\Delta\rho\mathbf{g}$ and other force densities like for instance the Lorentz force $\mathbf{F}_L$. Mass conservation is expressed by the continuity equation

$$\nabla \cdot \mathbf{u} = 0 \tag{3}$$

In the above equations p stands for pressure, t for time, and ρ and ν for the density and kinematic viscosity of the fluid, respectively. Concentration variations cause density differences $\Delta\rho$, which in turn give rise to free convection due to the presence of gravity $\mathbf{g}$. Under conditions of common electrochemical processes, the current density is determined solely by the faradaic current to a very good approximation. In our case, the current density,

$$\mathbf{j} = \sigma(\mathbf{E} + \mathbf{u} \times \mathbf{B}) - n_i F D_i \nabla c_i \tag{4}$$

with $\mathbf{E}$ denoting the electric field strength and σ the electric conductivity contains a term $\sigma(\mathbf{u} \times \mathbf{B})$ accounting for currents induced by the flow. For moderate magnetic induction $\mathbf{B}(\sim 1\text{T})$, induced currents can usually be neglected compared to faradaic ones (see, e.g., [9]). The rightmost term in equ. (4) (details of the derivation can be found in [8]) accounts for the charge transport by diffusion of the electroactive species. n_i denotes the charge number of the

electroactive species and F the Faraday constant. Charge transport by diffusion becomes important in case of concentration gradients, which typically evolve at electrodes and may lead to a limitation of the current by mass transfer. From equations (1) to (4), it becomes apparent that current distribution, flow field and mass transfer are strongly coupled. The velocity field and the current are connected through the Lorentz force,

$$\mathbf{F}_L = \mathbf{j} \times \mathbf{B} \tag{5}$$

occurring in equ. (2).

Depending on the material properties, additional body forces of magnetic origin may exist in the solution [9]. At present, the relative importance of the Lorentz force, the paramagnetic force due to concentration gradients (concentration gradient force)

$$\mathbf{F}_{\nabla c} = \frac{\chi_m B^2}{2\mu_0} \nabla c_i , \tag{6}$$

and the field gradient force imposed by gradients of the magnetic field, is discussed in the literature, e.g. [11-16]. In equ. (6) χ_m denotes the molar susceptibility, B the magnitude of the magnetic induction, and μ_0 the vacuum permeability, respectively.

This paper aims to demonstrate that a Lorentz force is most likely to be present when magnetic fields are applied to electrochemical systems, even in situations, where it appears to be absent at a first glance.

2. Primary and secondary flow in a cylindrical cell

Krause et al. [14] have observed limiting current, i.e. mass transfer, increases in case of perpendicular as well as in case of seemingly parallel electric and magnetic fields. While the former is in line with the common understanding of the "MHD effect", the latter finding was
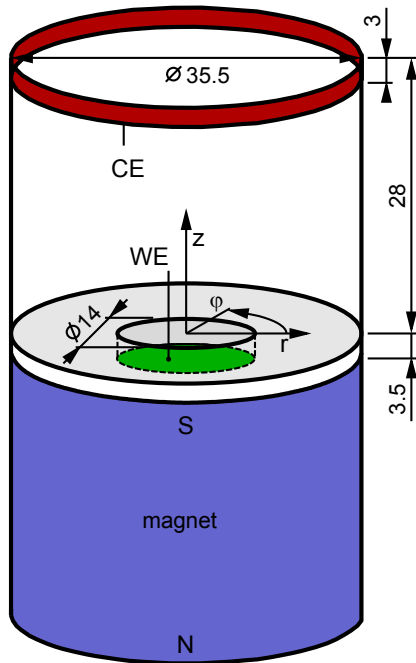
Fig. 1: Sketch of the cell
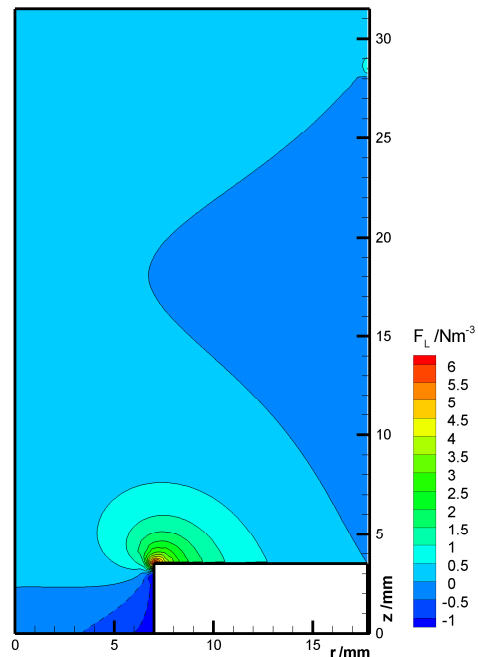
Fig. 2: Lorentz force distribution in the cell

somewhat unexpected and caused speculations about the role of $F_{\nabla c}$ in the process.

In order to properly assess the contribution of the Lorentz force, the force field acting in a cylindrical cell modeled after that used by Krause et al. [14] has been computed using the commercial finite element code Opera from Vector Field Ltd. Fig. 1 shows the experimental setup and Fig. 2 the Lorentz force distribution in a meridional plane of the cell. The magnetic field is relatively homogeneous and has mainly a *z*-component [17]. The primary current density distribution can be calculated by solving a Laplace equation for the electric potential with Dirichlet boundary conditions at the working electrode (WE) and counter electrode (CE). As can be expected, the current density is as well mainly axially directed. However, at the rim of the sinking containing the WE, the electric field lines spread radially outwards. According to equ. (5), an azimuthal Lorentz force results from the axial component of the magnetic induction and the radial currents. Since the radial currents are relatively strong, the Lorentz force density at the edge of the sinking is quite strong as well and dominates the force field. The remaining inhomogeneities of the force field are due to the not perfectly axial magnetic induction generated by the permanent magnet and radial currents in the top of the cell caused by the CE ring. These features are discussed in detail in [17]. The essential, though not unexpected, result of the calculations in the "parallel" field case is the presence of a strong circumferential Lorentz force near the WE.
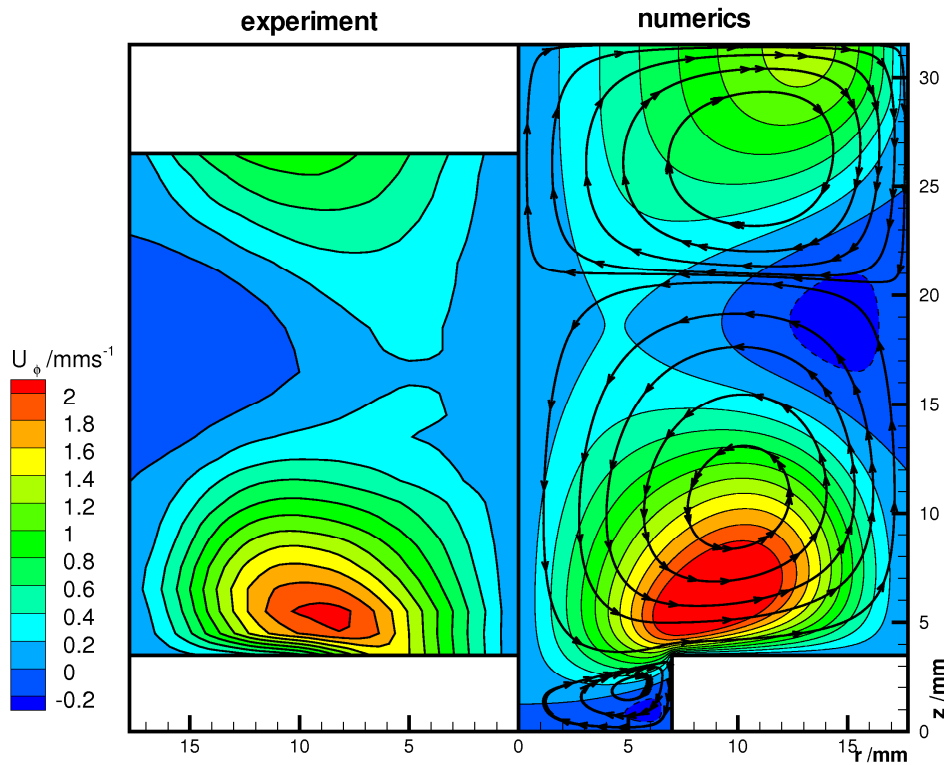
Fig. 3: Calculated (right) and measured (left) distribution of the azimuthal velocity component in the cell. Streamlines are added to the numerical results in order to visualize the secondary flow structure. Note that measurements were impossible for z<3.5mm and z>27mm.

As well known from natural convection, the presence of a body force in a fluid usually generates a flow. The flow driven by the Lorentz force in the cell shown in Fig. 1 has been measured by Particle Image Velocimetry (PIV) as well as calculated using the commercial Navier-Stokes solver FLUENT. In the experiments, an aqueous $CuSO_4/Na_2SO_4$ solution has been

used as electrolyte. Copper was either deposited at the cathodically polarized WE, or the copper of the WE has been dissolved in case of anodic polarization. Fig. 3 shows contours of the measured circumferential velocity component for the latter case. It corresponds to a stable density stratification. The copper depleted and therefore less dense solution from the CE flows on top of the copper rich, i.e. high density, solution at the WE. As expected, the flow velocity is largest near the location of the highest Lorentz force density at the rim of the WE sinking. However, the fluid is nowhere at rest. Instead, a relatively complicated flow structure can be found. Firstly, the primary azimuthal flow drives a secondary flow in the meridional plane. The action of the Lorentz force density distribution in the cell center can be understood in analogy to that of a small rotating disc. Rotating disc driven flows, sometimes also termed "von Karman swirling flows" [18], are quite common in turbomachinery and find application at "rotating disc electrodes" [19] in electrochemical investigations as well. As described e.g. by Schlichting [20], the rotation imposed on the fluid in the vicinity of the WE exerts a centrifugal force which throws the fluid radially outwards. Due to continuity expressed in equ. (3), the fluid is replaced by an axially downward motion in the centre of the cell. At the end, a secondary flow in the form of a toroidal vortex forms in the lower half of the cell. The remaining part of the flow structure can be explained by additional features of the Lorentz force field shown in Fig. 2. For this somewhat lengthy discussion, we refer to [17]. Despite the fact that density effects have not been included in the calculations, numerical and experimental results fit quite well.

Considering limiting current conditions, i.e. electrochemical reaction rates, in the cell, they are of course influenced by the Lorentz force driven flow shown in Fig. 3. Thus, there is no need to refer to additional forces of magnetic origin in order to explain limiting current changes, when a magnetic field is applied "parallel" to the electric field in the cell. Since on closer inspection, magnetic and electric field are very seldom really parallel.

3.   Flow field and concentration distribution at circular electrodes

Similar conclusions can usually be drawn for other cell geometries. Fig. 4 shows electric field and Lorentz force distribution in the lower half of a rectangular cell equipped with a disk electrode sitting on the tip of a rod. Again, the assumption of parallel electric and magnetic fields has been used in the literature [12] to justify the *a priori* negligence of Lorentz forces.
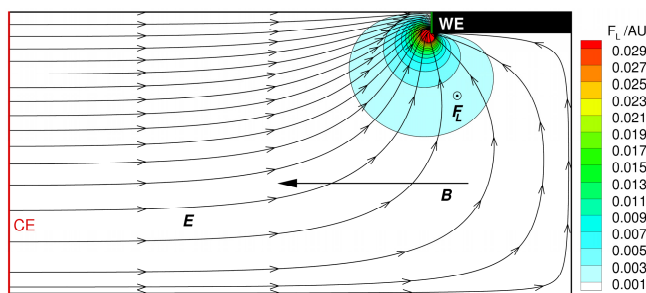
Fig. 4: Lorentz force distribution due to a homogeneous magnetic field and radial currents near the WE (only the lower part of the cell is shown).
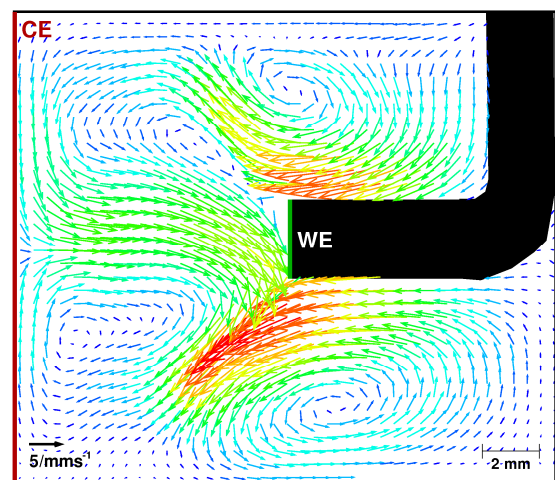
Fig. 5: In-plane velocity components in the midplane of the cell (secondary flow).

However, the electric field in the gap between the small WE and the much larger CE depicted in Fig. 4 – because of symmetry around the WE axis, only the lower part of the cell is shown – has not only components parallel to the WE axis. Radial currents arise again at the WE rim and generate together with the axially oriented magnetic induction a strong circumferential Lorentz force density there. This force density drives a primary flow in azimuthal direction which in turn gives rise to a secondary flow in the meridional plane. This secondary flow, PIV measurements are shown in Fig. 5, features an impinging jet and stagnation point at the WE. Thus, flow velocities in the direct vicinity of the WE are low. The WE is surrounded by a region of almost stagnant fluid. Reaction products will therefore accumulate at the WE. This is indeed the case as can be concluded from Fig. 6a. It shows a synthetic schlieren picture of the cell 44 s after applying a cathodic potential to the WE. Synthetic schlieren [21] or background oriented schlieren (BOS, [22]) measures the first spatial derivative of the refractive index. In simple chemical systems, like the one considered here, the refractive index is directly proportional to the concentration of the electroactive species. The contours shown in Fig. 6 are therefore similar to contours of the concentration field gradient.

This accumulation of reaction products at the WE has formerly been attributed to the concentration gradient force by Leventis and Dass [12]. As can be seen from equ. (6) the concentration gradient force does not depend on the current density at all. However, switching back to open circuit potential, i.e. turning off the applied electric field, results in the image shown in
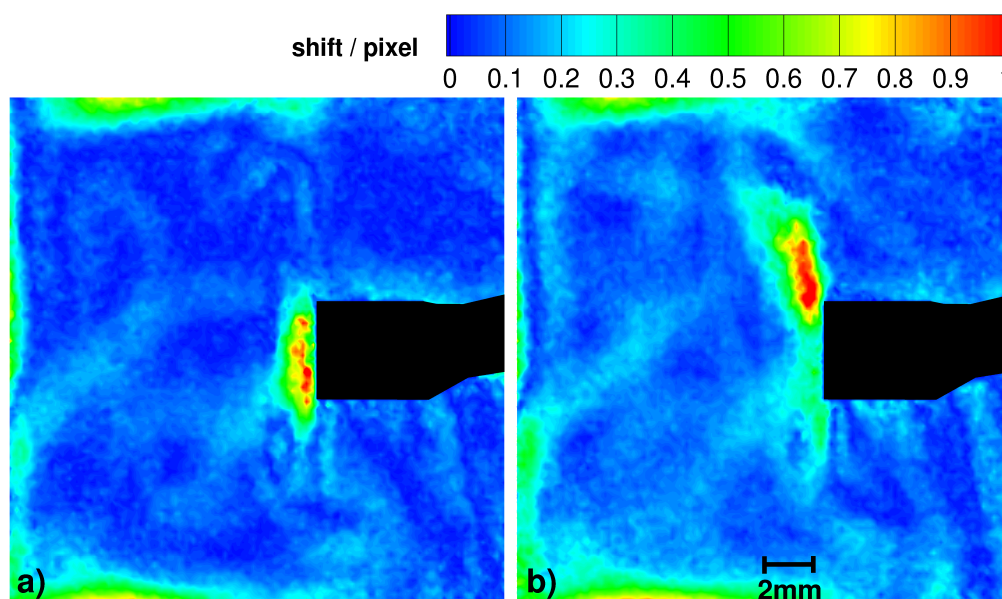
Fig. 6: BOS images of copper deposition at the WE. 44 s after the potential step (a) and 5 s after switching back to open cicuit potential (b).

Fig. 6b. The copper depleted solution does not stick to the WE, but rises upwards following a slightly curved path. Obviously, the behaviour of the solution depends on the current and can therefore not be attributed to the action of the concentration gradient force. In contrast, the Lorentz force induced flow is able to easily explain all observed features. It decays relatively quickly due to viscous dissipation if the current and thereby the driving Lorentz force vanishes. The stagnation point flow ceases to exist and buoyancy shifts the copper depleted solution upwards. The decaying azimuthal flow slightly deforms the plume path.

In addition, in the copper deposition case, the concentration gradient force would repel the solution from the WE. A detailed discussion of this additional effect can be found in [23].

4. Conclusions

Complex Lorentz force density distributions may arise from seemingly simple constellations of electric and magnetic fields. These Lorentz force distributions in turn lead to complex flow structures. It is particularly emphasized that the Lorentz force-induced motion of the electrolyte dominates even in such configurations where the electric and magnetic fields are, in a first sight, seemingly parallel. Simple field inhomogeneities, such as the edges of electrodes, give rise to a nonvanishing Lorentz force, which to a large extend determines the flow field in the whole cell.

The experiments brought strong evidence that the confinement of paramagnetic ions at circular electrodes is caused by Lorentz force driven convection and not by the action of the concentration gradient force.

References

[1]   A. H. Bucherer (1896) Die Wirkung des Magnetismus auf die elektromotorische Kraft, Annalen der Physik und Chemie, 294, 564

[2]   E. Z. Gak (1967) Problem of magnetohydrodynamic effect in strong electrolytes, Elektrokhimiya, 3, 89 (in Russian)

[3]   S. Mohanta and T. Z. Fahidy (1972) The effect of a Uniform Magnetic Field on Mass Transfer in Electrolysis, Canadian Journal of Chemical Engineering, 50, 248

[4]   T.Z. Fahidy (1983) Magnetoelectrolysis, Journal of Applied Electrochemistry, 13, 553

[5]   R. A. Tacken and L. J. J. Janssen (1995) Applications of Magnetoelectrolysis, Journal of Applied Electrochemistry, 25, 1

[6]   T. Z. Fahidy (1999) The Effect of Magnetic Fields on Electrochemical Processes, in B. E. Conway, J. O'M. Bockris and R. E. White (Eds.), Modern Aspects of Electrochemistry, No. 32 (pp. 333-354), New York, Kluwer

[7]   A. Alemany and J. P. Chopart (2007) An Outline of Magnetoelectrochemistry, in S. Molokov, R. Moreau and H. K. Moffatt (Eds.) Magnetohydrodynamics: Historical Evolution and Trends (pp. 391-407), Dordrecht, Springer

[8]   J. S. Newman (1991) Electrochemical Systems, Englewood Cliffs, Prentice Hall

[9]   G. B. Ngo Boum and A. Alemany (1999) Numerical simulations of electrochemical mass transfer in electromagnetically forced channel flows. Electrochimica Acta, 44, 1749

[10]   L. Landau and E. Lifschitz (1985) Elektrodynamik der Kontinua. Berlin, Akademie Verlag

[11]   J. M. D. Coey, F. M. F. Rhen, P. Dunne and S. McMurry (2007) The magnetic concentration gradient force – Is it real? J. Solid State Electrochem., 11, 711

[12]   N. Leventis and A. Dass (2005) Demonstration of the elusive concentration–gradient paramagnetic force. J. Am. Chem. Soc., 127, 4988

[13]   K. L. Rabah, J.-P. Chopart, H. Schloerb, S. Saulnier, O. Aaboubi, M. Uhlemann, D. Elmi and J. Amblard (2004) Analysis of the magnetic force effect on paramagnetic species. J. Electroanal. Chem., 571, 85

[14]   A. Krause, J. Koza, A. Ispas, M. Uhlemann, A. Gebert and A. Bund (2007) Magnetic field induced micro-convective phenomena inside the diffusion layer during the electrodeposition of Co, Ni and Cu. Electrochimica Acta, 52, 6338

[15]   J. Koza, M. Uhlemann, A. Gebert and L. Schultz (2008) The effect of magnetic fields on the electrodeposition of iron. J. Solid State Electrochem., 12, 181

[16]   N. Leventis, A. Dass and N. Chandrasekaran (2007) Mass transfer effects on the electropolymerization current efficiency of 3-methylthiophene in the magnetic field. J. Solid State Electrochem., 11, 727

[17]   C. Cierpka, T. Weier, G. Gerbeth, M. Uhlemann and K. Eckert (2007) Copper electrodeposition in seemingly parallel electric and magnetic fields: Lorentz force distributions and flow configurations. J. Solid State Electrochem., 11, 687

[18]   P. J. Zandbergen and D. Dijkstra (1987) Von Karman swirling flows. Ann. Rev. Fluid Mech, 19, 465

[19]   V. G. Levich (1962) Physicochemical Hydrodynamics. Englewood Cliffs, Prentice Hall

[20]   H. Schlichting (1954) Grenzschicht-Theorie. Karlsruhe, G. Braun

[21]   S. B. Dalziel, G. O. Hughes and B. R. Sutherland (1998) Synthetic Schlieren, in G. M. Carlomagno, I. Grant (Eds.): Proc. 8th Int. Symp. Flow Visualization

[22]   H. Richard and M. Raffel (2001) Principle and application of the background oriented schlieren (BOS) method. Meas. Sci. Technol., 12, 1576

[23]   T. Weier, K. Eckert, S. Mühlenhoff, C. Cierpka, A. Bund and M. Uhlemann (2007) Confinement of paramagnetic ions under magnetic field influence: Lorentz versus concentration gradient force based explanations. Electrochem. Comm., 9, 2479

Acknowledgements

VISUALISATION OF THE CONCENTRATION DISTRIBUTION AND THE FLOW FIELD IN SOLIDIFYING METALLIC MELTS BY MEANS OF X-RAY RADIOSCOPY

Stephan Boden, Sven Eckert, Bernd Willers, and Gunter Gerbeth

1. Introduction

It is well-known that the solidification of metallic alloys is significantly affected by the melt convection; see for instance [1-4]. A sufficient understanding of the interactive dynamics between the melt flow and the structure formation during solidification requires authentic knowledge of the velocity field especially in the vicinity of the solidification front. Velocity measurements in liquid metals are complicated by the specific material properties; especially the powerful optical methods as used for measurements in transparent liquids are obviously not available because of the opaqueness of the considered melts. Direct observation of the solidification process and the impact of convection thereon have been performed using transparent organic alloys (TOA) as model liquids [5, 6]. Such TOA's show similar interfacial characteristics during solidification as metals, however, significant differences in fundamental physicochemical properties restrict the full comparability.

The Ultrasound Doppler method has been applied to measure the melt convection in a solidifying Sn-15wt%Pb alloy [7]. It was demonstrated that this technique provides instantaneous profiles of the bulk flow, however, the spatial resolution of the method is not sufficient to reveal details of the flow structure just ahead of the solidification front.

Thermal convection in liquid tin and liquid lead in a thin rectangular mould was studied using radioactive tracer techniques [8]. A rapid quenching locks the tracer distribution which represents the flow pattern that occurred just at that moment. This method does not allow for a continuous observation of the process. Quantitative data with respect to the velocity field can hardly be derived.

Recently, X-ray radioscopic methods became an important diagnostic tool for solidification studies in metallic alloys. The technique enables real-time and in-situ observations of the solidification front with a spatial resolution of a few microns [9, 10]. The dimension of the solute boundary layers ahead of the solidification front can also be derived from image processing. A real-time X-ray radioscopic density visualisation system has been used to study natural convection in liquid gallium and gallium alloys [11, 12]. Based on local density differences arising from temperature gradients or gravitational stratification this technique delivers qualitative pictures of the flow pattern.

This paper presents an experimental investigation of solidifying Ga-In alloys using a microfocus X-ray tube. The X-ray facility provides a two-dimensional visualisation showing transient modifications of the local composition in the solidifying binary alloy. An estimate of the flow field ahead of the solidification front has been obtained by analysing the motion of brightness contours corresponding to gradients of the solute distribution.

2. Experimental set-up

The experimental setup is schematically depicted in Fig. 1 (right). The solidification experiments were carried out using a Ga-30wt%In alloy ($T_{Liquidus} = 35\ °C$, $T_{Solidus} = 15.3\ °C$)

prepared from 99.99% Ga and 99.99% In. The alloy was confined in a capillary slit container made from quartz glass. Two glass plates (25 mm x 35 mm) are aligned parallel with a gap of 150 µm. The container is equipped with two pouring nozzles where the liquid alloy is filled into the container by generating a suction pressure. This procedure avoids the occurrence of gas bubbles in the thin metallic film. An infrared lamp was applied to heat up the metal alloy above the liquidus temperature. The bottom part of the quartz glass container is in contact with a cooling system made from copper. A coolant flows through this heat sink whose temperature is controlled by a thermostat enabling both heating and cooling of the container bottom. Series of experiments have been realised applying multiple cycles of solidification and remelting processes.

The X-ray radioscopy setup is shown in Fig. 1 (left). A microfocus X-ray tube equipped with a tungsten target (phoenix X-ray XS225D-OEM) has been utilised. The X-ray tube generates a horizontally aligned divergent beam which penetrates the measuring volume through the container gap. After passing the measuring volume the attenuated X-ray beam impinges an X-ray image intensifier (Thales TH9438HX 9"), where the X-rays are converted into a two-dimensional visible light distribution which is recorded by a CCD camera (Kappa CF8/1 BV-3) with a scan rate of 50 half frames per second. The camera signal is digitalised by a computer based frame grabber card. Consecutively acquired image frames are directly transferred into the computer for data processing. Single frames were integrated to reduce the noise level of the particular images. In our experiments presented here an integration time of 440 ms was found to be sufficient to ensure an appropriate temporal sampling rate while keeping the amount of stored data manageable. Before post processing, each image frame was corrected taking into account the cameras dark current signal. Parallel to the image acquisition the CCD camera also delivers a live frame allowing an online control of the process.
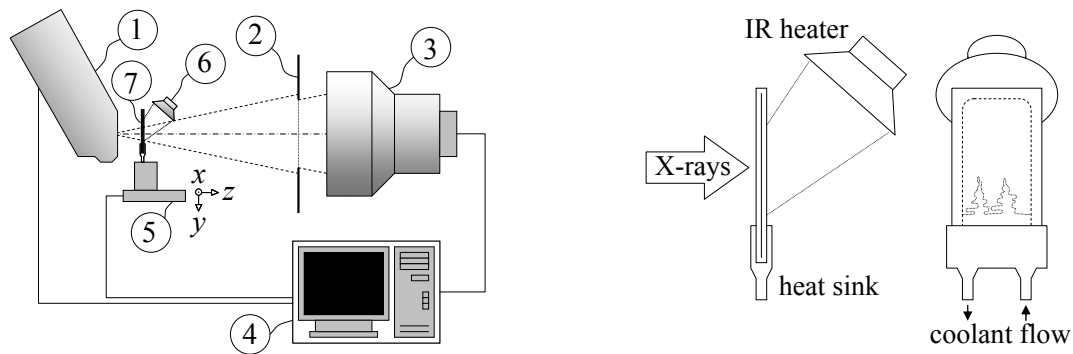
Fig. 1: Schematically drawing of the measurement setup: X-ray source (1), lead aperture (2), X-ray image intensifier with CCD camera (3), computer (4), translation stage (5), infrared heater (6), specimen (7) (left). Schematical drawing of the solidification experiment (right).

In the present experiments a tube voltage of 60 kV was chosen. Tube power was limited to 8 W to ensure a high spatial resolution, which is ultimately limited by the extent of the focal spot size. These specific parameters lead to a spatial resolution of 10 µm which has been verified by an additional reference measurement (not shown here).

The container position with respect to the beam was adjusted by means of a computer controlled three axis translation stage. The size of the measuring volume and the magnification ratio can be controlled by a suitable choice of the distances between the X-ray tube, the glass container and the X-ray image intensifier. In our experiments the field of view

was 5.8 mm by 5.8 mm field allowing the observation of both the dendrite structure of the solidifying alloy as well as the flow pattern appearing on a macroscopic scale.

The solidification experiment was carried out as follows. At first, the binary Ga-30wt%In alloy was melted and heated above the liquidus temperature. The melting process was controlled by real-time radioscopic observation to ensure a completely melted and homogenously distributed material before starting the solidification experiment. A homogeneous melt is considered to be achieved, if transient changes of local intensities in the live frame have been disappeared. Then, a reference image is computed by averaging the frames captured during this quasi-steady state. Thereafter, the cooling of the melt and the image acquisition was started.

3.   Results and Discussion

The X-ray radioscopy delivers a two-dimensional projection of the local density in the slit container corresponding to the distribution of the relative brightness P in the acquired images. The two-dimensional scalar field P is defined as follows

$$P = \frac{\Delta I}{I_0} = \frac{I - I_0}{I_0},$$
(1)

whereas I_0 and I denote the intensities at the respective pixel location obtained from the reference measurement before initialising the solidification and from the consecutively recorded images, respectively. The use of a relative brightness prevents artefacts arising from marginal insufficiencies of the experimental configuration such as slight ripples of the glass container and compensates local beam brightness and detector efficiency variations.

Fig. 2 displays six frames of a typical dendrite solidification series of the Ga-30wt%In alloy. The dark dendrite structure corresponds to the In-2wt%Ga crystals growing from the bottom of the container antiparallel with respect to gravitation. Zones with Ga enriched melt can be observed in the vicinity of the dendrite front which is less dense as compared with the initial composition. Therefore, an unstable density stratification occurs ahead of the solidification front resulting in the formation of ascending plumes containing Ga enriched melt. The frame sequence reveals the buoyancy-driven evolution and motion of the plumes. In the following we present an approach to derive information about the velocity field in the melt from the observed displacement of the brightness pattern.

Optical flow is a concept for calculating the motion of objects within a visual depiction. Horn and Schunck [13] define the optical flow as a distribution of apparent velocities describing the movement of brightness pattern in a digital image sequence. This definition gives the velocities of objects projected onto the image plane. The solidification process creates differences of the local composition within the melt leading to characteristic pattern of the transmitted light intensity. Here, the optical flow approach can also be applied to recover the flow structure in the melt. Several assumptions are necessary to compute the velocity field. The velocity measurement relies on the local information concerning the temporal and spatial gradients of the brightness distribution at each pixel. Assuming a solely two-dimensional motion parallel to the image plane, that analysis delivers in a first step the velocity component in the direction of the brightness gradient. Further constraints derived from physical considerations have to be imposed to compute the two-dimensional velocity field.

It is necessary to derive an equation relating the brightness changes occurring at the singular image pixels to the motion of the brightness pattern. We assume that the brightness of a particular point belonging to the pattern is constant,

$$\frac{dP}{dt} = 0 \qquad (2)$$

During the cooling of the sample it was observed that the mean brightness of frames decreases almost linearly with time. Corresponding corrections of the local brightness at each image point have been carried out to fulfil equ. (2). Furthermore, deformations of the pattern due to diffusion processes are considered to be negligible between two time steps of our analysis. Equ. (2) can also be written as

$$c_c = \frac{\partial P}{\partial t} + \frac{\partial P}{\partial x} \cdot u + \frac{\partial P}{\partial y} \cdot v = 0 \qquad (3)$$

with $u = dx/dt$ and $v = dy/dt$.

Another physical constraint coming from fluid mechanics is the assumption that the neighbouring points in the image should have similar velocities. This so-called smoothness constraint of the velocity field can be enforced by minimizing the square of the gradient of the optical flow velocity,

$$c_s{}^2 = \left(\frac{\partial u}{\partial x}\right)^2 + \left(\frac{\partial u}{\partial y}\right)^2 + \left(\frac{\partial v}{\partial x}\right)^2 + \left(\frac{\partial v}{\partial y}\right)^2 \qquad (4)$$

Our analysis of the flow field in the present paper followed the method proposed by Horn and Schunck [13] by minimizing

$$\int_\Omega \left(c_c{}^2 + \lambda c_s{}^2\right) dxdy \rightarrow \min \qquad (5)$$

whereas λ weights the influence of the regularisation term. In practice, appropriate spatiotemporal Gaussian smoothing was applied on the brightness measurements before solving relation (5) to obtain the velocity field with reasonable error. More details concerning the optical flow approach and its implementation to derive velocity field information can be found in [13-17].

The optical flow approach has been applied on the data obtained from the solidification experiment already presented in Fig. 2. Fig. 3 shows the results for the same time steps containing contour lines of the brightness and vectors of the optical flow velocity. A strong correlation between the concentration distribution and the flow field can be observed. An upwards velocity can be found in the bright plumes. The ascending plumes trigger the formation of durable vortices showing typical velocities of about 40 μm/s. It becomes apparent that the solidifying front at the plume positions falls behind the neighbouring regions. The feeding of the plumes from the circumjacent solute layers leads to a downsizing of the layer and an accelerated growth of the dendrites there.
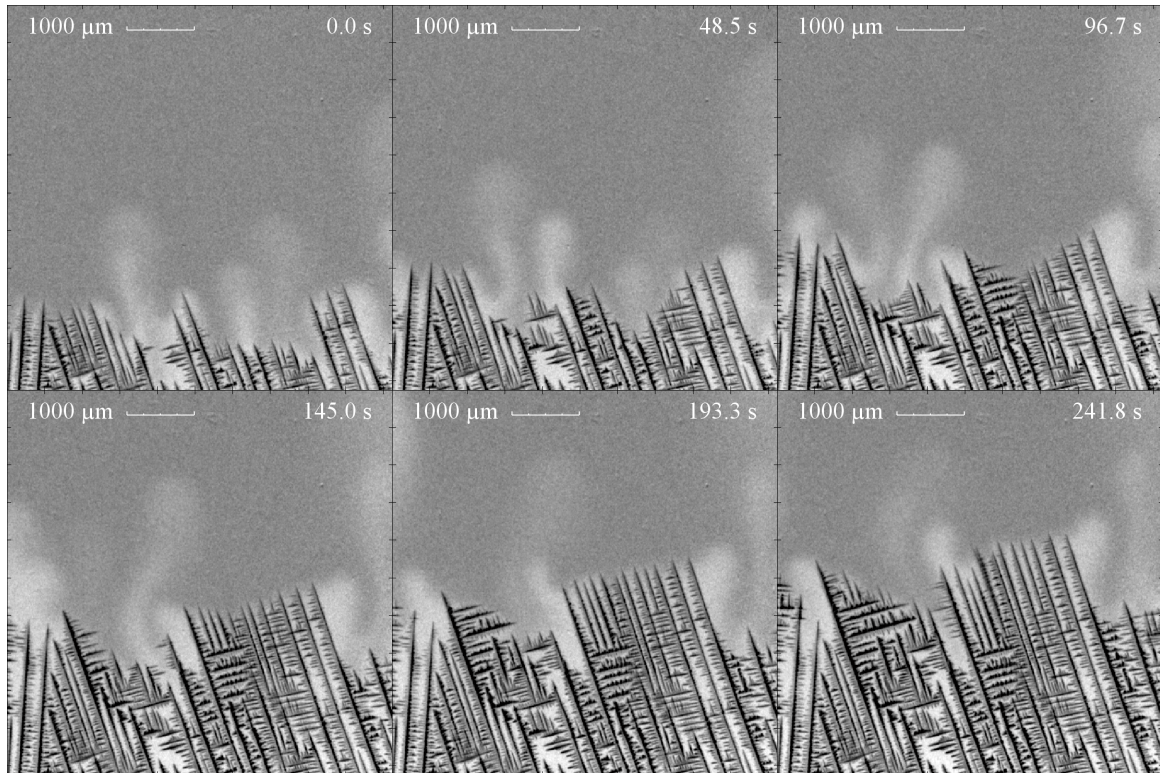
Fig. 2: Dendritic growth in Ga-30wt%In solidified directionally: a series of selected image frames obtained at different time steps applying an integration time of 8.8 seconds.
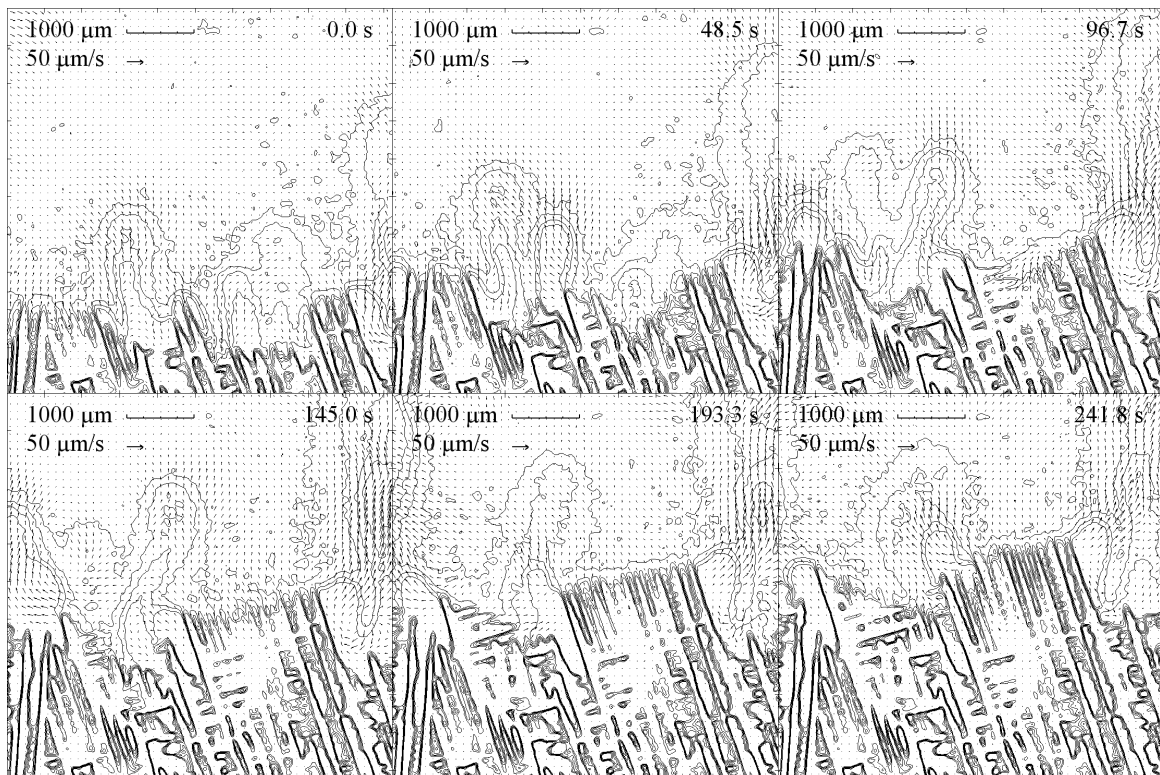
Fig. 3: Calculated instantaneous optical flow field (vector plot) at the given time offsets relative to the first image. Contour lines correspond to lines of constant brightness in the smoothed images.

4. Conclusions

The radioscopic technique was successfully applied to visualise concentration distribution variations and to estimate melt flow velocities as well as growth rates in solidifying binary Ga-30wt%In alloy. The applied algorithm to calculate the optical flow from the X-ray images delivers reliable information concerning the velocity field in regions where sufficiently large brightness gradients occur. On the other hand, an accurate measurement of the fluid velocity in zones with an almost homogeneous solute concentration appears as difficult. Moreover, the momentum and mass transport across the boundary of the field of view is not taken into account by the algorithm in the present form. Further investigations will be focussed on an improvement of the algorithm allowing a realistic mapping of the melt flow also at larger distances from the solidification front. The further work requires the consideration of additional constraints and the development of improved physical models to achieve a better adaptation of the optical flow approach to the solidification process.

References

[1]   J.H. Lee, S. Liu, R. Trivedi (2005), The effect of fluid flow on eutectic growth, Metall. Mat. Trans. 36A , 3111-3125

[2]   A.N. Turchin, D.G. Eskin, L. Katgerman (2005), Effect of melt flow on macro- and microstructure evolution during solidification of an Al-4.5% Cu alloy, Mat. Sci. Eng. A 413-414, 98-104

[3]   J.E. Spinelli, D.M. Rosa, I.L. Ferreira, A. Garcia (2004), The effect of melt convection on dendritic spacings of downward unsteady-state directionally solidified Al-Cu alloys, Mat. Sci. Eng. A 383, 271-282

[4]   B. Willers, S. Eckert, U. Michel, I. Haase, G. Zouhar (2005), The columnar-to-equiaxed transition in Pb-Sn alloys affected by electromagnetically driven convection, Mat. Sci. Eng. A 402, 55-65

[5]   B.T. Murray, A.A. Wheeler, M.E. Glicksman (1995), Simulations of experimentally observed dendritic growth-behavior using a phase-field model, J. Cryst. Growth 154, 386-400

[6]   M. Zhang, T. Maxworthy (2002), The interactive dynamics of flow and directional solidification in a Hele-Shaw cell Part 1. Experimental investigation of parallel shear flow, J. Fluid Mech. 470, 247-268

[7]   S. Eckert, B. Willers, G. Gerbeth (2005), Measurement of the bulk velocity during solidification of metallic alloys, Metall. Mat. Trans. 36A, 267-270

[8]   M.J. Stewart, F. Weinberg (1972), Fluid flow in liquid metals .2. Experimental observations, J. Cryst. Growth 12, 228-238

[9]   P. Curreri, W.F. Kaukler (1996), Real-time X-ray transmission microscopy of solidifying Al-In alloys, Metall. Mat. Trans. 27A, 801-808

[10]   R.H. Mathiesen, L. Arnberg, F. Mo, T. Weitkamp, A. Snigirev (1999) Time-resolved X-ray imaging of dendritic growth in binary alloys, Phys. Rev. Lett. 83, 5062-5065

[11]   J.N. Koster, T. Seidel, R. Derebail (1997), A radioscopic technique to study convective fluid dynamics in opaque liquid metals, J. Fluid Mech. 343, 29-41

[12]   J.N. Koster, R. Derebail, A. Grötzbach (1997), Visualisation of convective solidification in a vertical layer of eutectic Ga-In melt, Appl. Phys. A 64, 45-54

[13]   B.K.P. Horn, B.G. Schunck (1981), Determining optical-flow, Artificial Intelligence 17, 185-203

[14]   J.R. Bergen, P. Anandan, K.J. Hanna, R. Hingorani (1992), Hierachical model-based motion estimation, Lecture Notes in Comp. Sci. 588, 237-252

[15]   N. Cornelius, T. Kanade (1983), Adapting optical-flow to measure object motion in reflectance and X-ray image sequences, Proc. of the ACM Workshop on Motion, 50-58

[16]   J.M. Fitzpatrick (1988), The existence of geometrical density image transformations corresponding to object motion, Comp. Vis. Graph. Image Processing 44, 155-174

[17]   R.P. Wildes, M.J. Amabile, A.-M. Lanzilotto, T.-S. Leu (2000), Recovering Estimates of fluid flow from image sequence data, Comp. Vis. Image Understanding 80, 246-266

Acknowledgement

APPLICATION OF RATE THEORY MODELING TO CLUSTER EVOLUTION IN BINARY FE-CU ALLOYS

Uwe Birkenheuer, Frank Bergner, Andreas Ulbricht, Alexander Gokhman[1], and Abderrahim Almazouzi[2]

1. Introduction

The degradation of the mechanical properties of reactor pressure vessel steels caused by the irradiation with fast neutrons is a phenomenon, in which processes on a multitude of time and length scales are involved. It is not efficient and, in particular at the sub-nm and sub-μs scales, not even possible to cover all the important constituents of the damage process by means of experiments. Therefore, a multi-scale modeling approach has been adopted in recent years. This kind of approach is based on an interplay of models on different time scales, scale-bridging concepts as well as modeling oriented experiments.

Within the integrated project PERFECT of the 6th European Framework program (FP6) a set of well-defined model alloys was fabricated and neutron-irradiated under different irradiation conditions [1]. These samples were investigated by a series of complementary experimental techniques, including TEM (transmission electron microscopy), PAS (positron annihilation spectroscopy) and SANS (small-angle neutron scattering). The latter experiments were carried out at the SCK·CEN in Mol and evaluated at the FZD in Rossendorf. Four different neutron fluences were investigated at one and the same neutron flux. The material matrix comprises pure iron and a set of binary, ternary and quaternary model alloys such as Fe-1.2%Mn-0.7%Ni-0.1%Cu with compositions already quite near to real reactor pressure vessel (RPV) steels. We will focus on the two binary Cu-Fe model alloys Fe-0.3%Cu and Fe-0.1%Cu here. The aim of the present paper is to present a rate theory (RT) model which is able to reproduce the complete set of SANS data, in particular the volume fraction of the defect clusters and the peak radius of the size distribution function (SDF), for both model alloys and all four irradiation conditions (see Table 1). The dependence of the SANS data on the neutron fluence was found to be quite complex, suggesting that a pure Cu precipitation model might not be enough to explain the observations. And in fact, we were not able to find a suitable parameter set for a rate theory model based on pure Cu precipitates which could reproduce the experimental results even qualitatively. Therefore, we explicitly take into account the absorption of iron vacancies by the copper-rich precipitates for the simulation of the defect cluster evolution in our new Vacancy-Coupled Copper Clustering (V3C) model.

Table 1: Irradiation conditions for the Fe-0.1%Cu and Fe-0.3%Cu model alloys.

Parameter	Value
Temperature, T	300 °C
Neutron flux, φ ($E > 1$ MeV)	0.95×10^{18} n/m^{2}s
Dose rate, G_{dpa} ($E > 1$ MeV)	1.40×10^{-7} dpa/s
Dose	0.026, 0.051, 0.10, 0.19 dpa

---

[1] Department of Physics, South Ukrainian Pedagogical University, 65020 Odessa, Ukraine.
[2] Structural Materials Expert Group, Nuclear Materials Science Institute, SCK·CEN, B-2400 Mol, Belgium

## 2.	The rate theory model

Standard rate theory models for the formation of copper-rich precipitates in irradiated reactor pressure vessel steels as describe, for example, in Ref. [2] consist of the following three essentials: a balance equations for the evolution of each of the mobile point defects, vacancies and self-interstitial atoms (SIAs), a set of master equations for the evolution of the immobile defect clusters up to a given maximum size, and a model for the irradiation enhancement of the Cu mobility in the iron matrix. The balance equations read

$$\frac{dC_A}{dt} = G_A - k_{\text{vi}} C_\text{v} C_\text{i} - k_A C_A \quad , \quad A = \text{v, i} \quad , \tag{1}$$

where C_v and C_i are the concentrations of the vacancies and SIAs, respectively, measured in point defect per lattice site. Here, G_A are the generation rates of the point defects due to irradiation, $k_{\text{vi}} C_\text{v} C_\text{i}$ is the recombination rate of the vacancies and self-interstitials, and $k_A C_A$ the loss rates of each type A of point defect at the dislocations in the iron matrix with the decay rates k_A being proportional to the dislocation density ρ. The classical master equations are of the general form (e.g. Refs. [2,3])

$$\frac{dC_n}{dt} = f(C_{n-1}, C_n, C_{n+1}, C_\text{Cu}; p_1 = \gamma_{\text{Cu-Fe}}, p_2 = D_\text{Cu}^*) \quad , \tag{2}$$

where C_n is the concentration of the n-atomic defect clusters, measured in cluster per lattice site. Besides the concentration C_Cu of the Cu atoms in the iron matrix and the number of clusters per lattice site of given size n and adjacent sizes $n \pm 1$, the reaction rate $\frac{d}{dt} C_n$ also depends on a couple of material parameters $p_1, p_2, \dots$, the most important ones being the coherent specific Cu-Fe interface energy $\gamma_{\text{Cu-Fe}}$ and the irradiation enhanced Cu diffusion coefficient D_Cu^*. Assuming a vacancy assisted diffusion mechanism for the Cu atoms the irradiation enhancement of the Cu diffusivity can be modeled by [4]

$$D_\text{Cu}^* = D_\text{Cu} \cdot \frac{C_\text{v}(t)}{C_\text{v}^{\text{eq}}} \quad , \tag{3}$$

where C_v is the actual, irradiation-induced concentration of the vacancies in the iron matrix, while C_v^{eq} and D_Cu are the thermal vacancy concentration and the copper diffusion coefficient in the unirradiated material, respectively.

Often [4,5], the system of point defects and the copper subsystem can be treated independently, by replacing $C_\text{v}(t)$ by the steady-flux solutions C_v^{sf} of the balance equations (1) and (2). This is justified by the fact, that the typical time-scale of the point defect system is orders of magnitudes smaller than that of the copper system. Yet, as already mention above, there is quite some evidence for the copper precipitates in RPV steels and Cu-Fe model alloys of moderate Cu content actually being mixed defect clusters which contain both, Cu and vacancies (and other alloying elements). To allow for such mixed compositions, the defect clusters must be able to absorb vacancies. This is explicitly taken into account in our V3C (Vacancy-Coupled Cu-Clustering) model by letting the defect clusters act as additional vacancy sinks.

To this end, the simple decay rate k_v in Eq. (1) is replaced by

$$
\begin{aligned}
k_v(t) &= k_v^0 + \Delta k_v(t) \\
&= z_v D_v \rho + 4\pi D_v \sum_{n \geq 2} R_n C_n(t) / V_{Fe} \quad .
\end{aligned}
\tag{4}
$$

Here, D_v is the diffusion coefficient of the vacancies in the iron matrix, z_v the dislocation sink strength bias for vacancies, R_n the radius of a defect cluster of size n, and V_{Fe} the atomic volume of bcc iron. The new sink term $S_v = k_v(t) C_v$ consists of a static contribution $S_v^0 = k_v^0 C_v$ due to the given dislocation network in the material, and a dynamic contribution $\Delta S_v = \Delta k_v(t) C_v$ which depends on the actual defect cluster distribution. Because the latter term imposes the time modulation of the copper subsystem onto the point defect system, the balance equations cannot be solved independently of the copper subsystem anymore. Actually, the balance equations can still be solved in an adiabatic fashion with a slowly varying quasi-steady-flux solution $C_v^{q\text{-}sf}(t)$ being used in Eq. (3). However, regardless of this detail, the new V3C model constitutes a two-fold coupling between the point defect and the copper subsystem, a forward coupling which is mediated via the vacancy-dependence of the diffusion coefficient D_{Cu}^* entering the master equations (2) and a backward coupling which is caused by the Cu-cluster-dependence of the vacancy decay rate $k_v(t)$ entering the balance equations (1). For the self-interstitial atoms only a static contribution term $S_i = k_i C_i$ to the sink term is considered, because the (oversized) Cu clusters are assumed not to be able to absorb SIAs to a relevant amount.

Table 2: Material parameters adopted for the rate theoretical simulation. Here k is the Boltzmann constant and T the irradiation temperature (in K).

Parameter	Value	Reference
Interstitial diffusion coefficient at 300 °C, D_i	1.52×10^{-9} m^2/s	[9]
Vacancy diffusion coefficient at 300 °C, D_v	1.85×10^{-16} m^2/s	[9]
Copper migration energy, $E_{m,Cu}$	2.29 eV	[4]
Copper pre-exponential factor, $D_{0,Cu}$	7.2×10^{-6} m^2/s	this work
Copper diffusion coefficient at 300 °C, D_{Cu}	5.27×10^{-26} m^2/s	$D_{0,Cu} \exp(-E_{m,Cu}/kT)$
Vacancy formation energy, $E_{f,v}$	1.64 eV	a
Non-configurational vacancy entropy, ΔS_v	$3\,k$	a
Thermal vacancy concentration at 300 °C, C_v^{eq}	7.62×10^{-14}	$\exp(\Delta S_v/k - E_{f,v}/kT)$
Copper demixing temperature, Ω	6255 K	[4]
Non-configurational copper entropy, ΔS_{Cu}	$0.866\,k$	[4]
Recombination rate constant, k_{vi}	9.31×10^{11} / s	[9]
Dislocation density, ρ	0.9×10^{14} / m^2	[10]
Interstitial sink strength bias, z_i	1.2	[4]
Vacancy sink strength bias, z_v	1.0	[4]
Point defect production rate, G_A	2.56×10^{-8} / s	[11,12,13]

a For T around 300 °C essentially equivalent to $E_{f,v} = 1.6$ eV [4] and $\Delta S_v = 2.2\,k$ [14].

3. Computations

The irradiation conditions of the investigated model alloys Fe-0.1%Cu and Fe-0.3%Cu are summarized in Table 1, the material parameters adopted for the RT simulation in Table 2. The bcc lattice constant a_{Fe} of Fe is chosen to 2.8665 Å, that of Cu to a_{Cu} = 2.9607 Å [6]. The parameters listed here are essentially the same as those used in our previous studies on Cu precipitation [7,8].

The thermodynamic data for the Cu precipitation is taken from Ref. [4]. However, the pre-exponential factor for Cu diffusion suggested therein (0.63×10^{-4} m^2/s) had to be reduced by about one order of magnitude, in order to find the Ostwald ripening stage of the defect clusters to start at the experimentally observed cluster radii. The resulting value of 5.27×10^{-26} m^2/s for the irradiation enhance copper diffusion coefficient D_{Cu}^* is reasonably close to the values obtained from the Arrhenius parameters used in other simulation studies, but still consistently larger than the extrapolations of the available experimental data down to 300 °C (see Table 3 for details). In particular, our Cu diffusion parameters are very close to ones obtained from MD (molecular dynamics) simulations on the vacancies assisted Cu diffusion in bcc iron based on the ACKLAND97 embedded atom potential for Fe-Cu [6].

The interface energy $\gamma_{Cu\text{-}Fe}$ of the defect clusters in the Cu-rich model alloy with 0.3wt% Cu are calculated using the entropy extended version of the Cahn-Hilliard expression suggested by Mathon *et al.* [2],

$$\gamma_{Fe\text{-}Cu}^{0.3\%} = \gamma_{CH} := 1.08k\left[\Omega - T(1 + \tfrac{1}{2k}\Delta S_{Cu})\right]/a_{Cu}^2 \quad , \tag{5}$$

where Ω and ΔS_{Cu} are the demixing temperature and the non-configurational substitution entropy of Cu in Fe which are also used to calculated the solubility limit

$$C_{Cu}^{eq} = \exp(\Delta S_{Cu}/k - \Omega/T) \tag{6}$$

of Cu in iron. With the parameters given in Table 2 this results in $\gamma_{Fe\text{-}Cu}^{0.3\%}$ = 0.39 J/m^2 and C_{Cu}^{eq} = 4.33 x 10^{-5} at 300 °C. The interface energy of the Cu-poor model had to be fitted.

Table 3: Thermal diffusivity of Cu in a-Fe extrapolated to 300 °C (for the meaning of the symbols see Table 2).

Method	$E_{m,Cu}$ [eV]	$D_{0,Cu}$ [m^2/s]	$D_{Cu}^{300°C}$ [m^2/s]	Reference
RT simulation	2.29	0.63×10^{-4}	46.0×10^{-26}	[4]
RT simulation	2.29	0.072×10^{-4}	5.27×10^{-26}	this work
RT simulation	2.53	7.08×10^{-4}	4.01×10^{-26}	[15]
MD simulation	2.31	0.052×10^{-4}	2.54×10^{-26}	[16]
Exp., α-Fe(ferro)	2.53	0.47×10^{-4}	0.26×10^{-26}	[17]
Exp., α-Fe(para)	2.94	300×10^{-4}	0.04×10^{-26}	[18] [a]

[a] No Arrhenius-like behavior was observed for α-Fe(ferro) in that study.

4. Results

While distinct maxima showed up in the simulated cluster size distribution functions of the Cu-rich model alloy Fe-0.3%Cu at all four neutron fluences, with peak radii and volume fractions quite close to the experimental values, no copper precipitation could be observed with the Cahn-Hilliard interface energy γ_{CH} for the Cu-poor model alloy Fe-0.1%Cu model alloy. Instead, the concentration of the Cu clusters at the critical nucleation size of about 25 Cu atoms turned out to be seven orders of magnitude smaller than for Fe-0.3%Cu (with a critical nucleation size of about 10 atoms), in total agreement with classical nucleation theory, and the simulated system remained in the deterministic growth stage until cluster sizes far larger than the experimentally observed ones were reached. The only way to overcome this discrepancy within our vacancy-coupled Cu clustering model was to let the interface energy depend on the composition of the model alloy.
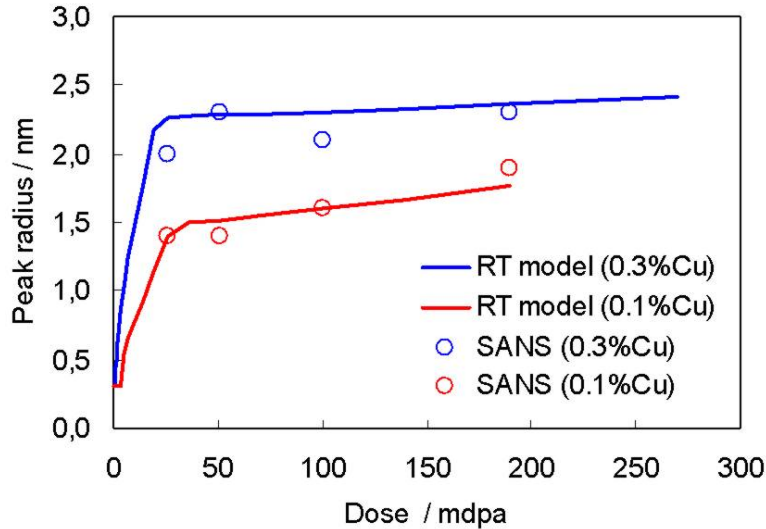
Fig. 1: Calculated peak radius of the Cu cluster distribution as a function of dose and comparison with experimental results obtained by SANS for both model alloys

By reducing the Fe-Cu interface energy for Fe-0.1%Cu to 73% of the Cahn-Hilliard value, i.e. to 0.29 J/m^2 at 300 °C, it is possible to reproduce the experimentally observed peak radii and volume fractions at all four neutron fluences for the Fe-0.1%Cu system as well (see Figs. 1 and 2). All other parameters are the same as for Fe-0.3%Cu. In particular, there is only one further adjusted parameter beside the interface energy reduction for Fe-0.1%Cu, the common pre-factor factor $D_{0,Cu}$ for the thermal Cu diffusivity in both alloys. A total of sixteen independent experimental data points could be reproduced this way (see Figs. 1 and 2) giving confidence that the chosen parameterization is reasonable. Based on the above observations we suggest, to model the temperature and

Fig. 2: Calculated volume fraction the Cu clusters as a function of dose and comparison with experimental results obtained by SANS for both model alloys.

74

composition dependence of the Fe-Cu interface energy in a multiplicative way, by following Mathon *et al.* [2] for the temperature dependence but adopting a linear dependence on the weight percentage *w* of Cu in the material:

$$\gamma_{\text{Fe-Cu}}^{w\%}(T) = \gamma_{\text{CH}}(T) \times \left(1.35w + 0.595\right) \tag{7}$$

with γ_{CH} as defined in Eq. (5).

Taking into account that both model alloys were subject to the same irradiation-induces vacancy production rate it is likely that in average the defect clusters of the Cu-poor model alloy take up more vacancies than the defect clusters in the Cu-rich material. Thus, in view of the quite substantial oversize of copper compared to iron the suggested reduction of the repulsive interface energy with increasing amount of vacancies in the defect clusters seems reasonable.

5.   Conclusions and Discussion

A vacancy-coupled rate theory model (RT) for Cu clustering (V3C) was established which explicitly takes into account the absorption of vacancies by Cu-rich precipitate clusters. Only two parameters, the Cu thermal diffusivity in iron and the reduction of the coherent interface energy in Fe-0.1%Cu compared to Fe-0.3%Cu were used in order to adjust the new RT model. Since the obtained value for the thermal Cu diffusion coefficient is the same for both materials and lies well in the range of reported diffusivities, effectively only one parameter was required, to reasonably reproduce the entire set of experimental data obtained by means of SANS for two neutron-irradiated Fe-Cu model alloys at four different doses. An analytical expression for the interface energy as a function of temperature and Cu content of the iron matrix is given. The suggested reduction of the interface energy between iron and mixed defect clusters of increasing vacancy content can easily be rationalized by the oversize of bcc copper compared to bcc Fe and is also corroborated by a more sound thermodynamic analysis of the underlying copper exchange processes.

References

[1]   K. Verheyen, M. Jardin, A. Almazouzi, Coincidence Doppler broadening spectroscopy in Fe, Fe-C and Fe-Cu after neutron irradiation, Journal of Nuclear Materials 351 (2006) 209-215.

[2]   M. H. Mathon, A. Barbu, F. Dunstetter, N. Lorenzelli, and C. H. de Novion (1997), Experimental study and modeling of copper percipitation under electron irradiation in dilute Fe-Cu binary alloys, Journal of Nuclear Materials 245, 224-237.

[3]   J. Schmelzer Jr., U. Lembke, and R. Kranold (2000), Nucleation and growth of AgCl clusters in a sodium borates glass: Numerical analysis and SAXS results, Journal of Chemical Physics 113, 1268-1275.

[4]   F. Christien and A. Barbu (2004), Modelling of copper precipitation in iron during thermal aging and irradiation, Journal of Nuclear Materials 324, 90-96.

[5]   A. Gokhman, J. Boehmert, and A. Ulbricht (2003), Kinetic study of copper percipitates under VVER-type reactor conditions, Radiation Effects & Defects in Solids 158, 783-792.

[6]   G. J. Ackland, D. J. Bacon, A. F. Calder, and T. Harry (1997), Computer simulation of point defect properties in dilute Fe-Cu alloy using a many -body interatomic potential, Philosophical Magazine A 75, 713-732.

[7]   A. Gokhman and J. Boehmert (2003), A kinetic study of vacancy cluster evolution under VVER-type reactor conditions, Radiation Effects & Defects in Solids 158, 499-511.

[8]   A. Gokhman, F. Bergner, A. Ulbricht, and U. Birkenheuer (2008), Cluster dynamics simulation of reactor pressure vessel steels under irradiation, Defect and Diffusion Forum 277, 75-80.

[9]   G. R Odette (1998), in: M. Davies (Ed.), Neutron Irradiation Effect in Reactor Pressure Vessel Steels and Weldments, Vienna, p.438-504.

[10]   A. Almazouzi, M. Jardin, M. Lambrecht, L. Malerba, M. Hernández-Mayoral, D. Gómez-Briceño, Ph. Pareige, E. Muslin, and B. Radiguet (2005), Characterization of neutron irradiated samples (REVE matrix), deliverable P26, work-package II-3, integrated project PERFECT, 6th European Framework program EURATOM.

[11]   C. H. M. Broeders and A. Yu. Konobeyev (2004), Journal of Nuclear Materials 328, 197-214.

[12]   R. E. Stoller (2000), The role of cascade energy and temperature in primary defect formation in iron, Journal of Nuclear Materials 276, 22-32.

[13]   A. F. Calder and D. J. Bacon (1993), A molecular dynamics study of displacement cascades in α-iron, Journal of Nuclear Materials 207, 25-45.

[14]   J. J. Burton (1972), Vacancy-formation entropy in cubic metals, Physical Review B 5, 2948-2957.

[15]   S. I. Golubov, A. Serra, Yu. N. Osetsky, and A. V. Barashev (2000), On the validity of the cluster model to describe the evolution of Cu precipitates in Fe-Cu alloys, Journal of Nuclear Materials 277, 113-115.

[16]   J. Marian, B. D. Wirth, G. R. Odette, and J. M. Perlando (2004), Cu diffusion in α-Fe: determination of solute diffusivities using atomic-scale simulations, Computational Materials Science 31, 347–367.

[17]   M. S. Anand and R. P. Agarwala (1966), Diffusion of Copper in Iron, Journal of Applied Physics 37, 4248-4251.

[18]   G. Salje and M. Feller-Kniepmeier (1977), The diffusion and solubility of copper in iron, Journal of Applied Physics 48, 1833-1839.

Acknowledgements

FRACTURE MECHANICS EVALUATION OF THE CORE WELDING SEAM OF THE NPP GREIFSWALD UNIT 1 WWER-440 REACTOR PRESSURE VESSEL

Hans-Werner Viehrig, Jan Schuhknecht, Udo Rindelhardt, and Frank-Peter Weiss

1.   Introduction

Nuclear plant operators must demonstrate that the structural integrity of the nuclear reactor pressure vessel (RPV) is assured during routine operations or under postulated accident conditions. The sampling of trepans from the four WWER-440/230 Greifswald NPP units offers the unique opportunity to investigate RPV steel aged under real operation conditions. The operation characteristic of the four Greifswald units and the applied trepanning procedure were described in detail in the Annual Report 2006 [1]. This paper presents the first fracture toughness test results. The investigated trepan 1-1 (A1 in [1]) originates from the Unit 1 RPV core welding seam SN0.1.4. Unit 1 was in operation over 13 cycles from 1974 to 1988, then thermally annealed and continuing operated for two years till 1990. It represents an annealed and re-irradiated condition. The main focus is laid on Master Curve testing according to the test standard ASTM E1921 [2]. In addition Charpy-V tests were performed.

2.   Material and specimens

First the trepan 1-1 representing the irradiated, annealed and re-irradiated (IAI) condition of the welding seam SN0.1.4 was investigated. Fig. 1 illustrates the location of the welding seam SN0.1.4 in the WWER-440 RPV. The welding seam is a multilayer submerged weld and consists of a welding root welded with an unalloyed Sv-08A wire and the filling material welded with the alloyed Sv-10KhMFT wire. Table 1 gives the chemical composition of the filling layer weld metal within trepan 1-1 at different thickness locations and the specifications of the manufacturing protocol [3]. The chemical compositions generally agree with the given information in the manufacturing protocol. The copper and phosphorus contents are within the range as specified in the manufacturing guidelines of the WWER-440/230, but both are clearly higher than in the specifications for the next generation (model 213) with maximum allowed P and Cu contents of 0.01% and 0.1%, respectively [4].
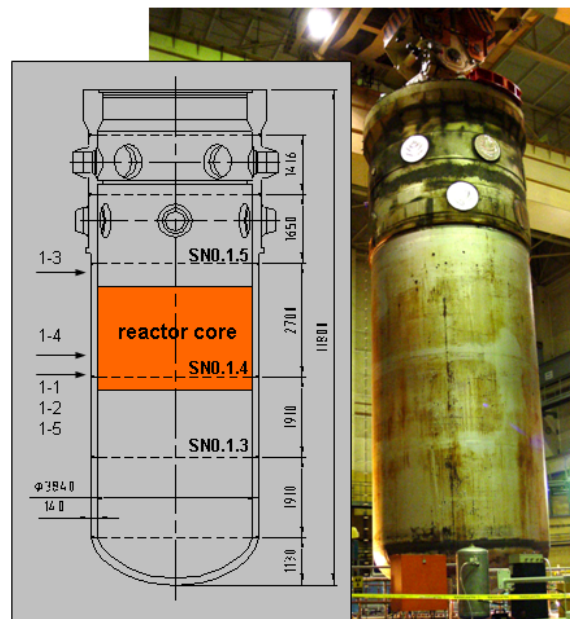
Fig. 1: RPV Greifswald Unit 1 and locations of the sampled trepans

The trepan 1-1 was cut into discs with a thickness of 10 mm using a wire travelling electro-erosion discharging machine (EDM). From a single disc 10 Charpy size SE(B) specimens with TS orientation were machined. TS orientation means specimen axis vertical to the RPV axis and crack extension direction through the RPV wall (welding seam). Fig. 2 shows the trepan and Fig. 3 exemplifies the cutting scheme of the disc 1-1.1. The location of the welding

seam within trepan 1-1 was metallographically examined and is schematically depicted in Fig. 2. The welding root is located within a distance of about 60 mm to 80 mm relative to the inner surface of the RPV wall.

Table 1: Chemical composition of Trepan 1-1 (Mass %)

Code disc	Thickness location[a] mm	C	Si	Mn	Cr	Ni	Mo	V	P	Cu
protocol[b]		0.05	0.47	1.22	1.48	0.23	0.41	0.16	0.037	0.103
1-1.1	8.3			1.06	1.49	0.22	0.40	0.14	0.038	0.125
1-1.3	21.9			0.97	1.35	0.19	0.43	0.14	0.030	0.141
1-1.12	93.8			0.93	1.23	0.22	0.40	0.09	0.028	0.141

[a]: distance from inner surface ; [b]: manufacturing protocol of the RPV Unit 1 welding seam SN0.1.4 [2]
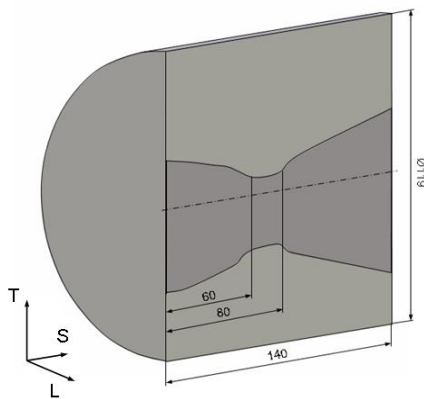
Fig. 2: Trepan 1-1 with the location of the welding seam.
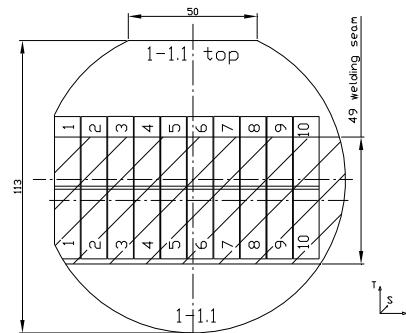
Fig. 3: Cutting scheme of disc 1-1.1

3.   Testing and evaluation

The test program to be performed on the trepans from the Greifswald RPV's is described elsewhere [1]. At first SE(B) specimens from discs with thickness locations shown in Table 2 were tested and evaluated according to ASTM E1921-05 [2]. The pre-cracked and side-grooved Charpy size SE(B) specimens were monotonously loaded until they failed by cleavage instability. Standard MC reference temperatures T_0 were evaluated with the measured J integral based cleavage fracture toughness values, K_{Jc}, applying the multi temperature procedure of ASTM E1921-05 [2]. In addition, the "Structural Integrity Assessment Procedures for European Industry", SINTAP, providing a modification of the MC analysis were used for the evaluation of the measured K_{Jc}- values. The SINTAP lower tail analysis consists of three steps and guides the user towards the most appropriate estimate of the reference temperature, T_0^{SINTAP}, describing the population having the lower toughness [5,6].

Instrumented Charpy V-notch impact tests on reconstituted specimens were performed according to DIN EN 10045-1 [7] and EN ISO 14556 (2000) [8]. The impact energy, lateral expansion and fracture appearance temperature curves were fitted by tanh approach. Charpy-V parameters as transition temperatures and the upper shelf energy were evaluated on specimens from 3 thickness locations.

4.   Results and discussion

Table 2 summarises the Master Curve (MC) and Charpy-V test results of the investigated discs of trepan 1-1. The table also contains the location of the discs within the trepan and the calculated neutron fluencies in the centre of the discs. The test results comprise the reference temperatures, T_0, evaluated according to ASTM E1921-05 [2] and the SINTAP procedure [5,6], T_0^{SINTAP}, as well as the Charpy-V parameters transition temperature related to a Charpy-V energy of 41J, TT_{41J}, and upper shelf energy, USE, of three thickness locations. T_0 data presented in Table 3 and depicted in Figure. 4 vary through the thickness of the trepan 1-1 and, thus, the welding seam. Through the wall thickness, T_0 shows a wavelike behaviour. After an initial increase of T_0 from 10°C at the inner surface to 50°C at 22 mm distance from it, T_0 again decreases to -41°C at a distance of 70 mm, finally increasing again to maximum 67°C towards the outer RPV wall. The lowest T_0 value was measured in the root region of the welding seam representing a uniform fine grain ferritic structure. Beyond the welding root T_0 shows a span of about 50 K. Fig. 5 shows the K_{Jc} values versus the test temperature normalised to T_0 of the individual discs. The K_{Jc} values generally follow the course of the MC, though the scatter is large. Nevertheless, the K_{Jc} values are close to or above the 2% fracture probability line. However, more than 5% of the K_{Jc} data fall below the 5% fracture probability lower bound ($K_{Jc(0.05)1T}$) curve. That strongly indicates that the material is not fully homogeneous, which is not unusual for the investigated multilayer weld metal.

Table 2: Location of the investigated discs within trepan 1-1, neutron fluences, MC test results according to ASTM E1921-05, SINTAP and Charpy-V parameter.

| code disc | distance from inner surface (centre disc) | $N_{E>0.5MeV}$ | | ASTM E1921 - 05 | | SINTAP | Charpy-V | |
| | | before* | after* | T_0 | σT_0 | T_0^{SINTAP} | TT_{41J} | USE |
	mm	10^{19} n/cm^2	10^{19} n/cm^2	°C	K	°C	°C	J
1-1.1	8	3.90	0.182	10.3	6.4	32.5	51.4	130.8
1-1.3	22	3.66	0.113	49.1	6.3	49.1	32.6	153.4
1-1.5	36	3.32	0.103	33.8	6.6	33.8		
1-1.6	42	3.13	0.098	-5.0	6.4	-5.0		
1-1.8	60	2.66	0.085	-4.5	6.0	5.0		
1-1.9	70	2.40	0.077	-40.7	6.4	-13.6		
1-1.11	84	2.07	0.068	-28.4	6.0	18.6		
1-1.12	94	1.85	0.061	19.8	6.3	45.1	20.1	120.3
1-1.14	107	1.59	0.053	-32.5	6.8	-32.5		
1-1.15	118	1.40	0.047	-7.0	6.3	-7.0		
1-1.17	131	1.16	0.040	63.1	6.6	63.1		

*annealing

The SINTAP MC evaluation enables conservative lower bound type fracture toughness estimates also for inhomogeneous materials. As shown in Table 2 the SINTAP MC evaluation gives reference temperatures T_0^{SINTAP} for the discs 1-1.1, 1-1.8, 1-1.9, 1-1.11 and 1-1.12 clearly higher than the standard T_0. The course of T_0^{SINTAP} through the welding seam SN0.1.4 in Fig.4 also shows the lowest values in the root region and an increase from the inner surface to 22 mm distance within the filling layers. The filling layer (disc 1-1.12) beyond the root has a T_0^{SINTAP} value comparable with that of disc 1-1.3.

Table 2 also contains the Charpy-V parameters ductile-to-brittle transition temperatures TT_{41J} and upper shelf energies from the filling layers of the welding seam. The evaluated TT_{41J} is 51°C at the location near the inner RPV wall and thus, close to the reported temperature of brittleness for the unirradiated condition, T_{K0}, of 46°C [3,10].
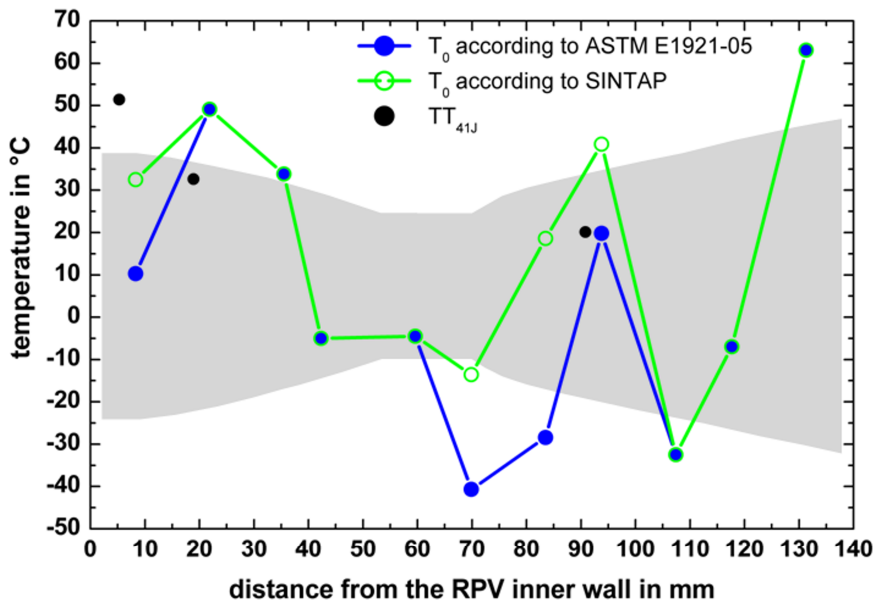
Fig. 4: Reference temperature T_0, T_0^{SINTAP} and Charpy-V transition temperature TT_{41J} through the welding seam SN0.1.4
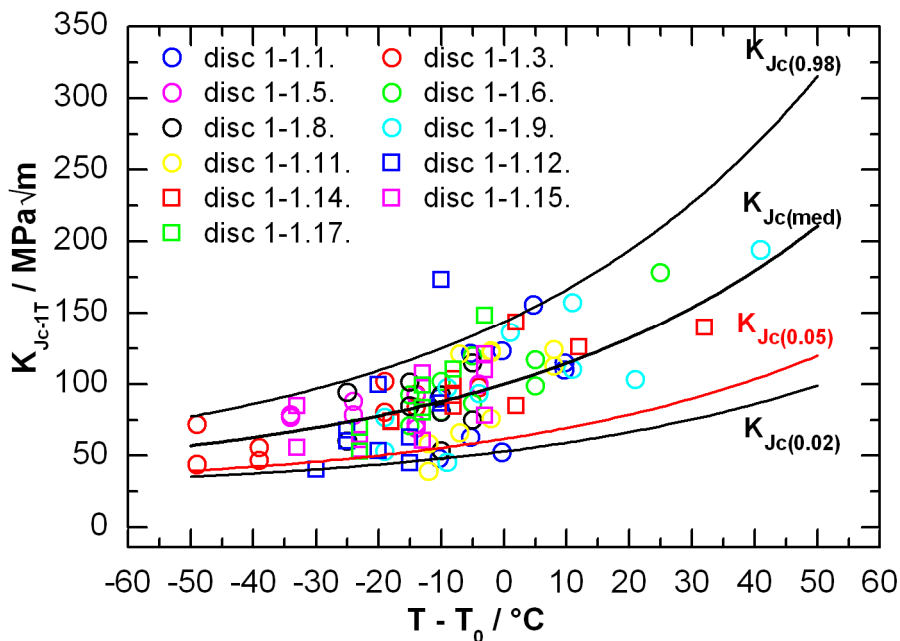
Fig. 5: K_{Jc} measured on Charpy size SE(B) specimens versus the test temperature normalised to T_0 of the appropriate disc.

In comparison with the standard MC evaluation Fig. 6 shows K_{Jc} values versus the test temperature normalised to T_0^{SINTAP} of the individual discs. With the reference temperature T_0^{SINTAP} representing the brittle fraction of a dataset all K_{Jc} values were enveloped with the fracture toughness curve for 5% fracture probability, $K_{Jc0.05}$.
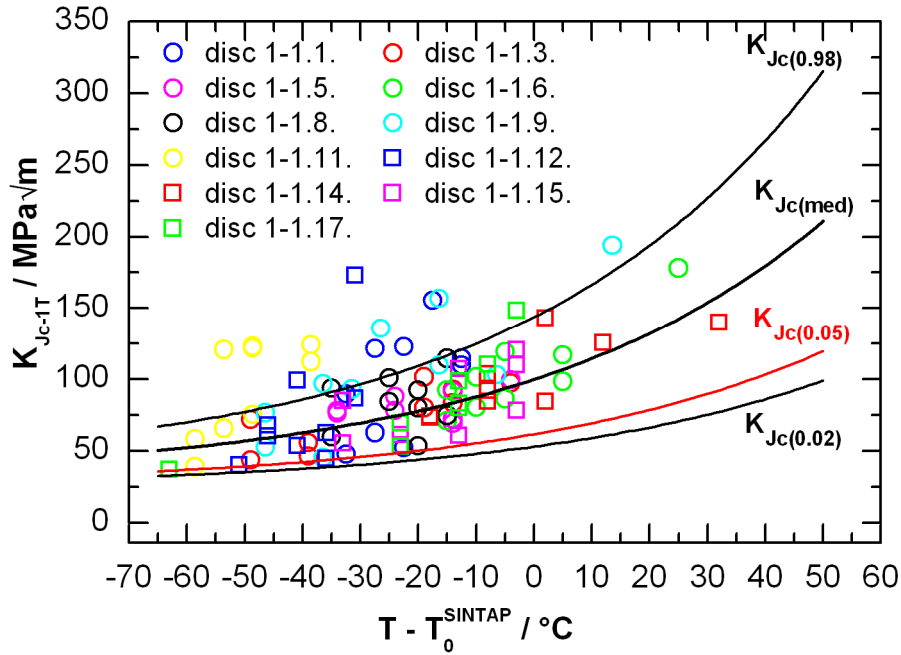
Fig. 6: K_{Jc} measured on Charpy size SE(B) specimens versus the test temperature normalised to T_0^{SINTAP} of the appropriate disc.

5. Summary and conclusion

The paper presents first results of the post mortem investigations performed into the reactor pressure vessels (RPV) of the Russian WWER-440 type reactors. Trepans were taken from the beltline weld and the base metal of the unit 1 RPV. This RPV was annealed after 15 years of operation and operated for two more years. At first the trepan of the beltline welding seam was investigated by Master Curve (MC) and Charpy V-notch testing. Specimens with TS orientation from 11 locations through the thickness of the welding seam were tested according to ASTM E1921-05 [2]. The reference temperature T_0 was calculated with the measured fracture toughness values, K_{Jc}, at brittle failure of the specimen. Generally the K_{Jc} values measured on pre-cracked and side-grooved Charpy size SE(B) specimens of the investigated weld metal follows the course of the Master Curve. The K_{Jc} values show a remarkable scatter. More values than expected lie below the 5% fractile. T_0 shows a wavelike behaviour through the welding seam. It increases from 10°C at the inner surface to 49°C at 22 mm distance and again decreases to -41°C at a distance of 70 mm, finally increasing again to maximum 67°C towards the outer RPV wall. The lowest T_0 value was measured in the root region of the welding seam. Beyond the welding root T_0 shows a span of about 50 K. The differences in T_0 through the beltline welding seam are not the result of the low re-irradiation but, rather caused by the non-homogenous structure of the multilayer welding seam. With the application of the MC modification in the SINTAP procedure [5,6] a reference temperature T_0^{SINTAP} can be evaluated which is based on the brittle constituent of a dataset. There are remarkable differences between T_0 and T_0^{SINTAP} indicating macroscopic inhomogeneous weld metal for some thickness locations. The fracture toughness curve for 5% fracture probability indexed with the SINTAP reference temperature RT_0^{SINTAP} envelops the K_{Jc} values.

Generally the effect of the recovery annealing was confirmed with the fracture toughness and Charpy-V testing. The TT_{41J} estimated with sub size KLST impact specimens [10] after the annealing was confirmed by the testing of standard Charpy V-notch specimens.

References

[1]   Viehrig, H.-W., Rindelhardt, U., Keller, W. (2006), Trepaning procedure applied at the RPV of the former Greifswald nuclear power plant, Forschungszentrum Dresden-Rossendorf e.V., Institute for Safety Research, Annual Report 2006, 76-80.

[2]   ASTM Test Standard E1921-05 (2005), Standard test method for determination of reference temperature, T_0, for ferritic steels in the transition range, Annual Book of Test Standards, Vol. 03.01, ASTM Intl., West Conshohocken, PA.

[3]   Böhmer, B., Böhmert, J., Müller, G., Rindelhardt, U., Utke, H. (1999), Embrittlement studies of the Reactor Pressure Vessel of the Greifswald -440 Reactors. Technical Report Task 4, Data Collection, European Commission, NUCRUS96601.

[4]   Davies, L.M. (1997), A Comparison of Western and Eastern Nuclear Reactor Pressure Vessel Steels, AMES Report No. 10, European Commission, Luxembourg, CD-NA-17327 EN-C.

[5]   Wallin, K., Nevasmaa, P., Laukkanen, A., Planman, T. (2004), Master curve analysis of inhomogeneous ferritic steels. Eng. Fract. Mech. 71 (16-17), 2329-2346.

[6]   Pisarski, H.G., Wallin, K. (2000), The SINTAP fracture toughness estimation procedure. Eng. Fract. Mech. 67 (6), 613-624.

[7]   DIN EN 10045-1 (2003), Metallic Materials: Charpy Impact Test; Part 1, DIN-Taschenbuch 19, Werkstoffprüfnormen für metallische Werkstoffe 1, Beut Verlag GmbH, 2003.

[8]   EN ISO 14556 (2003), Steel – Charpy V-Notch Pendulum Impact Test – Instrumented Test Method, DIN-Taschenbuch 19, Werkstoffprüfnormen für metallische Werkstoffe 1, Beut Verlag GmbH.

[9]   Konheiser, J., Rindelhardt, U., Viehrig, H.-W., Böhmer, B., Gleisberg, B. (2006), Pressure Vessel Investigations of the Former Greifswald NPP: Fluence Calculations and Nb Based Fluence Measurements, in ICONE14/FEDSM2006 Proceedings on DVD, Contribution ICONE 14-89578.

[10]   Ahlstrand, R.; Klausnitzer, E. N.; Langer, D.; Leitz, Ch.; Pastor, D. and Valo, M. (1993), Evaluation of the Recovery Annealing of the Reactor Pressure Vessel of NPP Nord (Greifswald) Units 1 and 2 by Means of Subsize Impact Specimens. Radiation Embrittlement of Nuclear Reactor Pressure Vessel Steels: An International Review (Fourth Volume), ASTM STP 1170. Lendell E. Steel, Ed., American Society for Testing and Materials, Philadelphia, 321-343.

Acknowledgement

Summaries of research activities

Accident analysis of nuclear reactors

The research is aimed at the enhancement of the predictive capability of computer simulations of accident scenarios in nuclear reactors. This is achieved by improvements of the neutron kinetics methods and by coupling of the FZDs reactor dynamics core model DYN3D to thermo-hydraulics system codes and to computational fluid dynamics (CFD) simulations. In particular, it is the objective to promote the basic understanding of coolant mixing phenomena relevant for boron dilution and pressurised thermal shock scenarios in Light Water Reactors (LWR). Moreover, the field of applicability of the reactor dynamics simulations is going to be extended to innovative reactor concepts. Concerning severe accidents in LWRs, the aim is to better ascertain the capabilities of measures for in vessel retention of corium melt during severe LWR accidents.

U. Grundmann,
S. Kliem,
Y. Kozmenkov,
S. Mittag,
U. Rohde,
F. Schäfer,
A. Gommlich,
G. Laczko,
B. Merk

Development, Validation and Application of the Code Complex DYN3D - ATHLET

In the course of the continuous improvement of the Rossendorf reactor dynamics code DYN3D, a multi-group transport approach was implemented for the improved description of spectral effects and to overcome the limitations of the diffusion approximation. Within this approach, even a pin-wise calculation of the power distribution is offered. To validate the new version of DYN3D, an OECD benchmark on mixed-oxide (MOX) cores was calculated. It was shown that the accuracy of the pin-wise power distribution was increased using the new models. A new, more effective numerical solution scheme was implemented, and the feasibility to perform even time-dependent kinetics calculations with pin-wise resolution in SP_3 transport approximation was shown. The extended code version was integrated into the European code platform NURESIM. An interface to the platform was developed based on the NURESIM software environment SALOME. Based on SALOME, an inter-active graphical pre-processor to elaborate DYN3D input decks and tools for the visualisation of the results were developed. The coupled code systems DYN3D-ATHLET and DYN3D-RELAP5 were validated on international benchmarks. In co-operation with the IPPE Obninsk in Russia, DYN3D and the coupled code complexes are used for analyses of alternative water cooled reactors. The expertise of the institute on thermo-hydraulic system codes is increasingly appreciated by industry. For example, thermo-hydraulic analyses were performed in charge of Vattenfall for a transient that had occurred at NPP Krümmel and for a hypothetical accident with emergency boron injection into Boiling Water Reactors. The code DYN3D is used by 12 organisations in 7 European countries and Russia. Several commercial licenses for DYN3D were granted to users in Germany and Europe. Concerning methodical developments in reactor theory, an analytical time-dependent neutron transport model was developed allowing a more accurate interpretation of measurements in pulsed sub-critical systems (ADS).

T. Höhne,	**Analysis of deboration transients**
S. Kliem,	The modelling of coolant mixing is highly relevant for nuclear reactor
U. Rohde,	safety, because mixing is the decisive only inherent mechanism to
T. Sühnel,	prevent serious consequences of boron dilution accidents. Experimental
R. Vaibar	investigations on coolant mixing in PWR at the ROCOM test facility

The modelling of coolant mixing is highly relevant for nuclear reactor safety, because mixing is the decisive only inherent mechanism to prevent serious consequences of boron dilution accidents. Experimental investigations on coolant mixing in PWR at the ROCOM test facility and accompanying CFD simulations were performed. Measured and calculated boron concentration distributions at the reactor core inlet were used directly as boundary conditions for the analysis of boron dilution transients by applying the DYN3D code. This expertise in mixing phenomena is used e.g. within a European TACIS project on boron dilution and overcooling transients in VVER type reactors. ROCOM is going to be involved in an OECD project, as reference facility for mixing tests.

A PhD thesis was completed on the development of advanced turbulence models for buoyancy driven mixing and their validation against experiments with well defined boundary conditions. This so-called VEMIX experiment represents a dedicated test facility of simple geometry delivering, by advanced instrumentation, data for CFD code validation.

funded by BMWi, EC and industries (VGB)

Simulation of sedimentation and re-suspension of insulating material in the reactor sump

E. Krepper,
A. Grahn,
G. Cartland-Glover

Insulating material (mineral wool) may be released from pipes and components during loss-of-coolant accidents in NPP and will be transported with the coolant towards the reactor sump. There it might lead to blockage of the sieves separating the suction chambers of the safety injection pumps from the sump leading to failure of the late phase emergency core cooling.

Within a research project funded by BMWi aimed at the simulation of the behaviour of mineral wool particles in the sump pool flow, models were developed for the re-suspension of sedimented isolation material. These models are based on different CFD approaches (e.g. particle tracking, solidification models) and also consider the effect of an impinging water jet, which can re-mobilise sedimented material. The work is done in co-operation with the University of Applied Sciences Zittau/Görlitz, where the experiments are performed, while FZ Dresden-Rossendorf is responsible for the CFD modelling. Up to now, the development was focussed on the elaboration of the single effect models. Recently, the complex interaction of the various models in simulation of a particle loaded sump flow in realistic sump geometry was demonstrated. CFD models developed by FZD were implemented into the CFD code ANSYS CFX and are successfully used by GRS and TÜV Süd.

funded by BMWi

In-vessel corium melt retention in LWRs

H.-G. Willschütz,
E. Altstadt

For a KONVOI reactor, the fracture mechanical investigation of the RPV with a postulated crack during thermal shock was finalised. The analyses show that crack growth is not to be expected.

An uncertainty and sensitivity analysis was started for the scenario with external flooding and homogeneous melt pool. Different input

parameters as for example the time of melt relocation, the emission coefficient for heat radiation or the liquidus temperature of the melt were varied. It was shown that the melt pool temperature depends most sensitively on the liquidus temperature. Due to crust formation, the material mass ablated from the RPV wall is decreasing with increasing liquidus temperature of the corium.

Materials and Components Safety

The change in the toughness behaviour of reactor pressure vessel materials is investigated as it results from neutron and gamma irradiation. The consequences are evaluated with respect to the safety of light water reactors (LWRs). For this purpose, material and fracture mechanical parameters of irradiated specimens have to be measured under hot cell conditions. The interpretation of the experiments is supported by finite element calculations. The micro-structural reasons and mechanisms of the neutron embrittlement are studied by small angle neutron scattering experiments and by nano-scaled modelling.

H.-W. Viehrig,
U. Rindelhardt,
E. Altstadt,
C. Zurbuchen,
J. Schuhknecht

Supported by
BMWi

Investigation of reactor pressure vessel material of the dismantled Greifswald NPP
Specimens with Charpy geometry were manufactured from the trepan of the core weld of unit 1. The material is irradiated, annealed and re-irradiated. Fracture resistance curves, impact toughness values and reference temperatures T_0 according to the master curve concept were measured. The fracture toughness values exhibit a significant scattering, which is typical for multi layer welds. The course of T_0 versus the wall thickness is rather irregular. The highest T_0 (+49.5 °C) is located at ¼ of the wall thickness while the lowest one (-61 °C) was found in the wall centre. For the irradiation conditions the highest T_0 was expected near the inner surface. Microstructural investigations are necessary to clarify the reason for the observed T_0 behaviour.

H.-W. Viehrig,
C. Zurbuchen,
E. Altstadt

Supported by
HSK

Application of the Master Curve Concept for irradiated material
A collaboration was established between the Swiss HSK and FZD to verify the master curve concept. The influence of specimen size, crack geometry and load rate is to be investigated. The specimens were made from a German pressure vessel steel (22 NiMoCr 3-7) originating from the NPP Biblis C which was never put into operation. It could be shown that T_0 is about 40 K lower for specimens with eroded notches (notch radius 0.6 mm) in comparison to specimens with fatigue crack. Therefore specimens with eroded notches provide non-conservative results.

H.-W. Viehrig,
J. Schuhknecht,
M. Abendroth

Supported by
BMWi

Small-Punch-Test (SPT) for characterisation of irradiated reactor materials
A joint BMWi project together with TUBA Freiberg was finished. In total 600 SPT-specimens from 3 RPV steels in 4 different irradiation conditions were tested. Using the measured load-displacement-curves the yield strength and the ultimate strength were recalculated. The deviation from values measured with the classical tension test was less than 5%. The available SPT technology now allows the investigation of highly irradiated materials.

F. Bergner,
A. Ulbricht,
C. Heintze,
R. Küchler

Analysis of the irradiation induced micro-structural changes
Small angle neutron scattering (SANS) experiments were performed at Cu containing weld material. Two irradiation conditions were investigated, where the final neutron fluence was the same but the flux differed by a factor of 34. It was shown that the size distribution of the defect clusters significantly depends on the neutron flux.

SANS measurements at irradiated Fe-Cr alloys revealed that the incoherent scattering part depends systematically on the Cr content and that the irradiation provokes the development of the α' phase. These measurement were done in preparation of an EU project dedicated to Gen-IV materials.

C. Heintze,
C. Recknagel

Characterisation of ion irradiated Gen-IV materials
In cooperation with the FZD Institute of Ion Beam Physics and Materials Research we started to simulate neutron irradiation induced damage by irradiation with ions. Using depth sensing nano hardness measurements it could be shown that the hardness in the thin damaged layer is significantly increasing with increasing ion fluence.

F. Bergner,
U. Birkenheuer,
A. Gokhman,
R. Küchler

Modelling of the irradiation induced embrittlement
Within a BMWi project the development of a new modular software package which is used to evaluate RPV steel embrittlement was finished. The rate theory models for Cu-vacancy clusters were validated using SANS data of Fe-Cu alloys with 0.1% and 0.3% Cu.

Furthermore, the flux effect observed in the SANS measurements of a weld material (see "*Analysis of the irradiation induced micro-structural changes*" above) was confirmed with a RT calculation. In this way a physical interpretation of the observed flux effect could be given.

Particle and radiation transport

The research project aimed at the development, verification and application of computational methods for particle and radiation transport. In recent years, the focus was on neutron/gamma/electron transport with applications in reactor physics, shielding and radiation physical experiments. The research project was terminated at the end of 2007.

J. Konheiser,
K. Noack,
G. Borodkin,
P. Borodkin

Calculations of the neutron/gamma irradiation load of the support structure of a VVER-440/230 reactor

Within the framework of the German-Russian scientific-technical collaboration, for the first time neutron and gamma fluences were calculated in the region of the reactor support structure of a Russian VVER-440 reactor of the first generation. Like the pressure vessel, the support structure is a not replaceable component. Since those reactors are approaching their projected lifetimes, the Russian Nuclear Safety Authority has to decide on termination or continuation of their operations. For that the accumulated radiation load is a decisive quantity because it allows to assess the material conditions. Neutron/gamma transport calculations were carried out with the Rossendorf Monte Carlo code TRAMO (FZD) and with the deterministic S_n-code DORT (SEC NRS Moscow). Both codes and their calculation models were validated by means of neutron activation measurements that were especially carried out in the region of the support structure. The results of both calculations show that the maximum value of the neutron fluence ($E_n >$ 0.5 MeV) accumulated during nominal reactor operation over the lifetime of forty full power years clearly exceeds the value 1×10^{18} n/cm^2. For this case the Russian reactor operation rules lay down that the operating company has to re-evaluate the mechanical stresses occuring in the support construction during normal reactor operations as well as during certain accident conditions and to prove that given limiting values are not exceeded. The calculation results obtained with TRAMO and DORT deviate considerably (up to 20%) in certain regions of the support structure. To unambiguously clear up the reason of the deviations the analysis must be continued.

K. Noack,
U. Rindelhardt,
A. Rogov

Within the framework of the Integrated Project EUROTRANS a project was developed for a new zero-power experimental facility (GUINEVERE) of a subcritical accelerator driven system (ADS) has been developed. The GUINEVERE facility consists of the accelerator, the beam guiding system and the lead-reflected small core with the composition of a lead-cooled fast reactor. By means of the Monte Carlo code MCNP5 FZD carried out both the shielding calculations for the whole building and the criticality calculations for the fuel storage. The neutron/gamma doses in the building and the criticality level of the fuel storage must meet the demands, which are defined by the Belgian Nuclear and Radiation Safety Authority. Based on the calculation results the final designs of several technical details could be determined. The report on the calculations was included in the application documents, which were forwarded to the Belgian Safety Authority to obtain the license of the GUINEVERE facility.

Thermal fluid dynamics of multiphase systems

It is the general aim of the work done in the field of thermal fluid-dynamics to qualify Computational Fluid Dynamics (CFD) codes for the simulation of complex two-phase flows that are relevant in industrial applications. To achieve this goal, closure models are needed for the interaction between the phases, i.e. mass, momentum and energy transfer. For the special case of dispersed bubbly flow, all these transfers strongly depend on the local bubble size distribution. For this reason, the gas phase has to be split into a number of size groups in case of poly-dispersed flows. Transfers between these groups are amongst others determined by bubble coalescence and fragmentation. The theoretical work is based on sound experiments at the TOPFLOW test facility using advanced two-phase measuring instrumentation, which is developed in the framework of the present project.

E. Krepper, *D. Lucas,* *S. Alissa*	**Qualification of CFD models** The validation of the Inhomogeneous MUSIG (MUlti Bubble SIze Group) model was continued relying on experimental data obtained at the TOPFLOW facility for upwards flow in vertical pipes as well as for 3D flow around an obstacle. In the result, the suitability of the model concept to poly-dispersed flows was confirmed. The implemented models for bubble forces are applicable in a wide range of parameters, while the transferability of the presently available models for bubble coalescence and fragmentation is still limited. One of the reasons is the limited quality of the predicted turbulence parameter in case of two-phase flows. To improve the simulations a turbulence model was implemented into the test solver, which considers additional source terms in the k-ε equation for bubble induced turbulence. In addition, a new extensive experimental database was generated on air-water flow in a vertical pipe which is an excellent basis for the improvement, test and validation of models for bubble coalescence and fragmentation. New model equations for the extension of the model were proposed which
Funded by BMWi	allow to consider flows with variable density and phase transfer.
Ch. Vallee, *T. Höhne*	**Experiments and CFD-simulations for stratified flows** The new horizontal channel with rectangular cross-section (HAWAC) was used for investigations on the hydraulic jump phenomenon. The experiments showed, that the position as well as the profile of the jump sensitively depend on the air flow rate. These data are suitable to validate CFD models for momentum transfer and coupling of the turbulence fields at a free surface. Pre-test CFD-simulations were done for the hot leg experiments using ANSYS-CFX. After completing an extensive series of air-water experiments with the pressure up to 0.5 MPa, first steam-water experiments were successfully performed at the hot leg model. They provide world-wide unique data including high-speed video observations of complex steam-water flows using the new developed pressure chamber technology. Data were obtained for co-current as well as for counter current flows. Special attention was paid to investigation of the Counter-Current Flow Limitation (CCFL) which is a
Funded by BMWi	safety-relevant phenomenon.
M. Schmidtke, *T. Höhne,*	**CFD-Simulations on the bubble entrained caused by a liquid jet** In the frame of the European project NURESIM, a new modelling

E. Bodele, *D. Lucas,* *E. Krepper*	strategy was applied to the simulation of bubble entrainment caused by the impingement of a liquid jet into a liquid pool. For practical applications, questions have to be answered as the mixing between hot water in a pool with cold water from the jet (e.g. in case emergency core cooling injection into the cold leg of a Pressurised Water reactor), or re-suspension of particles in the pool. In such a flow situation, the gas phase simultaneously occurs as continuous phase (gas above the pool surface) and dispersed phase (entrained bubbles). The Algebraic Interfacial Area Density Model allows applying different closure models, e.g. drag models, according to these different flow situations. The applicability of the model to control the bubble entrainment was
Funded by EU	demonstrated.

U. Hampel, *E. Schleicher,* *M. Bieberle,* *F. Fischer*	**Ultra fast X-ray tomography** Within the project „Ultra fast X-ray tomography" funded by the DFG unique experiments were conducted using the device installed at IKE Stuttgart. For the first time, two-phase flows in a fluidised bed were visualised with a time resolution of 5000 frames per second. In the frame of the TOPFLOW-II project, the electron beam tomography device was completed (max. 150 kV tube voltage, max. 65 mA beam current and xy-deflection unit for tomography of two-phase flows). It achieves up to 10.000 frames per second with a spatial resolution of 1
Funded by DFG *and BMWi*	mm. The device was used to record a two-phase flow in a bubble column. Such measurements are unique world-wide.

U. Hampel, *M. da Silva,* *D. Hoppe,* *A. Fleischer*	**High resolution measurement of flow patterns in a hydrodynamic coupling** Within the frame of an industrial project with Voith Turbo GmbH in Crailsheim, measurements within a rotating hydrodynamic coupling were performed using the surface conductivity sensor. This sensor was developed at FZD and is able to measure two-dimensional boundary flow patterns at the suction respectively pressure side of a chamber wall with 10.000 frames per second. In addition, high resolution gamma ray tomography was used to measure three dimensional phase distributions within the coupling chambers at approximately 3 mm spatial resolution. The unique data with high resolution in space and time provide new
Funded by Voith *Turbo GmbH*	insights for future improvements of the coupling design as well as for CFD code development and validation.

U. Hampel, *A. Bieberle,* *D. Hoppe,* *E. Schleicher,* *C. Zippe*	**Optimisation of the gamma ray tomography for void fraction measurements in fuel rod assemblies** The void fraction distributions in electrically heated BWR fuel rod assemblies was measured by gamma ray tomography at the KATHY test loop of AREVA NP GmbH in Karlstein (Germany). The high-resolution gamma ray tomography device was developed at FZD. A reduction of the counting error caused by temperature drift down to 0.5 % was achieved by a redesign of the detector array. This gamma ray device is
Funded by *AREVA NP*	the only one world-wide which is able to measure the spatial distribution of the void fraction in a fuel element.

M. J. Da Silva	**Investigations on air-water and oil-water two phase flows**

M. J. Da Silva

Investigations on air-water and oil-water two phase flows

Within the frame of a co-operation with the University of Nottingham comparative measurements were done for air-water and oil-water two-phase flows in inclined pipes. For the first time, the new developed capacitance wire mesh sensor was used for measurements of highly transient oil-water flows. The sensor comprises two wire planes of 32 wires each and provides up to 10.000 frames per second. The sensor is able to discriminate differences in the relative dielectric constant of $\Delta\varepsilon_r$ up to 1.

H. Kryk,
M. Schubert,
G. Hessel,
V. V. Kumar

Desulphurisation of acid mining effluents

Crucial factors for the efficiency of systems for electrochemical treatment of acid mine effluents are the residence time distributions (RTD) of the liquids within the compartments of the electrolytic cell. Therefore, the influences of internals and flow rates on the RTD were investigated using laser induced fluorescence (LIF) visualisation. It turned out, that residence time as well as back-mixing is strongly influenced by the pressure conditions in the compartments due to membrane positioning effects. The measurements are preconditions for the optimisation of the fluid flow within the cell.

Funded by LMBV/
VKTA

M. Schubert,
U. Hampel,
G. Hessel,
C. Zippe

Measurement of phase distributions in chemical reactors

A real high-resolution gamma ray tomography technique was applied to the quantitative analysis of the liquid flow texture in a laboratory cold flow trickle bed reactor for the first time. The phase distribution and thus the reactor performance are primarily influenced by the fluid distribution as well as by the surface properties of the filling material. It was shown, that the optimisation of feed-in components as well as of process parameters strongly depends on the properties of the reactor bed.

Liquid metal magnetohydrodynamics

Magnetohydrodynamics investigates the interaction of electrically conducting fluids (liquid metals and semiconductors, electrolytes) with magnetic fields. In various applications, the use of magnetic fields provides a comfortable contact-less possibility to control the transport processes in such melts. Moreover, problems as MHD turbulence, the homogeneous dynamo or the magnetorotational instability are the subject of intense basic research.

A. Cramer, *I. Grants,* *J. Pal,* *M. Röder,* *A. Kljukin,* *G. Gerbeth* *Supported by* *DFG*	**Basics of MHD flows and Experiments at MULTIMAG** The temperature fluctuations in turbulent buoyancy driven flows could be reduced by more than one order of magnitude by application of a rotating magnetic field (RMF). This flow control is attractive for the Czochralski (Cz) crystal growth process. With that background, a patent application has been submitted. For a further optimisation of the melt flow in the Cz configuration, a new experiment has been set up where various magnetic fields are superimposed in order to achieve a predefined temperature distribution in the melt. Already with an RMF alone the temperature gradients could be significantly influenced: depending on the field strength the ratio of horizontal to vertical temperature gradients could be varied between 0.5 and 20 at the triple point melt-crystal-gas.
Th. Gundrum, *F. Stefani,* *G. Gerbeth* *Supported by WGL* *and DFG*	**Experiments on the Magneto-Rotational Instability (MRI)** The necessary transport of angular momentum during the creation of stars or black holes in accretion disks can only be explained by a magnetically caused transition to turbulence. In the laboratory experiment this effect was observed in form of a travelling wave in an otherwise laminar rotating flow when an external helical magnetic field was applied. The MRI experiment was modified in such a way that symmetric boundary conditions emerge at the lower and upper end of the melt in order to minimize the influence of the end plates. In this way it became possible to distinguish between convective and absolute instabilities in the MRI experiment.
T. Weier, *Ch. Cierpka,* *G. Mutschke,* *V. Shatrov,* *G. Gerbeth* *Supported by* *DFG*	**Boundary layer control in electrolytes** The PIV measurement of the flow and the drag measurements at the electrolyte channel were synchronised. This enables to relate the detached vortex structures to the lift force acting on the profile, thus allowing to identify the optimal electromagnetic flow control with respect to the resulting forces. For the copper deposition in an electrolytic cell the flow field was measured by PIV, whereas the concentration distribution was determined by a background Schlieren method. It turned out that the so-called concentration gradient force, which in the literature is made responsible for the observed concentration distribution, is almost negligible. Instead, the resulting concentration field can consistently be explained if the flow field in the cell is correctly taken into account.

K. Timmel,
X. Miao,
S. Eckert,
G. Gerbeth

Modelling of the steel casting process

Extensive preparations were done for a new liquid metal loop working with tin-bismuth alloy. It represents a model of the continuous steel casting process, in particular of the related flow in the nozzle and in the mold. Building up of this facility was delayed due to the necessary reconstruction of the experimental hall which, however, provides now ideal conditions for all experimental works in the future. The construction of the new CONCAST facility was started in December.

S. Boden,
S. Eckert,
B. Willers

Radiography of solidifying metal melts

Using a microfocus X-ray tube the solidification of Ga-In alloy has been visualised for the first time. The flow in the melt has a strong impact on the heat and mass transfer, thus influencing significantly the concentration and temperature fields ahead of the solidification front. Eventually this has a determining influence on the macroscopic properties of the solidified alloy. Using the optical flow approach, the flow field in the melt was reconstructed from X-ray measurements. It turned out that the solutal convection modifies the concentration field and has, in this way, a strong influence on the dendrite growth.

TOPFLOW thermal hydraulic test facility

The acronym TOPFLOW stands for Transient Two Phase Flow Test Facility. This multipurpose thermal hydraulic facility is mainly used for the investigation of generic and applied steady state and transient two phase flow phenomena in either steam-water or air-water-mixtures. TOPFLOW has a maximum heating power of 4 MW and allows operation at pressures up to 7 MPa and temperature up to 285 °C in pipes and vessel geometries of industrial relevance. It has become the major experimental facility of the German CFD (Computational Fluid Dynamic) Research Alliance. In 2006, a contract was signed with Commissariat à l'Energie Atomique (CEA) France, Electricité de France (EDF), AREVA NP France, Institut de Radioprotection et de Sûreté Nucléaire (IRSN) France, and Paul Scherrer Institute (PSI) Switzerland, for a comprehensive experimental programme aiming at the investigation of pressurised thermal shock phenomena (PTS) using TOPFLOW.

To support the theoretical model development and the CFD code validation, a series of experiments was conducted at TOPFLOW at different test rigs in 2007.

M. Beyer, *H. Carl,* *K. Linder,* *H. Pietruske,* *H. Rußig,* *P. Schütz,* *M. Tamme,* *Ch. Vallee,* *S. Weichelt*	**Stratified two-phase flows experiments in the hot leg model of a pressurised water reactor during loss of coolant accident conditions** Co-current as well as counter current flow air water experiments were conducted at pressures up to 0.5 MPa. To enable steam-water experiments new materials for the thermal insulation of the test section inside the pressure tank were successfully tested. Additionally, a new technical solution for the lightening of the hot leg model was installed. Nitrogen is used for the inertisation of the atmosphere in the tank. After these preparations, the steam water hot leg experiments started in December 2007. Up to the end of 2007 different co-current and counter current flow experiments up to a pressure of 1.5 MPa and a temperature of 200 °C were carried out. The obtained results show a good agreement
supported by *BMWA*	with the results of other investigations which can be found in the literature.
M. Beyer, *H. Carl,* *K. Lindner,* *H. Pietruske,* *P. Schütz,* *S. Weichelt*	**Two phase flow experiments in the vertical test section DN200 with phase transfer** A new module was put into operation for the degassing of the feed-water to reduce the concentration of non-condensible gases in the two phase flow during the experiments with condensation and de-pressurisation. This module decreases the concentration of oxygen from 80% down to 3% (related to the maximum solubility). All components needed for condensation experiments were manufactured. The facility extension for these tests will start in 2008.
supported by *BMWA*	The equipment design for the experiments with de-pressurisation conditions was finished.
U. Hampel, *M. Beyer,* *H. Carl,* *F. Fischer,* *E. Schleicher,* *P. Schütz,* *M. Tschofen,*	**Experiments with a new vertical test tube DN50 using ultra fast X-ray tomography** The tube made from a special Ti-alloy was installed, checked and connected to the media supply pipes of TOPFLOW. After pressure test, this new module is ready for the experiments. The X-ray scanner was successfully put into operation. Also the software for data evaluation was implemented and the scanner was finally tested on a simple bubble column. For the first time, images of the gas distribution in a column

supported by BMWA

were obtained with a frequency of 5 kHz. The image processing software provides bubble recognition and bubble size measurement.

U. Hampel,
M. Beyer,
H. Carl,
H. Pietruske,
E. Schleicher,
P. Schütz,
M. Tschofen,
Ch. Vallee,

supported by Commissariat à l'Energie Atomique (CEA) France, Electricité de France (EDF), AREVA NP France, Institut de Radioprotection et de Sûreté Nucléaire (IRSN) France, and Paul Scherrer Institute (PSI) Switzerland.

TOPFLOW- pressurised thermal shock phenomena (PTS)

In January 2006, the TOPFLOW-PTS project was started. This project aims at the investigation of thermal hydraulic phenomena occurring in an emergency core cooling (ECC) scenario at French pressurised water reactors of the CPY type. The project is commissioned and run by a consortium of international industry and scientific partners, including Commissariat à l'Energie Atomique (CEA) France, Electricité de France (EDF), AREVA NP France, Institut de Radioprotection et de Sûreté Nucléaire (IRSN) France, and Paul Scherrer Institute (PSI) Switzerland. Experiments will be conducted in the TOPFLOW pressure tank on a 1:2.5 model of a reactor cold leg section, comprising main coolant pump, cold leg, ECC line and downcomer. In 2007, the test rig was finally designed and manufactured. The necessary TOPFLOW facility extensions were carried out such as media supply and cooling system. The required special instrumentation such as thermocouple lances, different wire mesh sensors, thermo needle probes and optical and IR observation techniques together with specialised data acquisition electronics was finally designed, built and successfully checked.

Publications

Publications in journals

Altstadt, E.; Beckert, C.; Freiesleben, H.; Galindo, V.; Grosse, E.; Junghans, A. R.; Klug, J.; Naumann, B.; Schneider, S.; Schlenk, R.; Wagner, A.; Weiss, F.-P.
A photo-neutron source for time-of-flight measurements at the radiation source ELBE
Annals of Nuclear Energy 34(2007), 36-50

Anikeev, A. V.; Bagryansky, P. A.; Deichuli, P. P.; Ivanov, A. A.; Kireenko, A. V.; Lizunov, A. A.; Murakhtin, S. V.; Prikhodko, V. V.; Solomakhin, A. L.; Sorokhin, A. V.; Stupishin, N. V.; Collatz, S.; Noack, K.
The synthesized hot ion plasmoid experiment at GDT
Fusion Science and Technology 51(2007), 79-81

Anikeev, A. V.; Bagryansky, P. A.; Ivanov, A. A.; Lizunov, A. A.; Murakhtin, S. V.; Prikhodko, V. V.; Solomakhin, A. L.; Noack, K.
Confinement of strongly anisotropic hot-ion plasma in a compact mirror
Journal of Fusion Energy 26(2007)1-2, 103-107

Avalos-Zuniga, R. A.; Xu, M.; Stefani, F.; Gerbeth, G.; Plunian, F.
Cylindrical anisotropic alpha^2 dynamos
Geophysical and Astrophysical Fluid Dynamics 101(2007)5/6, 389-404

Beckert, C.; Grundmann, U.; Mittag, S.
Multigroup diffusion and SP3 solutions for a PWR MOX/UO2 benchmark with the code DYN3D
Transactions of the American Nuclear Society and the European Nuclear Society 97(2007), 701

Bergner, F.; Schaper, M.; Hammer, R.; Jurisch, M.; Kleinwechter, A.; Chudoba, T.
Indentation response of single-crystal GaAs in the nano-, micro-, and macroregime
International Journal of Materials Research (2007)08, 735-741

Beyer, R.; Grosse, E.; Heidel, K.; Hutsch, J.; Junghans, A. R.; Klug, J.; Legrady, D.; Nolte, R.; Röttger, S.; Sobiella, M.; Wagner, A.
Proton-recoil detectors for time-of-flight measurements of neutrons with kinetic energies from some tens of keV to a few MeV
Nuclear Instruments and Methods in Physics Research A 575(2007), 449-455

Bieberle, A.; Kronenberg, J.; Schleicher, E.; Hampel, U.
Design of a high resolution gamma ray detector module for tomography applications
Nuclear Instruments and Methods in Physics Research A 527(2007)2, 668-675

Bieberle, A.; Schleicher, E.; Hampel, U.
Data acquisition system for angle synchronized gamma-ray tomography of rapidly rotating objects
Measurement Science and Technology 18(2007), MST/248418/PAP/167103

Bieberle, M.; Fischer, F.; Schleicher, E.; Koch, D.; Aktay, K. S. D. C.; Menz, H.-J.; Mayer, H.-G.; Hampel, U.
Ultra fast limited-angle type X-ray tomography
Applied Physics Letters 91(2007), 123516

Cartland Glover, G. M.; Höhne, T.; Kliem, S.; Rohde, U.; Weiss, F.-P.; Prasser, H.-M.
Hydrodynamic phenomena in the downcomer during flow rate transients in the primary circuit of a PWR
Nuclear Engineering and Design 237(2007)7, 732-748

Cierpka, C.; Weier, T.; Gerbeth, G.; Uhlemann, M.; Eckert, K.
Copper deposition and dissolution in seemingly parallel electric and magnetic fields: Lorentz force distributions and flow configurations
Journal of Solid State Electrochemistry 11(2007)6, 687-701

Cramer, A.; Pal, J.; Gerbeth, G.
Experimental investigation of a flow driven by a combination of a rotating and a traveling magnetic field
Physics of Fluids 19(2007)11, 118109

Da Silva, M. J.; Schleicher, E.; Hampel, U.
A novel needle probe based on high-speed complex permittivity measurements for investigation of dynamic fluid flows
IEEE Transactions on Instrumentation and Measurement 56(2007)4, 1249-1256

Da Silva, M. J.; Schleicher, E.; Hampel, U.
Capacitance wire-mesh sensor for fast measurement of phase fraction distributions
Measurement Science and Technology 18(2007)7, 2245-2251

Da Silva, M. J.; Sühnel, T.; Schleicher, E.; Vaibar, R.; Lucas, D.; Hampel, U.
Planar array sensor for high-speed component distribution imaging in fluid flow applications
Sensors 7(2007), 2430-2445

Dzugan, J.; Viehrig, H.-W.
Crack initiation determination for three-point-bend specimens
Journal of Testing and Evaluation, 35(2007)3, 245-253

Eckert, S.; Gerbeth, G.; Räbiger, D.; Willers, B.; Zhang, C.
Experimental modelling using low melting point metallic melts: Relevance for metallurgical engineering
Steel Research International 78(2007)5, 419-425

Eckert, S.; Nikrityuk, Petr A.; Räbiger, D.; Eckert, K.; Gerbeth, G.
Efficient melt stirring using pulse sequences of a rotating magnetic field: I-Flow field in a liquid metal column
Metallurgical and Materials Transactions B 38B(2007), 977-988

Galindo, V.; Grants, I.; Lantzsch, R.; Pätzold, O.; Gerbeth, G.
Numerical and experimental modeling of the melt flow in a traveling magnetic field for Vertical Gradient Freeze crystal growth
Journal of Crystal Growth 303(2007), 258-261

Gerbeth, G.
Abteilung Magnetohydrodynamik des Forschungszentrums Dresden-Rossendorf
Elektrowärme International (2007)3, 187-189

Gillemot, F.; Horvath, M.; Uri, G.; Fekete, T.; Houndeffo, E.; Acosta, B.; Debarberis, L.; Viehrig, H.-W.
Radiation stability of WWER RPV cladding materials
International Journal of Pressure Vessels and Piping 84(2007)8

Grants, I.; Gerbeth, G.
The suppression of temperature fluctuations by a rotating magnetic field in a high aspect ratio Czochralski configuration
Journal of Crystal Growth 308(2007)2, 290-296

Günther, U.; Kirillov, O.; Samsonov, B.; Stefani, F.
The spherically symmetric α^2-dynamo and some of its spectral peculiarities
Acta Polytechnica 47(2007)2-3, 75-81

Günther, U.; Rotter, I.; Samsonov, B.
Projective Hilbert space structures at exceptional points
Journal of Physics A 40(2007), 8815-8833

Günther, U.; Samsonov, B.; Stefani, F.
A globally diagonalizable α^2-dynamo operator, SUSY QM and the Dirac equation
Journal of Physics A 40(2007), F169-F176

Hampel, U.; Bieberle, A.; Hoppe, D.; Kronenberg, J.; Schleicher, E.; Sühnel, T.; Zimmermann, F.; Zippe, C.
High resolution gamma ray tomography scanner for flow measurement and non-destructive testing applications
Review of Scientific Instruments 78(2007), 103704

Hampel, U.; Hristov, H. V.; Bieberle, A.; Zippe, C.
Application of high resolution gamma ray tomography to the measurement of gas hold-up distributions in a stirred chemical reactor
Flow Measurement and Instrumentation 18(2007), 184-190

Höhne, T.
Numerical simulation of coolant mixing in a pressurized water reactor with different CFD methods based on complex meshes
International Journal of Nuclear Energy Science and Technology 3(2007)4, 399-412

Höhne, T.; Kliem, S.
Modeling of a buoyancy-driven flow experiment in pressurized water reactors using CFD-Methods
Nuclear Engineering and Technology 39(2007)4, 327-336

Höhne, T.; Kliem, S.; Weiß, F.-P.
Modeling of a buoyancy-driven flow experiment at the ROCOM test facility using the CFD-Code ANSYS CFX
atw - International Journal for Nuclear Power 3(2007), 168-174

Hoppe, D.; Zaruba, A.
Eine Untersuchung zur Beschreibung kleiner Luftblasen durch Ellipsoide / An investigation concerning the description of small bubbles by ellipsoids
Technisches Messen 1(2007), 29-35

Hozoi, L.; Birkenheuer, U.; Fulde, P.; Mitrushchenkov, A.; Stoll, H.
Ab initio wave function-based methods for excited states in solids: Correlation corrections to the band structure of ionic oxides
Physical Review B 76(2007), 085109

Kliem, S.; Danilin, S.; Hämäläinen, A.; Hadek, J.; Kereszturi, A.; Siltanen, P.
Qualification of coupled 3D neutron kinetic/thermal hydraulic code systems by the calculation of main steam line break benchmarks in a NPP with VVER-440 reactor
Nuclear Science and Engineering 157(2007)3, 280-298

Kliem, S.; Hemström, B.; Bezrukov, Y.; Höhne, T.; Rohde, U.
Comparative evaluation of coolant mixing experiments at the ROCOM, Vattenfall, and Gidropress test facilities
Science and Technology of Nuclear Installations 2007(2007), 25950

Kliem, S.; Sühnel, T.; Prasser, H.-M.; Weiß, F.-P.
Experimente an der Versuchsanlage ROCOM zur Kühlmittelvermischung bei Wiederanlauf der Naturzirkulation
atw - International Journal for Nuclear Power (2007), 352-360

Klug, J.; Altstadt, E.; Beckert, C.; Beyer, R.; Freiesleben, H.; Galindo, V.; Grosse, E.; Junghans, A. R.; Legrady, D.; Naumann, B.; Noack, K.; Rusev, G.; Schilling, K. D.; Schlenk, R.; Schneider, S.; Wagner, A.; Weiß, F.-P.
Development of a neutron time-of-flight source at the ELBE accelerator
Nuclear Instruments and Methods in Physics Research A 577(2007)3, 641-653

Kodeli, I.; Aldama, D. L.; de Leege, P. F. A.; Legrady, D.; Hoogenboom, J. E.; Cowan, P.
Multigroup coupled neutron-gamma cross-section library for deterministic and Monte Carlo borehole logging analysis
Nuclear Science and Engineering 157(2007)2, 210-224

Kozmenkov, Y.; Kliem, S.; Grundmann, U.; Rohde, U.; Weiss, F.-P.
Calculation of the VVER-1000 coolant transient benchmark using the coupled code systems DYN3D/RELAP5 and DYN3D/ATHLET
Nuclear Engineering and Design 237(2007)15-17, 1938-1951

Krepel, J.; Rohde, U.; Grundmann, U.; Weiß, F.-P.
DYN3D-MSR spatial dynamics code for Molten Salt Reactors
Annals of Nuclear Energy 34(2007), 449-462

Krepper, E.; Koncar, B.; Egorov, Y.
CFD modelling of subcooled boiling – concept, validation and application to fuel assembly design
Nuclear Engineering and Design 237(2007), 716-731

Krepper, E.; Reddy Vanga, B. N.; Zaruba, A.; Prasser, H.-M.; Lopez de Bertodano, M.
Experimental and numerical studies of void fraction distribution in rectangular bubble columns
Nuclear Engineering and Design 237(2007), 399-408

Kryk, H.; Hessel, G.; Schmitt, W.
Improvement of process safety and efficiency of Grignard reactions by real-time monitoring
Organic Process Research & Development 11(2007)6, 1135-1140

Kryk, H.; Hessel, G.; Schmitt, W.; Tefera, N.
Safety aspects of the process control of Grignard reactions
Chemical Engineering Science 62(2007), 5198-5200

Kuechler, R.; Noack, K.
Comparison of the solution behaviour of a pyrite/calcite mixture in batch and unsaturated sand column
Journal of Contaminant Hydrology 90(2007)3-4, 203-220

Lantzsch, R.; Galindo, V.; Grants, I.; Zhang, C.; Pätzold, O.; Gerbeth, G.; Stelter, M.
Experimental and numerical results on the fluid flow driven by a traveling magnetic field
Journal of Crystal Growth 305(2007), 249-256

Linse, T.; Kuna, M.; Schuhknecht, J.; Viehrig, H.-W.
Usage of small-punch-test for the characterisation of reactor vessel steels in the brittle-ductile transition region
Engineering Fracture Mechanics (2007)

Lucas, D.; Krepper, E.; Prasser, H.-M.
Modeling of the evolution of bubbly flow along a large vertical pipe
Nuclear Technology 158(2007), 291-303

Lucas, D.; Krepper, E.; Prasser, H.-M.
Use of models for lift, wall and turbulent dispersion forces acting on bubbles for poly-disperse flows
Chemical Engineering Science 62(2007), 4146-4157

Lucas, D.; Prasser, H.-M.
Steam bubble condensation in sub-cooled water in case of co-current vertical pipe flow
Nuclear Engineering and Design 237(2007), 497-508

Manera, A.; Lucas, D.; Prasser, H.-M.
Experimental investigation on bubble turbulent diffusion in a vertical large-diameter pipe by wire-mesh sensors and correlation techniques
Nuclear Technology 158 (2007) 275-290

Nievaart, V. A.; Legrady, D.; Moss, R. L.; Kloosterman, J. L.; van der Hagen, T. H. J. J.; van Dam, H.
Application of adjoint Monte Carlo to accelerate simulations of mono-directional beams in radiotherapy treatment planning
Medical Physics 34(2007)4, 1321-1335

Noack, K.; Rogov, A.; Ivanov, A. A.; Kruglyakov, E. P.
The GDT as neutron source in a sub-critical system for transmutation?
Fusion Science and Technology 51(2007), 65-68

Ošmera, B.; Boehmer, B.; Ballesteros, A.; Konheiser, J.; Kyncl, J.; Hordosy, G.; Keresztúri, A.; Belousov, S.; Ilieva, K.; Kirilova, D.; Mitev, M.; Smutný, V.; Polke, E.; Zaritsky, S.; Töre, C.; Ortego, P.
Accurate determination and benchmarking of radiation field parameters relevant for pressure vessel monitoring. A review of some REDOS project results
Journal of ASTM International Volume 4(2007)Issue 10

Ondrey, G. S.
A fast way to measure phase fractions in multiphase flow
Chemical Engineering 114(2007)12, 16

Pietruske, H.; Prasser, H.-M.
Wire-mesh sensors for high-resolving two-phase flow studies at high pressures and temperatures
Flow Measurement and Instrumentation 18(2007)2, 87-94

Prasser, H.-M.
Evolution of interfacial area concentration in a vertical air-water flow measured by wire-mesh sensors
Nuclear Engineering and Design 237(2007), 1608-1617

Prasser, H.-M.; Beyer, M.; Carl, H.; Gregor, S.; Lucas, D.; Pietruske, H.; Schütz, P.; Weiss, F.-P.
Evolution of the structure of a gas-liquid two-phase flow in a large vertical pipe
Nuclear Engineering and Design 237(2007), 1848-1861

Priede, J.; Gerbeth, G.
Matched asymptotic solution for the solute boundary layer in a converging axisymmetric stagnation point flow
International Journal of Heat and Mass Transfer 50(2007), 216-225

Priede, J.; Grants, I.; Gerbeth, G.
Inductionless magnetorotational instability in a Taylor-Couette flow with a helical magnetic field
Physical Review E 75(2007), 047303

Priede, J.; Grants, I.; Gerbeth, G.
Paradox of inductionless magnetorotational instability
Journal of Physics: Conference Series 64(2007), 012011

Pupasov, A.; Samsonov, B.; Günther, U.
Exact propagators for SUSY partners
Journal of Physics A 40(2007), 10557-10587

Ren, Z.; Gerbeth, G.
Electromagnetic processing of materials
Steel Research International 78(2007), 371-372

Rindelhardt, U.
Wasserkraftnutzung in Ostdeutschland
Wasserwirtschaft 97(2007)6, 33-36

Rohde, U.; Höhne, T.; Kliem, S.; Hemström, B.; Scheuerer, M.; Toppila, T.; Aszodi, A.;
Boros, I.; Farkas, I.; Muehlbauer, P.; Vyskocil, V.; Klepac, J.; Remis, J.; Dury, T.
Fluid mixing and flow distribution ín a primary circuit of a nuclear pressurized water reactor – Validation of CFD codes
Nuclear Engineering and Design 237(2007)15-17, 1639-1655

Shatrov, V.; Gerbeth, G.
Magnetohydrodynamic drag reduction and its efficiency
Physics of Fluids 19, 035109(2007)

Shatrov, V.; Priede, J.; Gerbeth, G.
Basic flow and its 3D linear stability in a small spherical droplet spinning in an alternating magnetic field
Physics of Fluids 19(2007)7, 78106

Sklyarchuk, V.; Plevachuk, Yu.; Gerbeth, G.; Eckert, S.
Melting-solidification process in Pb-Bi melts
Journal of Physics: Conference Series 79(2007), 012019

Sorriso-Valvo, L.; Carbone, V.; Stefani, F.; Nigro, G.
A statistical analysis of polarity reversals of the geomagnetic field
Physics of the Earth and Planetary Interiors 164(2007), 197-207

Stefani, F.; Gailitis, A.; Gerbeth, G.; Gundrum, T.; Xu, M.
Forward and inverse problems in MHD: numerical and experimental results
GAMM-Mitteilungen 30(2007)1, 159-170

Stefani, F.; Gundrum, T.; Gerbeth, G.; Rüdiger, G.; Szklarski, J.; Hollerbach, R.
Experiments on the magnetorotational instability in helical magnetic fields
New Journal of Physics 9(2007), 295

Stefani, F.; Xu, M.; Sorriso-Valvo, L.; Gerbeth, G.; Günther, U.
Oscillation or rotation: a comparison of two simple reversal models
Geophysical and Astrophysical Fluid Dynamics 101(2007)3-4, 227-248

Stieglitz, R.; Kliem, S.
Jahrestagung Kerntechnik - Sektionsbericht Sektion: Thermo- und Fluiddynamik
atw - International Journal for Nuclear Power 52(2007)10, 652-654

Thunman, M.; Eckert, S.; Hennig, O.; Björkvall, J.; Du, S.
Study on the formation of open-eye and slag entrainment in a gas stirred ladle
Steel Research International 78(2007)12, 847-854

Ulbricht, A.; Bergner, F.; Böhmert, J.; Valo, M.; Mathon, M.-H.; Heinemann, A.
SANS response of VVER440-type weld material after neutron irradiation, post-irradiation annealing and reirradiation
Philosophical Magazine 87(2007)12, 1855-1870

Vaibar, R.; Sühnel, T.; Da Silva, M. J.
Buoyancy driven turbulent flow and experimental validation at the VeMix test facility
Applied and Computational Mechanics 1(2007), 677-684

Vogel, M.
Wächter im Rohr
Physik Journal 6(2007)10, 14-15

Wagner, E.; Rindelhardt, U.
Stromgewinnung aus regenerativer Wasserkraft in Deutschland – Überblick
EW : Das Magazin für die Energiewirtschaft 106(2007)25-26, 52-57

Weier, T.; Eckert, K.; Mühlenhoff, S.; Cierpka, C.; Bund, A.; Uhlemann, M.
Confinement of paramagnetic ions under magnetic field influence: Lorentz- versus concentration gradient force based explanations
Electrochemistry Communications 9(2007), 2479-2483

Weier, T.; Shatrov, V.; Gerbeth, G.
Flow control and propulsion in weak conductors
Magnetohydrodynamics - Historical Evolution and Trends (2007), 295-312

Wuestenberg, E.; Hampel, U.; Schleicher, E.; Huettenbrink, K.; Zahnert, T.
Bilateral nasal remission spectroscopy allows the side separated continuous measurement of changes in swelling of the nasal mucosa
HNO 55(2007)4, 254-257

Zaruba, A.; Lucas, D.; Prasser, H.-M.; Höhne, T.
Bubble-wall interactions in a vertical gas-liquid flow: bouncing, sliding and bubble deformations
Chemical Engineering Science 62(2007), 1591-1605

Zhang, C.; Eckert, S.; Gerbeth, G.
The flow structure of a bubble-driven liquid metal jet in a horizontal magnetic field
Journal of Fluid Mechanics 575(2007), 57-82

Zhang, C.; Eckert, S.; Gerbeth, G.
Modification of bubble-driven liquid metal flows under the influence of a DC magnetic field
ISIJ International 47(2007)6, 795-801

Znojil, M.; Günther, U.
Dynamics of charged fluids and 1/l perturbation expansions
Journal of Physics A 40(2007), 7375-7388

Conference contributions and other oral presentations

Al Issa, S.; Beyer, M.; Prasser, H.-M.; Frank, T.
Reconstruction of the 3D velocity field of the two-phase bubbly flow around a half moon obstacle using wire-mesh sensor data
International Conference on Multiphase Flow, ICMF 2007, 09.-13.07.2007, Leipzig, Germany

Albrecht, T.; Metzkes, H.; Mutschke, G.; Grundmann, R.; Gerbeth, G.
Tollmien-Schlichting wave cancellation using an oscillating Lorentz force
ETC11 - EUROMECH European Turbulence Conference, 25.-28.06.2007, Porto, Portugal

Albrecht, T.; Metzkes, H.; Mutschke, G.; Grundmann, R.; Gerbeth, G.
Tollmien-Schlichting wave cancellation using an oscillating Lorentz force
5th International Symposium on Turbulence and Shear Flow Phenomena, 27.-29.08.2007, München, Germany

Azzopardi, B. J.; Omebere-Iyari, N. K.; Lucas, D.; Beyer, M.; Prasser, H.-M.
The characteristics of gas/liquid flow in large risers at high pressures
International Conference on Multiphase Flow, ICMF 2007, 09.-13.07.2007, Leipzig, Germany

Becker, G.; Rehm, W.; Kumerle, G.; Bächler, M.; Rindelhardt, U.
Comparing long term operation experience of large PV-systems
22. European Photovoltaic Solar Energy Conference, 03.-07.09.2007, Milano, Italy

Beckert, C.; Grundmann, U.
Development and verification of a multigroup SP3 method for reactor calculations
Annual meeting on nuclear technology 2007, 22.-24.05.2007, Karlsruhe, Germany

Beckert, C.; Grundmann, U.
A nodal expansion method for solving the multigroup SP3 equations in the reactor code DYN3D
M&C+SNA 2007 - Joint International Topical Meeting on Mathematics & Computations and Supercomputing in Nuclear Applications, 15.-19.04.2007, Monterey, United States

Beckert, C.; Grundmann, U.; Mittag, S.
Multigroup diffusion and SP3 solutions for a PWR MOX/UO2 benchmark with the code DYN3D
2007 ANS/ENS International Meeting, 11.-15.11.2007, Washington D.C., United States

Bergner, F.; Al Mazouzi, A.; Hernandez-Mayoral, M.; Ulbricht, A.
Combined TEM, PAS and SANS investigation of neutron-irradiated pure iron
Workshop on Structural Materials for Innovative Nuclear Systems (SMINS), 04.-06.06.2007, Karlsruhe, Germany

Bestion, D.; Anglart, H.; Peturaud, P.; Smith, B.; Krepper, E.; Moretti, F.; Macek, J.
Review of available data for validation of NURESIM two-phase CFD software applied to CHF investigations
NURETH-12 - International Topical Meeting on Nuclear Reactor Thermal Hydraulics, 30.09.-04.10.2007, Pittsburgh, USA

Bieberle, A.; Hampel, U.
Gamma ray computed tomography for fast rotating objects
5th World Congress on Industrial Process Tomography, 03.-06.09.07, Bergen, Norway

Bieberle, A.; Kronenberg, J.
A high-resolution gamma tomograph for void fraction distribution measurements in fuel element bundles
15th International Conference on Nuclear Engineering (ICONE15), 22.-26.04.07, Nagoya, Japan

Bieberle, A.; Schleicher, E.; Hampel, U.
Gamma ray CT – system for multiphase flow imaging
International Conference on Multiphase Flow 2007, 09.-13.07.07, Leipzig, Germany

Bieberle, M.; Hampel, U.
Image reconstruction for fast X-ray computed tomography of multiphase flows
International Conference on Multiphase Flow, ICMF 2007, 09.-13.07.2007, Leipzig, Germany

Bieberle, M.; Hampel, U.; Prasser, H.-M.; Schleicher, E.
Simulation study on multilayer limited angle scanned electron beam X-ray CT arrangements for two-phase flow measurements
5th World Congress on Industrial Process Tomography (WCIPT5), 03.09.2007, Bergen, Norway

Bieberle, M.; Schleicher, E.; Fischer, F.; Hampel, U.; Do Couto Aktay, K. S.; Koch, D.; Menz, H.-J.; Mayer, H.-G.
Ultra fast electron beam X-ray CT for two-phase flow measurements
Jahrestagung Kerntechnik 2007, 22.-24.05.2007, Karlsruhe, Germany

Biswas, K.; Hermann, R.; Gerbeth, G.; Priede, J.
Effect of electromagnetic stirring on microstructure evolution and mechanical properties of peritectic Ti-Al alloy
5th Decennial International Conference on Solidification Processing - SP07, 23.-25.07.2007, Sheffield, United Kingdom

Boden, S.; Eckert, S.; Willers, B.; Gerbeth, G.
Determination of the flow field in the vicinity of a solidification front by X ray radioscopy
2nd International Workshop on Measuring Techniques for Liquid Metal Flows (MTLM2007), 23.-25.04.2007, Dresden, Deutschland

Boden, S.; Willers, B.; Eckert, S.; Gerbeth, G.
Visualisation of the concentration distribution and the flow field in solidifying metallic melts by means of X-ray radioscopy
5th Decennial International Conference on Solidification Processing, 23.-25.07.2007, Sheffield, UK

Bund, A.; Ispas, A.; Mutschke, G.
Magnetic field effects on electrochemical metal depositions
International Conference on Magneto-Science ICMS2007, 11.-15.11.2007, Hiroshima, Japan

Cramer, A.; Eckert, S.; Gerbeth, G.
Measurement techniques for liquid metal flows
AMPERE meeting, 10.-11.07.2007, Paris, France

Cramer, A.; Priede, J.; Galindo, V.; Gerbeth, G.; Andersen, O.; Kostmann, C.
Heating of the edge of a metal sheet in the container-less melt extraction of fibres
HES-07 International Symposium on Heating by Electromagnetic Sources, 20.-22.06.2007, Padua, Italy

Da Silva, M. J.; Hampel, U.
Tomography applied to multiphase flow measurement
Workshop on Emerging Sensing Technologies for E&P, 07.-09.08.2007, Rio de Janeiro, Brazil

Da Silva, M. J.; Schleicher, E.; Hampel, U.
Capacitance wire-mesh tomograph for multiphase flow applications
5th World Congress on Industrial Process Tomography, 03.-06.09.2007, Bergen, Norway

Da Silva, M. J.; Schleicher, E.; Hampel, U.
A new wire-mesh tomograph for multiphase flow measurement
Multi-Phase Flow: Simulation, Experiment and Application, 25.-27.04.2007, Dresden, Germany

Da Silva, M. J.; Schleicher, E.; Hampel, U.
Novel wire-mesh sensor for the investigation of non-conducting fluids
International Conference on Multiphase Flow, ICMF 2007, 09.-13.07.2007, Leipzig, Germany

Eckert, S.; Boden, S.; Galindo, V.; Gerbeth, G.; Stefani, F.; Willers, B.
Neue Möglichkeiten der Modellierung und Beeinflussung der Strömungsverhältnisse in Gießprozessen
VDG-Seminar "Technologie des Feingießens - Innovation durch fundiertes Wissen", 23.-24.05.2007, Bad Dürkheim, Deutschland

Eckert, S.; Nikrityuk, Petr A.; Willers, B.; Räbiger, D.; Eckert, K.; Gerbeth, G.
Prospective profit by using modulated magnetic fields during unidirectional solidification of metal alloys
3rd Sino-German Workshop 2007, 16.-19.10.2007, Shanghai, China

Eckert, S.; Zhang, C.; Gundrum, T.; Gerbeth, G.
Application of the Ultrasonic Doppler Method in liquid metal flows: examples and perspectives
2nd International Workshop on Measuring Techniques for Liquid Metal Flows (MTLM2007), 23.-25.04.2007, Dresden, Deutschland

Frank, T.; Lifante, C.; Krepper, E.
Practical calculation of bubble column flow with CFX-11
5th Joint FZD & ANSYS Workshop & Short Course on Multiphase Flows: Simulation, Experiment & Application, 25.-27.04.2007, Dresden, Germany

Frank, T.; Prasser, H.-M.; Beyer, M.; Al Issa, S.
Gas-liquid flow around an obstacle in a vertical pipe – CFD simulation & comparison to experimental data
International Conference on Multiphase Flow, ICMF 2007, 09.-13.07.2007, Leipzig, Germany

Gailitis, A.; Lielausis, O.; Platacis, E.; Gerbeth, G.; Stefani, F.
Current status of Riga dynamo experiment
MHD Laboratory Experiments for Geophysics and Astrophysics, 01.-03.10.2007, Catania, Italy

Galindo, V.; Grants, I.; Lantzsch, R.; Pätzold, O.; Gerbeth, G.; Zhang, C.
Flüssigmetallströmung unter dem Einfluß eines elektromagnetischen Wanderfeldes bei der Kristallzüchtung nach der VGF-Methode - Numerische Simulation und Modell-Experimente -
Workshop Strömungssimulation, 30.11.2007, Dresden, Germany

Gerbeth, G.; Eckert, S.; Galindo, V.; Willers, B.
The use of cold liquid metal modeling exemplified at the magnetic field control of the aluminum investment casting
3rd Sino-German Workshop 2007, 15.-19.10.2007, Shanghai, China

Gerbeth, G.; Grants, I.; Gundrum, T.; Stefani, F.
Liquid Metal Magnetohydrodynamics – astrophysical relevance and engineering applications
Fifth International Conference on Fluid Mechanics, 15.-19.08.2007, Shanghai, China

Gerbeth, G.; Gundrum, Th.; Stefani, F.; Hollerbach, R.; Rüdiger, G.
Experimental results on magnetorotational instability
Julius Hartmann Meeting, 15.-16.02.2007, Coventry, UK

Gerbeth, G.; Shatrov, V.
On magnetohydrodynamic drag reduction and flow control behind a body
6th International Congress on Andustrial and Applied Mathematics (ICIAM 07), 16.-20.07.2007, Zurich, Switzerland

Giesecke, A.; Stefani, F.
Numerical simulations of the onset of dynamo action with a hybrid finite volume/ boundary element method (FV-BEM)
10th MHD Days, 26.-29.11.2007, Garching, Germany

Gokhman, A.; Bergner, F.; Ulbricht, A.; Birkenheuer, U.
Cluster dynamics simulation of reactor pressure vessel steels under irradiation
4th International Workshop "Diffusion and Diffusional Phase Transformations in Alloys" DIFTRANS-2007, 16.-21.07.2007, Sofiyivka (Uman), Cherkasy region, Ukraine

Gundrum, T.; Gerbeth, G.; Stefani, F.; Rüdiger, G.; Szklarski, J.; Hollerbach, R.
Helical magnetorotational instability in a liquid metal Taylor-Couette experiment
15th International Couette-Taylor Workshop, 09.-12.07.2007, Le Havres, France

Günther, U.; Kirillov, O.; Stefani, F.
The spherically symmetric α^2-dynamo, resonant unfolding of diabolical points and third-order exceptional points in Krein space related setups
Analytic and algebraic methods in physics., 20.02.2007, Prague, Czech Republic

Günther, U.; Rotter, I.; Samsonov, B.
On projective Hilbert space structures at exceptional points
Many-body open quantum systems: From atomic nuclei to quantum dots, 14.-18.05.2007, Trento, Italy

Günther, U.; Rotter, I.; Samsonov, B.
Projective Hilbert space structures at exceptional points and their extension to line bundles over spectral Riemann surfaces
Analytic and algebraic methods III, 19.06.2007, Prague, Czech Republic

Günther, U.; Rotter, I.; Samsonov, B.
Projective Hilbert space structures at exceptional points and Krein space related boost deformations of Bloch spheres
7th Workshop Operator Theory in Krein Spaces and Spectral Analysis, 13.-16.12.2007, Berlin, Germany

Günther, U.; Samsonov, B.
Projective Hilbert space structures near exceptional points and the quantum brachistochrone
6th International Workshop on Pseudo-Hermitian Hamiltonians in Quantum Physics, 16.- 18.07.2007, London, United Kingdom

Günther, U.; Stefani, F.; Znojil, M.
PT-symmetric quantum mechanics, the hydrodynamic Squire equation and UV-IR-duality
International conference "Modern Analysis and Applications (MAA 2007)" dedicated to the centenary of Mark Krein, 09.-14.04.2007, Odessa, Ukraine

Hampel, U.
Measurement techniques and experimental investigations for multiphase flows
Multi-Phase Flows: Simulation, Experiment and Application, 25.-27.04.2007, Dresden, Germany

Hampel, U.
Röntgen- und Gamma-Tomographie in der Technik
Lehrerfortbildung 2007, 16.2.2007, Dresden, Germany

Hampel, U.
Tomographie von Mehrphasenströmungen
Sommerschule des Graduiertenkollegs PoreNet, 18.7.2007, Dresden, Germany

Hampel, U.; Bieberle, A.; Schleicher, E.; Hoppe, D.; Zippe, C.
Industrial application of gamma ray CT
International Conference on Multiphase Flow ICMF 2007, 09.-13.07.2007, Leipzig, Germany

Hampel, U.; Bieberle, A.; Schleicher, E.; Zippe, C.; Hoppe, D.
High resolution gamma ray tomography of a rotating hydrodynamic coupling
5th World Congress on Industrial Process Tomography (WCIPT5), 03.-06.09.2007, Bergen, Norway

Höhne, T.
CFD-simulation of thermal hydraulic benchmark V1000CT–2 using ANSYS CFX
15th International Conference on Nuclear Engineering (ICONE15), 22.04.2007, Nagoya, Japan

Höhne, T.
CFD studies on boron dilution scenarios in VVER type reactors - use of best practice guidelines
COVERS/ WP3 Training, 09.10.2007, Dresden-Rossendorf, Germany

Höhne, T.; Kliem, S.
Simulation von Vermischungsvorgängen
Workshop Strömungssimulation, 30.11.2007, Dresden, Germany

Höhne, T.; Krepper, E.; Weiss, F. P.; Stosic, Z.; Salnikova, T.
CFD application in nuclear engineering/industry
15th International Conference on Nuclear Engineering, 22.-26.04.2007, Nagoya, Japan

Höhne, T.; Rohde, U.; Melideo, D.; Moretti, F.; D'Auria, F.; Shishov, A.; Lisenkov, E.
Pre-test CFD simulations of Gidropress mixing facility experiments using ANSYS CFX
17th Symposium of AER on VVER Reactor Physics and Reactor Safety, 24.-29.09.2007, Yalta, Ukraine

Höhne, T.; Vallee, C.
Benchmark proposal for stratified horizontal two-phase flow phenomena
German CFD Network, 9th Meeting,, 25.-26.01.2007, Köln, Deutschland

Höhne, T.; Vallee, C.
Experimental and numerical prediction of horizontal stratified flows using the HAWAC facility
ANSYS Conference & 25th CADFEM Users' Meeting, 21.-23.11.2007, Dresden, Germany

Höhne, T.; Vallee, C.
Experimente und CFD Simulationen zu geschichteten Strömungen in horizontalen Kanälen
Fachsitzung Anwendung von CFD-Methoden in der Reaktorsicherheit, Jahrestagung Kerntechnik, 22.-24.05.2007, Karlsruhe, Germany

Höhne, T.; Vallee, C.; Prasser, H.-M.
Experimental and numerical prediction of horizontal stratified flows
International Conference on Multiphase Flow ICMF 2007, 09.07.2007, Leipzig, Germany

Kirillov, O.; Günther, U.
Asymptotic methods for spherically symmetric MHD α^2-dynamos
6th International Congress on Industrial and Applied Mathematics (iciam 07), 16.-20.07.2007, Zürich, Switzerland

Kliem, S.
AER working group D on VVER safety analysis – report of the 2007 meeting
17th Symposium of AER on VVER Reactor Physics and Reactor Safety, 24.-29.09.2007, Yalta, Ukraine

Kliem, S.
Analyse von Borverdünnungstransienten in Druckwasserreaktoren
Seminar für Energieverfahrenstechnik, 18.12.2007, Dresden, Germany

Kliem, S.; Bousbia Salah, A.; Rohde, U.; D'Auria, F.
Application of the SUSA and CIAU methods to the calculation of a NPP start-up experiment using a coupled code system
First Workshop on OECD Benchmark for Uncertainty Analysis Modeling, 10.-11.05.2007, Paris, France

Kliem, S.; Hemström, B.; Bezrukov, Y.; Höhne, T.; Rohde, U.
Comparative evaluation of coolant mixing experiments at the ROCOM, Vattenfall, and Gidropress test facilities
Annual Meeting of the AER Working Group D, 08.-09.05.2007, Paris, France

Kliem, S.; Höhne, T.; Rohde, U.; Kozmenkov, Y.
DYN3D/ATHLET and ANSYS CFX calculations of the OECD VVER-1000 coolant transient benchmark
5th International conference on safety assurance of NPP with WWER, 29.05.-01.06.2007, Podolsk, Russia

Kliem, S.; Kozmenkov, Y.; Höhne, T.; Rohde, U.
DYN3D/ATHLET calculations of exercise 2 – influence of coolant mixing on the power behaviour
V1000CT5 Workshop, 07.05.2007, Paris, France

Kliem, S.; Rohde, U.
Boron dilution analyses at reactor shutdown conditions using the coupled code DYN3D/ATHLET
Annual Meeting on Nuclear Technology 2007, 22.-24.05.2007, Karlsruhe, Germany

Kliem, S.; Rohde, U.
DYN3D/ATHLET calculations of a boron dilution transient during natural circulation conditions
NURETH-12 - International Topical Meeting on Nuclear Reactor Thermal Hydraulics, 30.09.-04.10.2007, Pittsburgh, United States

Kliem, S.; Rohde, U.
Second dynamic AER benchmark – comparison of results
Annual Meeting of the AER Working Group D, 08.-09.05.2007, Paris, France

Konheiser, J.; Viehrig, H.-W.; Rindelhardt, U.; Noack, K.; Gleisberg, B.
Greifswald VVER-440 RPV investigations: neutron dosimetry and material tests
5th International Conference: Safety Assurance of NPP with WWER, 29.05.-01.06.2007, Podolsk, Russia

Krepper, E.; Cartland-Glover, G.; Grahn, A.; Weiß, F.-P.; Alt, S.; Hampel, R.; Kästner, W.; Seeliger, A.
CFD-modelling of mineral wool in the containment sump
Annual Meeting on Nuclear Technology 2007, 22.-24.05.2007, Karlsruhe, Germany

Krepper, E.; Cartland-Glover, G.; Grahn, A.; Weiss, F.-P.; Alt, S.; Hampel, R.; Kästner, W.; Seeliger, A.
CFD-modelling of insulation debris transport phenomena in water flow
NURETH-12 - International Topical Meeting on Nuclear Reactor Thermal Hydraulics, 30.09.-04.12.2007, Pittsburgh, USA

Krepper, E.; Frank, T.; Lucas, D.; Prasser, H.-M.; Zwart, P. J.
Inhomogeneous MUSIG model – a population balance approach for polydispersed bubbly flows
International Conference on Multiphase Flow - ICMF 2007, 09.-13.07.2007, Leipzig, Germany

Krepper, E.; Frank, T.; Lucas, D.; Prasser, H.-M.; Zwart, Philip J.
Inhomogeneous MUSIG model – a population balance approach for polydispersed bubbly flows
NURETH-12 - International Topical Meeting on Nuclear Reactor Thermal Hydraulics, 30.09.-04.10.2007, Pittsburgh, USA

Krepper, E.; Lucas, D.; Prasser, H.-M.; Beyer, M.; Frank, T.
CFD simulation of the two-phase flow around an obstacle applying an inhomogeneous multiple bubble size class approach
5th Joint FZD & ANSYS Workshop & Short Course on Multiphase Flows: Simulation, Experiment & Application, 25.-27.04.2007, Dresden, Germany

Krepper, E.; Scheuerer, G.
Interfacial heat and mass tansfer models
5th Joint FZD & ANSYS Workshop & Short Course on Multiphase Flows: Simulation, Experiment & Application, 25.04.2007, Dresden, Germany

Laczkó, G.
Investigation of the radial ionisation distribution of heavy ions with an optical particle track chamber and Monte-Carlo simulation
Institutskolloquium bei der Physikalisch-Technischen Bundesanstalt, 24.05.2007, Braunschweig, Germany

Lantzsch, R.; Grants, I.; Pätzold, O.; Stelter, M.; Gerbeth, G.
Vertical gradient freeze growth with external magnetic fields
The 15th International Conference on Crystal Growth, 11.-17.08.2007, Salt Lake City, Utah, USA

Lenz, M.; Czarske, J.; Eckert, S.; Gerbeth, G.
Ultrasound velocimeter with frequency modulated signals for 2d2c measurements of non-stationary flows with high temporal resolution
2nd International Workshop on Measurement Techniques for Liquid Metal Flows (MTLM2007), 23.-25.04.2007, Dresden, Deutschland

Linse, T.; Kuna, M.; Schuhknecht, J.; Viehrig, H.-W.
Application of the small-punch-test to irradiated reactor vessel steels in the brittle-ductile transition region
ASTM E10 Fifth Symposium on Small Specimen Test Techniques, 31.01.-01.02.2007, Anaheim, USA

Lucas, D.
Modellentwicklung und Validierung von CFD-Codes für Mehrphasenströmungen
Workshop Strömungssimulation, 29.06.2007, Dresden, Germany

Lucas, D.; Bestion, D.; Bodèle, E.; Scheuerer, M.; F. D'Auria, D. Mazzini; Smith, B.; Tiselj, I.; Martin, A.; Lakehal, D.; Seynhaeve, J.-M.; Kyrki-Rajamäki, R.; Ilvonen, M.; Macek, J.
On the simulation of two-phase flow pressurized thermal shock (PTS)
NURETH-12 - International Topical Meeting on Nuclear Reactor Thermal Hydraulics, 30.09.-04.10.2007, Pittsburgh, Pennsylvania, United States

Lucas, D.; Krepper, E.; Prasser, H.-M.; Manera, A.
Stability effect of the lateral lift force in bubbly flows
International Conference on Multiphase Flow - ICMF 2007, 09.-13.07.2007, Leipzig, Germany

Lucas, D.; Prasser, H.-M.; Krepper, E.; Beyer, M.
Experiments and simulation on bubbly flow in a complex 3D flow field
45th European Two-Phase Flow Group Meeting, 22.-25.05.2007, Toulouse, France

Manera, A.; Ozar, B.; Paranjape, S.; Ishii, M.; Prasser, H.-M.
Comparison between wire-mesh sensors and conductive needle-probes for measurements of two-phase flow parameters
15th International Conference on Nuclear Engineering (ICONE15), 22.-26.04.2007, Nagoya, Japan

Merk, B.
Consequences of different fuel cycle options on the produced plutonium mass in the German reactor park
Jahrestagung Kerntechnik 2007, 22.-24.05.07, Karlsruhe, Germany

Merk, B.
An analytical solution for a simple time dependent neutron transport problem with external source
20th International Conference on Transport Theory, 22.-28.07.07, Obninsk, Russia

Merk, B.; Koch, R.
On the effect of discretisation in HELIOS 1.9
Studsvik 2007 UGM, 31.05.-01.06.2007, West Palm Beach, United States

Moretti, F.; Melideo, D.; D'Auria, F.; Höhne, T.; Kliem, S.
CFX simulations of ROCOM slug mixing experiments
15th International Conference on Nuclear Engineering (ICONE15), 22.-26.04.2007, Nagoya, Japan

Mutschke, G.
Numerische Simulationen zur elektrolytischen Kupferabscheidung in externen Magnetfeldern
Workshop Strömungssimulation, 29.06.2007, Dresden, Germany

Mutschke, G.; Gerbeth, G.; Bund, A.
The role of magnetic forces in electrochemical reactions - numerics and experiments
58th Annual Meeting of the International Society of Electrochemistry, 09.-14.09.2007, Banff, Canada

Mutschke, G.; Weier, T.; Albrecht, T.; Gerbeth, G.; Grundmann, R.
Electromagnetic control of separation at hydrofoils
IUTAM Symposium on Unsteady Separated Flows and their Control, 18.-22.06.2007, Kerkyra (Corfu), Greece

Noack, B. R.; Schlegel, M.; Ahlborn, B.; Mutschke, G.; Morzynski, M.; Compte, P.; Tadmor, G.
A finite-time thermodynamics of unsteady shear flows
60th Annual Meeting of the Divison of Fluid Dynamics, 18.-20.11.2007, Salt Lake City, Utah, USA

Noack, B. R.; Schlegel, M.; Ahlborn, B.; Mutschke, G.; Morzynski, M.; Comte, P.
A finite-time thermodynamics of unsteady flows - from the onset of vortex shedding to developed homogeneous turbulence
Joint European Thermodynamics Conference IX, 12.-15.06.2007, Saint Entienne, France

119

Noack, K.
The GDT-based fusion neutron source as driver of minor actinide burners
Institutsseminar, 24.08.2007, Uppsala, Sweden

Pedchenko, A.; Bojarevics, A.; Priede, J.; Gerbeth, G.; Hermann, R.
Numerical and experimental study of a two-phase cylindrical stirrer
3rd Sino-German Workshop on Electromagnetic Processing of Materials, 15.-19.10.2007, Shanghai, China

Plevachuk, Yu.; Sklyarchuk, V.; Eckert, S.; Gerbeth, G.
New measurements of physical properties of PbBi alloys
IV International Workshop on Materials for HLM cooled Reactors and Related Technologies, 21.-23.05.2007, Rom, Italy

Plevachuk, Yu.; Sklyarchuk, V.; Yakymovych, A.; Gerbeth, G.; Eckert, S.
Microsegregation in liquid Pb-based eutectics
4th International Workshop on Functional and Nanostructured Materials, 01.-06.09.2007, Gdansk, Poland

Prasser, H.-M.; Beyer, M.
Bubble recognition algorithms for the processing of wire-mesh sensor data
International Conference on Multiphase flow, ICMF 2007, 09.-13.07.2007, Leipzig, Germany

Prasser, H.-M.; Frank, T.; Höhne, T.; Lucas, D.
CFD Modellierung in der Sicherheitstechnik - Möglichkeiten und Grenzen
ProcessNet-Jahrestagung 2007, 16.-18.10.2007, Aachen, Deutschland

Priede, J.; Gerbeth, G.
Absolute versus convective helical magnetorotational instability in a Taylor-Couette flow
MHD Laboratory Experiments for Geophysics and Astrophysics, 01.-03.10.2007, Catania, Italy

Rindelhardt, U.
Kernenergie im 21. Jahrhundert - Herausforderungen und Möglichkeiten
VDE-Informationsveranstaltung, 18.04.2007, Chemnitz, Deutschland

Rindelhardt, U.
FZD research activities for VVER NPPs
Best Practice Seminar COVERS, 20.-22.06.2007, Madrid, Spain

Rindelhardt, U.; Bodach, M.
Operational experiences with megawatt PV plants in central Germany
22. European Photovoltaic Solar Energy Conference, 03.-07.09.2007, Milano, Italy

Rindelhardt, U.; Viehrig, H.-W.; Konheiser, J.; Noack, K.; Gleisberg, B.
RPV material investigations of the former VVER-440 Greifswald NPP
15th International Conference on Nuclear Energy (ICONE15), 22.-26.04.2006, Nagoya, Japan

Roelofs, F.; Class, A.; Jeanmart, H.; Ciampichetti, A.; Gerbeth, G.; Fazio, C.
European research on thermal hydraulics for heavy liquid metal ADS applications
ENC 2007 - European Nuclear Conference, 16.-19.09.2007, Brussels, Belgium

Roelofs, F.; Jager, B.; Class, A.; Jeanmart, H.; Schuurmans, P.; Ciampichetti, A.; Gerbeth, G.; Stieglitz, R.; Fazio, C.
European research on HLM thermal hydraulics for ADS applications
IV International Workshop on Materials for HLM cooled Reactors and Related Technologies, 21.-23.05.2007, Rom, Italy

Ruyer, P.; Seiler, N.; Beyer, M.; Weiß, F.-P.
Application of the moment-density method in CFD code to model bubble size distribution
European Two-Phase Flow Group Meeting 2007, 29.-31.05.2007, Toulouse, France

Ruyer, P.; Seiler, N.; Beyer, M.; Weiss, F.-P.
A bubble size distribution model for the numerical simulation of bubbly flows
International Conference on Multiphase Flow, ICMF 2007, 09.-13.07.2007, Leipzig, Germany

Samsonov, B.; Günther, U.
Non-Hermitian dynamics and a Hilbert space "relativity principle"
6th International Workshop on Pseudo-Hermitian Hamiltonians in Quantum Physics, 16.-18.07.2007, London, United Kingdom

Schleicher, E.; Da Silva, M. J.; Paul, S.; Hampel, U.
HF-Modulationsspektroskopie zur Bestimmung optischer Parameter in trüben Medien
8. Dresdner Sensor-Symposium, 11.12.2007, Dresden, Germany

Schleicher, E.; Hampel, U.; Da Silva, M. J.; Thiele, S.
Fast optical tomography for transient process diagnostics
5th World Congress on Industrial Process Tomography, 03.-06.09.2007, Bergen, Norway

Sklyarchuk, V.; Plevachuk, Yu.; Gerbeth, G.; Eckert, S.
Melting-solidification process in Pb-Bi melts
XIII International Seminar on Physics and Chemistry of Solids, 10.-13.06.2007, Ustron, Poland

Skorupa, W.; Rossner, M.; Neelmeijer, C.; Eichhorn, F.; von Borany, J.; Werner, H.; Eule, A.-C.; Schucknecht, T.; Klemm, V.; Rafaja, D.
A new casting technique for the restoration of lead pipes in old organs
E-MRS 2007 Spring Meeting, Workshop: Science & Technology of Cultural heritage Materials : Art conservation and Restoration, 28.05.-01.06.2007, Strasbourg, France

Sorriso-Valvo, L.; Carbone, V.; Stefani, F.; Bourgoin, M.
Statistical properites and clustering of dynamo reversals observed from paleomagnetic records, experimental dynamo, numerical simulations and simplified models
AGU Fall Meeting, 10.-14.12.2007, San Francisco, USA

Stefani, F.
Wie entsteht das Magnetfeld der Erde?
Abschlusskolloquium der Forschergruppe "Magnetofluiddynamik", 31.05.-01.06.2007, Ilmenau, Deutschland

Stefani, F.
Hydromagnetische Dynamos in und auf der Erde
Geophysikalisches Kolloquium, 12.06.2007, Münster, Deutschland

Stefani, F.
Dynamoeffekt und Magnetorotationsinstabilität: Kosmische Magnetfelder im Laborexperiment
Lehrstuhlseminar Magnetofluiddynamik, TU Dresden, 05.12.2007, Dresden, Germany

Stefani, F.
Das Alpha und das Omega experimenteller Dynamos
Ehrenkolloquium zum 80. Geburtstag von Professor Fritz Krause, 05.06.2007, Potsdam, Deutschland

Stefani, F.; Gerbeth, G.
What to expect from next generation liquid metal experiments on dynamo action and magnetorotational instability?
Experimental dynamo meeting, 22.-23.01.2007, Paris, France

Stefani, F.; Gerbeth, G.; Gundrum, T.; Rüdiger, G.; Szklarski, J.; Hollerbach, R.
Results of the PROMISE experiment on helical magnetorotational instability
MHD Laboratory Experiments for Geophysics and Astrophysics, 01.-03.10.2007, Catania, Italy

Stefani, F.; Gerbeth, G.; Günther, U.; Xu, M.; Sorriso-Valvo, L.
An elementary model of Earth's magnetic field reversals
LGIT Research Seminar, 22.03.2007, Grenoble, France

Stefani, F.; Gerbeth, G.; Günther, U.; Xu, M.; Sorriso-Valvo, L.
Noise induced relaxation oscillations and earth's magnetic field reversals
XXIV IUGG General Assembly, 02.-13.07.2007, Perugia, Italy

Stefani, F.; Gundrum, T.; Gerbeth, G.; Rüdiger, G.; Szklarski, J.; Hollerbach, R.
Experimental results on the magnetorotational instability in helical magnetic fields
49th Annual Meeting of the Division of Plasma Physics, 12.-16.11.2007, Orlando, USA

Vaibar, R.; Sühnel, T.
Buoyancy driven flow in the VeMix test facility
Seminar on Numerical Analysis and Tutorial - SNA'07, 22.-26.01.2007, Ostrava, Czech Republic

Vallee, C.
Hydraulic jump in a closed horizontal two-phase flow channel
International Conference on Multiphase Flow 2007, 09.-13.07.2007, Leipzig, Germany

Vallee, C.
Experiments on the interface dynamics of stratified air/water flows
Jahrestagung Kerntechnik 2007, 22.-24.05.2007, Karlsruhe, Germany

Vallee, C.; Deendarlianto,.; Lucas, D.; Beyer, M.; Pietruske, H.
Air/water flow experiments in the hot leg model of the TOPFLOW facility
10th Meeting of the German CFD Network, 17.-18.09.2007, Garching, Germany

Vallee, C.; Höhne, T.
Experimental investigation and CFD validation of horizontal air/water slug flow
15th International Conference on Nuclear Engineering (ICONE15), 22.-26.04.2007, Nagoya, Japan

Viehrig, H.-W.; Rindelhardt, U.; Schuhknecht, J.
Post mortem investigations of the NPP Greifswald WWER-440 reactor pressure vessels
19th International Conference on Structural Mechanics in Reactor Technology (SMiRT-19), 12.-17.08.2007, Toronto, Canada

Weier, T.; Cierpka, C.; Gerbeth, G.
Coherent structure eduction from PIV data of an electromagnetically forced separated flow
IUTAM Symposium on Unsteady Separated Flows and Their Control, 18.-22.06.2007, Korfu, Greece

Weier, T.; Cierpka, C.; Gerbeth, G.
Vortex structures in the separated flow on an inclined flat plate under electromagnetic forcing: influences of excitation wave form, frequency, and amplitude
5th International Symposium on Turbulence and Shear Flow Phenomena, 27.-29.08.2007, München, Germany

Weier, T.; Cierpka, C.; Shatrov, V.; Mutschke, G.; Gerbeth, G.
Electromagnetic flow control in weakly conducting fluids
6th International Congress on Industrial and Applied Mathematics (ICIAM 07), 16.-20.07.2007, Zürich, Switzerland

Weiss, F.-P.; Alt, S.; Cartland-Glover, G.; Grahn, A.; Hampel, R.; Kästner, W.; Krepper, E.; Seeliger, A.
Investigation of the behaviour of mineral wool in the reactor sump
Quadripartite Meeting on Sump Screen Blockage, 17.-18.10.2007, Erlangen, Germany

Willers, B.; Dong, J.; Metan, V.; Smieja, F.; Eckert, S.; Eigenfeld, K.
The influence of alternating magnetic fields on structure formation in Al-Si alloys during solidification
5th Decennial International Conference on Solidification Processing, 23.-25.07.2007, Sheffield, United Kingdom

Willers, B.; Räbiger, D.; Dong, J.; Eckert, S.; Nikrityuk, P. A.; Eckert, K.
Melt stirring during directional solidification using modulated magnetic fields
EUROMAT2007 - European Congress on Advanced Materials and Processes, 10.-13.09.2007, Nürnberg, Germany

Willschütz, H.-G.; Weiß, F.-P.
Sicherheit von Kernkraftwerken - Beiträge des Forschungszentrums Dresden-Rossendorf
Vortragsreihe des VDI, Dresdner Bezirksverein - Arbeitskreis Energietechnik, 06.02.2007, Dresden, Deutschland

Zhang, C.; Eckert, S.; Gerbeth, G.
Rising gas bubbles in a liquid metal under the influence of external magnetic fields
International Conference on Multiphase Flow - ICMF2007, 09.-13.07.2007, Leipzig, Germany

Zhang, C.; Eckert, S.; Gerbeth, G.
Velocity measurements in liquid metal two-phase flows by means of the ultrasonic Doppler method
2nd International Workshop on Measuring Techniques for Liquid Metal Flows (MTLM2007), 23.-25.04.2007, Dresden, Deutschland

Zhang, C.; Eckert, S.; Gerbeth, G.
Experimental results on the flow structure in liquid metal two-phase
International Symposium on Multi-Phase Flows: Simulation, Experiment and Application, 25.-27.04.2007, Dresden, Deutschland

Zhang, C.; Eckert, S.; Gerbeth, G.
Effect of various magnetic fields on a liquid metal bubble plume
3rd Sino-German Workshop 2007, 16.-19.10.2007, Shanghai, China

Zippe, C.; Hoppe, D.; Bieberle, A.; Hampel, U.
Concepts for a sub-millimetre resolving gamma ray CT for nondestructive testing applications
5th World Congress on Industrial Process Tomography, 03.-06.09.2007, Bergen, Norway

Zurbuchen, C.; Viehrig, H.-W.
Master Curve applicability to highly neutron irradiated reactor pressure vessel steels - results of a BMWi grant project
33. MPA-Seminar, 11.-12.10.2007, Stuttgart, Germany

Contributions to proceedings and other collected editions

Al Issa, S.; Beyer, M.; Prasser, H.-M.; Frank, T.
Reconstruction of the 3D velocity field of the two-phase bubbly flow around a half moon obstacle using wire-mesh sensor data
International Conference on Multiphase Flow, ICMF 2007, 09.-13.07.2007, Leipzig, Germany,
paper:S6_Thu_D_60

Albrecht, T.; Metzkes, H.; Mutschke, G.; Grundmann, R.; Gerbeth, G.
Tollmien-Schlichting wave cancellation using an oscillating Lorentz force
ETC11 - EUROMECH European Turbulence Conference, 25.-28.06.2007, Porto, Portugal
ADVANCES IN TURBULENCE XI. Springer Proceedings in Physics vol. 117. Proceedings of the 11th EUROMECH European Turbulence Conference, Heidelberg: Springer, 978-3-540-72603-6, 218-220

Albrecht, T.; Metzkes, H.; Mutschke, G.; Grundmann, R.; Gerbeth, G.
Tollmien-Schlichting wave cancellation using an oscillating Lorentz force
5th International Symposium on Turbulence and Shear Flow Phenomena, 27.-29.08.2007, München, Germany
Proceedings of the 5th International Symposium on Turbulence and Shear Flow Phenomena, vol. 2, 419-423

Altstadt, E.; Willschütz, H.-G.
Modelling of the Corium-RPV-Wall interaction in the frame of an in-vessel-retention scenario
Jahrestagung Kerntechnik 2007, 22.-24.05.2007, Karlsruhe, Deutschland
Beiträge zur Jahrestagung Kerntechnik 2007, Proceedings on CD-ROM, Paper 328, Berlin: INFORUM Verlags- und Verwaltungsgesellschaft mbH, 293-299

Azzopardi, B. J.; Omebere-Iyari, N. K.; Lucas, D.; Beyer, M.; Prasser, H.-M.
The characteristics of gas/liquid flow in large risers at high pressures
International Conference on Multiphase Flow, ICMF 2007, 09.-13.07.2007, Leipzig, Germany
Gas/liquid flow in large risers; paper: S6_Thu_A_47

Becker, G.; Rehm, W.; Kumerle, G.; Bächler, M.; Rindelhardt, U.
Comparing long term operation experience of large PV-systems
22. European Photovoltaic Solar Energy Conference, 03.-07.09.2007, Milano, Italy, 3-936338-22-1, 2956-2959

Beckert, C.; Grundmann, U.
Development and verification of a multigroup SP3 method for reactor calculations
Annual meeting on nuclear technology 2007, 22.-24.05.2007, Karlsruhe, Germany

Beckert, C.; Grundmann, U.
A nodal expansion method for solving the multigroup SP3 equations in the reactor code DYN3D
M&C+SNA 2007 - Joint International Topical Meeting on Mathematics & Computations and Supercomputing in Nuclear Applications, 15.-19.04.2007, Monterey, United States

Bergner, F.; Al Mazouzi, A.; Hernandez-Mayoral, M.; Ulbricht, A.
Combined TEM, PAS and SANS investigation of neutron-irradiated pure iron
Workshop on Structural Materials for Innovative Nuclear Systems (SMINS), 04.-06.06.2007, Karlsruhe, Germany
Proceedings, Le Seine Saint-Germain: OECD, Nuclear Energy Agency

Bestion, D.; Anglart, H.; Peturaud, P.; Smith, B.; Krepper, E.; Moretti, F.; Macek, J.
Review of available data for validation of NURESIM two-phase CFD software applied to CHF investigations
NURETH-12 - International Topical Meeting on Nuclear Reactor Thermal Hydraulics, 30.09.-04.10.2007, Pittsburgh, USA

Bieberle, A.; Hampel, U.
Gamma ray computed tomography for fast rotating objects
5th World Congress on Industrial Process Tomography, 03.-06.09.07, Bergen, Norway, IPS01

Bieberle, A.; Kronenberg, J.
A high-resolution gamma tomograph for void fraction distribution measurements in fuel element bundles
15th International Conference on Nuclear Engineering (ICONE15), 22.-26.04.07, Nagoya, Japan
Proceedings of the ICONE15, Paper No. ICONE15-10440

Bieberle, A.; Schleicher, E.; Hampel, U.
Gamma ray CT – system for multiphase flow imaging
International Conference on Multiphase Flow 2007, 09.-13.07.07, Leipzig, Germany
Programme and Abstracts of the 6th International conference on Multiphase Flow, S7-Thu_C55

Bieberle, M.; Hampel, U.
Image reconstruction for fast X-ray computed tomography of multiphase flows
6th International Conference on Multiphase Flow, ICMF 2007, 09.-13.07.2007, Leipzig, Germany
Proceedings of ICMF 2007

Bieberle, M.; Hampel, U.; Prasser, H.-M.; Schleicher, E.
Simulation study on multilayer limited angle scanned electron beam X-ray CT arrangements for two-phase flow measurements
5th World Congress on Industrial Process Tomography (WCIPT5), 03.-06.09.2007, Bergen, Norway
Proceedings of the 5th World Congress on Industrial Process Tomography

Bieberle, M.; Schleicher, E.; Fischer, F.; Hampel, U.; Do Couto Aktay, K. S.; Koch, D.; Menz, H.-J.; Mayer, H.-G.
Ultra fast electron beam X-ray CT for two-phase flow measurements
Jahrestagung Kerntechnik 2007, 22.-24.05.2007, Karlsruhe, Germany
Proc. Jahrestagung Kerntechnik 2007, CD-ROM plus, 27-30

Bodach, M.; Gasch, S.; Rindelhardt, U.; Hiller, W.; König, S.; Mehlich, H.
Monitoring von PV-Anlagen mittels terrestrischer Strahlungsdaten
22. Symposium Photovoltaische Solarenergie, 07.-09.03.2007, Staffelstein, Germany
Tagungsband, Beitrag 75, 978-3-934681-53-8

Boden, S.; Willers, B.; Eckert, S.; Gerbeth, G.
Visualisation of the concentration distribution and the flow field in solidifying metallic melts by means of X-ray radioscopy
5th Decennial International Conference on Solidification Processing, 23.-25.07.2007, Sheffield, UK
Proceedings of the 5th Decennial International Conference on Solidification Processing, Sheffield, 978-0-9522507-4-6, 311-315

Cierpka, C.; Weier, T.; Gerbeth, G.
Electromagnetic control of separated flows using periodic excitation with different wave forms
King, Rudibert: Active Flow Control, Notes on Numerical Fluid Mechanics and Multidisciplinary Design (NNFM), Vol. 95, Berlin: Springer, 2007, 978-3-540-71438-5, 27-41

Cramer, A.; Galindo, V.; Gerbeth, G.; Priede, J.; Bojareviecs, A.; Gelfgat, Y.; Andersen, O.; Kostmann, C.; Stephani, G.
Tailored magnetic fields in the melt extraction of metallic filaments
LMPC 2007 International Symposium on Liquid Metal Processing and Casting, 02.-05.09.2007, Nancy, France
Tailored magnetic fields in the melt extraction of metallic filaments, 305-311

Cramer, A.; Pal, J.; Zhang, Ch.; Eckert, S.; Gerbeth, G.
Experimental investigation of time-dependent flow driven by a travelling magnetic field
11th EUROMECH European Turbulence Conference, 25.-28.06.2007, Porto, Portugal
Springer Proceedings in Physics 117: Advances in Turbulence XI, Berlin: Springer, 978-3-540-72603-6, p.750

Cramer, A.; Priede, J.; Galindo, V.; Gerbeth, G.; Andersen, O.; Kostmann, C.
Heating of the edge of a metal sheet in the container-less melt extraction of fibres
HES-07 International Symposium on Heating by Electromagnetic Sources, 20.-22.06.2007, Padua, Italy, 88-89884-07-X, 445-452

Da Silva, M. J.; Hampel, U.
Tomography applied to multiphase flow measurement
Workshop on Emerging Sensing Technologies for E&P, 07.-09.08.2007, Rio de Janeiro, Brazil
Proceedings of Workshop on Emerging Sensing Technologies for E&P

Da Silva, M. J.; Schleicher, E.; Hampel, U.
Capacitance wire-mesh tomograph for multiphase flow applications
5th World Congress on Industrial Process Tomography, 03.-06.09.2007, Bergen, Norway
Proceedings of the 5th World Congress on Industrial Process Tomography: VCIPT, 978 0 85316 265 0, 624-629

Da Silva, M. J.; Schleicher, E.; Hampel, U.
A new wire-mesh tomograph for multiphase flow measurement
Multi-Phase Flow: Simulation, Experiment and Application, 25.-27.04.2007, Dresden, Germany
Proceedings of FZR & ANSYS Multiphase Flow Workshop

Da Silva, M. J.; Schleicher, E.; Hampel, U.
Novel wire-mesh sensor for the investigation of non-conducting fluids
International Conference on Multiphase Flow, ICMF 2007, 09.-13.07.2007, Leipzig, Germany
Proceedings of 6th International Conference on Multiphase Flow, paper S7_Thu_B_51, 978-3-86010-913-7

Da Silva, M. J.; Sühnel, T.; Thiele, S.; Schleicher, E.; Hampel, U.; Kernchen, R.
Electrical conductivity surface sensor for two-phase flow imaging in a hydrodynamic coupling
International Conference on Multiphase Flow, 09.-13.07.2007, Leipzig, Germany
Proceedings of 6th International Conference on Multiphase Flow, paper PS7_12, 978-3-86010-913-7

Frank, T.; Prasser, H.-M.; Beyer, M.; Al Issa, S.
Gas-liquid flow around an obstacle in a vertical pipe – CFD simulation and comparison to experimental data
International Conference on Multiphase Flow, ICMF 2007, 09.-13.07.2007, Leipzig, Germany
paper:S6_Thu_B_50

Frisani, A.; Del Nevo, A.; D'Auria, F.; Höhne, T.; Kliem, S.; Rohde, U.
Three-dimensional thermal-hydraulics analysis of ROCOM mixing experiment by RELAP5-3D© code
NURETH-12 - International Topical Meeting on Nuclear Reactor Thermal Hydraulics, 30.09.-04.10.2007, Pittsburgh, USA
CD-ROM, paper 159

Gerbeth, G.; Grants, I.; Gundrum, T.; Stefani, F.
Liquid metal magnetohydrodynamics – astrophysical relevance and engineering applications
F.G. Zhuang, J.C. Li: New Trends in Fluid Mechanics Research, Peking: Tsinghua-Springer, 2007, 690-693

Gokhman, A.; Bergner, F.; Ulbricht, A.; Birkenheuer, U.
Cluster dynamics simulation of reactor pressure vessel steels under irradiation
4th International Workshop "Diffusion and Diffusional Phase Transformations in Alloys" DIFTRANS-2007, 16.-21.07.2007, Sofiyivka (Uman), Cherkasy region, Ukraine
Proceedings of the 4th International Workshop "Diffusion and Diffusional Phase Transformations in Alloys", 75-76

Gundrum, T.; Gerbeth, G.; Stefani, F.; Rüdiger, G.; Szklarski, J.; Hollerbach, R.
Helical magnetorotational instability in a liquid metal Taylor-Couette experiment
15th International Couette-Taylor Workshop, 09.-12.07.2007, Le Havre, France
Proceedings of the 15th International Couette-Taylor Workshop, Le Havre, 266-269

Günther, U.; Zhuk, A.
Phenomenology of brane-world cosmological models
Astrophysics And Cosmology After Gamow - Theory And Observations: Gamow Memorial International Conference Dedicated To The 100th Anniversary of George Gamow, 08.-14.08.2004, Odessa, Ukraine
Astrophysics and Cosmology after Gamow: Theory and Observations, Cambridge, UK: Cambridge Scientific Publishers Ltd, UK, 978-1-904868-38-5, 79-98

Hampel, U.
Measurement techniques and experimental investigations for multiphase flows
Multi-Phase Flows: Simulation, Experiment and Application, 25.-27.04.2007, Dresden, Germany
Proceedings of Multi-Phase Flows: Simulation, Experiment and Application

Hampel, U.; Bieberle, A.; Schleicher, E.; Hessel, G.; Zippe, C.; Friedrich, H.-J.
High resolution gamma ray tomography and its application to the measurement of phase fractions in chemical reactors
Multiphase Flow - the Ultimate Measurement Challenge, 10.-13.12.2006, Macao, China
Proceedings of the 5th International Symposium on Measurement Techniques for Multiphase Flows and 2nd International Workshop on Process Tomography: American Institute of Physics, 753-759

Hampel, U.; Bieberle, A.; Schleicher, E.; Hoppe, D.; Zippe, C.
Industrial application of gamma ray CT
International Conference on Multiphase Flow ICMF 2007, 09.-13.07.2007, Leipzig, Germany
Proceedings of the International Conference on Multiphase Flow 2007, Paper No. PS/_10

Hampel, U.; Bieberle, A.; Schleicher, E.; Zippe, C.; Hoppe, D.
High resolution gamma ray tomography of a rotating hydrodynamic coupling
5th World Congress on Industrial Process Tomography (WCIPT5), 03.-06.09.2007, Bergen, Norway
Proceedings of the 5th World Congress on Industrial Process Tomography, 978 0 85316 265 0, 683-689

Hampel, U.; Fischer, F.; Mattausch, G.
Anwendung der Elektronenstrahltechnik zur ultraschnellen Tomographie von Mehrphasenströmungen
in: Jahresbericht 2006, Fraunhofer Institut für Elektronenstrahl- und Plasmatechnik, München: Fraunhofer, 2007, 57-58

Höhne, T.
CFD-simulation of thermal hydraulic benchmark V1000CT–2 using ANSYS CFX
15th International Conference on Nuclear Engineering (ICONE15), 22.-26.04.2007, Nagoya, Japan
CD-Rom, ICONE15-10259

Höhne, T.; Rohde, U.; Melideo, D.; Moretti, F.; D'Auria, F.; Shishov, A.; Lisenkov, E.
Pre-test CFD simulations of Gidropress mixing facility experiments using ANSYS CFX
17th Symposium of AER on VVER Reactor Physics and Reactor Safety, 24.-29.09.2007, Yalta, Ukraine
Proceeding, 555-571

Höhne, T.; Vallee, C.
Experimental and numerical prediction of horizontal stratified flows using the HAWAC facility
ANSYS Conference & 25th CADFEM Users' Meeting, 21.-23.11.2007, Dresden, Germany
CD-ROM, paper 679

Höhne, T.; Vallee, C.; Prasser, H.-M.
Experimental and numerical prediction of horizontal stratified flows
International Conference on Multiphase Flow ICMF 2007, 09.-13.07.2007, Leipzig, Germany
CD-ROM, paper S5_Tue_C_23

Hozoi, L.; Birkenheuer, U.; Fulde, P.
Ab initio method for excited states in solids: correlation corrections to the band structure of oxides
J.-M. Rost, S. Flach, U. Gneise: MPI for the Physics of Complex Systems: Scientific Report 2005-2006, Dresden: MPI-PKS, 2007, 86-91

Hristov, H. V.; Boden, S.; Hampel, U.; Kryk, H.
Numerical simulation of two-phase flow in a stirred reactor
International Conference on Multiphase Flow, ICMF 2007, 09.-13.07.2007, Leipzig, Germany
Paper No PS6_8

Kliem, S.
AER working group D on VVER safety analysis – report of the 2007 meeting
17th Symposium of AER on VVER Reactor Physics and Reactor Safety, 24.-29.09.2007, Yalta, Ukraine
Proceedings of the 17th Symposium of AER on VVER Reactor Physics and Reactor Safety, Budapest, 9789633726358, 573-579

Kliem, S.; Höhne, T.; Rohde, U.; Kozmenkov, Y.
DYN3D/ATHLET and ANSYS CFX calculations of the OECD VVER-1000 coolant transient benchmark
5th International conference on safety assurance of NPP with WWER, 29.05.-01.06.2007, Podolsk, Russia
Proceedings of the 5th International conference on safety assurance of NPP with WWER

Kliem, S.; Rohde, U.
Boron dilution analyses at reactor shutdown conditions using the coupled code DYN3D/ATHLET
Annual Meeting on Nuclear Technology 2007, 22.-24.05.2007, Karlsruhe, Germany
Proceedings of the Annual Meeting on Nuclear Technology 2007: INFORUM GmbH, 51-57

Kliem, S.; Rohde, U.
DYN3D/ATHLET calculations of a boron dilution transient during natural circulation conditions
NURETH-12 - International Topical Meeting on Nuclear Reactor Thermal Hydraulics, 30.09.-04.10.2007, Pittsburgh, United States
Proceedings of the 12th International Topical Meeting on Nuclear Reactor Thermal Hydraulics, CDROM, paper 053, 0894480588

Konheiser, J.; Viehrig, H.-W.; Rindelhardt, U.; Noack, K.; Gleisberg, B.
Greifswald VVER-440 RPV investigations: neutron dosimetry and material tests
5th International Conference: Safety Assurance of NPP with WWER, 29.05.-01.06.2007, Podolsk, Russia
Conference Proceedings, paper 137

Krepper, E.; Beyer, M.; Frank, T.; Lucas, D.; Prasser, H.-M.
Application of a population balance approach for polydispersed bubbly flows
International Conference on Multiphase Flow - ICMF 2007, 09.-13.07.2007, Leipzig, Germany
Poster No PS6_6

Krepper, E.; Cartland-Glover, G.; Grahn, A.; Weiß, F.-P.; Alt, S.; Hampel, R.; Kästner, W.; Seeliger, A.
CFD-modelling of mineral wool in the containment sump
Annual Meeting on Nuclear Technology 2007, 22.-24.05.2007, Karlsruhe, Germany

Krepper, E.; Cartland-Glover, G.; Grahn, A.; Weiss, F.-P.; Alt, S.; Hampel, R.; Kästner, W.; Seeliger, A.
CFD-modelling of insulation debris transport phenomena in water flow
NURETH-12 - International Topical Meeting on Nuclear Reactor Thermal Hydraulics, 30.09.-04.10.2007, Pittsburgh, USA

Krepper, E.; Frank, T.; Lucas, D.; Prasser, H.-M.; Zwart, P. J.
Inhomogeneous MUSIG model – a population balance approach for polydispersed bubbly flows
International Conference on Multiphase Flow - ICMF 2007, 09.-13.07.2007, Leipzig, Germany
Paper No S_6_Thu_B_51

Krepper, E.; Frank, T.; Lucas, D.; Prasser, H.-M.; Zwart, Philip J.
Inhomogeneous MUSIG model – a population balance approach for polydispersed bubbly flows
NURETH-12 - International Topical Meeting on Nuclear Reactor Thermal Hydraulics, 30.09.-04.10.2007, Pittsburgh, USA

Lucas, D.; Bestion, D.; Bodèle, E.; Scheuerer, M.; F. D'Auria, D. Mazzini; Smith, B.; Tiselj, I.; Martin, A.; Lakehal, D.; Seynhaeve, J.-M.; Kyrki-Rajamäki, R.; Ilvonen, M.; Macek, J.
On the simulation of two-phase flow pressurized thermal shock (PTS)
NURETH-12 - International Topical Meeting on Nuclear Reactor Thermal Hydraulics, paper [035], 30.09.-04.10.2007, Pittsburgh, Pennsylvania, United States

Lucas, D.; Krepper, E.; Prasser, H.-M.; Manera, A.
Stability effect of the lateral lift force in bubbly flows
International Conference on Multiphase Flow - ICMF 2007, 09.-13.07.2007, Leipzig, Germany
paper S1_Mon_C_9

Lucon, E.; Viehrig, H.-W.
Round-Robin exercise on instrumented impact testing of precracked Charpy specimens (IAEA Coordinated Research Program Phase 8)
2007 ASME Pressure Vessels and Piping Division Conference, 22.-26.07.2007, San Antonio, Texas, USA
Proceedings of PVP2007: ASME Publications

Manera, A.; Ozar, B.; Paranjape, S.; Ishii, M.; Prasser, H.-M.
Comparison between wire-mesh sensors and conductive needle-probes for measurements of two-phase flow parameters
15th International Conference on Nuclear Engineering (ICONE15), 22.-26.04.2007, Nagoya, Japan
paper ICONE15-10312

Merk, B.
Consequences of different fuel cycle options on the produced plutonium mass in the German reactor park
Jahrestagung Kerntechnik 2007, 22.-24.05.07, Karlsruhe, Germany

Merk, B.
An analytical solution for a simple time dependent neutron transport problem with external source
20th International Conference on Transport Theory, 22.-28.07.07, Obninsk, Russia
Book of Abstracts

Moretti, F.; Melideo, D.; D'Auria, F.; Höhne, T.; Kliem, S.
CFX simulations of ROCOM slug mixing experiments
15th International Conference on Nuclear Engineering (ICONE15), 22.-26.04.2007, Nagoya, Japan
ICONE15-10461

Noack, B. R.; Schlegel, M.; Ahlborn, B.; Mutschke, G.; Morzynski, M.; Comte, P.
A finite-time thermodynamics of unsteady flows - from the onset of vortex shedding to developed homogeneous turbulence
Joint European Thermodynamics Conference IX, 12.-15.06.2007, Saint Entienne, France
Proceedings, 129-132

Pahl, E.; Birkenheuer, U.
Frozen local hole approximation
J.-M. Rost, S. Flach, U. Gneise: MPI for the Physics of Complex Systems: Scientific Report 2005-2006, Dresden: MPI-PKS, 2007, 81-86

Prasser, H.-M.; Beyer, M.
Bubble recognition algorithms for the processing of wire-mesh sensor data
International Conference on Multiphase Flow, ICMF 2007, 09.-13.07.2007, Leipzig, Germany
paper:S7_Thu_B_50

Rindelhardt, U.; Bodach, M.
Operational experiences with megawatt PV plants in central Germany
22. European Photovoltaic Solar Energy Conference, 03.-07.09.2007, Milano, Italy
Operational Experiences with Megawatt PV Plants in Central Germany, 3-936338-22-1, 2952-2955

Rindelhardt, U.; Viehrig, H.-W.; Konheiser, J.; Noack, K.; Gleisberg, B.
RPV material investigations of the former VVER-440 Greifswald NPP
15th International Conference on Nuclear Energy (ICONE15), 22.-26.04.2006, Nagoya, Japan
Proceedings of ICONE-15, JSME No 07-202, Contribution 15-1035

U., Rindelhardt; Th., Sander; J., Zschernig
Elektroenergiebereitstellung
W. Schufft: Taschenbuch der Elektrischen Energietechnik, München: Hanser-Verlag, 2007, 978-3-446-40475-5

Ruyer, P.; Seiler, N.; Beyer, M.; Weiss, F.-P.
A bubble size distribution model for the numerical simulation of bubbly flows
International Conference on Multiphase Flow, ICMF 2007, 09.-13.07.2007, Leipzig, Germany
paper: S6_Thu_A_48

Schleicher, E.; Da Silva, M. J.; Paul, S.; Hampel, U.
HF-Modulationsspektroskopie zur Bestimmung optischer Parameter in trüben Medien
8. Dresdner Sensor-Symposium, 10.-12.12.2007, Dresden, Germany
Dresdner Beiträge zur Sensorik, Band 29, Dresden: TUDpress, Verlag der Wissenschaft GmbH, ISBN-13: 978-3-940046-45-1, 79-82

Schleicher, E.; Hampel, U.; Da Silva, M. J.; Thiele, S.
Fast optical tomography for transient process diagnostics
5th World Congress on Industrial Process Tomography, 03.-06.09.2007, Bergen, Norway

Stefani, F.; Gerbeth, G.; Günther, U.; Xu, M.; Sorriso-Valvo, L.
Noise induced relaxation oscillations and earth's magnetic field reversals
IUGG XXIV 2007, 02.-13.07.2007, Perugia, Italy
Earth: our changing planet, Proceedings of IUGG XXIV General Assembly, Perugia: Umbria Scientific Meeting Association, 978-88-95852-25-4, 2483

Thiele, S.; Da Silva, M. J.; Hampel, U.
Development of a high-speed capacitive surface sensor for fluid distribution imaging
IEEE SENSORS 2007 Conference, 28.-31.10.2007, Atlanta, USA
Proceedings of the 6th Annual IEEE Conference on Sensors 2007 Atlanta, Stoughton, Wisconsin, USA: The Printing House, Inc., 1-4244-1262-5, 236-239

Ulbricht, Andreas; Bergner, Frank; Hein, Hieronymus; Kammel, Martin
Flux dependene of cluster formation in neutron irradiated weld material
4th European Conference on Neutron Scattering, 25.-29.06.2007, Lund, Sweden
Poster Presentations 4th European Conference on Neutron Scattering, Lund: Media-Tryck, 434-434

Vaibar, R.; Sühnel, T.; Da Silva, M. J.
Buoyancy driven turbulent flow and experimental validation at the VeMix test facility
Computational Mechanics 2007, 05.-07.11.2007, Castle Nectiny, Czech Republic

Vallee, C.
Hydraulic jump in a closed horizontal two-phase flow channel
International Conference on Multiphase Flow 2007, 09.-13.07.2007, Leipzig, Germany
Paper N° S5_Fri_A_63

Vallee, C.
Experiments on the interface dynamics of stratified air/water flows
Jahrestagung Kerntechnik 2007, 22.-24.05.2007, Karlsruhe, Germany
Jahrestagung Kerntechnik 2007 - Fachsitzung, Berlin: INFORUM Verlags- und Verwaltungsgesellschaft, 23-26

Vallee, C.; Höhne, T.
Experimental investigation and CFD validation of horizontal air/water slug flow
15th International Conference on Nuclear Engineering (ICONE15), 22.-26.04.2007, Nagoya, Japan

Viehrig, H.-W.; Lucon, E.
IAEA coordinated research project on Master Curve Approach to monitor fracture toughness of reactor pressure vessel steels: effect of loading rate
2007 ASME Pressure Vessels and Piping Division Conference, 22.-26.07.2007, San Antonio, Texas, USA
Proceedings of PVP2007: ASME Publication

Viehrig, H.-W.; Rindelhardt, U.; Schuhknecht, J.
Post mortem investigations of the NPP Greifswald WWER-440 reactor pressure vessels
19th International Conference on Structural Mechanics in Reactor Technology (SMiRT-19), 12.-17.08.2007, Toronto, Canada
Proceedings of the 19th International Conference on Structural Mechanics in Reactor Technology

Viehrig, H.-W.; Rindelhardt, U.; Schuhknecht, J.
Post mortem investigations of the NPP Greifswald WWER-440 reactor pressure vessels
33. MPA-Seminar Werkstoff- und Bauteilverhalten in der Energie- und Anlagentechnik, 11.-12.10.2007, Stuttgart, Germany
Proceedings 33. MPA-Seminar "Werkstoff- & Bauteilverhalten in Energie- & Anlagentechnik", Stuttgart: Materialprüfungsanstalt Universität Stuttgart, 4-1-4-9

Weier, T.; Cierpka, C.; Gerbeth, G.
Vortex structures in the separated flow on an inclined flat plate under electromagnetic forcing: influences of excitation wave form, frequency, and amplitude
5th International Symposium on Turbulence and Shear Flow Phenomena, 27.-29.08.2007, München, Germany
Proceedings of the 5th International Symposium on Turbulence and Shear Flow Phenomena, 1105-1110

Weiß, F.-P.; Willschütz, H.-G.
Wie sicher sind Kernkraftwerke? - Stand der Sicherheitsforschung
50 Jahre Forschung für die friedliche Nutzung der Kernenergie, 28.09.2006, Dresden, Deutschland
Sitzungsberichte der Leibniz-Sozietät, Berlin: Leibniz-Sozietät e.V., 978-3-89626-689-7, 91-114

Willers, B.; Dong, J.; Metan, V.; Smieja, F.; Eckert, S.; Eigenfeld, K.
The influence of alternating magnetic fields on structure formation in Al-Si alloys during solidification
5th Decennial International Conference on Solidification Processing, 23.-25.07.07, Sheffield, United Kingdom
Proceedings of the 5th Decennial International Conference on Solidification Processing, Sheffield, 978-0-9522507-4-6, 168-171

Zhang, C.; Eckert, S.; Gerbeth, G.
Rising gas bubbles in a liquid metal under the influence of external magnetic fields
International Conference on Multiphase Flow - ICMF2007, 09.-13.07.2007, Leipzig, Germany, No. 279

Zippe, C.; Hoppe, D.; Bieberle, A.; Hampel, U.
Concepts for a sub-millimetre resolving gamma ray CT for nondestructive testing applications
5th World Congress on Industrial Process Tomography, 03.-06.09.2007, Bergen, Norway

Zurbuchen, C.; Viehrig, H.-W.
Master Curve applicability to highly neutron irradiated reactor pressure vessel steels - results of a BMWi grant project
33. MPA-Seminar, 11.-12.10.2007, Stuttgart, Germany
Proceedings 33. MPA-Seminar "Werkstoff- & Bauteilverhalten in Energie- & Anlagentechnik", Stuttgart: Materialprüfungsanstalt Universität Stuttgart, 1861-5414

FZD reports and other reports

Abendroth, M.; Altstadt, E.
COVERS WP4 Benchmark 1: Fracture mechanical analysis of a thermal shock scenario for a VVER-440 RPV
Wissenschaftlich-Technische Berichte / Forschungszentrum Dresden-Rossendorf; FZD-474
2007

Höhne, T.; Konheiser, J.; Kozmenkov, K.; Noack, K.; Schäfer, F.; Schleicher, U.; Rindelhardt, U.; Rohde, U.; Ulbricht, A.; Weiß, F.-P.
Scientific-technical cooperation between FZR and Russia in the field of NPP safety research
Wissenschaftlich-Technische Berichte / Forschungszentrum Dresden-Rossendorf; FZD-468
2007

Lucas, D.; Krepper, E.
CFD models for polydispersed bubbly flows
Wissenschaftlich-Technische Berichte / Forschungszentrum Dresden-Rossendorf; FZD-486
2007

Prasser, H.-M.; Beyer, M.; Carl, H.; Al Issa, S.; Schütz, P.; Pietruske, H.
Experiments on two-phase flow in a vertical tube with a moveable obstacle
Wissenschaftlich-Technische Berichte / Forschungszentrum Dresden-Rossendorf; FZD-483
2007

Prasser, H.-M.; Beyer, M.; Carl, H.; Manera, A.; Schütz, H.; Pietruske, P.
Experiments on upwards gas/liquid flow in vertical pipes
Wissenschaftlich-Technische Berichte / Forschungszentrum Dresden-Rossendorf; FZD-482
2007

Prasser, H.-M.; Lucas, D.; Beyer, M.; Vallée, C.; Krepper, E.; Höhne, T.; Manera, A.; Carl, H.; Pietruske, H.; Schütz, P.; Al Issa, S.; Zaruba, A.; Shi, J.-M.; Weiß, F.-P.
Construction and execution of experiments at the multi-purpose thermal hydraulic test facility TOPFLOW for generic investigations of two-phase flows and the development and validation of CFD codes - Final report
Wissenschaftlich-Technische Berichte / Forschungszentrum Dresden-Rossendorf; FZD-481
2007

Prasser, H.-M.; Lucas, D.; Beyer, M.; Vallée, C.; Krepper, E.; Höhne, T.; Manera, A.; Carl, H.; Pietruske, H.; Schütz, P.; Zaruba, A.; Al Issa, S.; Shi, J.-M.; Weiß, F.-P.
Aufbau und Durchführung von Experimenten an der Mehrzweck-Thermohydraulikversuchsanlage TOPFLOW für generische Untersuchungen von Zweiphasenströmungen und die Weiterentwicklung und Validierung von CFD-Codes - Abschlussbericht
Wissenschaftlich-Technische Berichte / Forschungszentrum Dresden-Rossendorf; FZD-480
2007

Shi, J.-M.; Rohde, U.; Prasser, H.-M.
Turbulent dispersion of bubbles in poly-dispersed gas-liquid flows in a vertical pipe
Wissenschaftlich-Technische Berichte / Forschungszentrum Dresden-Rossendorf; FZD-487
2007

Shi, J.-M.; Rohde, U.; Prasser, H.-M.
Validation of the multiple velocity multiple size group (CFX10.0 N x M MUSIG) model for polydispersed multiphase flows
Wissenschaftlich-Technische Berichte / Forschungszentrum Dresden-Rossendorf; FZD-487
2007

Vallée, C.; Höhne, T.; Prasser, H.-M.; Sühnel, T.
Experimental investigation and CFD simulation of slug flow in horizontal channels
Wissenschaftlich-Technische Berichte / Forschungszentrum Dresden-Rossendorf; FZD-485
2007

Vallée, C.; Prasser, H.-M.; Sühnel, T.
Experimentelle Untersuchung von geschichteten Luft/Wasser Strömungen in einem horizontalen Kanal
Wissenschaftlich-Technische Berichte / Forschungszentrum Dresden-Rossendorf; FZD-484
2007

Viehrig, H.-W.; Zurbuchen, C.
Anwendung des Master Curve-Konzeptes zur Charakterisierung der Zähigkeit neutronenbestrahlter Reaktordruckbehälterstähle
Wissenschaftlich-Technische Berichte / Forschungszentrum Dresden-Rossendorf; FZD-476
2007

Weiß, F.-P.; Rindelhardt, U. (Editors)
Annual Report 2006 - Institute of Safety Research
Wissenschaftlich-Technische Berichte / Forschungszentrum Dresden-Rossendorf; FZD-465
2007

Kliem, S.
Realistische Simulation von Reaktivitätsstörfällen mit gekoppelten neutronenkinetisch-thermohydraulischen Systemcodes - Abschlussbericht
Forschungszentrum Rossendorf 2007; FZD\FWS\2007\11

Laczkó, G.; Kliem, S.; Rohde, U.
Erweiterung des ATHLET – Datensatzes des KKK um das 4-Quadranten-Modell des Rückströmraumes und Ergebnisse der Simulation der Transiente vom 28.06.2007
Forschungszentrum Rossendorf 2007; FZD/FWS/2007/10

Al Issa, S.
Two phase flow 1D turbulence model for poly disperse upward flow in a vertical pipe
Forschungszentrum Rossendorf 2007; FZD\FWS\2007\09

Kliem, S.
Entwicklung und Anwendung einer Methodik zur Analyse unterstellter Borverdünnungsstörfälle im Nachkühlbetrieb
Forschungszentrum Rossendorf 2007; FZD\FWS\2007\08

Altstadt, E.
Bestimmung der Eigenfrequenzen von Brennelementen
Forschungszentrum Rossendorf 2007; FZD\FWS\2007\04

Kryk, H.; Schubert, M.; Hessel, G.
Begleitende Untersuchungen zur Pilotierung eines Verfahrens zur elektrochemischen Aufbereitung saurer Wässer aus Tagebaurestseen (Zwischenbericht)
Forschungszentrum Rossendorf 2007; FZD\FWS\2007\06

Bieberle, A.; Hampel, U.; Hoppe, D.
Gammatomographie zur Messung von Voidverteilungen im SWR-Bündel am KATHY-Versuchsstand in Karlstein, Abschlussbericht 2007
Forschungszentrum Rossendorf 2007; FZD\FWS\2007\07

Lucas, D.
Synthesis report on work package 2.1: Pressurized Thermal Shock (PTS) - T0+24
Forschungszentrum Rossendorf 2007; FZD\FWS\2007\05

Kliem, S.; Sühnel, T.
Experimente an der Versuchsanlage ROCOM zum Einfluss der Dichtedifferenz auf die Kühlmittelvermischung bei postulierten Störfällen mit kleinem Leck im heißen Strang
Forschungszentrum Rossendorf 2007; FZD\FWS\2007\02n

Stefani, F.; Gerbeth, G.; Gundrum, Th.; Avalos-Zuniga, R.
The missing link: what can dynamo simulation learn from dynamo experiments?
Forschungszentrum Rossendorf 2007; FZD\FWS\2007\03

Heintze, C.
Metallographic examination, depth-sensing microhardness and modulus of Eurofer'97
Forschungszentrum Rossendorf 2007; FZD\FWS\2007\01

Granted patents

Dietrich Hoppe, Michael Christen
Anordnung zur quantitativen Bildrekonstruktion
DE 10144261B4

Jochen Zschau
Anordnung und Verfahren zur Bestimmung der Phasenverteilung in strömenden Mehrphasenmedien
DE 10318548B4

Horst-Michael Prasser, Dr. Dudlik, Andreas, Alexander Apostolidis, Stefan Schlüter, Günter Wickl
Vorrichtung zur Vermeidung von Druckstößen in Rohrleitungssystemen
DE 102004025983B4

Eckhard Schleicher, Marco Jose da Silva
Anordnung zur Messung der lokalen elektrischen Impedanz und der Temperatur in Fluiden
DE 102005046663B3

Frank Stefani, Gunter Gerbeth, Thomas Gundrum, Sven Eckert, Andreas Cramer
Verfahren und Anordnung zur kontaktlosen Bestimmung von räumlichen Geschwindigkeitsverteilungen in elektrisch leitfähigen Flüssigkeiten
EP 1285277B1

Janis Priede, Gunter Gerbeth, Regina Hermann, Günther Behr, Ludwig Schutz , Hans-Jörg Uhlemann
Verfahren und Vorrichtung zum Ziehen von Einkristallen durch Zonenziehen
DE 10328859B4

Sven Eckert, Bernd Willers, Gunter Gerbeth, Vladimir Galindo, M. Ziemann, Hans-Walter Katz, Uwe Hewelt
Verfahren zur kontrollierten Formfüllung beim Gießen metallischer Werkstoffe
DE 102006008432B4

PhD and diploma theses

PhD theses

Gábor Laczkó
Investigation of the radial ionisation distribution of heavy ions with an optical particle track chamber and Monte-Carlo simulations
Universität Frankfurt/Main

Markus Schubert
Performance enhancement of trickle bed reactors
TU Dresden

Carsten Beckert
Entwicklung des Neutronentransportcodes TransRay und Untersuchungen zur zwei- und dreidimensionalen Berechnung effektiver Gruppenwirkungsquerschnitte
TU Dresden

Diploma theses

Anne Voigt
POD-basierte Simulation und Optimierung der elektromagnetischen Kontrolle abgelöster Strömungen
TU Dresden

Michael Röder
Experimentelle Untersuchung von Temperaturverteilungen in einem durch Lorentzkräfte beeinflussten Rayleigh-Bénard-System
HTW Dresden

Carmen Recknagel
Registrierende Nanohärtemessung und begleitende Atomkraftmikroskopie an unbestrahlten und ionenbestrahlten Stählen
TU Dresden

Sebastian Paul
Evaluierung und Erweiterung eines HF-Modulations-Laserspektrometers zur Bestimmung optischer Parameter in trüben Medien
HTW Dresden

Andreas Weller
Validierung, Erweiterung und Anpassung eines FE-Modells zur Simulation einer RDB-Bodenkalotte in einem Kriechverfahrensexperiment
TU Bergakademie Freiberg

Martin Mann
Bestimmung der Wasserausbreitung im Reaktorgebäude bei einem Rohrleitungsleck im Wasserbereich der Kondensationskammer
TU Dresden

Martin Ritterath
Konzeption und Aufbau eines schnellen Vielkanalmesssystems zur digitalen Erfassung von Thermoelementsignalen für extreme Bedingungen
TU Dresden

Sebastian Thiele
Entwicklung und Aufbau eines kapazitiven Oberflächensensors für die Phasenverteilungs- und Geschwindigkeitsmessung zweiphasiger Strömungen
TU Dresden

Awards

U. Hampel, M. Bieberle, F. Fischer, E. Schleicher, D. Hoppe

Technologiepreis des FZD 2007
Ultraschnelle Elektronenstrahl-Röntgen-Computertomographie
Date of award: 6 February 2008

S. Thiele

Student Paper Award, Third Place
IEEE Sensors 2007 Atlanta / USA
Development of a high-speed capacitive surface sensor for fluid distribution imaging
Date of award: 30 October 2007

Beste Diplomarbeit am Institut für Festkörperelektronik (IFE) Dresden 2007
Entwicklung und Aufbau eines kapazitiven Oberflächensensors für die Phasenverteilungs- und Geschwindigkeitsmessung zweiphasiger Strömungen
Date of award: November 2007

M. da Silva

Best Poster Award Graduate Meeting FZD 2007
Capacitance wire mesh sensor for two-phase flow measurement
Date of award: 28 September 2007

F. Fischer

Best Presentation Award Graduate Meeting 2007
Ultra fast X-ray tomography for two-phase flow measurement
Date of award: 28 September 2007

A. Bieberle

Award winner of ICONE-15 Student Competition, Nagoya/Japan
A high-resolution gamma tomography for void fraction distribution measurements in fuel bundles
Date of award: 20 April 2007

H.-G. Willschütz

Karl-Wirtz-Preis 2007 der KTG
Thermomechanische Analyse und Simulation eines Reaktordruckbehälters in der Spätphase eines Kernschmelzunfalls
Date of award: 21 May 2007

Guests

Dong, Jie Dr.
01 January 2007 - 30 June 2007
Shanghai Jiao Tong University / China

Bousbia Salah, Anis Dr.
30 October 2006 - 30 April 2007
University of Pisa / Italy

Kuchin, Aleksander
15 April 2007 – 22 April 2007
State scientific and technical center on nuclear and radiation safety, Kiev / Ukraine

Khalimonchuk, Vladimir Dr.
15 April 2007 – 22 April 2007
State scientific and technical center on nuclear and radiation safety, Kiev / Ukraine

Ovdiyenko, Yuri
15 April 2007 – 06 May 2007
State scientific and technical center on nuclear and radiation safety, Kiev / Ukraine

Prikhodko, Vadim
06 May 2007 – 30 June 2007
Budker Institute of Nuclear Physics, Novosibirsk / Russian Federation

Ren, Zhongming Prof.
09 May 2007 – 14 May 2007
University of Shanghai / China

Fautrelle, Yves Prof.
29 May 2007 – 31 May 2007
SIMaP Laboratory, Grenoble / France

Borodkin, Pavel
10 June 2007 – 31 December 2007
Scientific and Engineering Centre for Nuclear and Radiation Safety (SEC-NRS) of
ROSTECHNADZOR, Moscow / Russian Federation

Tsofin, Vladimir
12 June 2007 – 17 June 2007
Scientific and Engineering Centre for Nuclear and Radiation Safety (SEC-NRS) of
ROSTECHNADZOR, Moscow / Russian Federation

Khrennikov, Nikolai Dr.
12 June 2007 – 17 June 2007
Scientific and Engineering Centre for Nuclear and Radiation Safety (SEC-NRS) of
ROSTECHNADZOR, Moscow / Russian Federation

Danitcheva, Irina Dr.
12 June 2007 – 17 June 2007
Scientific and Engineering Centre for Nuclear and Radiation Safety (SEC-NRS) of
ROSTECHNADZOR, Moscow / Russian Federation

Samsonov, Boris Prof.
27 June 2007 – 14 July 2007
23 July 2007 – 27 August 2007
24 October 2007 – 05 November 2007
Tomsk State University / Russian Federation

Gokhman, Oleksander Prof.
01 August 2007 – 31 October 2007
Southukrainian State University of Education, Odessa / Ukraine

Pivovarov, Valeriy Dr.
07 August 2007 – 30 September 2007
Institute of Physics and Power Engineering, Obninsk / Russian Federation

Ivanov, Alexandre Prof.
19 September 2007 – 27 September 2007
Budker Institute of Nuclear Physics, Novosibirsk / Russian Federation

Matveev, Yuriy Dr.
22 August 2007 – 30 September 2007
Institute of Physics and Power Engineering, Obninsk / Russian Federation

Kirillov, Oleg Dr.
03 September 2007 – 31 October 2007
Lomonosov Moscow State University / Russian Federation

Otahal, Jan
01 November 2007 – 31 December 2007
Brno University / Czech Republic

Ovdiyenko, Yuri
04 November 2007 – 10 November 2007
State scientific and technical center on nuclear and radiation safety, Kiev / Ukraine

Jerjemenko, Maxim
04 November 2007 – 10 November 2007
State scientific and technical center on nuclear and radiation safety, Kiev / Ukraine

Anikeev, Andrey Dr.
28 November 2007 – 19 December 2007
Budker Institute of Nuclear Physics, Novosibirsk / Russian Federation

Plevachuk, Yuriy
03 December 2007 – 06 December 2007
Lviv University / Ukraine

Priede, Janis
16 December 2007 – 19 December 2007
Coventry University / United Kingdom

Glivici, Varvara
19 December 2007 – 22 December 2007
Moldova State University, Chisinau / Moldova

FZD fellows

Hoogenboom, Eduard Prof.
03 September 2007 - 07 September 2007
15 October 2007 – 20 October 2007
25 November 2007 – 30 November 2007
Delft University of Technology / Netherlands

Anglart, Henryk Prof.
08 October 2007 – 07 November 2007
Royal Insitute of Technology, Stockholm / Sweden

Meetings und workshops

Kick-Off-Meeting of the EU Integrated Project MAGFLOTOM (**Mag**netic **flo**w **tom**ography in technology, geophysics, and ocean flow research)
12 participants
Rossendorf, 01-02 February 2007

EU ISTC Contact Expert Group Meeting on Severe Accident Management (CEG-SAM)-Meeting
35 participants
Rossendorf, 07-09 March 2007

2nd International Workshop on Measuring Techniques for Liquid Metal Flows (MTLMF2007)
110 participants
Dresden, 23-25 April 2007
Supported by EU, Deutsche Forschungsgemeinschaft in the framework of the Collaborative Research Centre SFB609, and German Alliance for Competence in Nuclear Technology

ANSYS-FZD Short Course and Workshop
Multi-Phase Flow: Simulation, Experiment and Application
108 participants
Dresden, 25-27 April 2007
Supported by German Alliance for Competence in Nuclear Technology

International Conference on Multi-Phase Flow (ICMF)
800 participants
Leipzig, 09-13 July 2007
FZD was member of the Local Organising Committee

EU COVERS (**Co**llaborative R&D in the area of **V**V**ER** operational **S**afety and mobilisation of national programmes) **Training Course on Materials Ageing**
27 participants
Rossendorf, 08 October 2007

EU COVERS (**Co**llaborative R&D in the area of **V**V**ER** operational **S**afety and mobilisation of national programmes) **Training Course on Operational Safety**
40 participants
Rossendorf, 09 October 2007

3rd Sino-German Workshop on Electromagnetic Processing of Materials
65 participants
Shanghai, 15-19 October 2007
Supported by Sino-German Center for Research promotion Beijing and Deutsche Forschungsgemeinschaft in the framework of the Collaborative Research Centre SFB609

PhD Students Seminar of Kompetenzzentrum Ost für Kerntechnik
30 participants
Dresden, 12 December 2007

Seminars of the institute

Dr. K. Noack, Dr. A. Rogov
Ist die GDT-Fusionsneutronenquelle als Driver in einem unterkritischen System zur Transmutation von minoren Aktiniden geeignet?
11 January 2007

Dr. H. Kryk, G. Hessel, Dr. W. Schmitt
Online-Monitoring von Grignard-Reaktionen
25 January 2007

Prof. K. Kugeler, Dr. I.M. Tragsdorf, N. Pöppe (RWTH Aachen)
Hochtemperaturreaktoren – weltweiter Stand und Erwartungen
08 February 2007

Dr. E. Krepper, Dr. D. Lucas
Das polydisperse Multi-Size Group Model MUSIG im CFD-Code ANSYS-CFX und seine Validierung an Experimentaldaten
22 February 2007

J. Konheiser, Prof. U. Rindelhardt, Dr. H.-W. Viehrig, Dr. B. Gleisberg (VKTA)
Erste Ergebnisse der Materialuntersuchungen vom Reaktordruckbehälter des Blockes 1 des KKW Greifswald
16 March 2007

C. Beckert
Entwicklung des Neutronentransportcodes TransRay und Untersuchungen zur 2D- und 3D-Berechnung effektiver Gruppenquerschnitte
05 April 2007

St. Wissel (Universität Stuttgart)
Die Bedeutung der Kernenergie in liberalisierten Energiemärkten und im Hinblick auf eine nachhaltige Energieversorgung
20 April 2007

Dr. G. Cartland-Glover, Dr. E. Krepper
Modelling of sedimentation, re-suspension and dispersion in particle-loaded fluid flows
10 May 2007

Y. Fautrelle (EPM/SIMaP Laboratory Cedex / France)
Applications of MHD to materials processing
30 May 2007

St. Bugat (Chef de Groupe Comportement des Matériaux et des Structures EDF R&D/Dpt. MMC)
A software integration platform for prediction of irradiation damage effects on reactor components
31 May 2007

M. Große (FZ Karlsruhe)
Vergleich des Notkühlverhaltens von PWR und WWER
07 June 2007

M. da Silva, Dr. D. Hoppe
Räumlich und zeitlich hoch auflösende Strömungsmessung in einer rotierenden
Turbokupplung mittels Leitfähigkeitsflächensensoren und Gammatomografie
21 June 2007

M. Bieberle, F. Fischer
Ultraschnelle Röntgen-CT mit gescanntem Elektronenstrahl für die Untersuchung transienter
Prozesse
29 September 2007

E.-A. Reinecke (FZ Jülich, Institut für Energieforschung, Sicherheitsforschung und Reaktortechnik)
Experimentelle und theoretische Untersuchungen zum Betriebsverhalten katalytischer H_2-Rekombinatoren
18 October 2007

C. Zurbuchen, Dr. H.-W. Viehrig
Anwendung des Master-Curve-Konzeptes zur Charakterisierung der Zähigkeit
neutronenbestrahlter Reaktordruckbehälterstähle
04 October 2007

Prof. E. Hoogenboom (Delft University of Technology / Netherlands)
Monte Carlo methods in reactor physics: basics, current capabilities and perspectives
15 October 2007

Prof. H. Anglart (KTH Stockholm / Sweden)
The analysis of critical heat flux in light water reactor
22 October 2007

J. Otahal
Untersuchung von Zweiphasenströmungen in einem Schaumzerstäuber
01 November 2007

Dr. U. Grundmann, C. Beckert
Mehrgruppenmethode und SP_3-Transportnäherung in DYN3D
28 November 2007

M. da Silva
Kapazitäts-Gittersensor: Prinzip und Anwendung
13 December 2007

Lecture courses

Frank-Peter Weiß
Zuverlässigkeit und Sicherheit technischer Systeme
TU Dresden, Fakultät Maschinenwesen
Summer semester 2007 and winter semester 2007

Matthias Werner
Zuverlässigkeit und Sicherheit technischer Systeme
TU Dresden, Fakultät Maschinenwesen
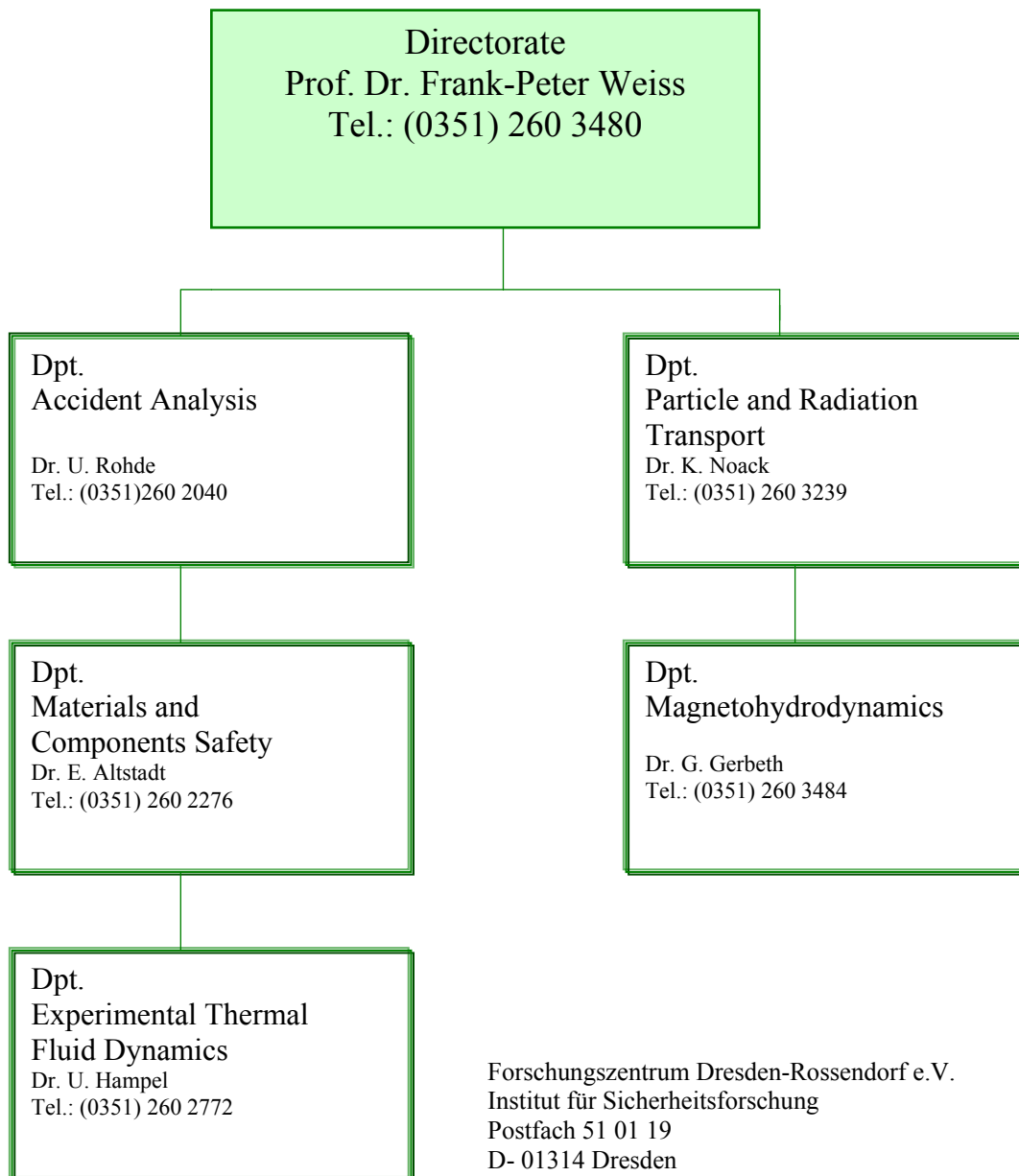Summer semester 2007 and winter semester 2007

Udo Rindelhardt
Erneuerbare Energien I und II
Technische Universität Chemnitz, Fakultät für Elektrotechnik/Informationstechnik
Summer semester 2007 and winter semester 2007

Uwe Hampel
Computertomographie in der Medizin und Prozessdiagnostik
TU Dresden, Fakultät Elektro- und Informationstechnik
Summer semester 2007 and winter semester 2007

Departments of the institute

Directorate
Prof. Dr. Frank-Peter Weiss
Tel.: (0351) 260 3480

Dpt.
Accident Analysis

Dr. U. Rohde
Tel.: (0351)260 2040

Dpt.
Particle and Radiation
Transport
Dr. K. Noack
Tel.: (0351) 260 3239

Dpt.
Materials and
Components Safety
Dr. E. Altstadt
Tel.: (0351) 260 2276

Dpt.
Magnetohydrodynamics

Dr. G. Gerbeth
Tel.: (0351) 260 3484

Dpt.
Experimental Thermal
Fluid Dynamics
Dr. U. Hampel
Tel.: (0351) 260 2772

Forschungszentrum Dresden-Rossendorf e.V.
Institut für Sicherheitsforschung
Postfach 51 01 19
D- 01314 Dresden

Personnel

Director: Prof. Dr. F.-P. Weiß

Scientific Staff
Abendroth, Martin Dr.
Altstadt, Eberhard Dr.
Beckert, Carsten
Bergner, Frank Dr.
Beyer, Matthias
Birkenheuer, Uwe Dr.
Bodele, Emmanuel Dr.
Borodkin, Gennady
Carl, Helmar Dr.
Cartland-Glover, Gregory Dr.
Chatrov, Viktor Dr.
Cramer, Andreas Dr.
Dong, Jie
Eckert, Sven Dr.
Galindo, Vladimir Dr.
Gerbeth, Gunter Dr.
Giesecke, André
Grahn, Alexander Dr.
Grants, Ilmars Dr.
Grundmann, Ulrich Dr.
Gundrum, Thomas
Günther, Uwe Dr.
Hampel, Uwe Dr.
Hoppe, Dietrich Dr.
Höhne, Thomas Dr.
Hristov, Hristo Vesselin Dr.
Kliem, Sören
Klukins, Alexandrs Dr.
Koch, Reinhard Dr.
Krepper, Eckhard Dr.
Kryk, Holger Dr.
Kussin, Johannes Dr.
Kozmenkov, Yaroslav
Küchler, Roland Dr.
Laczko, Gabor Dr.
Legrady, David Dr.
Lucas, Dirk Dr.
Merk, Bruno Dr.
Mittag, Siegfried Dr.
Mutschke, Gerd
Noack, Klaus Dr.

Pal, Josef Dr.
Rindelhardt, Udo Prof. Dr.
Rogov, Anatoli Dr.
Rohde, Ulrich Dr.
Schäfer, Frank Dr.
Schleicher, Eckhard
Schmidtke, Martin
Schmitt, Wilfried Dr.
Schubert, Markus
Stefani, Frank Dr.
Ulbricht, Andreas Dr.
Viehrig, Hans-Werner Dr.
Weier, Tom Dr.
Werner, Matthias Dr.
Willers, Bernd
Willschütz, Hans-Georg Dr.
Xu, Mingtian Dr.
Zhang, Xiugang Dr.
Zurbuchen, Conrad

PhD Students
Al Issa, Suleiman
Bieberle, André
Bieberle, Martina
Bilodid, Yuri
Boden, Stephan
Buchenau, Dominique
Cierpka, Christian
Da Silva, Marco
Fischer, Frank
Heintze, Cornelia
Liao, Yixiang
Miao, Xincheng
Räbiger, Dirk
Schlemmer, Tobias
Schuhknecht, Jan
Timmel, Klaus
Tusheva, Polina
Vallee, Christophe
Wondrak, Thomas
Zhang, Chaojie

Technical Staff
Berger, Torsten
Bombis, Doris
Borchardt, Steffen
Erlebach, Stephan
Fleischer, Andreas
Forker, Klaus
Futterschneider, Hein
Gommlich, André
Henke, Steffen
Hessel, Günther
Konheiser, Jörg
Kunadt, Heiko
Lindner, Klaus
Losinski, Claudia
Müller, Gudrun Dr.
Nowak, Bernd
Pietzsch, Jens
Pietruske, Heiko
Richter, Annett
Richter, Henry
Richter, Joachim
Roßner, Michaela
Rott, Sonja
Rußig, Heiko
Schleßiger, Heike
Schneider, Gisela
Schütz, Peter
Skorupa, Ulrich
Sühnel, Tobias
Tamme, Marko
Tschofen, Martin
Vetter, Petra
Webersinke, Wolfgang
Weichelt, Steffen
Weiß, Rainer
Wollrab, Eginhard
Zimmermann, Wilfried
Zippe, Cornelius Dr.